Measurement of the Transverse Momentum Differential Cross-Section for Z $\longrightarrow \mu^+\mu^-$ Events in $\bar{p}p$ Collisions at $\sqrt{s} = 1.8$ TeV

by

Mark T. Krasberg

A dissertation submitted in partial fulfillment
of the requirements for the degree of
Doctor of Philosophy
(Physics)
in The University of Michigan
2003

Doctoral Committee:

Professor J. Wehrley Chapman, Chair
Professor Dante Amidei
Professor Hugh Aller
Professor August Evrard
Professor Y. P. Yao

Table of Contents

Chapter

List of Tables

Table

List of Figures

Figure

List of Appendices

Appendix

Chapter 1

Introduction

In 1961 Sheldon Lee Glashow, while working on electroweak unification gauge theory, developed a model in which he introduced a massive neutral intermediate vector boson, called Z [1],[2],[3]. By 1967 Steven Weinberg and Abdus Salam had independently solved the theoretical problems with this model and developed their own self-consistent theory. The main advantage of their theory was that it utilized a mathematical concept known as spontaneous symmetry breaking (also known as the Higgs mechanism [27]), a by-product of which was a massive Z (in previous theories the mass of the Z had to be inserted into the theory by hand). By 1971 Gerard t'Hooft had shown that this model was renormalizable - this meant that the infinities within the theory could be canceled, which in turn meant that physics quantities of interest were calculable and experimental predictions could be made.

In 1983, Z-mediated processes which were predicted by the Glashow-Weinberg-Salam standard model were observed at CERN [27]. This was a great triumph not only for the architects of the standard model (they shared the Nobel prize for physics in 1979) but also the experimenters who were able to dramatically confirm certain important aspects of the model (Carlo Rubbia and Simon van der Meer shared the 1984 Nobel prize).

Experimenters continue to put a lot of effort into looking for new physics not described by the standard model and into making ever more stringent tests of the model. The standard model has withstood the challenge, and through repeated experimental confirmation over the last two decades it has become generally accepted by particle physicists as a correct although incomplete representation of nature on its smaller scales. However, many of the predictions that can be derived from the standard model are currently beyond our ability to test. The standard model contains a large number of experimentally determined parameters. Many of these are particle masses. There is little insight as to why particles are as heavy as they are. To further the understanding of physics beyond the standard model, physicists pursue measurements that exhibit behavior not described by the standard model. This thesis represents one such pursuit.

The main experimental apparatus that is used today to do particle physics and test aspects of the standard model is a high energy particle accelerator. One of these accelerators is at Fermilab, located in Batavia, Illinois. Between 1992 and 1996 the Fermilab Tevatron was operated in collider mode. In this mode protons and antiprotons are accelerated to nearly the speed of light and then collided head-on inside the Collider Detector at Fermilab (CDF). The particles that are created as a result of these collisions are then detected and analyzed. The proton-antiproton collisions occur with enormous impacts. An individual collision at the Tevatron between a quark from a proton and an antiquark from an antiproton (this is called an "event") very occasionally results in the creation of a Z gauge boson. Because of the tremendous energy associated with some of these collisions (this depends on the original impact parameter between the quark and antiquark), Zs can be produced with large velocity components perpendicular to the original proton-antiproton direction, and hence large transverse momentum (Pt). The Tevatron can produce Zs with higher Pt than any other accelerator. This makes the production of Zs at CDF particularly interesting. Zs are short-lived particles which very quickly decay into lighter more stable particles. One possible decay mode of a Z is into two high momentum muons. Often these muons will have high transverse momentum. CDF is uniquely designed to detect particles that decay into fragments with large transverse momentum. In fact, the CDF detector is optimized for the detection of high Pt objects, including high Pt Z decay products such as muons. From the detection of two suitable muon candidates it is possible to reconstruct the fleeting existence of a Z particle and also to study many of its properties.

The Z is currently seen as an important particle in tests of the standard model. Its role as mediator of the weak neutral current and its mixing with the photon in ElectroWeak theory positions it critically in the standard model. Since Z particles are massive they require a high-energy collision if they are to be produced. Until fairly recently no device had been built that could operate at the energy scale required to create Z particles, and hence these particles had previously gone undiscovered. Nowadays the energy reaches of the world's most powerful colliders extend to slightly above the Z energy scale, and it is at this energy scale where new phenomena are most likely to be found. The Tevatron is one such accelerator. In fact, it is the world's highest energy hadron collider.

In this thesis the Z gauge boson production rate (or cross-section) at CDF as a function of the Z transverse momentum is studied in the dimuon channel. These measurements extend over a very large range of transverse momenta. The standard model predicts what this spectrum should look like. Through a careful study of the Z transverse momentum spectrum at CDF the theoretical spectrum is compared to the experimental one, and deviations between theory and experiment are examined as an indication of new physics processes. Such a process is most likely to be found at the high Pt end of the spectrum. For example, the high energy of the collisions in the Tevatron brings up the possibility of the creation of non-standard model high-mass particles which cannot be created in any other accelerator, and these exotic particles, in certain models, are expected to decay into high Pt Zs. This would lead to an anomalous tail in the experimental Z Pt spectrum which would not be present in the standard model spectrum. No evidence for new physics is found. The standard model parameterizations, which can only be determined from experiment, are then studied. In this work, CTEQ 5L structure functions are used [44].

The organization of the thesis is as follows. In chapter 2 the experimental apparatus is described. An overview of the Fermilab Tevatron as well as the relevant parts of the CDF detector which are used in this analysis is given. Chapter 3 describes how the high Pt muon data set, which was the starting point for this analysis, was created. In chapter 4 the procedure for measuring the Z Pt spectrum is explained. In Chapter 5 the integrated luminosity measurement is described in full. Chapter 6 discusses the main sources of background in the data and a qualitative way to remove the background events from the final data set. Chapter 7 describes the identification and selection of dimuon Z events. The combined identification and trigger selection efficiencies for single high Pt muons are determined at this stage. Particular attention is first paid to the kinematical and geometrical aspects of the selection. Following this a detailed explanation of the trigger selection is given. Next, a quantitative determination of the different background removal efficiencies is performed. The final muon kinematical, geometrical and trigger efficiencies are then presented, as well as the final integrated luminosity value for each trigger region and also for each overlap region. Chapter 8 shows the raw uncorrected Z mass and Z Pt spectra. A minimum chi-squared fit is performed during a comparison of the data to the Monte Carlo in order to determine the tracking error scale factor. This analysis requires that the measurement errors for the track parameters be of the correct magnitude. Since the standard CDF measurement errors are underestimated, it is necessary to determine a factor with which to scale (increase) the measurement errors. The final set of corrections are applied to the detector simulation part of the Monte Carlo. In fact, the Monte Carlo is used to determine more accurately the different single high Pt trigger efficiency values. The Monte Carlo output is then compared to the data. The raw Z Pt spectrum histogram is compared to the corresponding Monte Carlo histogram, and it is found that the Monte Carlo must be tuned at the event generation level in order to obtain agreement between the two. In chapter 9 the Monte Carlo is used to produce the detector-independent Z Pt spectrum histogram. This histogram corresponds to the Z Pt spectrum with the effects of the acceptance and the tracking errors removed.

Finally, the conversion to “number of events per inverse picobarn per GeV” is made by applying an overall scale factor. The final spectrum obtained is then compared to the correponding spectrum in the electron channel. Appropriate conclusions are drawn. No evidence for physics beyond the standard model is observed.

Chapter 2

Experimental Apparatus

The Fermi National Accelerator Laboratory (Fermilab) is a high-energy physics laboratory located in Batavia, Illinois. The Tevatron synchrotron, the world's most powerful accelerator, operates there. Its function is to accelerate protons and antiprotons in opposite directions around a 1km radius ring to a speed a fraction of a percent less than that of the speed of light.

The particles travel the ring in controlled bunches inside a vacuum. These bunches meet head-on at predetermined locations or interaction regions around the ring. Since the cross section for a proton to strike an antiproton is so low relative to the densities of the beams, almost all of the protons and antiprotons pass by one another without colliding. However, during a crossing, occasionally a quark from a proton and an antiquark from an antiproton collide. One or more quark-antiquark collisions during an individual crossing is called an "event".

CDF [4] is centered at one of the interaction regions. It is used to study the physics of the $\bar{p}p$ collisions that occur there. In a single event it is possible for a vast number of different types of particles to come spewing out of an interaction region in all directions.

CDF is designed to detect and identify many of the particles that can be created during an event. It is also designed to measure several of the properties of the newly created particles themselves. This is achieved via a vast array of different detector subsystems, including charged particle tracking detectors, sampling calorimeters and muon detection chambers. These detectors operate over a large range of solid angle around the interaction region. In this chapter both the Tevatron and the CDF detector are described. CDF's muon detection systems are explained in detail, since these systems are the ones that are primarily used in this analysis.

2.1 Fermilab Tevatron

A schematic view of the Fermilab accelerators is shown in figure 2.1. [17] First a Cockroft-Walton (not shown) accelerator is used to accelerate negatively ionized hydrogen atoms to 750keV. The hydrogen atoms then enter the LINAC, a 500ft linear accelerator, where they are accelerated to 400MeV. The electrons are then stripped from the hydrogen atoms and the resulting proton beam is inserted into the Booster, a 250 foot radius synchrotron. After about twenty thousand revolutions their energy is elevated to 8 GeV by successive boosts from radio frequency cavities. The protons are also organized in discrete bunches by this acceleration process. Next the protons enter a 1km radius Main Ring, also a synchroton. It accelerates the protons to 150 GeV, whereupon they are ready to enter the Tevatron's ring (it lies directly underneath the Main Ring). The Tevatron accelerates the protons to their final energy of 900 GeV. In the data collected for this thesis each proton bunch typically contained 10^{11} particles, and there were usually a total of six bunches in the Tevatron at one time.

Antiprotons are produced by extracting a 120 GeV proton beam from the Main Ring and directing it at a tungsten target. One of the particle types that is produced as a by-product of the resulting impacts is antiprotons. The antiprotons are collected, stored and eventually injected first into the Main Ring, and then into the Tevatron. In the data collected for this thesis each antiproton bunch typically contained 3×10^{10} particles, and again there were usually six bunches in the Tevatron. Production of antiprotons is a fairly time-consuming operation and to some extent the successful operation of the Tevatron revolves around how quickly antiprotons can be accumulated. Both the proton and antiproton

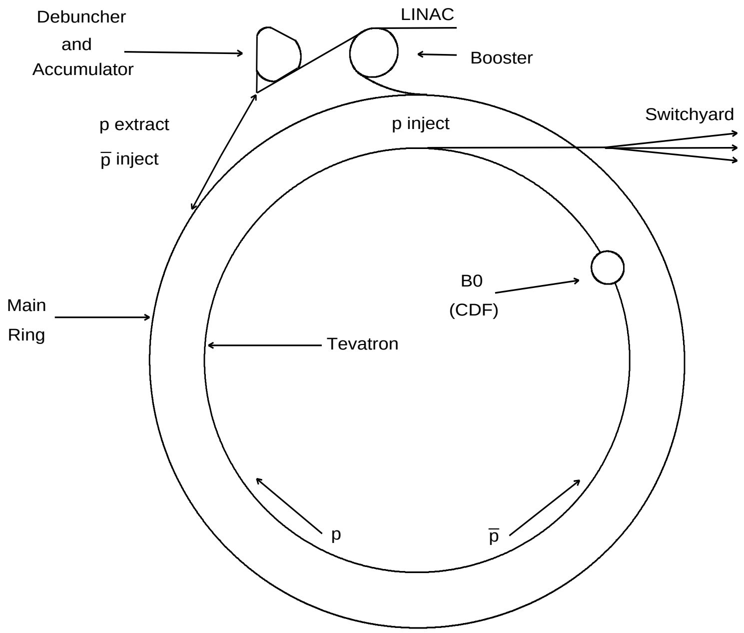

Figure 2.1: Schematic view of the Fermi National Accelerator Laboratory's Tevatron.

beams travel at an energy of 900 GeV in the Tevatron, for a total combined center of mass energy of 1.8TeV.

A "store" begins when the proton and antiproton bunches are ready to be inserted into the Tevatron. Once a store begins no further protons or antiprotons can be added. A store lasts until the rate of collisions becomes too infrequent to warrant continued operation of the Tevatron, or until the store is "lost". Particle depletion occurs either through attrition stemming from the loss of particles through the $\bar{p}p$ collisions themselves, or else from losses sustained as the beams go around the ring. Hence, the rate of collisions is greatest at the beginning of a store when the number of particles is most numerous.

The instantaneous luminosity gradually decreases as the number of protons and antiprotons orbiting the Tevatron decrease. The original design of the Tevatron called for six different interaction regions, "A-zero" thru "F-zero". These regions are located at six equidistant positions around the ring (the number of interaction regions being equal to the number of bunches is not a coincidence). Only two of these regions are currently used. They are B-zero (where CDF is located) and D-zero (where a detector called D-zero is located). By electrostatically deflecting the beams around the unused interaction regions, collisions are allowed to occur only at B-zero and D-zero. This was done to prevent collisions from occurring in the unused interaction regions, which would result in a corresponding unnecessary decay in the instantaneous luminosity.

It takes about a day for enough antiprotons to be accumulated for a store to begin. Stores typically have as large an initial instantaneous luminosity as possible, and they also last as long as is practical so that the overall delivered integrated luminosity is as large as possible. Stores typically last half a day, although many things can and do go wrong to cause the stores to be lost prematurely. For example, besides normal mechanical and electrical failures, the colliding beams have succumbed to nasty lightning strikes, a cherry tree falling on a power station, a cooling water inlet valve getting clogged with dirty lake water, and the accidental clicking on the "abort beam" window with a mouse. To maximize the total integrated luminosity that gets delivered by the accelerator to the two interaction regions, antiproton accumulation continues whilst stores are active.

$\bar{p}p$ collisions were first studied using the CDF detector at the Fermilab Tevatron during run zero in 1988-1989. The total integrated luminosity which CDF was able to analyze for this run was approximately 5 pb^{-1}. After this run the CDF detector was upgraded and the D-zero detector was installed at the D-zero interaction region. This thesis uses data from runs 1a and run 1b. Run 1a ran from August 1992 thru May 1993, when a total of 22 pb^{-1} of analyzable data was collected by CDF. Run 1b ran from 1994 to 1995 and a total of 89 pb^{-1} was collected during this period.

Technical and operational improvements in the Tevatron over the years have led to an increase in the peak instantaneous luminosity, from $2 \times 10^{30}\mathrm{cm}^{-2}\mathrm{s}^{-1}$ during run 0, to $\sim 2 \times 10^{31}\mathrm{cm}^{-2}\mathrm{s}^{-1}$ during run 1b. The higher luminosities cause significant problems for data taking, and these will be explained later. Note that the large instantaneous luminosity mentioned above means that the average number of proton-antiproton interactions per bunch crossing is greater than 2.

2.2 Collider Detector at Fermilab

Figure 2.2 shows an isometric view of the CDF detector [18]. It has both approximate azimuthal symmetry (this is symmetry in the plane that is perpendicular to the beam direction) and forward-backward symmetry. In the study of the physics of $\bar{p}p$ collisions, of primary interest are the deeply inelastic large impact collisions [22]. This type of collision is more likely to result in the production of particles with a large fraction of their momentum in the transverse plane, which means that they would be more likely to be pointed towards the central region of the detector. Unfortunately, almost all of the $\bar{p}p$ collisions are elastic and quasi-elastic small angle scatter, where the proton and the antiproton make a glancing blow off one another and end up both traveling down the beam pipe after the collision. For example, whilst the total $\bar{p}p$ collision cross section is roughly equal to 80mb ($1\text{mb} = 1 \times 10^{-25}\text{cm}^{-2}$), the cross section for a $\bar{p}p$ collision at CDF resulting in the production of a Z particle is only 6nb, which means that a Z particle is created on average only once every 15 million collisions.

The desire to analyze high transverse momentum events means two things. First, the precision detector subsystems tend to be centrally located. Second, a great deal of effort is made to record only data with head-on collisions (hard scattering), and to ignore the rest. This is accomplished via the trigger, and this will be explained in detail at the end of this chapter.

A cross-sectional view of one quadrant of the CDF detector is shown in figure 2.3. The CDF coordinate system is also shown here. The coordinate system's origin lies at the center of the detector, which is located in the bottom right corner of the picture. The z-axis points down the beamline in the direction the protons are traveling and the y-axis points upwards, leaving the x-axis pointing in the horizontal direction that is defined by the standard right-handed convention. The azimuthal angle ϕ is measured from the horizontal,

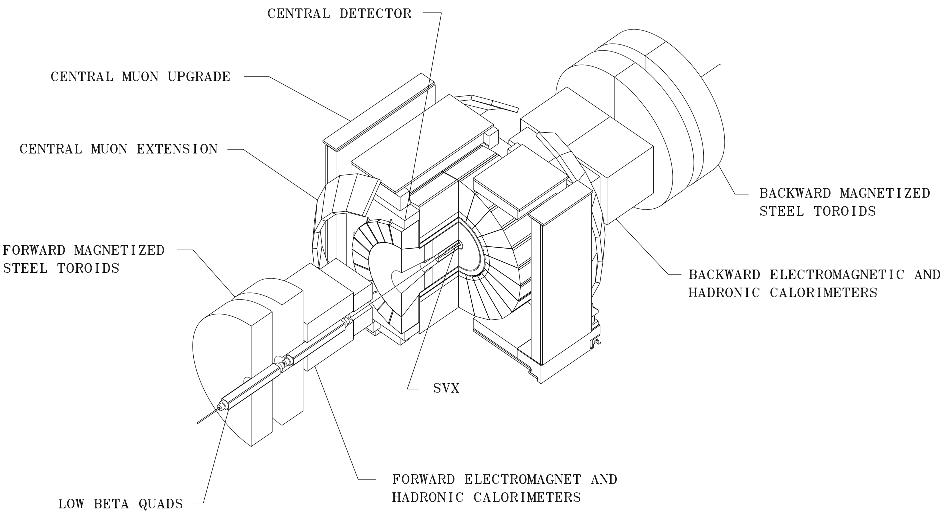

Figure 2.2: An isometric view of the CDF detector.

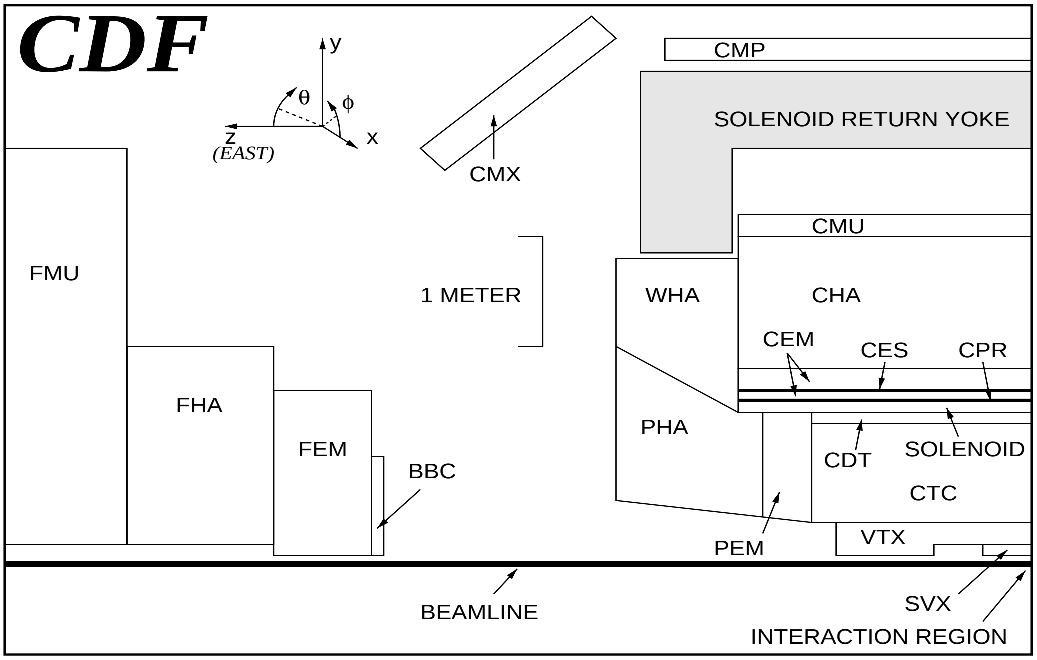

Figure 2.3: A sideview of one quadrant of the CDF detector.

and the polar angle θ is measured from the positive z-axis. A useful coordinate variable is called pseudorapidity (η), which is defined by the equation:

$$\eta = -\ln\left(\tan\left(\frac{\theta}{2}\right)\right)$$

This variable is used often instead of the polar angle θ because particle distributions tend to be somewhat flat in this variable. Hence, knowing the extent of the η-coverage for a detector is often more useful than knowing the θ-coverage.

As can be seen from the figure, a particle originating in the interaction region and exiting through the thin 1.9cm radius beryllium beam pipe will usually pass through one or more different detector subsystems.

2.3 Silicon Vertex Detector

This detector closest to the interaction region is called the Silicon Vertex Detector (SVX) [5], a 4-layer silicon microstrip vertex detector. The SVX had two primary functions. First, to find events with displaced vertices (production or decay origins). Second, to improve the tracking precision and identify multiple vertices. The SVX was also required to survive the continuous radiation it received as a result of operation of the Tevatron and still be working at the end of the run.

The SVX is capable of providing accurate initial track trajectories for charged particles in the transverse plane. It is able to distinguish whether or not a track originated as little as 17 microns away from other track vertices. This is particularly useful in the attempt to identify secondary vertices, where a newly created particle might travel a few tens of microns away from the interaction point before decaying into other particles which then travel through the SVX. The excellent resolution of the SVX was very important in the discovery of the top quark.

However, the SVX is only 51cm long. Whilst the $\bar{p}p$ interaction region has a sigma in the transverse plane of a few tens of microns, the sigma in the z-direction is about 30cm. Hence, the beam elongation in the z-direction means that the geometrical acceptance of the SVX is about 60%. Because of the fact that this analysis does not involve displaced vertices, and also because of the fact that the geometrical acceptance of the SVX is incomplete, the SVX is not used in this analysis.

2.4 Vertex Drift Chamber

The Vertex Drift Chamber (VTX) [24] lies outside of the SVX and is used to measure the $\bar{p}p$ interaction vertex along the z-axis. The VTX has a radius of 22cm and extends out to 1.5m in both directions along the beamline. It is used to determine a track's primary vertex position along the z-axis to a resolution of 1mm.

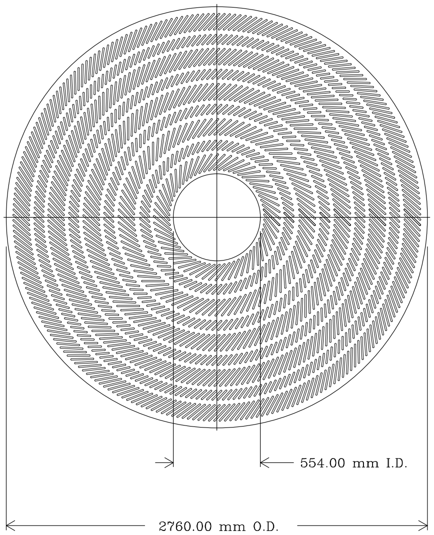

Figure 2.4: An end view of the Central Tracking Chamber (CTC).

2.5 Central Tracking Chamber

The Central Tracking Chamber (CTC) [19] provides three-dimensional tracking information at CDF. An end view of the CTC is shown in figure 2.4. The CTC is a 3.2m long drift chamber, with an inner radius of 31cm and an outer radius of 132cm. It consists of 6152 sense wires arranged into 9 superlayers. The 9 superlayers have 5 axial layers interleaved with 4 stereo layers. The 5 axial layers each have 12 layers of wires that are parallel to the beam direction and provide $r-\phi$ information. The 4 stereo layers each have 6 layers of wires that are tilted at $\pm 3^{\circ}$ with respect to the beam direction and provide $r-z$ information. Combining the data from the axial and stereo layers gives precise three-dimensional tracking information.

2.6 Solenoid

The SVX, VTX and CTC are all enclosed by a solenoid which produces a 1.4 Tesla magnetic field. This magnetic field bends the paths of charged particles in the transverse plane. By identifying tracks from the three-dimensional CTC hit positions and analyzing their curvature due to the magnetic field, the CTC is used to determine a track's momentum.

2.7 Beam-beam Counters

The beam-beam counters (BBC) [21] are located in both the forward and backward directions. They lie near the beam-line, almost six meters from the interaction region. They are comprised of two planes of scintillators and they cover a pseudorapidity range from $3.24 < |\eta| < 5.88$ (this corresponds to an angular deviation range from the beam-line from $0.32°$ to $4.47°$).

Low angle hadronic jets are produced in almost every $\bar{p}p$ collision. The jets become more numerous near the beam line where they can hit the beam-beam counters. The BBCs have excellent timing resolution and can be used to determine when a collision occurred. The main purpose of the BBCs is to measure the instantaneous luminosity, which can be derived from the rate of coincidences in the counters. The BBCs are also sometimes used as part of the trigger. The trigger filters out the potentially interesting events from the uninteresting ones. For some classes of events to pass the trigger the requirement is made that the BBCs fired at the same time that a particle bunch crossing was expected.

2.8 Calorimetry

Beyond the solenoid and tracking systems are the electromagnetic and hadronic calorimeters. They provide almost complete coverage, encompassing most of 2π in the azimuthal coordinate and extending from η=-4.2 to η=4.2 in the pseudorapidity coordinate (this corresponds to an angular range of $\theta \simeq 2°$ to $\theta \simeq 178°$) [23].

Calorimeter Subsystem	Geometric Coverage η Range	Energy Resolution	Absorption Thickness
CEM	$0.0 < \|\eta\| < 1.1$	$13.7\%/\sqrt{E_T} \oplus 2\%$	$18\ X_0$
PEM	$1.1 < \|\eta\| < 2.4$	$22\%/\sqrt{E} \oplus 2\%$	18-21 X_0
FEM	$2.2 < \|\eta\| < 4.2$	$26\%/\sqrt{E} \oplus 2\%$	$18\ X_0$
CHA	$0.0 < \|\eta\| < 0.9$	$50\%/\sqrt{E_T} \oplus 3\%$	$4.5\ \lambda_0$
WHA	$0.7 < \|\eta\| < 1.3$	$75\%/\sqrt{E} \oplus 4\%$	$4.5\ \lambda_0$
PHA	$1.3 < \|\eta\| < 2.4$	$106\%/\sqrt{E} \oplus 6\%$	$5.7\ \lambda_0$
FHA	$2.4 < \|\eta\| < 4.2$	$137\%/\sqrt{E} \oplus 3\%$	$7.7\ \lambda_0$

Table 2.1: Properties of the different CDF calorimeters. Thicknesses are given in radiation lengths (X_0) for the electromagnetic calorimeters and in pion interaction lengths (λ_0) for the hadronic calorimeters.

The calorimetry is divided into three separate η regions, the central, end-plug and forward. Each region consists of both an electromagnetic calorimeter (CEM, PEM, FEM) and a hadronic calorimeter (CHA/WHA, PHA, FHA). The central electromagnetic calorimeters are comprised of lead interspersed with scintillator, and are all approximately 18 radiation lengths thick. One radiation length of a material is defined as that thickness of a material which reduces the mean energy of a beam of electrons passing through it by a factor e (e=*2.7*). The hadronic calorimeters use iron instead of lead. They are also much thicker, being between four and eight pion absorption lengths thick (1 pion absorption length approximately equals 18 radiation lengths).

Each calorimeter is segmented in $\eta - \phi$ space to form projective towers which point back towards the nominal interaction point (the center of the CDF detector). Table 2.1 shows each detector's geometrical coverage in pseudorapidity, its energy resolution and its thickness.

The calorimeters are used to determine the total energy of an electromagnetic or hadronic track or group of related tracks, called a jet. An electron or hadron will tend to interact with the dense absorbing material of the calorimeter as it passes through it. The result is called a "shower", so called because the interaction typically exhibits a cascade effect. Usually all of the energy of the electron or hadron gets deposited inside the calorimeter, and the calorimeter scintillators measure a known fraction of the total energy deposition. A muon meanwhile interacts weakly with the absorbing material and will deposit only a small amount of its energy in the calorimeter as it passes through. The calorimetry is used in this analysis mainly to aid in the identification of muons. Muon candidates are required to have deposited only the expected minimum ionizing energy in the calorimeter.

2.9 Muon Detectors

The muon detectors lie outside of the hadron-absorbing calorimeters. There are four sets of muon chambers, the Central Muon System (CMU), the Central Muon Upgrade (CMP), the Central Muon Extension (CMX) and the Forward Muon System (FMU). These detectors are located at different regions of pseudorapidity as exhibited in figure 2.3

The chambers closest to the interaction region are the CMU. These chambers are located approximately 3.5 meters from the interaction region. They are segmented into 24 15-degree wedges in phi, and also into both east and west (ie. forward and backward) halves. Each wedge contains 48 drift chambers. The drift chambers are arranged cylindrically around the beam-line, and the sense wires of the chambers are parallel to the beam-line. Each wedge is further segmented into three 5-degree towers. Each tower consists of four layers of four rectangular drift cells (see figure 2.5). Alternating layers are radially aligned, and each radially aligned pair is offset 2mm from the neighboring pair. A muon will usually pass through all four layers, resulting in four distinct chamber drift times. The timing difference in the chamber drift times for one pair is used to determine the muon track's angle relative to a radial line and the ϕ ambiguity (uncertainty regarding which side of the wire was passed by the track) is resolved by using information from the slightly offset pair.

The 2,304 CMU chambers themselves are 2.3 meters long by 6.3cm wide by 2.7cm high. There are gaps between the east and west sections, and also between the wedges themselves. In pseudorapidity the chambers cover the range $0.03 < |\eta| < 0.63$ (this corresponds to an angular range of 1.5 degrees to 34.1 degrees from $\eta = 0$). These gaps mean that the CMU covers only about 84% of the total solid angle.

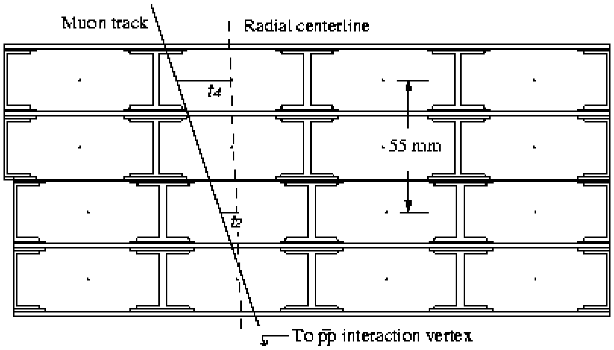

Figure 2.5: Chamber configuration for a Central Muon System (CMU) 5-degree tower

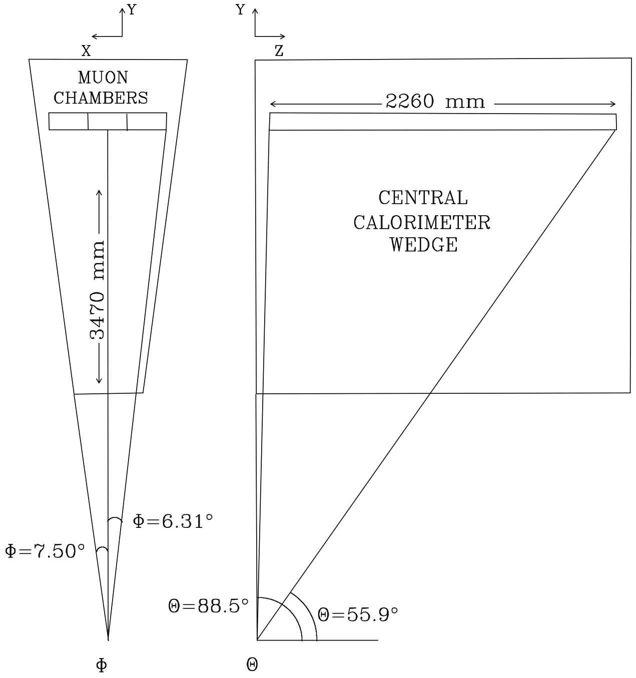

Figure 2.6: Chamber layout of the Central Muon System (CMU)

Approximately three absorption layers of steel lie beyond the CMU, and beyond that lies the Central Muon Upgrade (CMP). The CMP [31] and its associated absorption steel was installed for the 1992 collider run. The main reason for adding this system was to reduce the "punchthrough" problem. CMU punchthrough occurs when high energy hadrons fail to be absorbed completely by the calorimetry. This can result in fake muon hits in the CMU and consequently undesired triggers (the trigger is described fully in the next section). The CMP provides confirmation that the particle that hit the CMU was indeed a muon. It should be noted that the material in front of the CMP will absorb muons with a transverse momentum less than about 1.8 GeV.

The CMP is an incomplete box which only partially surrounds the CMU. The solenoidal field return yoke steel acts as an absorber for the top and bottom CMP regions, whilst the side north and south regions have their own steel absorbing walls.

The 1,088 CMP chambers are 640cm long and are arranged in four half-cell staggered layers. The CMP sense wires are parallel to the beam direction. Because the CMP layout is box-like the radial distance from a CMP chamber to the nominal interaction point is not constant. The variation in this distance is from about 4 meters to 6 meters. Since the CMP chambers are a fixed length, the η coverage of the CMP varies as a function of ϕ. The CMP chambers closest to the interaction region extend to $\eta = 0.63$ as do their sister CMU chambers. At other ϕ values the η coverage is less, leading to a gap in η coverage. The "η-gap" region is defined as that part of the solid angle covered by the CMU that would also be covered by the CMP were the CMP chambers longer. This region will be referred to in later chapters.

In addition to the η-gap region there are several large gaps in the CMP box structure, notably at the top and bottom ($\phi = 90^\circ$ and $\phi = 270^\circ$) where there is no solenoidal field return yoke and consequently no chambers. Approximately 63% of the $|\eta < 0.6$ solid angle is covered by the CMP, and 53% is covered by both the CMU and the CMP.

Farther out in pseudorapidity is the Central Muon Extension (CMX). The CMX was also installed for the 1992 run and was designed to extend the CMU coverage. CMX covers

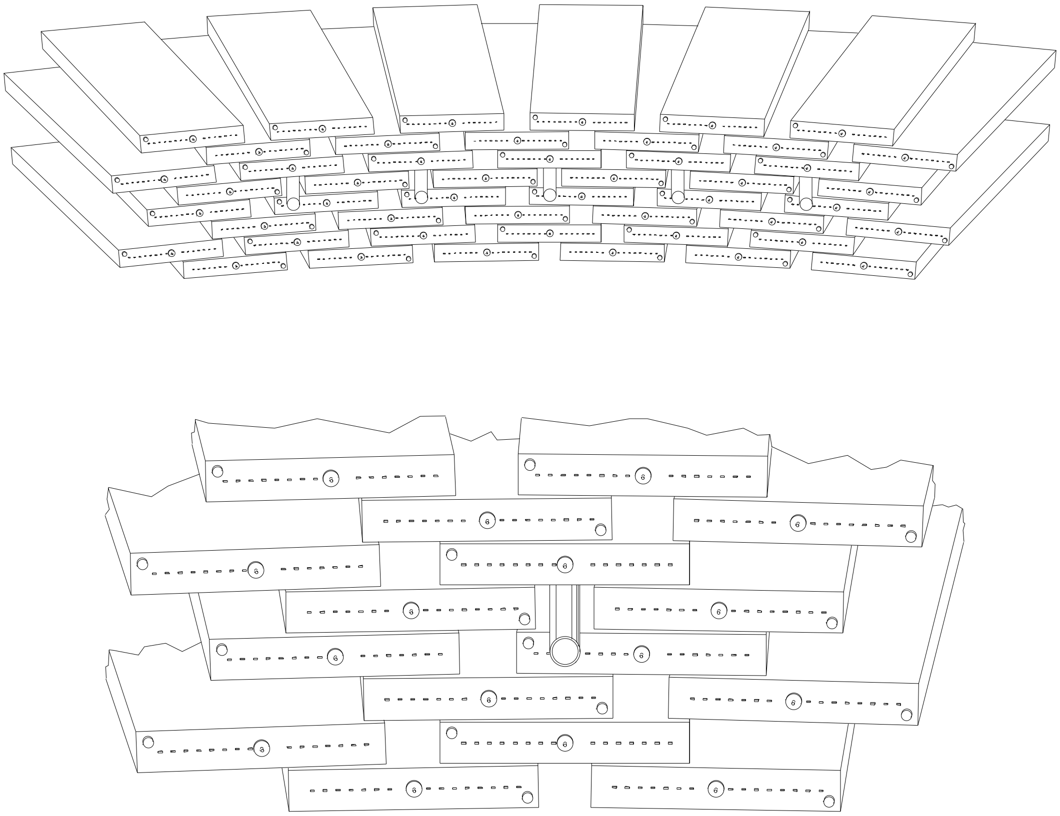

Figure 2.7: Illustration of conical shape of a CMX wedge

the pseudorapidity range $0.6 < |\eta| < 1.0$. It consists of four conical arches which total 1,728 chambers that are sandwiched between scintillators (the latter is used in triggering). Each arch consists of nine 15-degree wedges. A wedge is further segmented into three 5-degree towers, and each tower is made up of 16 drift chambers. The CMX is 8 layers deep and the sense wires are arranged as radially aligned pairs. A radially aligned sense wire pair defines a plane that includes the beam line. The conical shape of the CMX means that neighboring pairs overlap more at the high eta end than they do at the low eta end. At the largest distance from the beam line the cells are half-cell staggered. This can be seen in figure 2.7.

2.10 Trigger

The instantaneous luminosity at CDF ranged from very low values up to about $20 \times 10^6 \mathrm{pb}^{-1}\mathrm{s}^{-1}$. The individual bunches of protons and antiprotons were timed to pass through each other near the center of the CDF detector every 3.5μs. This corresponds to a rate of about 300kHz. Each crossing is potentially the source of collisions (called events). Since the total $\bar{p}p$ cross-section is nearly 100mb at Tevatron energies, over two million collisions per second occur at Run 1B peak luminosities corresponding to six collisions per crossing on average. Ten trillion collisions were examined by the CDF trigger logic over the course of the experiment.

CDF had the capability of recording only a handful of events per second (less than ten) due to the large number of readout channels (more than one hundred thousand). The time required to readout all of the individual detector subsystems plus the time to save the data onto permanent media after extraction from the electronics prohibited higher readout rates. Each event which was saved to a file contributed approximately 200kbytes to its length.

By far the largest fraction of the $\bar{p}p$ collisions are uninteresting small angle interactions. Very occasionally the interacting beam particles would undergo a violent head-on collision. These high impact collisions serve as our probe of the nature of physical forces at small distances. It is these close encounters that are most interesting. CDF was able to record approximately 30 million events during run 1. Approximately one in every seventeen million collisions results in the production of a Z-boson. Since Z-boson production is the subject of this thesis, it was of vital importance for this work that the efficiency be high for the collection of events where Z-bosons are produced. Given the limitation on the number of events that could be recorded, very good rejection of unwanted small-angle collisions was also critical. The trigger electronics provided the needed selectivity.

The trigger [35] selects events of interest at three distinct stages in a process designed to lower the 300kHz event-crossing rate down to the manageable 10Hz of data that could be recorded. The event selections were designed to insure that the 10Hz of data retained was as useful for physics analysis as possible.

Every 3.5μs, shortly before the proton and anti-proton beams were to collide in the CDF detector, all systems of CDF were reset and enabled for data-taking. When the beams crossed, the electronic systems recorded all available data for the event. The selection of "interesting" events took place in three stages, called level 1, level 2 and level 3. Level 1 event examination was performed by custom, hard-wired electronics and took place during the 3.5μs time between beam crossings. If an event was found to be interesting by the level 1 circuitry, the pre-crossing reset of the detector was inhibited and all data retained. No new triggers were permitted and all collisions following the level 1 accepted event were ignored while the stored event was further examined by the level 2 circuitry. Level 2 evaluation was performed by a set of programmable processors. The time for the level 2 decision varied and was terminated when the event was either rejected or sent on to level 3. The typical time for level 2 processing was tens of microseconds. Level 3 evaluation took place after all data was read from the detector (this took a few of milliseconds). A collection of commercial processors shared the task of level 3 examination. Since the data was removed from the detector electronics for level 3 processing, the inhibit of data taking was released as soon as the event was read into the memory of the level 3 system. During the inhibit period the detector was said to be dead for data taking and the accumulated time spent in this state is referred to as the detector dead-time.

2.10.1 Level One

The level one trigger decision was made during the time between crossing and hence it incurred no dead-time. The selection process used limited detector information and reduced the event rate by roughly 150, the ratio of events into level 1 to events accepted by level 1 (from 300kHz input to 2kHz output). Early implementations of the trigger required coincidence of signals in the east and west BBC counters located in the low angle regions near the particle beams themselves. Whenever an inelastic collision occurs between a quark and an anti-quark in the $\bar{p}p$ system, the spectator quarks (the quarks in the proton and anti-proton that didn't participate in the collision) produce a large number of particles that exit the detector in the low angle region. Signals from these low angle particles were detected in CDF by beam-beam counters on both sides of the beam-line and used to select only events where inelastic collisions occurred. These counters, BBC, aided in the rejection of cosmic rays and detector noise signals which would have otherwise contributed to the level 1 acceptance rate.

However, as the collider luminosity grew during the run the effectiveness of the BBC counters as part of the trigger was compromised. At large luminosities where several collisions occurred each crossing, the beam-beam counters became saturated. The BBC counters were used in the trigger only during the first part of run 1a.

The main function of the level 1 trigger was the selection of events based on a quick examination of both the calorimeter and muon chamber information. In the case of the calorimetry, if the total transverse energy deposited in any of the 2048 trigger units (called towers) was above a certain threshold, then level 1 accepted the event. There were 2048 hadronic and electromagnetic projective trigger towers. The calorimeter trigger computed the transverse energy for each tower as $E_t = Esin\theta$. Different thresholds were applied for different detector subsystems (6 GeV for the CEM, 25 GeV for the FHA).

The level 1 muon trigger, which was important for this analysis, will be explained in detail. In short, if the transverse momentum of any particle which had the signature of a muon was above a certain threshold, then level 1 accepted the event. The main function of a muon chamber is to detect and measure the passage of charged particles. The measured arrival time of the electronic signal relative to the particle passage time determines how close the charged particle has come to the sense wire of the chamber. In the CDF detector the muon chambers have maximum drift times up to 1.6μs which is a large fraction of the total time between beam crossings necessitating a rapid generation of trigger decisions.

The CMU and the CMX chambers were arranged in pairs with radially aligned sense wires that were parallel to the beam line, one layer being further away from the beam line than the other. Any charged particle emanating from the collision point that reached the muon chambers had to first pass the axially oriented magnetic field of the solenoid. This field deflected the radial velocity component of the particle's momentum away from its initial radial direction in proportion to the inverse of the radial momentum component. By constructing the detector with wires that were radially aligned, a simple means to measure the particle's angle relative to the radial direction was possible. The time difference between outputs from radially aligned wires provided a measurement which was inversely proportional to the particle's transverse momentum. A selection of a small time difference is a selection of high transverse momentum and a selection of a large time difference is a selection of low transverse momentum.

Maximum differential timing thresholds were imposed in the CMU and CMX subsystems in order to select events in which there was at least one muon with a transverse momentum above some minimum value. Multiple scattering of muons, the left-right ambiguity of the chamber drift-times, and the timing resolution of the electronics in effect smeared the correspondence between the timing difference from the drift times and the transverse momentum of the charged particle in question. The trigger made use of timing differences that correspond to 90% efficiency for the desired muon momentum threshold.(ie 90% of the muons at a given transverse momentum threshold passed the trigger for a given timing differential setting). In the case of the CMU the transverse momentum threshold was 6 GeV and the timing differential cut was 40ns. The timing selections were accomplished via electronics boards called MU1T. (Note that these boards contained an additional lower threshold which was used for dimuon triggers). In the case of the CMX the transverse momentum threshold was 10 GeV and the timing differential cut was 42ns, and this was accomplished via electronics boards called MX1T. The differential time cuts were tuned to the correct average value using tracks measured in the full CDF tracking system. An added uncertainty in the measured transverse momentum from the CMX resulted from the non-uniform magnetic field in this region. The MX1T cards were built with similar functions to the MU1T cards. The cards provided two timing thresholds, one of which was used for single muon triggers (high threshold) and one for dimuon triggers (low threshold).

The differential timing signal from a single 4 layer chamber was found to be inadequate for the rejection of unwanted triggers both in the CMU and CMX. In the CMU the unwanted, false, triggers were a result of punchthrough of hadronic tracks some of which satisfied the differential timing requirements after multiple coulomb scattering into nearly radial directions. Many particles produced in inelastic $\bar{p}p$ collisions enter material along the beam-line producing secondaries that enter the CMX chambers. These secondaries appear to be radial as measured in the CMX and hence satisfy the trigger threshold. Triggers from these unwanted sources had to be suppressed to keep the trigger rate at manageable levels. For the CMU region the additional layers of the CMP were used. For the CMX region a minimum ionizing signal was required from the calorimeter along with a Hadronic TDC digitization in the tower ahead of the CMX chamber.

The muon systems were arranged logically in five-degree trigger towers (not to be confused with a calorimeter "tower" which is fifteen-degree wedge in azimuth). These towers existed for both the west and east halves of the detector. A five-degree trigger tower for either the CMU or the CMX was comprised of sixteen muon chambers. Approximately half of the chambers were redundant from purely a geometrical viewpoint, but they were very important from an efficiency standpoint. An individual chamber **or chamber-pair** was not fully efficient at detecting the passing of a charged particle. Chambers contain insensitive regions due to wall thickness and occasionally became noisy and had to be disabled. Good overall efficiency necessitated some redundancy. A second pair of chambers provided this redundancy. If any radially aligned pair of chambers fired within the timing differential threshold, then the corresponding five-degree tower for that subsystem reported a muon track seen.

In the case of the CMU confirmation for the muon track was provided by the CMP. The CMP is comprised of 1088 chambers located behind additional steel and arranged in a box-like formation four layers deep around the CMU. Since the tubes of the CMP are not

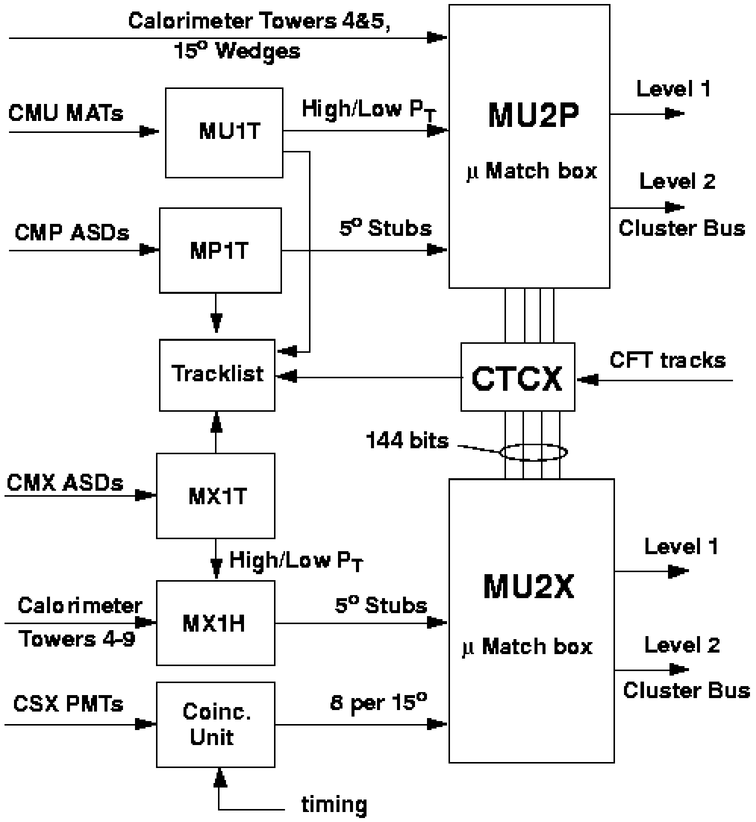

Figure 2.8: Muon trigger flow schematic

arranged as projective pairs, no differential timing requirement can be applied. Instead a pattern matching scheme was developed to insure that any candidate CMP muon exhibit the features expected of a muon. This included the requirement that the pattern of chambers with observed hits be consistent with the CMU track within the expected multiple scattering uncertainty.

During the design of the CMP, computer simulations were performed to determine all patterns of two layer hits that result from muons with the desired transverse momenta. These patterns were associated with all five-degree CMU towers through which the muon passed. From the simulations it was determined that each accepted pattern of CMP chambers was typically associated with two adjacent CMU towers although occasionally the association was with three.

When a muon was seen to pass through a particular CMU region it was found to exhibit one of the CMP patterns associated with that particular CMU region. The CMP trigger hardware was built to exploit this correlation. A one megabyte look-up table was prepared and instrumented such that for each stored CMP pattern a mask of associated five-degree CMU towers could be fetched and compared to the CMU towers. The CMP patterm sensing circuits and lookup memories were implemented in a system called MP1T. The mask output of the MP1T was logically ANDed with CMU tower five-degree trigger information. In this way the CMP was used at level 1 to confirm that a high transverse momentum muon had indeed passed through the CMU.

It should be noted that the CMP did not provide complete coverage of the CMU and thus was not able to provide confirmation masks for all of the CMU towers. For those towers (there were 20 of them) CMP confirmation was not required in the trigger. These towers made up what was known as the "CMU-only" region of the trigger. The towers which required confirmation hits in the CMP (there were 52 of them) composed the "CMU-CMP" region of the trigger. The electronics boards which combined the level 1 CMU and CMP information to make the final level 1 trigger decision retained the match information for level 2 tasks and are called MU2P (See figure 2.8).

The trigger rate from the CMU-CMP region was lowered substantially when compared to the CMU-only region as a result of the added reqirement. The fraction of "good" events in the CMU-CMP set was also higher than that of the CMU-only events. At high luminosity some rate limitation was necessary. As the luminosity increased the CMU-only trigger rates were kept in check by prescaling (meaning that only a randomly selected subset of the passing events were actually accepted). Acceptance of all the CMU-CMP triggers preferentially over CMU-only events resulted in the largest collection of events of interest.

In the case of the CMX, confirmation that a high Pt muon traversed the chambers was provided by several subsystems. One of these subsystems, the CSX, consists of scintillators located on both sides of the CMX. A particle traversing a radially aligned CMX pair will also pass through the scintillators. These scintillators are required to detect the particle.

Unfortunately, the CMX trigger rate was way too high at the start of run 1a. For about half of this run the CMX trigger was rate-limited and as such it did not provide much useful information. During a temporary one-week shutdown of the accelerator the CMX trigger underwent a major and successful modification. This trigger change enabled the CMX trigger to provide useful data for this thesis for about half of run 1a and all of run 1b. Muons are minimum ionizing particles and as such they deposited small amounts of energy in the calorimetry on their way through and out of the CDF detector. Cables were strung linking the CHA (this is the calorimetry subsystem that a particle would pass through on its way to the CMX) to electronics boards called MX1H which then fed into the level 1 CMX trigger decision-making boards. The requirement that was added to a CMX chamber trigger (MX1T) and a CSX scintillator trigger was that energy had to be observed in the corresponding CHA trigger tower (MX1H). The electronics boards which combined the level 1 MX1T and CSX and MX1H information also performed some level 2 tasks, and they were called MU2X (See figure 2.8). The additional CHA requirement worked well (it was definitely worth the small reduction in overall efficiency), although like the CMU-only even the CMX trigger had to be prescaled at the highest luminosities.

As has been stated, the final level 1 trigger decision had to be made before the general electronic reset was sent. Given the speed of the electronics and the large dimensions of the detector (which meant the speed the signals traveled along the wires was actually important) the final level 1 decision was made at the last possible moment (the electronics board responsible for this was called FRED, the meaning of this acronym is unknown). FRED had one trigger bit reserved for the high threshold CMU trigger, one trigger bit reserved for the high threshold CMX trigger, one trigger bit for the BBCs and the rest were reserved for electron and dimuon triggers. Different trigger bit combinations were required by the different level 1 triggers at different times. For example, early in run 1a the BBC trigger bit was required to have fired (in addition to other trigger bits), but later on in the run this requirement was dropped.

In summary, there were three high Pt muon triggers at level 1. They were "CMU-only", "CMU-CMP" and "CMX". In this thesis the three trigger regions will be referred to as "U", "P" and "X". The CMU-CMP trigger ("P" region) was never prescaled, but the other two triggers were prescaled when the luminosity became large. Not all the muon triggers were working at all times. In fact, the CMX trigger was not working for the first half of run 1a. The beam-beam counters were used as part of the trigger in the first part of run 1a only. Specific trigger efficiency problems and their solutions are described later in section 4.3.

2.10.2 Level Two

Whenever an event passed level 1 dead time was incurred. Level 2 performed a more sophisticated test on the event and this took approximately 20μs. During this time the beams continued to collide, but the electronics recorded none of the information it otherwise would have and the data from these events was lost. Level 2 reduced the event rate from about 2kHz to about 40Hz. Level 2 did not use the full event information to make its decision since a full electronics readout took over 2000μs. However, the extra

20μs meant that information had become available which helped immensely in the decision-making process that was unavailable at level 1.

Calorimeter clustering information was available at level 2. Level 1 used individual energy values which had been measured in each of the 2048 calorimeter triggers. These towers are arranged in an η,ϕ map. However, high energy hadronic jets tended not to be isolated to an individual trigger tower. At level 2 an algorithm was applied which looked for jet candidates spread out over several neighboring towers. This algorithm in effect added the transverse energy depositions of neighboring towers together until no more neighbors could be found which passed a nominal energy threshold. This method allowed the total transverse energy of each jet candidate to be made available at level 2. In addition, global summations and missing transverse energy estimations were made. A global transverse imbalance of deposited energy in the detector implies that energy was not observed and that some particles failed to deposit energy into the calorimeter as they exited the detector. This unobserved energy is called "missing transverse energy" or MET for short).

The Central Fast Tracker (CFT) provided two-dimensional track information. The CTC had five axial layers and four stereo layers. CTC chamber hits had associated drift times which gave corresponding position information. Look-up tables identified patterns of hits in the axial layers (these layers provided longitudinal information) to measure the transverse momentum of individual tracks as they curved outwards through the CTC. The CFT categorized the transverse momentum of individual tracks into one of eight possible transverse momentum ranges or bins. It also provided the ϕ position of the track. At level 2 muon chamber stubs which passed level 1 were required to match a CFT track above an appropriate transverse momentum (this value was 12 GeV). At the start of the run "fifteen degree matching" was used, meaning the CFT track was in effect made three towers wide. A high Pt CMU/CMX stub had to match to the tower which corresponded to the ϕ position of the track as determined by the CFT or one tower on either side of it. Fifteen degree matching was used because of the ambiguity in the actual track position due to the resolution of the CFT. The CFT provided a better estimation of track position than this and midway through run 1a an electronics board called the Track-List Board (TRL) was installed which had the capability to implement “five degree matching”. This was actually better than the CFT resolution and look-up tables were used to make the track-to-stub match five or ten degrees (it all depended on how close the track in question was to a tower edge). The purpose of the tighter matching was to further reduce unwanted triggers and the track list board was successful in this regard. However, the TRL board was found to have an inefficiency for a large part of the rest of run 1a. See section 4.3 for an analysis of this problem and its solution).

2.10.3 Level Three

When an event passed level 2 a full readout of the electronics occurred. This took over 2000μs. Level 3[40] then performed a final test on the event and reduced the trigger rate from about 40Hz to a manageable 10Hz. After event digitization no more dead time occurred. Level 3 consisted of a bank of Silicon Graphics computers which operated in parallel. There were forty-eight CPUs and 96 input buffers. Each input buffer was capable of holding the information for one event and each processor was capable of processing one event at a time. The extra input buffers were necessary to allow for the possibility of random bursts of level 2 triggers which would otherwise have saturated the level 3 inputs (after all, the theoretical maximum for the level 2 trigger rate was close to 500 Hz). The code which determined whether or not an event passed level 3 was a scaled down version of the full CDF offline event reconstruction code.

With the level 3 input rate being below 48Hz, a level 3 CPU had over one second to process an individual event. With this amount of time it was not necessary to use completely customized hardware and speed-optimized software. Level 3 performed a large fraction of the full CDF offline reconstruction such as tracking, vertexing, calorimeter clustering, and muon reconstruction. Level 3 was able to reconstruct the existence of actual particles in the event and select events based on the properties of these believed-to-have-existed particles.

In the case of the high Pt inclusive muon trigger level 3 imposed only loose quality cuts on the muon. For example, there had to be a CTC track with a transverse momentum greater than 18 GeV which matched to an associated muon stub (a muon which is the decay product of a Z particle typically has a Pt over 40 GeV). Additionally, a muon candidate was rejected if a large amount of energy was deposited into the matching hadronic calorimeter tower.

Chapter 3

Data Set

CDF recorded data for approximately thirty million events during run 1. These events were stored on hundreds of data tapes and totaled approximately six terabytes of data. The events on these tapes were preselected by the trigger with a host of different selection criteria, and only a small fraction of them would prove useful for this thesis.

After the data had been recorded, the first task for this analysis was to select a general data set which could be used. The full 30 million event data set was too big for repeated use and it was necessary to select a manageable subset of it. As programming code was written and refined it would be necessary to analyze and reanalyze this subset data set many times. This is why accessibility was important. Ultimately it was desired that the data set be small enough to fit on hard disk, otherwise it would have ended up on much less accessible data tapes.

This thesis studies the properties of Zs via the detection of their decay products, specifically high Pt muons. The level three high Pt muon preselection streams were thus the logical starting point for the creation of the data set.

The level three track reconstruction code determined the momentum of the tracks which the CTC detected. Level three also grouped muon chamber hits into stubs and tried to match stubs to tracks via track extrapolation. Stubs which were matched to tracks were assigned a value “dx”. “dx” is the distance from the extrapolated track path to the chamber stub location and is a measure of how well the stub matched to the track. Level 3 also determined the hadronic and electromagnetic energy depositions associated with each track.

If an event was to pass the level 3 high Pt muon trigger there had to be a level 3 track in the event which had a Pt greater than 18GeV (this value was relaxed to 15GeV during run 1b). There also had to be an associated muon stub in roughly the expected position via the track-to-stub matching process. A CMU stub had to have a dx less than 10cm. In the case of the CMP this matching requirement was 25cm and for the CMX it was 40cm.

Level 3 tended to overestimate the momentum of CTC tracks during track reconstruction. An underestimation could result in the rejection of important events, so it was important to avoid underestimations. Approximately one third of the level 3 high Pt muon tracks disappeared during full offline track reconstruction but it was very rare for additional high Pt tracks to emerge from offline.

For an event to reach the inclusive high Pt muon data set it had to first pass one of the high Pt level 3 muon streams. A further set of offline selection cuts were then applied. It was verified that all of the following cuts were fully efficient or at least almost fully efficient for the Z to $\mu^+\mu^-$decay channel.

First, a possible high Pt muon track had to have an offline reconstructed track Pt of at least 18GeV. Muons from Z decays typically have a Pt around 40GeV. Figure 3.1 shows this distribution. The procedure for making this plot will be given in a later chapter.

Second, the track's associated hadronic energy deposition in the calorimeter was required to be less than 6GeV. This cut rejected high Pt jet events, which tend to deposit much more energy than 6GeV in the hadronic calorimeter. Muons are minimum ionizing particles and a high Pt muon typically deposited 2GeV or less in the hadronic calorimeter. Figure 3.2 shows this distribution. The procedure for making this plot will be given in a later chapter.

Third, a muon stub in either the CMU, CMP or CMX was required to be associated with the high Pt track. The stub's associated "dx" matching value had to be less than 10cm

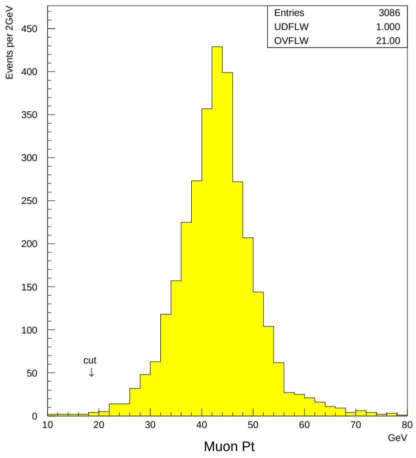

Figure 3.1: Unbiased distribution of the track Pt for Z candidate muons

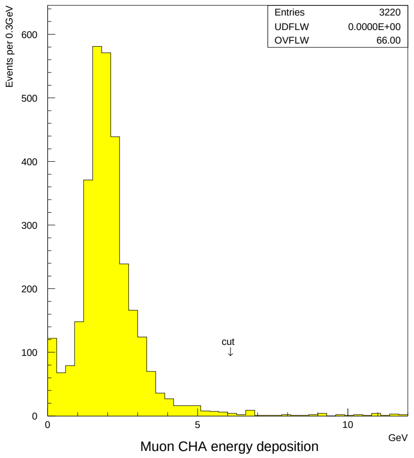

Figure 3.2: Unbiased distribution of the CHA energy deposition for Z candidate muons

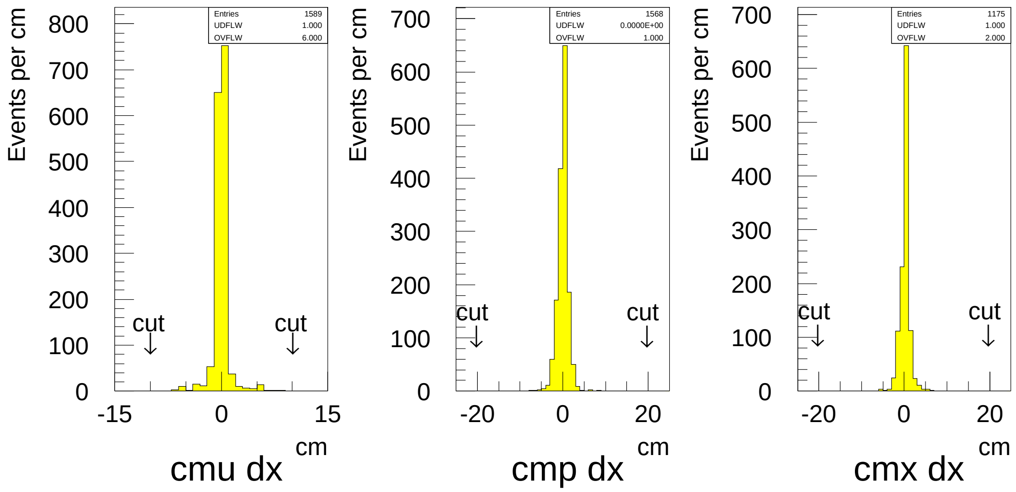

Figure 3.3: Unbiased distribution of dx matching values for Z candidate muons in the CMU, CMP and CMX

for the CMU, 20cm for the CMP or 20cm for the CMX. Figure 3.3 shows these distributions for the different detector subsystems. The procedure for making this plot will be given in a later chapter.

The selection process resulted in data sets for runs 1a and 1b of 64,677 and approximately 250,000 events respectively. At 200kbytes per event this corresponds to about 500 gigabytes of file space. Whilst this may not be enormous by today's standards, when the data was recorded 500 gigabytes was very considerable. It was not necessary to save all 200kbytes of data for each event (at CDF an event in this form is called a "full DST event"). Instead a smaller version of the event, called a "PAD", was used. PAD events were compressed versions of DST events. A PAD event was typically about one tenth the size of a full DST event and was stripped of many large pieces of detector information which were not necessary for most analyses. Furthermore, much of the data within an event was reorganized in the PAD version to minimize the utilized file space. PAD events were suitable for this analysis.

Consequently, the inclusive muon data set for run 1 was about 40 gigabytes, which met the initial disk space goal. It contained about one quarter of a million events which had passed the selection criteria.

Chapter 4

Method for Determining the Z Pt spectrum

The goal of this thesis is to determine the Z transverse momentum spectrum in the muon decay channel at the energy of the Fermilab Tevatron. CDF detects only a fraction of the muons which are created in this decay channel, and hence the Z transverse momentum can be determined for only a fraction of the Zs which are actually observed. It is necessary to make a large number of corrections to the experimental data, some of which are complex. If the original Z transverse momentum distribution is to be inferred, special care must be taken since selection criteria and efficiency is correlated to the original transverse momentum of the Z.

Many corrections are applied to the data with the help of Monte Carlo Simulations. In a Monte Carlo a large number of events are simulated via a computer, and the desired correction factors are obtained by examination of the effect of the apparatus and selection criteria have on the "simulated" data. The Monte Carlo is checked at many levels to ensure that it conforms to reality, and that the correction factors obtained are accurate.

4.1 Geometrical Coverage

Almost immediately after creation, a Z will decay, and the products from this decay sometimes will be two muons (one positively charged and the other negatively charged). If the Z is created at or near rest, then the muons, by conservation of momentum and energy, will travel in opposite directions at half the total energy of the Z, or at an energy equal to roughly half the mass of the Z. If the Z is moving in the transverse plane, then the same applies as before except the muon momenta will be boosted in the direction the Z was originally moving and hence the muons will have a distribution of momenta above and below the value seen for a decay at rest.

This thesis utilizes the central muon detector elements CMU, CMP and CMX. These detectors provide coverage for centrally directed muons (the coverage provided by these detectors is almost complete out to η=1), and hence they are better at detecting muons from Zs with larger transverse momenta.

Monte Carlo's are used to determine what fraction of Zs (as a function of the Z transverse momentum) will produce muons which are aimed at the different muon detection subsystems. An added complication results from the fact that not all detector subsystems were working all the time. It is necessary to simulate this behavior in the Monte Carlo as well since what is ultimately desired is the Z transverse momentum spectrum per unit of integrated luminosity.

4.2 Detection Efficiency

In order for the Z transverse momentum in an event to be determined the trigger has to detect the presence of the event and it must be written to tape. The event must also pass the selection criteria to remain in the Z event sample. These selection cuts include specific trigger requirements. Ultimately, only Z events where at least one of the muons in the event cause the high Pt muon trigger to “fire” are of interest. This primary “trigger” muon has to pass stringent “gold” selection cuts, whilst the second muon is required to pass “silver” selection cuts.

The efficiency of each applied cut must be determined, as well as individual detector subsystem efficiencies and corresponding trigger efficiencies.

4.3 Specific Trigger Efficiency Issues

In the study of Zs extreme care must be taken to correctly identify whether an individual track had caused an event to trigger. The different trigger levels ultimately make trigger decisions which pertain to the topology of an entire event, not an individual track. Their decisions are supposed to be based on the trigger information which is available for each track in an event. Unfortunately, it was found that the information from which the final trigger decision was made was not always the same as the individual track information digitizations.

There are two main types of efficiency concerns. There can be events where the complete data readout implied there should not have been a trigger and yet there was a trigger. While confusing, the way to deal with such events is to simply reject them. The second type of efficiency problem is much more problematic - these are events where the complete data readout implied that a given track should have triggered and it did not. Such events have grave implications in the study of Zs - they can mean that it is impossible to know for sure which muon (or both) was responsible for the trigger.

There were level 1 and level 2 efficiency problems which were both of the latter more problematic type. However, they were fairly minor problems and by making extra selection cuts it was possible to correct for them. These problems will be discussed thoroughly in later chapters. The level 1 problem is described in section 7.4.1 and the level 2 problem is described in section 7.4.2.

4.4 Background Events

An event which passes the final Z selection cuts is not necessarily a Z event. Known sources of background include “punchthrough” events, cosmic rays, multiple vertex events and muon pairs produced by a mechanism called Drell-Yan. “Punchthrough” events occur when some piece of a high energy particle or jet manages to get through the calorimeter and hit the muon chambers, causing that track to be interpreted as a muon when in fact it is not. This in turn can cause the event to be mistakenly interpreted as a Z. Cosmics, which are primarily muons, can fake a Z because a muon which travels completely through the CDF detector appears, when assumed to be emanating from the collision region, to have one charge on one side of the detector and the opposite charge on the other side. This is because the CDF detector's magnetic field causes a muon moving towards the center of the detector to travel along the same trajectory as it's oppositely charged counterpart moving away from it. As part of the Z selection criteria, cuts are applied on the data sample to reduce cosmics to a minimum. However, these cuts are not fully efficient at rejecting background. Multiple vertex events are events where two independent high energy tracks originated from different $\bar{p}p$ collisions, causing the event to be mistakenly interpreted as a Z. Drell-Yan is a process in which a photon can decay into two muons. If the photon is of comparable energy to that of a Z then there is no way to distinguish between the Z decay and the Drell-Yan produced pairs. Fortunately the cross-section for Drell-Yan events is very small at these energies.

Corrections must be applied to remove these background events from the final spectrum. This is performed using the invariant mass of the two muons. Zs measured in the CDF detector exhibit a very narrow invariant mass (the Z lineshape) resonance, and the number of background events in the final Z sample can be determined via a careful examination of the tails of the invariant mass distribution.

4.5 The Monte Carlo and the Error Scale Factor Determination

The Z transverse momentum and Z invariant mass are measured using the momenta of the two muons and conservation of momentum and energy principles. Each Z candidate event thus has an experimentally determined Z transverse momentum and an experimentally determined Z invariant mass. Errors in these values are determined using error propagation. Individual muon track momentum values are determined from CTC tracking data where a best fit curve which corresponds to a particular track momentum is fitted to a set of points which represent the CTC chamber hit positions. The errors in the track parameters can be determined from how well the curve fits to the data points. These errors are self-consistent but have been determined to be off by an overall scale factor because the absolute error scale is unknown. A simple analogy can be used to explain this last statement.

Suppose you had many cookie jars with an assortment of jellybeans in each one and you were asked to estimate the number of jellybeans in each jar. You could guess the number of jellybeans in each jar with your eye, and you could also make an estimation of the error in each guess. You could then empty out each jar one jellybean at a time and find out exactly how many jellybeans were actually in each jar. Hopefully (if you were good at estimating) your overall guesses would sometimes have been too high and sometimes they would have been too low. When the jars were full of jellybeans then your error estimate would have been large, and when the jars were almost empty your error estimate would have been small. What you wouldn't know unless you counted the jellybeans in each jar was how well you were estimating the error (for a Gaussian distribution 68% of your jellybean guesses should come within one standard deviation of the actual value). In all likelihood you would probably either always overestimate the error (in which case a much larger fraction of your jellybean guesses would be within one sigma of the actual value than you would expect) or else you would always underestimate it (in which case too few of your guesses would be within one sigma of your error estimate). In other words, your error estimates would likely be wrong by an overall scale factor. However, in this jellybean experiment you have counted the actual number of jellybeans in each jar, and it is therefore possible to determine what the error scale factor is.

The errors are based on Gaussian Distributions. The tails are non-Gaussian. A best approximate fit to the data cannot determine which events come from the central or the tails in the distribution. A first order correction to these non-Gaussian tails can be obtained by the introduction of a scale factor for the error estimates. The known natural lineshape of the Z is used to set the scale factor.

The natural Z lineshape is well-known. The Z mass distribution which is obtained experimentally is much broader (see figure 8.7), because it has been smeared by the errors inherent in the tracking data. Error propagation is used to determine the error in the Z mass for each Z candidate. By adjusting the error scale factor, the natural spread of the Z is broadened to a "best fit" representation of the experimentally observed distribution. The scale factor determined for this "best fit" is then used to modify the Monte Carlo to best mimic the observed data.

At this stage all corrections which need to be made to the Monte Carlo have been applied. These corrections include selection efficiencies, integrated luminosities (for each trigger region), fiducial corrections, and the application of the error scale factors. In fact, the Monte Carlo is used to more accurately determine the single high Pt muon trigger efficiencies.

4.6 The Z Pt Measurement

The measured Z Pt spectrum is then compared to the spectrum produced by the Monte Carlo. The shapes are found to be close but are not in agreement. This is because of higher order effects in the Monte Carlo event generator. The solution is to "tune" the Monte Carlo so that the shapes of the measured and Monte Carlo Z Pt spectra match. There are tuning parameters built into the Monte Carlo for adjusting the hight and width and also the location of the peak of the Z Pt spectrum. The parameters are tuned until a match is obtained between the Monte Carlo and the data Z Pt spectra. Excellent agreement is obtained, and consequently the Monte Carlo generated Z Pt spectrum is believed to correctly represent the actual detector-independent Z Pt spectrum. A simple method for determining the errors in the Z Pt spectrum is performed.

After all corrections have been applied, the final Z Pt spectrum plot is produced. The overall cross-section for Z production in the muon channel is calculated, as well as the Z Pt differential cross-section. Both measurements are found to agree very well with the corresponding measurements in the electron channel.

Chapter 5

Measurement of the Integrated Luminosity

Table 5.1 shows the breakdown of the integrated luminosity by level 2 trigger. There are three time periods to consider. These are run 1a pre-shutdown, run 1a post-shutdown, and run 1b. The run 1a shutdown occurred just prior to run 46146. Run 1b began with run number 55242. It was also necessary to further subdivide the run 1a post-shutdown CMX trigger into two time periods. Despite all of the improvements which were made to the CMX trigger during the shutdown, its trigger rate once again became a problem at the highest luminosities which were being achieved by the accelerator. After run 46409 dynamic prescaling of the CMX trigger was implemented.

The last three columns of table 5.1 contain the integrated luminosity information. The "delivered" integrated luminosity corresponds to the integrated luminosity which was delivered to CDF by the accelerator and does not depend on the trigger region. The "working" integrated luminosity corresponds to the integrated luminosity at CDF when the hardware in the detector trigger region was operational. For example, in the pre-shutdown era of run 1a (runs 40100 to 46145) the "U" (CMU-only) hardware was "working" for 13.25pb^{-1} out of a delivered 14.38pb^{-1}. In the same time period the "P" (CMU-CMP) hardware was "working" for 12.95pb^{-1} and the "X" hardware was not "working" well enough to be used in this analysis.

The "live" integrated luminosity corresponds to the integrated luminosity at CDF when the trigger region was both "working" and "not prescaled". As the instantaneous

trigger region	run	run start	run end	L2 trigger table name	delivered int lum pb^{-1}	working int lum pb^{-1}	live int lum pb^{-1}
U	1a	40100	46145	CMU_CMP_CFT_9_2	14.38	13.25	13.25
	1a	46146	47835	CMUNP_CFT_9_2_5DEG	6.27	6.14	6.14
	1b	55245	71023	CMNP_CFT_12_5DEG	89.84	89.54	33.73
	total				110.49	108.93	53.12
P	1a	40100	46145	CMU_CMP_CFT_9_2	14.38	12.95	12.95
	1a	46146	47835	CMUP_CFT_9_2_5DEG	6.27	5.63	5.63
	1b	55242	71023	CMUP_CFT_12_5DEG	89.84	88.69	88.69
	total				110.49	107.27	107.27
X	1a	40100	46145	no useful trigger	14.38	0.00	0.00
	1a	46146	46408	CMX_CFT_13_5DEG	*1.36	1.04	1.04
	1a	46409	47835	CMX_CFT_13_ET_5DEG	4.91	4.65	4.18
	1b	55242	71023	CMX_CFT_12_5DEG	89.84	89.32	35.28
	total				110.49	95.01	40.50

trigger table name	a label used in CDF to characterize data acquired via a particular trigger path
delivered int lum	integrated luminosity delivered to the trigger region
working int lum	integrated luminosity for the working trigger region
live int lum	final integrated luminosity including trigger prescale
pb^{-1}	integrated luminosity values have an accuracy of 3.3%

Table 5.1: Live integrated luminosities by region

luminosity delivered by the accelerator gradually increased, the trigger rates tended to increase at a faster than linear rate. To avoid hardware saturation individual level 2 triggers which were deemed less important than other triggers were prescaled (sometimes the relative increase in a particular region's trigger rate over another region's trigger rate caused that trigger to lessen in stature). As the accelerator luminosity increased, the weekly, often heated, meetings by the "Trigger Working Group" decided the fate of individual triggers.

Only the CMX trigger was prescaled during run 1a. During run 1b both the CMU-only and the CMX trigger regions were prescaled. The effect of prescaling meant that these triggers were "live" for slightly less than half of the available integrated luminosity.

If the Monte Carlo simulation of the detector is to correctly represent the distribution of events among the samples taken with particular detector configuration, the "live" integrated luminosity for each detector configuration must be known. Table 5.1 shows this distribution. However, for a given trigger region it is also vital to know the "live integrated luminosity overlap" between each of the various trigger regions (ie the correlation between live intervals). Detectors being "live" at differing times presents a very different situation from detectors all being "live" simultaneously. Therefore, in addition to the "live integrated luminosity", the "live integrated luminosity overlap" for each pair of trigger regions was determined.

Unfortunately, determination of the overlap figures is a convoluted process. This has to do with the way CDF keeps track of individual level 2 trigger integrated luminosities. What makes this process especially difficult is the use of dynamic prescales. For a given set of runs it is possible to determine the "live" integrated luminosity for a given level 2 trigger (this was done in table 5.1). To determine the "live integrated luminosity overlap" two steps have to be taken.

Step one involves determining the "live integrated luminosity" for each trigger during the time period when each of the other triggers was "working". This is called the "uncorrected live integrated luminosity overlap". It is "uncorrected" because the effect of the prescales has not yet been taken into account; this is done in step two.

trigger region	run	run start	run end	L2 trigger table name	working int lum pb^{-1}	live int lum pb^{-1}	uncorrected live int lum overlap pb^{-1}
U	1a	40100	46145	CMU_CMP_CFT_9_2		13.25	0.00
	1a	46146	47835	CMUNP_CFT_9_2_5DEG		6.14	5.49
	1b	55245	71023	CMNP_CFT_12_5DEG		33.73	32.92
total					108.93	53.12	38.41
X	1a	40100	46145	no useful trigger		0.00	0.00
	1a	46146	46408	CMX_CFT_13_5DEG		1.04	1.04
	1a	46409	47835	CMX_CFT_13_ET_5DEG		4.18	3.68
	1b	55242	71023	CMX_CFT_12_5DEG		35.28	34.44
total					89.32	40.50	39.16

pb^{-1} integrated luminosity values have an accuracy of 3.3%

Table 5.2: Uncorrected live integrated luminosity overlap for trigger regions which were sometimes prescaled

Note that the only overlap measurement of significance is that between the "U" and the "X" trigger regions. The "P" trigger region was never prescaled. Consequently, all other overlaps can be obtained via simple addition or subtraction using table 5.1. Not only that, but the "P" trigger was operational 97.1% of the time. During the short periods when the "P" trigger region was inoperable, the "U" and "X" trigger regions were usually inoperable as well. Therefore, the "live" integrated luminosity values for the "U" and "X" trigger regions for periods when the "P" trigger region was not "working" are small.

Table 5.2 shows the relevant "uncorrected live integrated luminosity overlap" measurement for the "U" and "X" trigger regions. As an example, in the case of the "X" trigger region, 89.32pb^{-1} of luminosity was delivered during "working" intervals, and 40.50pb^{-1} of luminosity was delivered during "live" periods. During the period the "X" trigger was "working", the "U" trigger was "live" for 39.16pb^{-1} (this is the "uncorrected live integrated luminosity overlap").

The term "uncorrected" is used because it is not the actual overlap. The "X" trigger example shows that during the delivery of 89.32pb^{-1} of "working" "X" luminosity, the "X"

correlation description	correlation factor	fraction of events triggered by A	fraction of events triggered by B	fraction of events triggered by A or B	fraction of events with 2 triggers
completely correlated	1.0	.50	.50	.50	.50
zero correlation	0.0	.50	.50	.75	.25
completely anti-correlated	-1.0	.50	.50	1.00	.00

Table 5.3: Effect of the prescale correlation factor

trigger was “live” for 40.50pb^{-1} and the “U” trigger was “live” for 39.16pb^{-1}. It is necessary to determine the “prescale correlation factor”, how often one region was “live” when the other region was also “live”.

To illustrate why this is necessary, consider two hypothetical trigger regions “A” and “B”. Suppose the overall efficiency of each trigger region is perfect, but suppose each region is prescaled half of the time.

Consider only Z events where one muon enters each of the two trigger regions. If the prescales are completely anti-correlated, then whenever one prescale is on the other is off and vice versa. In this anti-correlated case all events would be accepted by the trigger logic (after the prescale), but no event would have triggers for both muons because the two triggers would never be “live” simultaneously.

Next consider the case where the prescales are completely correlated. Whenever one prescale is on the other prescale would also be on, and whenever one prescale is off the other prescale would also be off. Only half of the events would pass the muon trigger, and both muons in each passing event would pass the trigger.

Finally consider the case of completely uncorrelated prescales. In this case, by random chance, the prescales would overlap half of the time, and 75% of the events would have successful triggers. One third of the triggered events would have two muons which passed the trigger. Table 5.3 illustrates the effect of these hypothetical prescale correlation factors.

As can be seen from the table, the number of events entering the final data set is very dependent on the live integrated luminosity overlap between the triggers. In the final analysis evaluation of the prescale correlation factor involves a careful study of the Z-muon data set. Discussion of this analysis is presented at the end of the next chapter.

Chapter 6

The Background

The non-Z events which contaminate the dimuon invariant mass and dimuon Pt plots are comprised mainly of cosmics (the cosmic filter was not perfect), Drell-Yann (photon to dimuon) events, punch-through events (where a jet fakes a muon), and multiple vertex events (where two independent high Pt muons originating from different vertices can fake a Z-event. The small Drell-Yann cross-section is simulated adequately within the Monte Carlo and hence the only backgrounds of real interest are cosmic ray, punch-through, and multiple vertex events. It was necessary to have a thorough understanding of the background and the selection efficiencies of the cuts designed to minimize this background. A clear understanding of the selection process makes it possible to determine quantitatively the number of background events in the final sample, and to determine the efficiency of all of the cuts which were used to select a "pure" sample of Z events (this is performed in the following chapter). After all selection cuts have been applied the background present in the final sample is determined to be extremely small.

A Z-candidate event is required, at a minimum, to contain a second track identified as a muon which passes a set of "silver" selection cuts. The selected "silver" muon must have more than a minimum Pt, be contained in a fiducial region (it had to be pointed at superlayer 4 or higher within the CTC), be associated with a track that deposited a limited energy in the hadronic and electromagnetic calorimeters, and pass several quality cuts including a series of cuts devoted to the elimination of the cosmic ray background. In addition to individual track cuts, there were global requirements on the dimuon mass, and on a common vertex for the dimuon. The efficiency of any cut which was not emulated within the Monte Carlo had to be determined by independent means. Every effort was made to adjust the Monte Carlo parameters to accurately represent the experimental data. However, the Monte Carlo does not simulate cosmic rays and the removal of cosmic rays does result in the loss of a small number of Z events. This is one example of a Z event selection efficiency which is not taken into account by the Monte Carlo. These externally determined selection efficiencies can then be inserted into the Monte Carlo, in order to obtain a precise correspondence between the Data and the Monte Carlo.

Figure 6.1 is a useful flowchart which shows the main decisions that are made during background removal. It also shows the studies which are required in order to perform the different efficiency calculations as well as the final background contamination estimates. This flowchart will be particularly useful in the following chapter when the efficiencies and background estimates are determined quantitatively. This information presented in this chapter can be regarded as a qualitative introduction into the understanding of the background.

6.1 Punch-through events

It is possible for some fragment from a jet to pass through the calorimeter and then on to the muon chambers. This is known as "punch-through". When punch-through occurs the jet is typically a high energy one, and consequently such a jet will tend to deposit a lot of energy in the calorimeter. In the selection of Z events there are cuts imposed on the total amount of energy that is allowed to be deposited in the calorimeter associated with a track taken to be a muon, and these cuts reject most of the punch-through. However, it is believed that a small number of punch-through events are misidentified as Z-events.

It is possible to estimate the number of events in the final Z-sample which are actually punch-through events. This is done by studying events which pass all of the Z cuts except for the opposite-sign charge cut (meaning the two identified "muons" have the

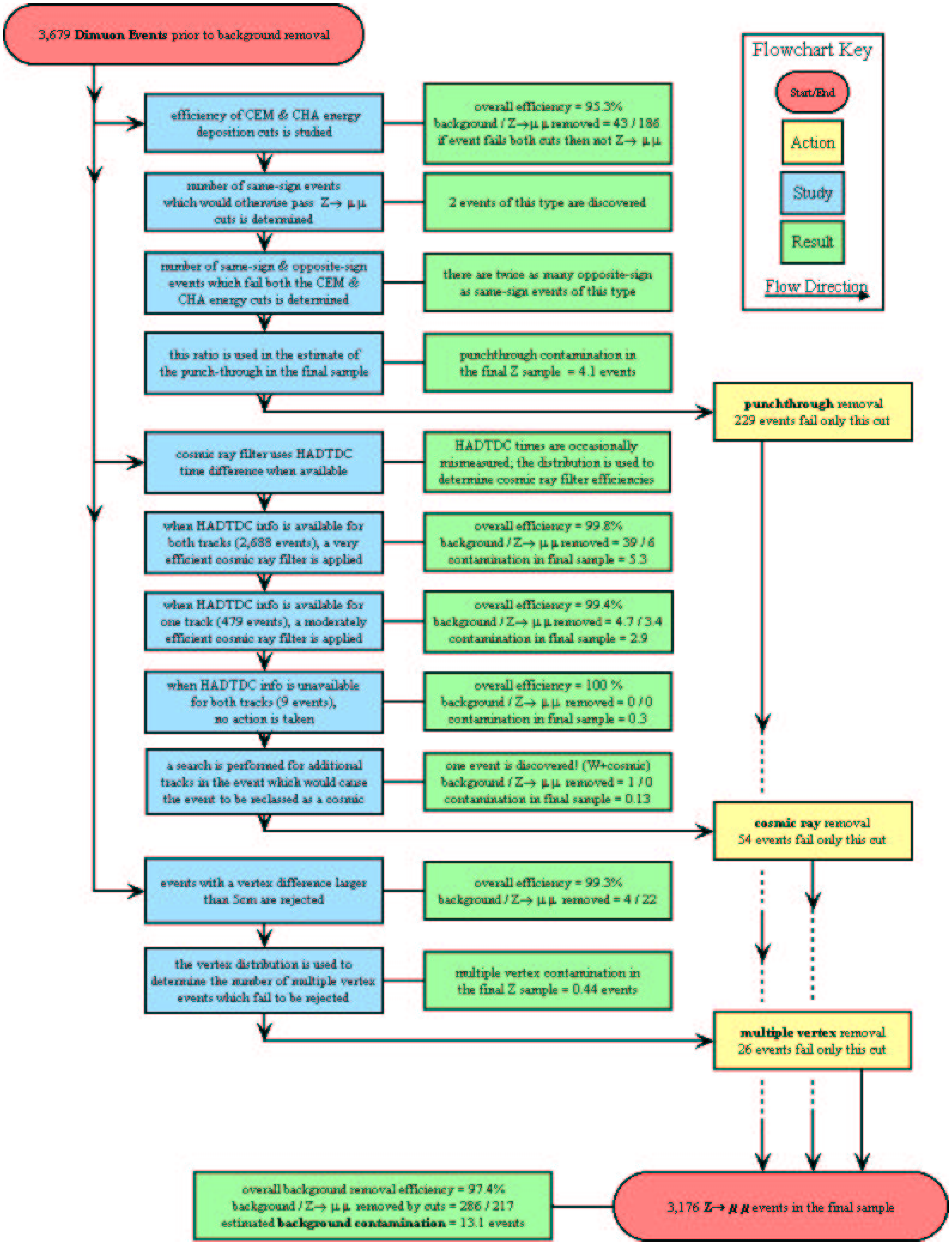

Figure 6.1: Flowchart illustrating the background removal process

same charge). Such same-sign events are believed to be punch-through events. It is believed that a roughly equivalent number of punch-through events will exist within the sample of Z events (where the "muons" are oppositely charged).

Two legitimate "punch-through" events were discovered within the sample of same-sign charge events, which implies that the number of punch-through events in the final Z sample is very small. This is important because such events can have strange Z Pt values (since they are not Z events to begin with). This will be explained in detail in the next chapter.

The number of "punch-through" events which contaminate the final set of Z events can then be estimated. To accomplish this, first, the ratio of opposite-sign to same-sign "punch-through" events which are rejected by both of the calorimeter cuts (it will be shown that all events which fail both of the calorimeter cuts appear to be non-Z events) is determined. The number of same-sign "punch-though" events which pass all of the calorimeter cuts is then scaled by this ratio. The resulting number is an estimate for the number of "punch-through" events which are believed to contaminate the final Z sample.

6.2 Cosmic Rays

It is hypothesized that cosmic rays are moving in a downward direction (as opposed to moving upwards through the earth). They thus enter the CDF detector somewhere through its upper hemisphere, and they exit somewhere through its lower hemisphere. Cosmic rays strike any muon chamber in their path, and they sometimes pass very close to the beamline. A muon moving towards the detector's center will trace the very similar path as a pair of oppositely-charged muons moving away from the detector's center. The offline tracking code will typically interpret a solitary cosmic ray track as two oppositely-charged oppositely-directed tracks which emanate from a vertex near the beamline.

Cosmic rays can fake a Z-event in one of two ways. The first and most common mechanism is for a cosmic ray to pass through the detector coincident in time to a beam crossing, triggering one of the muon detectors in its path. The offline analysis code interprets such an event as a candidate Z-event, if the invariant mass of the two oppositely-charged oppositely-directed tracks formed from the cosmic ray is close to the mass of the Z. As will be seen, there were several dozen events of this type prior to the removal of cosmic rays. These events are expected to be "quiet". Apart from the cosmic ray, there are typically few other tracks in the event. The existence of jets of particles in cosmic ray events should be extremely rare.

The second, less likely, way for a cosmic ray to fake a Z-event occurs when a cosmic ray passes through the CDF detector coincident with another event which has resulted in the creation of a highly energized muon (for example, W-events often result in a solitary highly energized muon). It is possible for a "legitimate" $\bar{p}p$ created event to include a cosmic ray track (as determined by offline tracking), such that the composite event appears to contain a dimuon invariant mass near the Z. As will be shown, the number of events of this type is very small (only one event of this type was discovered in the entire data set). However, events of this type are especially important to remove because the arbitrary association of two independent muons (producing a Z-like invariant mass) can result in a large Z transverse momenta. In this case the uncorrelated tracks are not typically back-to-back. There is also no reason to expect that events of this type will be "quiet" since there are other tracks from the $\bar{p}p$ collision within the event.

6.2.1 Z events and 10 GeV Jets

The absence of jets (10 GeV is a reference scale), are integral to CDF's ability to estimate the number of cosmic ray events.

Figure 6.2 shows the distribution of the number of 10 GeV jets in the final sample of Z candidate events. Almost one-third of the Z-candidate events (1,049 out of 3,171) contain at least one 10 GeV jet. Cosmic ray events are not expected to contain any 10 GeV jets, and hence it is possible to estimate the number of cosmic ray events in a sample of Z-like events by determining the fraction of events in the sample which contain at least one 10 GeV jet.

A cosmic ray that is interpreted as the two tracks of a Z must contain back-to-back

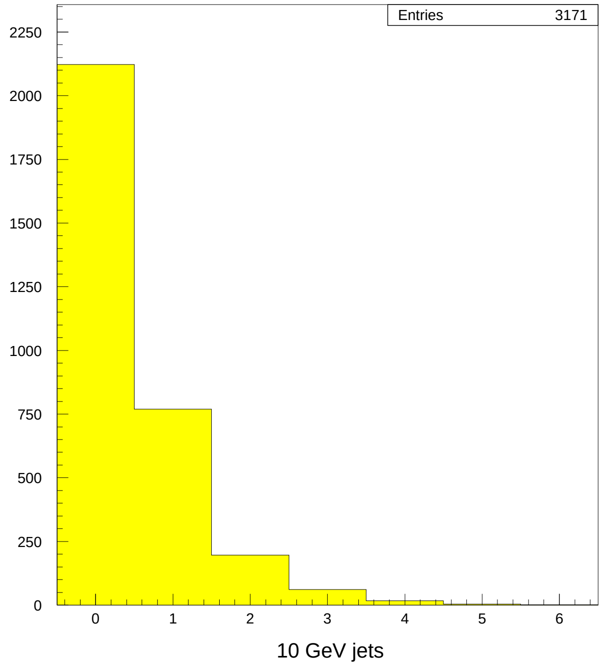

Figure 6.2: distribution of 10 GeV jets for the final sample of Z candidate events

tracks. The sample of Z events where the angle between the tracks that form the Z is greater than 160 degrees must contain the cosmic ray background. A comparison of the fraction of events with 10 GeV jets in them back-to-back relative to the remaining events yields the fraction of cosmic ray background.

It should be noted that Z events with a smaller angular track seperation are more likely to have jets associated with them. If a sample of Z-like events is selected where the angular separation between the tracks that form the Z is greater than or equal to 160 degrees, then the fraction of events containing at least one 10 GeV jet is reduced from one third to about one quarter (160 out of 664 events).

6.2.2 The Hadron TDC's

The Hadron TDC's provide an excellent handle for determining which Z-like events are in fact cosmic ray events. The Hadron TDC's provide accurate timing information for a track between scintillators on the top and bottom of the detector. For a "legitimate" Z-event, the hadronic TDC's timing information should exhibit nearly equal flight times for the two muon tracks, since the two muons will have been created at the same moment and will reach the muon detectors at roughly the same time. However, for a cosmic ray event, the hadron TDC's timing information for the track in the upper hemisphere is earlier than the hadron TDC's timing for the track in the lower hemisphere (by the total flight time to cross the detector). This time difference can be used to help to identify cosmic ray events.

Figure 6.3 shows the distribution of hadron TDC timing information for all tracks, prior to the implementation of cuts designed to remove cosmic rays. Note that the hadron TDC time difference cannot solely be used to identify cosmic ray events because they do not provide complete geometrical coverage. Only 85% of the total Z sample of events has such data. The coverage is actually better for more centrally directed tracks, since the hadronic calorimeter provides coverage out to an eta of about 0.9 and fewer tracks beyond this have hadron TDC timing information. If only the dimuon events are considered for which both legs pass through superlayer 6 or higher, nearly 90% of the events have hadron

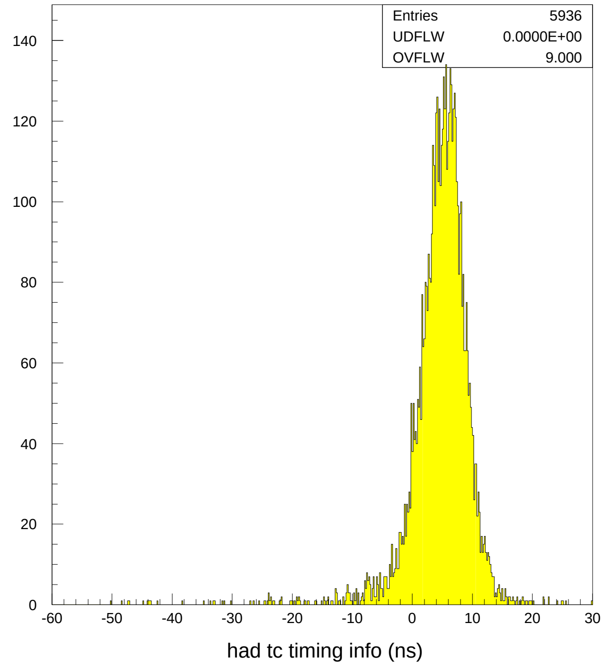

Figure 6.3: $\mu^+\mu^-$hadron TDC timing information, all tracks

TDC timing information available for both legs. Hadron TDC timing information is almost always available for at least one of the two tracks - only 9 of the events are missing hadron TDC timing information for both of the muon tracks, implying that there is some hadron TDC timing information present for 99.7% of the events.

Figure 6.4 shows a logarithmic plot of the time difference for dimuon events prior to either the application of the cosmic ray filter or the requirement that the dimuon mass be between 60 GeV and 120 GeV. Of interest is the bump between 15ns and 31ns, which is believed to be caused by cosmic ray events. There are a small number of events which have what appear to be mismeasured timing information (the time difference is large). It is believed that this happens when the original muon is missed and the scintillator registers the passing of a particle at some later point in time. For the same reason there are also events which have a time difference which is comparable to the time difference of the cosmic ray

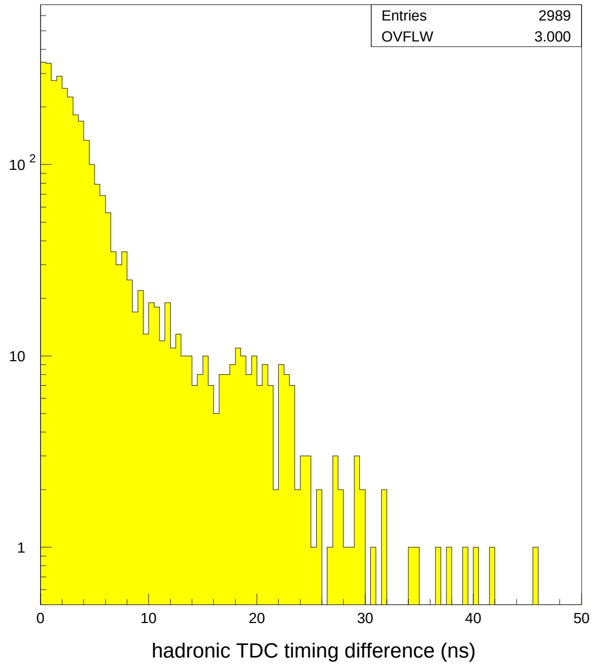

Figure 6.4: $\mu^+\mu^-$hadron TDC timing difference

events (the cosmic ray events are are a bump on a falling spectrum). Hence, in the removal of cosmic rays factors other than the hadron TDC time difference must be used, in order to reject as little of the signal as possible.

6.2.3 Strategy for Implementing a Cosmic Ray Filter

The CDF tracking code assumes that the particles travel from the center of the detector outwards, which is wrong for an incoming cosmic ray track. This often results in a poorly measured track, which in turn can cause poor vertexing. Additionally, a cosmic ray track can give rise to a poor chi-squared fit when the track is constrained to the vertex defined by the beam spot, if there is no beam vertex near to where the cosmic ray track made its closest approach to the beamline. Cosmic rays are removed according to the following strategies. In all cases the appropriate efficiencies will need to be determined.

1. The large luminosities that the accelerator was often run at meant that it was typical to find more than one primary vertex in the same event. Hence, it was possible for two high Pt tracks in an event which came from separate collisions to fake a Z event. It was possible to identify most of these events by imposing a maximum distance of 5 cm between the beam-constrained muon track vertices. In addition to removing randomly correlated multiple vertex events, this cut also removed events with highly mismeasured tracks. which included both cosmic ray events and "legitimate" Z events. Removing "legitimate" Z events which had at least one highly mismeasured track was actually beneficial because the Monte Carlo could not be relied on to reproduce experimental tail effects accurately. This cut had a negligible effect on rejecting cosmic ray events, because there were other handles (see below) which did a much better job. It became possible to decouple this cut from the final version of the cosmic ray filter. This cut was implemented for the purpose of rejecting multiple vertex events, and was not needed in order to reject cosmic ray events.

2. When beam-constraining was performed on each track, the chi-squared of the fit was initially required to be a reasonable value, otherwise the event was rejected (this is a standard CDF cut). This cut would have removed both cosmic ray events and "legitimate" Z events, except that the cut was relaxed to the point that it had no effect on the final sample at all. This relaxation was done because the cosmic ray filter was determined to be very successful at rejecting cosmic rays, and applying a chi-squared cut on beam-constraining needlessly complicated matters.

3. Events which have hadron TDC times for both high Pt muon tracks which makes the event likely to be a cosmic ray are rejected. This involves requiring that the upper and lower hemispheres of the detector each have one of the tracks, that the tracks be approximately back-to-back, and that the hadron TDC time difference for the two tracks must be within an appropriate value range. This cut will reject a small number of "legitimate" Z events, in addition rejecting most of the cosmic ray events.

4. Events which have tracks in each hemisphere of the detector and which are also approximately back-to-back and which also have hadron TDC information for only one of the two tracks are rejected if the existing hadron TDC timing information is consistent with that of a cosmic ray. To accomplish this, different cuts are imposed depending on whether or not the track which has hadron TDC timing information available is an upper hemisphere track or a lower hemisphere track, which gives rise to different efficiencies. The efficiencies of these cuts are not very good, because of the lack of hadron TDC timing information in the events (it is only present for one of the two tracks). However, there are not very many events of this type to begin with, and the strategy is a reasonable one.

5. All additional tracks in each event are studied in a search for possible cosmic rays. Each additional track is coupled to each of the candidate high Pt muon tracks, and the hadron TDC time difference (if it is available) is used to determine if any of the resulting track pairs are consistent with being a cosmic ray. This search discovered only one event of this type. It is hypothesized that in this event a cosmic ray passed through the detector coincident with a W-muon event being produced, and the W-muon candidate coupled to one of the two cosmic ray tracks to fake a Z event). This search was only performed if the hadron TDC time difference was available. It was possible to estimate the number of cosmic ray events which this search missed because hadron TDC timing information was lacking (since the efficiency of the search was fairly high, and since the search discovered only one event, then the number of events the search missed turned out to be small).

6.2.4 Initial Identification of a Sample of Cosmic Rays Events

Prior to the application of cuts designed to remove cosmic rays, a study was conducted to determine the appropriate hadron TDC timing and angular track separation parameters which were needed in order to implement an efficient cosmic ray filter. First, diumons were selected which had tracks in each of the detector's hemispheres. Both tracks were required to have hadron TDC times. If the time difference was positive (negative) for the lower hemisphere track relative to the upper hemisphere track, this determined the event was classed as "downward-moving" ("upward-moving").

Plots of the angular separation between the tracks (prior to beam-constraining) for both the "downward-moving" and the "upward-moving" events were made. A spike in the nearly back-to-back region for the "downward-moving" events could immediately be seen, an obvious artifact of cosmic rays. Upper and lower limits for the hardon TDC time difference were then implemented as part of the cosmic ray selection process. The limits were adjusted in order to minimize the number of upward-moving "legitimate" Z events in the angular distribution plots, while at the same maximize the number of events in the downward-moving events which were believed to be mostly cosmic rays. This method made it possible to set the lower and upper hadron TDC timing limits to be 15ns and 31ns, respectively, which corresponds to the time-of-flight for a cosmic ray which can fake a Z to traverse the detector.

Figure 6.5 shows the two angular distributions, with the obvious large surplus of back-to-back downward-moving events. Figure 6.6 shows this surplus explicitly when the upward-moving events are subtracted from the downward-moving events. This plot supports the choice of an angular separation of 160 degrees as an appropriate angular lower limit for the selection of cosmic rays.

Several different methods could then be used to determine how many cosmic rays had actually been selected within the downward-moving sample. First, with the specified cuts, 48 downward-moving events were seen and only 3 upward-moving events were selected. Under the assumption that the events which appeared to have upward-moving tracks are not cosmics, this implies that the downward-moving sample contains $45^{+1.7}_{-1.7}$ cosmic ray events, and $3^{+1.7}_{-1.7}$ Z events.

Second, if the selected 48 downward-moving events were indeed mostly cosmics then there should be a lack of 10 GeV jets in these events. As has been stated, the expectation for a random sample of Z events with a non-beam-constrained angular separation between

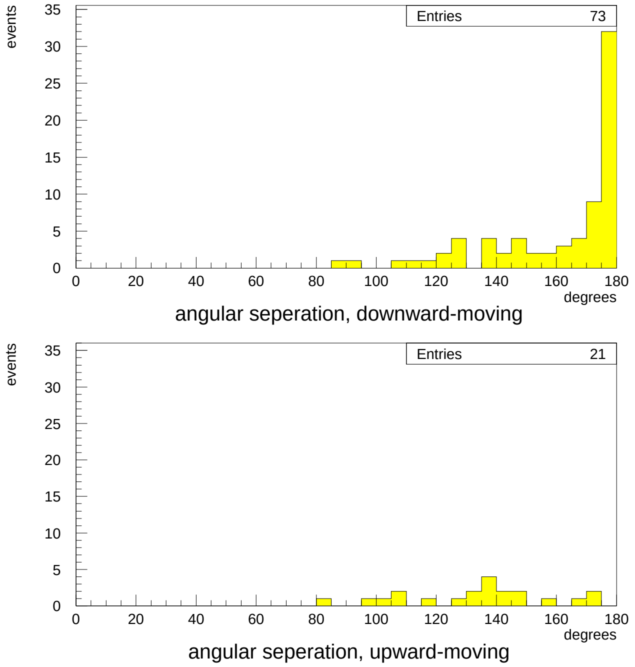

Figure 6.5: angular separation for downward-moving vs upward-moving events, using hadron TDC timing limits

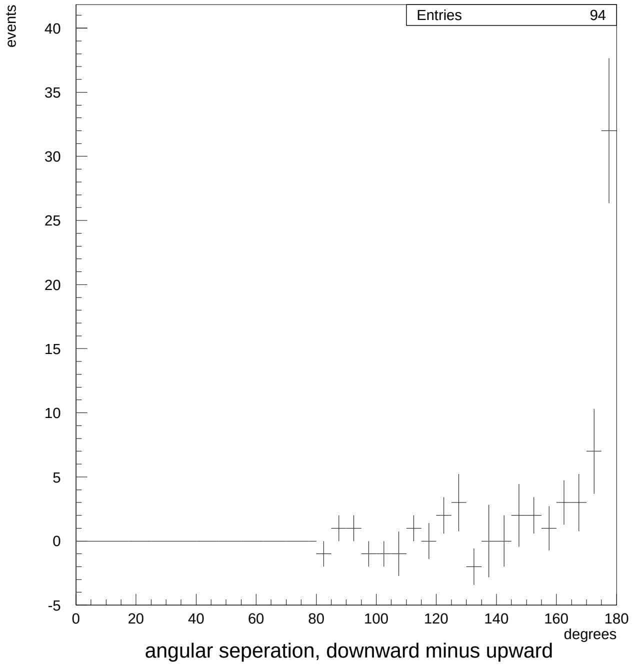

Figure 6.6: angular separation of downward-moving events minus upward-moving events

the muon tracks greater than 160 degrees is for one quarter of the events in the sample to contain at least one 10 GeV jet. If the 48 downward-moving events were Z-events, then roughly 12 of the events should contain at least one 10 GeV jet. Since the upward-moving sample contained only one such event, and since there is no reason to expect more "downward-appearing" physics events than "upward-appearing" physics events (this was verified with the Monte Carlo) then the expectation is for there to be 1^{+1}_{-1} physics events with at least one 10 GeV jet in the sample of downward-moving events.

In the sample of 48 downward-moving events, 3 events were found which contained at least one 10 GeV jet. This is consistent with the 1^{+1}_{-1} prediction above. Note that the 3 events with 10 GeV jets are believed to be Z events, and the invariant masses of these events were in fact all close to 90 GeV (they were 85 GeV, 88 GeV and 89 GeV). Three Z+jet events in this sample implies a total number of Z events in our selected sample of $12^{+6.8}_{-6.8}$, which implies there were $36^{+6.8}_{-6.8}$ cosmic rays in the sample of 48 selected events, which is consistent with the initial $45^{+1.7}_{-1.7}$ figure.

Figure 6.7 shows the invariant mass distribution for the selected sample of 48 downward-moving events. The mass spectrum does not exhibit the characteristics of a Z mass peak, although there is no doubt that the event sample, while made up mostly of cosmic ray events, does indeed contain a small number of Z events.

Having determined the appropriate hadron TDC time difference upper and lower limits in order to select a sample of predominantly cosmic rays, it became possible to determine appropriate single track hadron TDC timing cuts in order to select or reject a sample of cosmic rays when the hadron TDC timing information was only available for one of the two tracks.

Figure 6.8 shows the relevant hadron TDC timing distributions for the upper hemisphere tracks, and figure 6.9 shows the relevant hadron TDC timing distributions for the lower hemisphere tracks. As can be seen from the plots, it is possible to determine both the cosmic ray rejection efficiency and the Z-event acceptance efficiency for an arbitrary single track hadron TDC timing cut. The only complication which arises is in taking account the

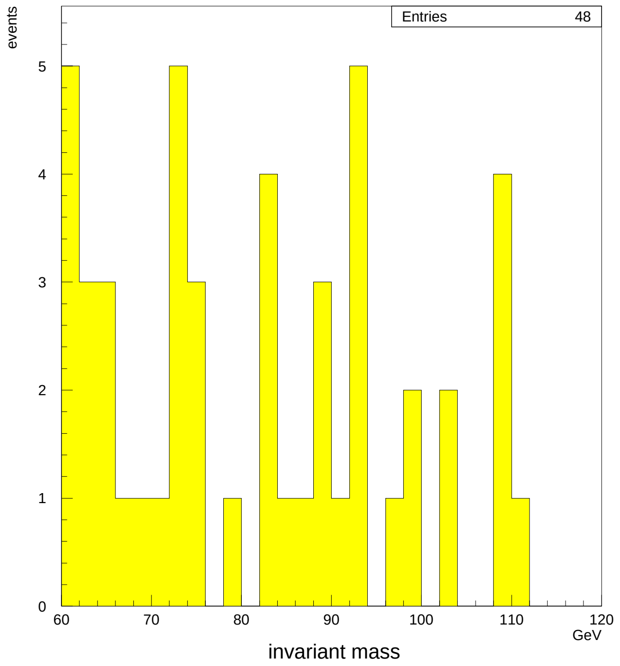

Figure 6.7: invariant mass of predominantly cosmic ray events

fact that the cosmic ray sample is not a pure sample to begin with. In the case of the upper hemisphere tracks, an appropriate timing cut on single tracks would be around -10ns. As can be seen from figure 6.8, demanding that upper hemisphere tracks have a hadron TDC timing above -10ns would be efficient at both rejecting cosmic ray events and at accepting legitimate Z events. Almost all of the upper hemisphere cosmic ray events have a hadron TDC time below -10ns, and almost all of the legitimate Z events have an upper hemisphere hadron TDC time greater than -10ns. For the lower hemisphere tracks, figure 6.9 implies that a reasonable set of timing cuts would create a window to accept events between -5ns and +15ns. It is readily apparent that cutting on the lower hemisphere outward-moving track's hadron TDC time is less efficient than cutting on the incoming upper hemisphere track's hadron TDC time, since in this case it is much harder to differentiate a cosmic ray track from a legitimate physics track. For example, a large fraction of the lower hemisphere cosmic ray tracks have a hadron TDC time which would fall within the proposed timing window to accept physics events.

To determine the selection efficiency of each cut accurately all cuts must be studied one-at-a-time. As in the previous chapter, each selection efficiency is determined by first relaxing only the cut being studied, and determining specifically that cut's efficiency. What was done of significance in this chapter was to determine what were appropriate cuts in the identification and rejection of cosmic rays. In the chapter which follows all cuts will have already been imposed, except for the specific cut being studied. In this way, the efficiency of each cut can be determined.

6.3 Multiple Vertex events

It is possible that the muons within a misidentified Z-event actually originated at two different interactions. For example, it is possible for there to have been two different interactions within the same beam-crossing, which produced two independent muon tracks, and these muon tracks were then misidentified as being part of the same Z-event.

A maximum track vertex separation cut is part of the Z-event selection process.

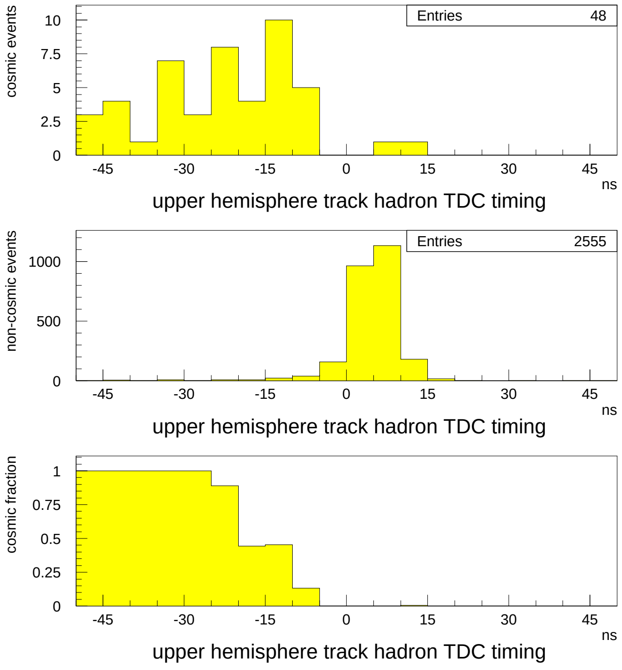

Figure 6.8: upper hemisphere hadron TDC timing information, cosmic fraction

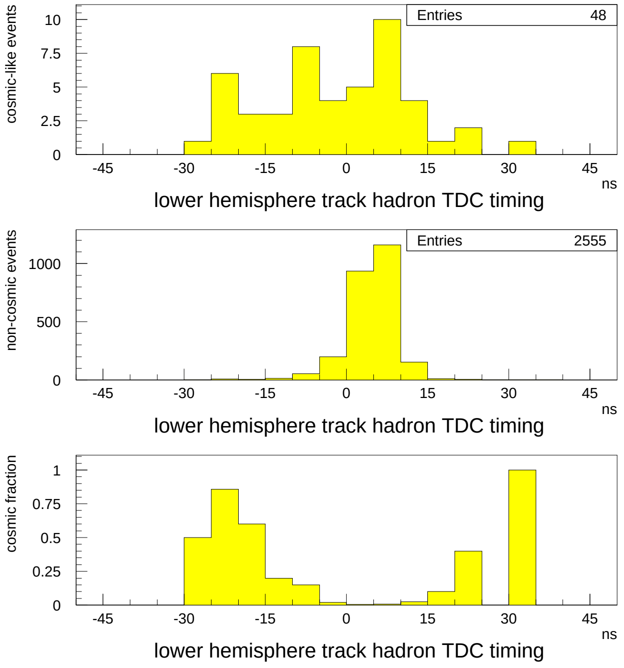

Figure 6.9: lower hemisphere hadron TDC timing information, cosmic fraction

The probability that a multiple vertex event would occur with a vertex separation which was within the Z-event maximum vertex separation cut, relative to the probability that a multiple vertex event would occur with a vertex separation which was outside the Z-event maximum vertex separation cut, was estimated. After estimating the number of multiple vertex events which had a vertex separation outside of the Z-cut maximum vertex separation (yet passed all other Z-event cuts), it was then possible to estimate the background number of multiple vertex events contained within the final Z sample.

Chapter 7

Identification and Selection of Z Candidate Events

The selection criteria that are applied to the high Pt muon sample in order to extract a sample of Z candidate events are extensive. All of the selection criteria are designed to purify the Z-sample which is ultimately selected. They also serve to reject background and spurious non-Z events.

1. At least two high Pt muons must have been successfully reconstructed by the offline tracking code.
2. At least one muon must have passed “gold” selection criteria. This is a fairly stringent set of cuts which require an appropriate muon stub.
3. A second muon must have passed “silver” selection criteria, a less stringent set of cuts than the “gold” selection cuts. Muon stubs are not required to be associated with “silver” muons, only a track of sufficient quality.
4. A “gold” muon must additionally have caused the event to be written to tape. In other words, a “gold” muon in the event must have been accepted by levels 1, 2 and 3.
5. The dimuon invariant mass (the “Z-mass”) of the event must fall within a suitable range.

7.1 Geometrical Coverage

There are three different muon systems as they are defined in this analysis. Regions 1 and 2 are mutually exclusive by design since no CMU region participates in both the "U" and the "P" trigger regions. It is assumed (and also verified) that there is effectively no correlation between the muon momentum and its selection efficiency, for the case of high Pt muons.

1. CMU-only (where the CMP is not required as part of the trigger)
2. CMU-CMP (where the CMP is required as part of the trigger)
3. CMX

Note that these three regions are usually referred to as "U", "P" and "X" within the analysis.

7.2 Efficiency Determination Method

It is desired at this stage to determine the probability that a given high Pt muon will pass the identification and selection criteria and cause the event to be written to tape (which would mean that the event would wind up in the high Pt muon data set). This has to be done for each detector system.

It is vital to determine these efficiencies. These numbers will later be introduced into the Monte Carlo so that simulated Z-event distributions correspond as closely as possible to the measured Z-event distributions. The procedure will be to apply acceptance and selection filters for the Monte Carlo generated events and to compare the resulting Monte Carlo distribution to the corresponding measured distributions. For example, muons from high transverse momentum Zs tend to migrate towards the low η central region where the CMU is located. Hence, the Z-muon detection efficiency depends on the original Z transverse momentum. This characteristic of the detector must be taken into account. In this experiment the muon detection efficiency in the low-η CMU region is higher than in the slightly higher-η CMX region, resulting in a larger fraction of muons which hit the CMU being written to tape. Thus the CDF detector as a whole is better at detecting Zs with a larger transverse momentum. Hence the different efficiencies must be taken into account if Monte Carlo simulations are to be used to extract the parameter of Z production.

The determination of these efficiencies was perhaps the most complex and labor-intensive part of this thesis. Extraordinary care had to be taken in order to determine the correct values.

Both selection efficiencies and trigger efficiencies were obtained using the Z-muon sample. This sample was used because it was the largest high statistics unbiased sample available. There are approximately ten times as many high-Pt muons from W-decay events which could have been used. However, almost all of these events were written to tape solely because the high Pt muon in the event successfully fired levels 1, 2 and 3 of the trigger. It is not possible to do muon selection and trigger efficiency studies using single-muon events which were written to tape solely because of the muon that is being studied. The number of events with high Pt muons from W-decays which were written to tape because of a non-muon trigger was negligible. It is the Z-muon sample which provides the best statistics for this study.

In Z-muon events, there are two high Pt muons. For this study one muon is required to trigger and to pass all the selection and trigger cuts required to be included in the final sample. Then the other muon in the event is studied in an unbiased way. A careful examination reveals the desired efficiency values. The easiest way to do this would be to study only Z events where the two muons enter different detector systems. The CDF trigger design makes this sample the ideal choice. The final muon trigger decision at each level is global in nature. In effect it is the logical OR of all of the trigger decisions for that subsystem (for that level). When there are two or more high Pt candidate muons in the same trigger region, the global nature of the trigger decision does not immediately make it obvious which candidate muon produced the trigger (or perhaps both muons did). It is necessary to go to extraordinary lengths to figure out which candidate muon generated the trigger. This is done via a careful and complete simulation of the trigger electronics using the individual event data readout as the input to the simulation. By studying events where the two muons enter different parts of the same detector subsystem, the overall statistics and therefore the accuracy of the study can be improved.

A source of consternation (apart from the global nature of the trigger decisions) was the fact that track reconstruction occurs during both online data taking and then again offline (where a more complete track reconstruction occurs). To complete a trigger analysis in this situation it is necessary to match the offline reconstructed track to the online reconstructed track, which in turn must be matched to muon stubs and detector hits and to also any trigger associating these matches with signals seen in the event. Therefore, it is necessary to deal with both offline tracks and stubs and online tracks and stubs in a consistent and coordinated approach. A computer subroutine called CMUSWM ("CMU-swim") was used to simulate the trajectory of the muon as it exited the detector (using the measured tracking parameters as input). This made it possible to match tracks to stubs and trigger towers. Also, a full simulation of the high Pt muon trigger was used. This simulation utilizes the time digitizations recorded for each of the detector channels in a computational emulation of the trigger electronics. This trigger simulation effectively made it possible to match trigger signals to actual tracks. The reliability of the simulation can be checked by comparison of the simulated global OR with the hardware generated OR. The full information regarding which muon (or both) generated the trigger was retained in the simulation in contrast to the simpler OR performed in the hardware.

A failure to match tracks to stubs to trigger decisions properly during either an efficiency study or during event selection would result in biases. These biases often lead to an overestimation of a particular efficiency, or else an overselection of the events within a sample. As an example (and there are numerous to choose from), suppose two muons of a Z both enter different parts of the CMU-CMP region. One muon, or even some spurious set of hits not associated with either muon, could produce a global level 1 high Pt CMU-CMP muon trigger, but the other leg might fail level 1. The muon which failed to generate level 1 could in turn satisfy levels 2 and 3, while the muon which had successfully triggered level 1 could fail one or both of these levels. In this case the event would be written to tape because all three levels of the trigger had been satisfied. However, neither of the muons on their own would have triggered the event, and, for this reason, the event should be excluded from the final Z-muon data set. Without a complete understanding of the trigger it is impossible to exclude such an event.

The Z transverse momentum efficiencies are to be determined from a Monte Carlo simulation assuming a single track satisfied the selection criteria at all levels. The data analysis accomplishes these same conditions by matching an offline muon to an online muon and then by examining the online muon as it progresses through the selection process. Geometrical cuts are applied based on the muon's measured tracking parameters, using the routine CMUSWM to match tracks to stubs and ultimately to trigger towers and detector hits. A candidate "gold" muon must pass levels 1, 2 and 3 in order for the event to be included in the final sample. The muon trigger simulation matches all trigger decisions to each and every muon track candidate. Near-perfect agreement is found between the simulation and the actual data (all discrepancies were either eliminated or else taken into account in the final determination of the detector efficiency).

Only with a complete trigger simulation was it possible to reject events which would otherwise have biased the final sample. Two important terms will now be defined which will be used throughout this analysis to describe the different types of biases which needed to be understood.

Underselection of events; an "under event" occurs when the event selection criteria results in a smaller-than-desired data sample (ie Z-muon events are deselected). While it is desired to have as large a data set as possible, underselection is not usually a problem in that it should still result in consistency. For example, if a tighter-than-necessary selection cut is applied to a particular quantity, then fewer events will make it into the final data set than otherwise. However, an efficiency study would produce a correspondingly lower-than-possible selection efficiency. When this selection efficiency is used as part of the Monte Carlo simulation, a smaller-than-possible acceptance would follow. An analysis would generate correct results, albeit with smaller-than-possible statistics.

Overselection of events; an "over event" occurs when the selection criteria are too loose resulting in a biased data sample which is larger than it should be. "Over" events can result in inconsistencies between the Monte Carlo simulation and the data. Overselection of events is the main problem which must be minimized. In this analysis the Monte Carlo uses an overall single track efficiency to determine the acceptance. For example, it is important not to allow events into the final data sample which made it there via a "sharing" between the muons of different levels of the trigger. This would result in a final data set with too many events, and a calculated single track efficiency which was too large. The overefficiency would then be used in the Monte Carlo simulation to generate a set of simulated events whose characteristics would differ from those of the data events. In this example the Monte Carlo determined acceptance would be biased high because the selection efficiency would be biased high.

Because of the potential problem with "over" events into the data sample I will present a second example which will be discussed in detail later. For a large fraction of the data there was an electronics problem associated with the level 2 muon trigger. This resulted in occasional random triggers (when none should have occurred) and also in non-triggers (when they should have occurred) on a track-by-track basis. The selection criteria in this analysis adequately dealt with the extra random triggers because a simulated level 2 trigger is required in this analysis. The random false-triggers were deselected as part of the normal selection process. However, the random non-triggers cause two problems. First, the resulting data set is smaller than it should have been because many events which experienced a random non-trigger were not written to tape. Second, and more importantly, within the smaller-than-it-should be data set there are events where one or more of the muon candidates experienced random non-triggers, and other muon candidates triggered normally. This actually leads to an overselection of events for the final data set, due to the global nature of the level 2 trigger. This happens because it is impossible to determine whether an event was written to tape because of a particular muon candidate within the event. Nothing can be done to eliminate the "over" events from the data set without drastically reducing the size of the data set. All that can be done is to try to estimate their impact and adjust the results accordingly later on.

To summarize, in this analysis, an effort has been made to compensate for the overselection of events. There was no way to avoid them entirely but at least their impact has been minimized. The selection efficiency determination was optimized, and the largest possible set of unbiased Z events was obtained.

7.3 Z Event Selection Criteria

The selection criteria which are used to select Z candidate events from the high Pt muon sample. These cuts are more selective than those for the all "muon" selection:

1. "Gold" muons are required to point at superlayer 8 of the CTC. "Silver" muons are required to point at superlayers 4 thru 8 of the CTC.
    - This is determined using the CMUOTR fiducial routine.
2. Muon stub offline Pt $>$ 18 GeV.
    - The muon's offline reconstructed track Pt must be greater than 18 GeV.
3. Muon stub beam constrained Pt $>$ 20 GeV
    - For each individual run the beam spot is well defined (in the x and y coordinates at least). The information is used to effectively add an additional point to the list of CTC hits for a given track, and hence a more accurate determination of the momentum of a given track is obtained, assuming that the track originated at the collision point.

4. Hadronic energy < 6 GeV

    - The requirement puts a limit on the amount of hadronic energy deposited in the hadronic calorimeter in the region of the track. The cut's primary purpose is to reject non-muon particles.

5. Electromagnetic energy < 2 GeV

    - The requirement puts a limit on the amount of electromagnetic energy deposited in the electromagnetic calorimeter in the region of the track. The cut's primary purpose is to reject non-muon particles.

6. The maximum vertex separation must be < 5 cm

    - The requirement puts a limit on how far apart the originating tracks are allowed to have originated. For a legitimate Z-event the muons originate at the same point. However, since experimental data is being used, it is necessary to allow for the possibility of small tracking errors.

7. The muon must pass the cosmic filter.

    - The cosmic filter attempts to reject cosmic events. One of the ways it does this is to examine the timing of the hadron TDCs for tracks which are nearly 180 degrees apart. Such tracks are either two particles traveling outward towards opposite corners of the detector, or else they correspond to one particle traveling through the detector (a cosmic ray). If the muon is a cosmic ray then the hadron TDCs will record distinctly different times. If the tracks originated simultaneously at the center of the detector (from the decay of a Z) then the hadron TDCs will be hit at approximately the same time. It is possible to place cuts on this time difference, and consequently to reject cosmic ray events. Unfortunately, only a fraction of muon tracks have available hadron TDC timing data.

8. Individual detector cuts necessary for a high Pt muon to be classed as "gold". (Note that the requirements are more stringent than before)

    - For muons in the CMU-only region: CMU dx $<$ 2cm and the CMU must be classed as having been in good working order for the run in question.

    - For muons in the CMU-CMP region: CMP dx $<$ 5cm and both the CMU and the CMP must be classed as having been in good working order for the run in question.

    - For muons in the CMX only region: CMX dx $<$ 6cm and the CMX must be classed as having been in good working order for the run in question.

9. The muons within the event must be oppositely charged.

10. The dimuon invariant mass for the event must lie between 60 GeV and 120 GeV.

7.4 Z Event Trigger Criteria

A "gold" muon must pass levels one, two and three. The following criteria are used to determine this. Note that CMUSWM is used to determine whether the muon should be classed as "U" (CMU-only region), "P" (CMU-CMP region) or "X". In this determination the best possible tracking parameters are used as inputs for CMUSWM, namely the beam constrained tracking parameters.

7.4.1 Level One

For "U" (CMU-only): A five-degree CMU-only tower within 0.5 degrees (in phi) of the predicted CMUSWM'd CMU-only phi position must have fired (adjoining CMU-only towers are considered if they are also "U"; if the adjoining tower is classified as "P" then it is not considered). The event must also have fired the global level 1 CMU-only trigger (this is expected to happen given the above requirements).

For "P" (CMU-CMP): A five-degree CMU-CMP tower within 0.5 degrees (in phi) of the predicted CMUSWM'd CMU-CMP phi position must have fired (if the adjoining tower is not a CMU-CMP tower then it is not considered). The event must also have fired the global level 1 CMU-CMP trigger (this is expected to happen given the above requirements). The corresponding MP1T simulated trigger tower must also have fired (this includes a timing cut on the CMP chamber hits and will be explained in detail below).

For "X": A five-degree CMX tower within 0.75 degrees (in phi) of the predicted CMUSWM'd CMX phi position must have fired (if the adjoining tower is not a CMX tower then it is not considered). The event must also have fired the global level 1 CMX trigger (this is expected to happen given the above requirements). The corresponding MH1T simulated trigger bit (a data bank called the TOWE bank is used during this determination) must also have fired (this includes a timing cut on the CMX chamber hits and will be explained in detail below). Also, the corresponding MU2X tower (the logical AND of the MX1T and MH1T trigger bits) must have triggered.

The above includes several nonstandard level 1 trigger cuts (nonstandard from the context of other CDF analyses).

The CMUSWM phi cuts are implemented to verify that a trigger tower has fired within a fraction of a degree of the predicted trigger tower. This cut is necessary to prevent the overselection of events problem. The tracking parameters are not known exactly, and multiple scattering means that a muon will hit a muon detector over a smeared range of phi values, rather than at one specific point. For approximately one in five tracks two adjoining trigger towers are allowed as possible trigger sources, and for the other 80% of the tracks only the trigger tower that is predicted by CMUSWM is considered. These ratios are slightly different for CMX because the CMX is further away from the collision point than the CMU. The CMUSWM phi cuts were determined via a very careful examination of how well the CMUSWM prediction compares to the observed level 1 trigger. The desire here was to make the CMUSWM phi cuts as tight as possible so that spurious triggers in nearby towers could be eliminated. It was also desired to accept as many good muons as possible.

In the case of the CMP and the CMX there are additional simulated trigger tower cuts which include timing cuts on the chamber hits. The CMP and CMX chambers can have much longer drift times than the CMU (of the order 1.6μs). The muon trigger is supposed to make a level 1 trigger decision before FRED makes its own final level 1 trigger decision. Unfortunately, it turned out that on occasion the muon trigger decision arrived too late - sometimes FRED made its final decision before the muon trigger decision arrived. This occurred when there were important chamber hits near the maximum allowed drift times in the CMP or the CMX ("important" in this context means that these hits made the difference as to whether or not the trigger fired). This is problematic when a different muon, or some other happening in the event, was responsible for the event being written to tape. In this situation the global level 1 muon trigger decision cannot be completely trusted. Luckily, this problem is not very serious (of the order 1 percent). Also, it was possible to use the CMP and CMX chamber hit times to simulate the muon trigger in order to fail muons when the simulation indicated that the trigger signal would arrive after FRED had already made its decision. The agreement between the level 1 CMP and CMX simulated trigger and the actual response is excellent. Therefore, a study was performed to determine what the maximum FRED-allowed CMP and CMX drift times were, and cuts which corresponded to these values were then implemented. These cuts were used as part of the trigger simulation, which was used to determine whether or not an individual muon did indeed produce a level 1 trigger. Hence, it was possible to eliminate this late-trigger problem from future considerations. This study is shown later in this chapter.

7.4.2 Level Two

A full level 2 trigger simulation was run for tracks which passed the above level 1 requirements to determine if they would also pass level 2. It was especially important to use a track-by-track level 2 simulation at this stage because the global level 2 high Pt trigger was unreliable (at the 3% level) for approximately one third of the data. Tables which illustrate this are shown later in this chapter.

The cause was a handshaking problem between the track list card and another important level 2 card. The track list card was implemented near the end of run 1a to reduce the number of unwanted level 2 triggers. It used tighter matching between the track position and the trigger towers (so-called "5-degree matching" instead of "15-degree matching"). This resulted in what are now believed to have been occasional random firings and non-firings of the level 2 high Pt muon trigger. The full level 2 trigger simulation included a determination of whether or not the level 2 trigger should have fired on a track-by-track basis, since level 2 makes its decision on a track-by-track basis.

It is believed that the tracklist card handshaking problem resulted in an occasional incorrect level 2 trigger decision being made for individual tracks. The problem is unfortunately believed to have been random in nature, and there is no way to expunge this problem from the data because the problem existed for a large fraction of the run. It is relatively easy to eliminate events that were not supposed to have made it to tape, by demanding that the muons first pass the level 2 simulated trigger (which does not include the random undesired firings). However, the random non-firings of the trigger have serious consequences for events that have an additional level 2 high pt muon track in the same detector region, as is the case for many Z events. It is impossible to state for sure if a given muon triggered properly, because the level 2 decision for a given subsystem is global in nature and is the logical OR of the level 2 result for all of the tracks within that detector subsystem. As has been stated, this type of event leads to "over" events, and there is no way to eliminate them from the final data set. This data is an important part of the sample used to determine the final selection efficiency. The trigger uncertainty is a problem which must be dealt with.

As an example, suppose two muons are pointed at different parts of the CMU detector. Suppose both muons trigger at level 1. Suppose also that both muons are supposed to generate a level 2 trigger (according to the full level 2 trigger simulation), and suppose the global level 2 CMU trigger is indeed generated. The handshaking problem means that it is impossible to know if both muons did indeed generate level 2 triggers, or if only one of them actually triggered level 2, and the second track had a random level 2 fail. A random level 2 fail would mean that one of the two tracks should not pass the imposed trigger requirement. But as far as can be known, both muons passed. There is no way to fail tracks that fall into this category. Alternately, suppose the track which has the random level 2 fail passes level 3, and suppose the track which passes level 2 fails level 3. Then the event should not be in the final Z sample at all, because there was no muon which by itself passed all levels of the trigger. There is no way to eliminate events like this from the final sample.

All that can be done is to correct the final efficiency values by taking the "over" event problem into account. As has been stated the problem was at the 3% level for about one third of the data, so it was at the 1% level overall.

The above includes nonstandard level 2 trigger cuts (nonstandard from the context of other CDF analyses). To my knowledge no CDF analysis has ever used the full level 2 muon trigger simulation, or more specifically, the tracklist card simulation, whereby the final level 2 trigger decision can be predicted for an individual track.

7.4.3 Level Three

A full level 3 trigger simulation was run for tracks which passed the above levels one and two conditions. CMUSWM was used again to restrict the stub match to muon stubs within a fraction of a degree in phi of the CMUSWM'd level 3 tracking parameters for the tracks of interest.

Two nonstandard level 3 trigger cuts were used (nonstandard from the context of other CDF analyses). CMUSWM was used to restrict the stub match. This requirement removed few events because phi restrictions had already been imposed. Additionally, CMP only level 3 stubs were allowed in the "P" region. Specifically, while it was required that a muon in this region pass both the CMU-CMP level 1 and two triggers, no actual CMU stub was required to pass level 3. A CMU stub is expected in conjunction with CMU level 1 and two trigger firings, but the presence of a good quality stub is not guaranteed. At level 3 the only requirement imposed on the CMU-CMP region was that there be an appropriate level 3 CMP muon stub. This resulted in not only a slightly higher calculated efficiency but also a correspondingly larger number of Z events in the final sample.

7.5 The Trigger Simulation

Each muon is flagged as "gold", "silver" or "fail". The Z-sample is selected from events containing at least one "gold" muon, while a secondary muon in the event must be either "gold" or "silver", and the dimuon invariant mass must fall within a Z selection range. The overall selection efficiency for each of the detector regions is then determined.

There are three types of events which need to be considered.

1. A "gold" muon entered one muon detector and a "silver" muon missed all three muon detectors.
2. A "gold" muon entered one muon detector region and the other muon in the event entered a different muon detector.
3. Both muons entered the same detector region.

Let ϵ_{CMU}, ϵ_{CMP} and ϵ_{CMX} represent the overall muon selection efficiencies for the three different trigger regions (ϵ_{CMU} stands for "efficiency in the CMU-only region", and ϵ_{CMP} stands for "efficiency in the CMU-CMP region", and ϵ_{CMX} stands for "efficiency in the CMX region").

"Type 1" events are relatively uninteresting because they do not enter into the overall selection efficiency calculation. This is because the secondary leg (which missed all of the muon detectors) could not have caused the event to be written to tape, and hence no efficiency studies can be performed.

However, "type 2" and "type 3" events are important for selection efficiency calculations. Here, one "gold" muon causes an event to reach the final data set, and the other

region	good run events	good triggers	over triggers	under triggers
U and P	31222	25260	0	0
X	31168	6583	0	0
Summary			0	0

Table 7.1: level 1 FRED simulation results

muon can then be studied in an unbiased way. The reverse holds true if the secondary muon is classed as "gold" as well. Some bookkeeping is required to correctly handle the dual use of a single event. Both types of events can be used as part of the overall efficiency studies for each detector region.

In what follows, a sample of 31,302 events from runs 1a and 1b is used. This data set is made up of all events with at least one high Pt muon (loose cuts), and the final Z sample was extracted from these events.

7.5.1 Level One FRED Simulation

The FRED output trigger decision was compared via a simulation of the FRED inputs. The performance of two FRED trigger decisions were of interest, the high Pt CMU trigger, and the high Pt CMX trigger (note FRED makes no distinction at level 1 between the "U" region and the "P" region).

As can be seen from table 7.1, FRED performed flawlessly.

7.5.2 Level 1 Muon Trigger Simulation

The final level 1 muon trigger decision for each of the three muon trigger regions is compared to the corresponding FRED input. The final level 1 muon trigger decision is determined via a simulation of the level 1 trigger (see table 7.2). Note that the CMU and CMUP level 1 trigger decisions are indistinguishable because they feed to the same FRED input, but it is possible to separate the two during the simulation of level one.

region	good triggers	over triggers	under triggers
raw U	3669	1	0
raw P	21891	2	0
raw X	6583	5	0
raw CMH	757	0	0

Table 7.2: level 1 muon trigger simulation results

This enables potential problems to be diagnosed. An "over trigger" would occur when the corresponding FRED input was not seen and the muon trigger simulation predicted it should have generated, and an "under trigger" would occur if the corresponding FRED input was present when the muon trigger simulation predicted it should not have been. This definition might seem backwards, but the purpose is to maintain consistency with the definition of "over efficiencies". Recall that "over efficiencies" cannot be adequately unraveled, while "under efficiencies" are troublesome but manageable. All that needs to be done to account for "under efficiencies" is to remove them with the aid of the appropriate simulation. Region "CMH" refers to a time during run 1a when the CMX trigger was being used in an experimental mode in conjunction with the hadron TDCs. The trigger was successfully simulated, but no events from this period were used in this analysis.

On careful examination, it can be seen that there were several "over" events. Although they are apparently small in number, it is important to realize that the numbers in these studies are always biased. This is because most of the events in this high Pt muon sample are single muon events, and "over events" in this case correspond to events which were not triggered by the track being studied. Problem events amounting to only a small fraction of the overall sample can actually be an indication of a more serious problem if the underlying event selection process is biased, as is the case here. An "over efficient" event will not make it into the final sample unless something else in the event causes the event to be written to tape. So while table 7.2 indicates a ratio of one in one thousand or one in ten thousand, the problem is actually closer to the one in one hundred level. Table 7.3 shows

region	good triggers	over triggers	under triggers
raw U	114	1	0
raw P	430	1	0
raw X	653	5	0
raw CMH	47	0	0

Table 7.3: non-muon triggered subset of the level 1 muon trigger simulation results

the ratio obtained from the unbiased subset of table 7.2 events, triggered by non-muons. The statistics are smaller, but the results with regards to the muons are unbiased. As can be seen in a comparison of tables 7.2 and 7.3, almost all of the “over” triggers but only a small fraction of the “good” triggers from the muon-triggered sample actually make it into the non-muon triggered sample. Hence a seemingly minor problem turns out to be significantly more serious than it naively appears to be.

Specifically, in the case of the CMX, a negligible five out of sixty-five hundred events is actually five out of six hundred and fifty events, and represents a roughly 1% effect.

The reason for the “over” efficiencies was introduced earlier in section 7.4.1. In some events the muon trigger decision did not arrive at the FRED inputs before FRED made its final trigger decision. This delayed arrival was a consequence of the level 1 muon trigger gate being slightly too long to be consistent with the FRED decision. This inconsistency affected both the CMP and the CMX. This problem only affected the CMP and CMX trigger regions, because the CMU chambers have much shorter drift times. To deal with this problem a full simulation of the CMP and CMX trigger was performed beginning with individual TDC readout times. The chamber drift times were software gated in the simulation to eliminate the events where the final trigger decision arrived too late at the FRED inputs. See table 7.4.

Note that the two “under” CMU events in table 7.4 are the same events as the two “under” CMP events because the corresponding FRED input signals are indistinguishable. The CMU numbers only changed here because the CMP numbers changed.

region	good triggers	over triggers	under triggers
raw U	3669	1	2
raw P	21889	1	2
raw X	6566	1	17
raw CMH	757	0	2

Table 7.4: level 1 gated muon trigger simulation results

region	good triggers	over triggers	under triggers
unbiased U	114	1	1
unbiased P	429	0	1
unbiased X	636	1	17
unbiased CMH	47	0	1

Table 7.5: level 1 gated muon trigger simulation results

The gated simulation drastically reduced the number of problem "over" events. At the same time it created a small group of "under" events, and these events cannot now pass the final set of cuts, since this gated simulation will be used in our selection process. However, this small event reduction is well worth the price for having complete confidence in our final overall level 1 selection efficiencies.

To quantify the importance of the remaining "over" events after the gated simulation is added to the trigger selection, it is necessary to again extract the non-muon triggered subset. The statistics here are smaller, but as expected the effect is more pronounced. See table 7.5. As can be seen in tables 7.3 and 7.5, the importance of the effect has been drastically reduced using the gated simulation. The only real concern is the single over efficient CMU event (one out of one hundred fourteen events is worth worrying about).

A larger sample of 94,934 events was then used to further quantify the importance of the CMU problem. Table 7.6 shows the results of this study. Approximately 1% of the time CMU triggers failed to arrive at the FRED inputs for some unknown reason. However, this

region	good triggers	over triggers	under triggers
unbiased U	433	4	1
unbiased P	809	0	1
unbiased X	1132	1	35
unbiased CMH	219	0	1

Table 7.6: non-muon subset of level 1 gated muon trigger simulation results, using a larger initial data sample

region	good triggers	over triggers	under triggers
old U	588	0	0
new U	3286	109	2
new P	21382	4	0
new X	6205	222	15

Table 7.7: level 2 simulation results

problem did not exist for the "P" region of the level 1 trigger. Consequently the suspicion must lie with the signals for the CMP mask, which suppress the CMP trigger requirement for specific five-degree towers. A correction corresponding to a 1% failure rate was included in the final efficiency calculations.

7.5.3 Level Two Muon Trigger Simulation

The same degree of care was taken at level 2. A complete simulation of the level 2 muon trigger was performed (this analysis is unique in this regard), and the results are shown in table 7.7.

Level 2 employed the "old" 15-degree matching during the first part of run 1a and the "new" "5-degree matching" for the latter part of run 1a and for all of run 1b. In table 7.7 "old U" refers to the "15-degree" matching period, and "new U", "new P" and "new X" refer to the "5-degree" matching period. There was no need to study "old X" because events

region	good triggers	over triggers	under triggers
old U	51502	0	1
new U	4636	6	4
new P	10127	20	1
new X	5839	283	4

Table 7.8: level 2 run 1a simulation results

region	good triggers	over triggers	under triggers
old U	0	0	0
new U	37774	5127	96
new P	89961	1365	22
new X	41408	5001	1393

Table 7.9: level 2 run 1b simulation results

that were written to tape because of the CMX triggers are only used in this analysis during the "new X" period. The "old U" level 2 worked as intended. There are no discrepancies during this period. There are a large number of discrepancies, both "under" and "over", in the "new" implementation of level 2. Most of these discrepancies can be attributed to the fact that the "new U" and "new X" trigger regions were often prescaled by level 2. It follows from this prescale that we should expect over efficient events, because sometimes the simulation of level 2 will predict a corresponding level 2 trigger, and the prescale means that no trigger occurred. However, the "new P" trigger region was never prescaled, and therefore there should be zero discrepancies between the level 2 trigger simulation and the data, but unfortunately some discrepancies exist. Furthermore, we should also never expect to see under efficient events in any of the "new" level 2 trigger regions, but the corresponding entries here are non-zero as well, unfortunately.

These discrepancies are due to the Track List Board (TRL) Level 2 handshaking problem described in section 7.4.2 which caused random firings and random non-firings

region	good triggers	over triggers	under triggers
unbiased old U	11038	0	0
unbiased new U	231	2	2
unbiased new P	286	6	1
unbiased new X	185	23	1

Table 7.10: unbiased level 2 run 1a simulation results

region	good triggers	over triggers	under triggers
unbiased old U	0	0	0
unbiased new U	282	79	1
unbiased new P	512	18	0
unbiased new X	178	68	1

Table 7.11: unbiased level 2 run 1b simulation results

of the level 2 trigger. A careful study of this problem was done using a an 83,051 event inclusive muon data set from run 1a, and a 228,181 inclusive muon data set was used from run 1b. After run 64165 the level 2 processor was replaced by an alpha processor. This coincidentally fixed the handshaking problem, and hence the problem only needs to be studied for the appropriate time period. Tables 7.8 and 7.9 show the results. Again, the large over efficiency values are mostly due to the prescales for "U" and "X". What is required is to quantify the importance of the problem. This was accomplished by doing an unbiased study. This is performed in tables 7.10 and 7.11.

During run 1a the "U" and "P" trigger regions were never prescaled (but the "X" was prescaled). A prescaled event will show up as an "over" level 2 event. Hence, in a study of problematic run 1a "over" events, only the "U" and "P" rows can be used. During run 1b, only the "P" region was never prescaled, and so this is the only class that can be studied. "Under" events can be legitimately studied in all cases, because they are never supposed to occur.

region	good triggers	over triggers	under triggers
U	3567	0	0
P	21808	0	0
P only	578	0	0
X	6784	0	0

Table 7.12: level 3 muon trigger simulation

It was determined that there was no reason to expect the handshaking problem to depend on the trigger region. Hence the TRL-L2PROC handshaking failure rate was determined to be 1.5% (6+2 / 286+6+231+2) for the duration of run 1a when this problem existed (which was only for about one third of run 1a), and 3.4% (18 / 512+18) for the duration of run 1b when this problem existed (which coincidentally was for about one third of run 1b). Averaged over all of run 1a and run 1b the problem corresponded to just over 1%, and this correction is made to the final efficiency values.

7.5.4 Level Three Muon Trigger Simulation

It would be easy if everything was as simple as level 3. Level 3 makes a software cut, and therefore level 3 can be simulated exactly. The numbers are shown in table 7.12. There are zero discrepancies, as expected.

7.6 Event Classifications

It is now possible to calculate the overall selection efficiencies, as a function of trigger region, since all aspects of the selection can be associated with individual tracks, and the behavior of the detector is now well-understood for an individual track.

7.6.1 Z Event Muon Distribution by Trigger Region

Each muon is associated with one of the four individual trigger regions. For simplicity we are calling these regions “U”, “P”, “X” and “I”. “U” represents the CMU-only region, “P” the CMU-CMP region, “X” its namesake, and “I” or “CMI” represents the central region not covered by a working muon detector system. Only events which pass the final Z cuts are studied. At least one leg must pass “gold” cuts, and the secondary leg must pass either “gold” or “silver” cuts. There are thirty possible geometrical configurations for a Z event. For example, the primary leg can be “P” and the secondary leg can be “X”, or the primary leg can be “U” and the secondary leg can be “I”. Additionally, each leg can be either “gold” or “silver”, and the secondary leg can be either “5th axial”, “4th axial” or “3rd axial”. If both legs are “gold” then one leg is arbitrarily assigned as the primary leg. Events such as these are double counted in table 7.13, because both legs are effectively unbiased. If only one of the muons passes “gold” cuts, then only the secondary leg is studied because it is the leg which is unbiased. If one of the muon regions was not classed as fully working during a particular run, then any leg that would have been given that classification is reclassed as “I”.

Interpretation of table 7.13 is simple. The second row is “P-U”. There were 175 Z events which had a gold “P” leg, and the other leg was pointed at the “U”. In 62 of these events both legs were gold, and in 113 events the primary leg was classified as gold, and the secondary leg was classified as silver. Rows where the detector regions are alike are slightly more complicated. The fifth row is “P-P”. There were 415 Z events which had a gold “P” leg, and the other leg was also pointed at the “P”. In 264 of these events both legs were gold. Hence there were a total of 679 secondary “P” legs which could be studied in an unbiased way. In the case of the CMX, it is possible for the secondary leg to be not only a standard “5th” axial, but also “4th” and “3rd” axial, and the same goes for the CMI category. The meaning of “5th” and “4th” and “3rd” axial will be explained in detail in a later chapter. The rarer “4th” and “3rd” axial legs are not used in any of the trigger efficiency calculations in this chapter.

primary region	secondary region	total events	total G-G	5th G-S	4th G-S	3rd G-S
U	U	60	33	27		
P	U	175	62	113		
X	U	43	26	17		
U	P	90	62	28		
P	P	415	264	151		
X	P	185	152	33		
U	X	39	26	9	3	1
P	X	523	152	339	31	1
X	X	88	53	25	9	1
U	I	264	0	162	50	52
P	I	1220	0	757	225	238
X	I	314	0	194	54	66
ALL	**ALL**	**3176**	**590**	**1864**	**372**	**359**

Table 7.13: Z events classed by secondary leg

There are a total of 3,176 Z events which pass the final cuts. 583 of them had at least one leg in the "U", 2,394 of them had at least one leg in the "P", 1,014 of them had at least one leg in the "X", and 1,798 of them had one leg entering the uncovered "I" region, which encompasses both areas of the central region not covered by a muon detector system and also muon detector systems which were deemed not to have been working properly for the run in question. For example, for a large part of run 1a the CMX system was classified as "I".

590 of the events were triggered successfully by both muons. For 2,454 of the events, both tracks were pointed at the 5th axial superlayer ("5-5" events). For 372 events, the primary triggered track was pointed at the 5th axial superlayer and the secondary non-triggered track was pointed at the 4th axial superlayer ("5-4" events). For 359 events, the primary triggered track was pointed at the 5th axial superlayer and the secondary non-triggered track was pointed at the 3rd axial superlayer ("5-3" events).

primary region	secondary region	total secondaries	stub and dx	L1 sim	L1 dat	L1 trig	L2 sim	L2 trig	L3 trig
U	U	97	85		80	80	69	69	68
P	U	177	155		136	136	125	62	62
X	U	41	36		28	28	27	24	24
U	P	90	87	73	73	73	65	65	62
P	P	680	661	596	595	595	532	532	520
X	P	179	177	163	163	163	154	152	147
U	X	33	30	28	28	28	27	24	24
P	X	497	490	375	375	375	331	150	147
X	X	131	130	109	109	109	106	106	104

total secondaries	number of “gold” or ”silver” muons whose partner is “gold”
stub and dx	effect of requiring the stub and dx cut
L1 sim	effect of requiring the level 1 trigger simulation (w/gated muon chambers)
L1 dat	effect of requiring that the corresponding muon trigger tower fires
L1 trig	effect of requiring that the FRED outputs trigger level 1
L2 sim	effect of requiring that the track fires the level 2 trigger simulation
L2 trig	effect of requiring that the track fires the level 2 trigger
L3	effect of requiring that the muon trigger level 3

Table 7.14: Z events classed by secondary leg, effect of the different cuts

7.6.2 Z Event Muon Classifications

Table 7.14 presents a matrix of event counts for Z events as selection criteria are applied. The application of the “L2 trig” requirement depletes significantly certain rows because of prescaling. With this table we can calculate the overall efficiencies for each of our cuts as a function of trigger region (called “U”, “P” and “X” for simplicity). However special care must be exercised when calculating the efficiency of “L2 trig” because of the prescale. This will be dealt with in detail below. Not shown is the effect of the superlayer-8 cut, which ensured that each track passed through all of the CTC axial superlayers. This cut was fully efficient for the CMU and CMP detectors, but in the case of the CMX it was possible for a track to miss superlayer-8 and still hit the detector. From the event sample it was determined that the efficiency of the superlayer-8 cut was $94.55^{+0.89}_{-1.02}\%$.

7.6.3 The Level Two Prescale Efficiency Calculation

The level 2 prescale is problematic. This is readily apparent by examining several rows of table 7.14. Consider the "CMP CMX" row. The "L2 sim" entry is 331 and the "L2 trig" entry is only 150. The "P" trigger was never prescaled, and it was almost always operational when the "X" trigger was working. This means that the "X" trigger was prescaled more than half of the time (if the "X" trigger was inoperative the leg would have been classed as "I"). Consider the "P U" row. The "L2 sim" entry is 125 and the "L2 trig" entry is 62. This means that the "U" trigger was prescaled about half the time.

Now look at the "X U" row. The "L2 sim" entry is 27 and the "L2 trig" entry is 24. The reason the values are so similar is that when these triggers were prescaled it was usually at the same time. More importantly, the trigger prescales are correlated. When the instantaneous luminosity was high the prescales for both the "X" and the "U" regions were typically on, and when the luminosity was low the prescales for both the "X" and the "U" regions were typically off.

As a final example, look at the "X X" row. The "L2 sim" value is 106 and the "L2 trig" value is 106. If the prescale was on, then we wouldn't expect to get any CMX-CMX Zs. If the prescale was off, then we would expect all events which passed L2sim to also pass L2trig, and that is what happened.

These examples imply that only events which have a golden leg in the "X" region should be considered when calculating the selection efficiency for the "L2 trig" column, if dimuon Z events are to be used for this calculation. This cuts down on the statistics considerably, and hence if the calculation was done this way the overall errors on the final selection values would be large. Luckily, there is another way to do this. The overall live integrated luminosity values which were obtained in the previous chapter can be used to derive the overall selection efficiencies for the "L2 trig" column (only a small modification needs to be made to take into account the TRL-L2PROC handshaking problem).

7.7 Calculation of "Silver" Selection Efficiencies

It is now possible to calculate selection efficiencies. The efficiency of an individual cut is given by N_{good}/N_{total}. One sigma upper and lower limits are determined via a summed binomial distribution program [6],[7],[8]. All cuts are studied one-at-a-time. Each selection efficiency is determined by first relaxing only the cut being studied, thereby accepting more events than the set of Z-candidate events in the final sample, and determining specifically that cut's efficiency.

However, it is not quite that simple. It is necessary to take into account the effects of correlated cuts. For example, if two cuts reject the same set of events, then relaxing one cut and not the other will not bring any more events into the sample being studied. It is necessary to relax both cuts simultaneously, if the cuts in question overlap.

For example, in removing punch-through events cuts are placed on both the hadronic and electomagnetic energy depositions in the calorimeter. These cuts overlap in their effectiveness. Hence, it is not sufficient to relax one of these cuts, study its effect, and then to do the same for the partner cut. It is necessary to relax both cuts simultaneously and study the impact of each cut, and to determine the impact of the combined set of cuts.

The purpose of many of the "silver" selection cuts is to remove background events. Figure 6.1 is a useful flowchart which shows the main decisions that are made during background removal. It also shows the studies which are required in order to perform the different efficiency calculations as well as the final background contamination estimates.

There are two types of efficiencies, global efficiencies (which affect how many events are selected) and single track efficiencies (which also affect how many events are ultimately selected, but in a more complex way because there are two tracks to consider).

7.7.1 Efficiency of the electromagnetic and hadronic energy deposition cuts

A 2 GeV electromagnetic energy deposition cut and a 6 GeV hadronic energy deposition cut are standard CDF muon identification cuts. These cuts are imposed on both muon tracks. The purpose of the cuts is to remove "punch-through" events (figure 6.1 is a useful guide which shows the steps required to achieve this). If no energy deposition cuts are applied to one of the muon tracks, it was found that 229 additional events would be accepted. These events are divided into three groups, those that fail the electromagnetic energy deposition cut but pass the hadronic energy deposition cut (120 events), those that pass the electromagnetic energy deposition cut but fail the hadronic energy deposition cut (66 events), and those that fail both cuts (43 events).

7.7.1.1 The first group; events which fail the electromagnetic energy deposition cut but pass the hadronic energy deposition cut

There is no reason to believe that a significant number of background events are present in the group of 120 events which fail to pass the electromagnetic energy cut but pass the hadronic energy cut. Figure 7.1 shows a direct comparison between the dimuon mass of the normalized Z-candidate events (shaded region) and the dimuon mass of the failing events (shown as points including error bars). There is a systematic mass shift in the dimuon mass for this group of events, which suggests removing them.

The events in this group do tend to have more jets in them than the jet distribution which was shown in figure 6.2. This is to be expected given the parameter which is being cut on. Preferentially cutting on high jet activity represents a potential problem, since there could be a correlation between the number of jets and the Pt of the Z (and a lot of effort is being made not to bias the Z Pt distribution).

Figure 7.2 shows a direct comparison between the Z Pt of the normalized final set of Z-candidate events (shaded region) and the Z events which fail the hadronic energy deposition cut (shown as points including error bars). The x-axis uses non-linear binning. The first bin, for example, includes events with a Z Pt between 0 and 2 GeV, while the 10th bin includes events with a Z Pt between 33 and 45 GeV, and the last bin includes events with a Z Pt between 180 and 270 GeV. The plot appears to show that this cut may indeed preferentially eliminate events which have a larger Z Pt. However, the plot also demonstrates that this correlation, if it exists, is small. There is no reason to believe that

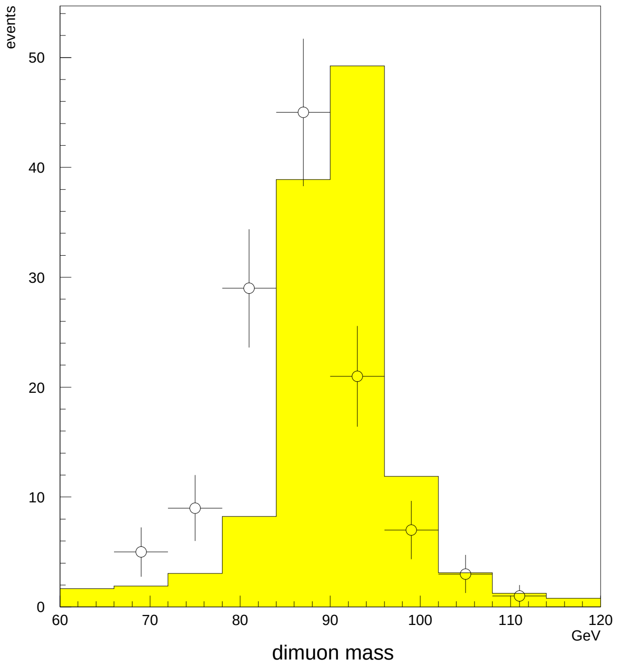

Figure 7.1: dimuon mass for CEM failing, CHA passing events, compared to final Z event distribution

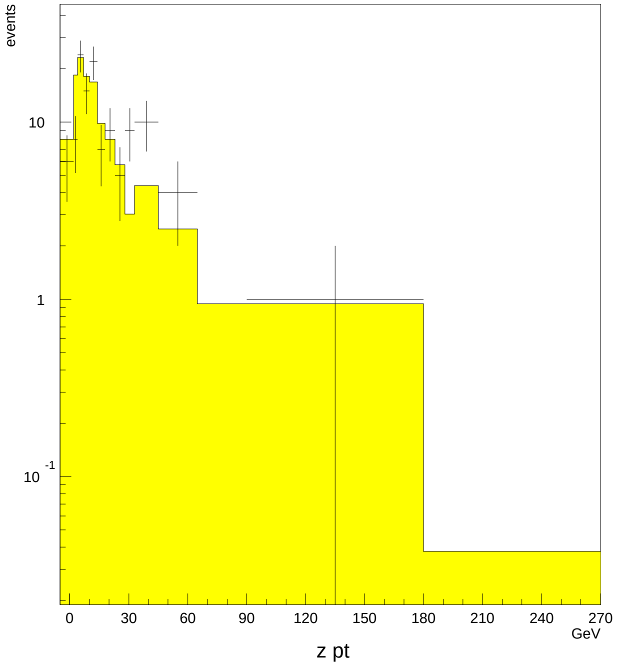

Figure 7.2: dimuon Pt for CEM failing, CHA passing events, compared to final Z event distribution

the Monte Carlo will not, when the identical set of cuts are implemented, reject events with a similar Z Pt distribution as found in the data.

7.7.1.2 The second group; events which pass the electromagnetic energy deposition cut but fail the hadronic energy deposition cut

There is no reason to believe that there is a significant number of background events present in the group of 66 events which fail to pass the electromagnetic energy cut but fail the hadronic energy cut. Figure 7.3 shows a direct comparison between the dimuon mass of the normalized Z-candidate events (shaded region) and the dimuon mass of the failing events (shown as points including error bars). The agreement is good except for the lowest bin.

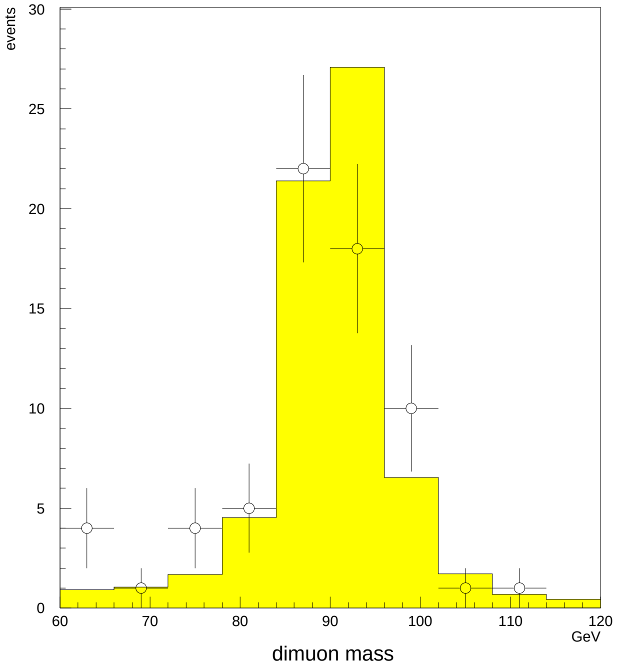

Figure 7.3: Dimuon mass for CEM passing, CHA failing events, compared to final Z event distribution

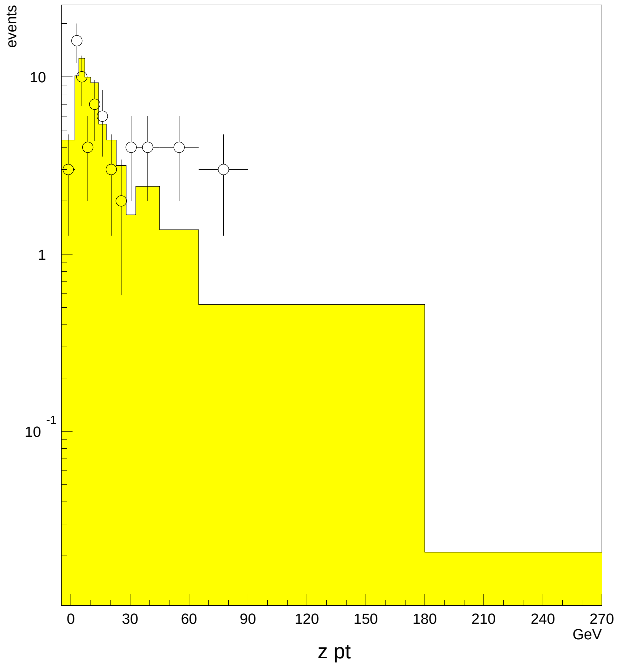

Figure 7.4: dimuon Pt for CEM passing, CHA failing events, compared to final Z event distribution

The events in this group do tend to have more jets in them than the jet distribution which was shown in figure 6.2. This is to be expected given the way the events are being selected. Preferentially cutting on jet activity represents a potential bias, since there could be a correlation between the number of jets and the Pt of the Z.

Figure 7.4 shows a direct comparison between the Z Pt of the normalized final set of Z-candidate events (shaded region) and the Z events which fail the hadronic energy deposition cut (shown as points including error bars). The plot appears to show that this cut may indeed preferentially eliminate events which have a larger Z Pt. However, the plot also demonstrates that this correlation, if it exists, is small. It is believed that the Monte Carlo will, when the identical set of cuts are implemented, reject events with a similar Z Pt distribution as found in the data.

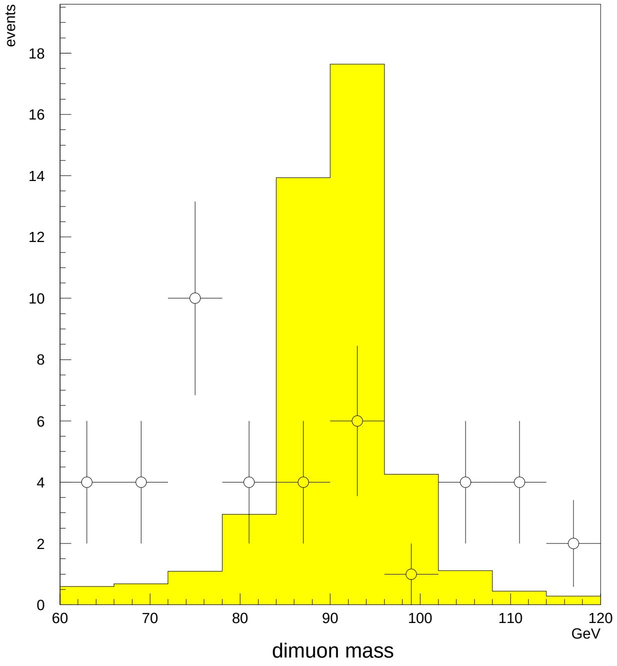

Figure 7.5: dimuon mass for CEM failing, CHA failing events, compared to final Z event distribution

7.7.1.3 The third group; events which fail both the electromagnetic energy deposition cut and the hadronic energy deposition cut

Figure 7.5 shows a direct comparison between the dimuon mass of the normalized Z-candidate events (shaded region) and the dimuon mass of the failing events (shown as points including error bars). This graph demonstrates that there is no reason to think that any of the 43 events are Z-events since there is no Z-mass peak of any kind.

7.7.1.4 Summary of the efficiency of the electromagentic and hadronic energy deposition cuts

As has been stated, there is no obvious set of background events present within either the first or the second group of events above. This implies that the number of background

Combined Electromagnetic and Hadronic Energy Deposition Cut Efficiency
$95.3^{+0.3}_{-0.4}\%$

Table 7.15: final set of efficiencies for the combined electromagnetic and hadronic energy deposition cuts

"punch-through" events which pass the final cuts and make it into the selected set of Z events is very small. In the next section, titled "efficiency of the opposite-sign charge cut", the expected number of "punch-through" events which make it into the final sample of Z events is calculated.

Here, only the efficiency of the combined electromagnetic and hadronic energy deposition cuts is determined. It is necessary to take into account the effect of double "gold" events (events where both high Pt muons would cause the event to be written to tape), and also to only consider the rejected events which are believed to be Z-events. There are 3,176 events in the final sample, 579 double "gold" events, and the first two groups comprise a total of 186 events. Consequently, the combined efficiency is determined to be $95.3^{+0.3}_{-0.4}\%$. This is shown in table 7.15.

7.7.2 Efficiency of the opposite-sign charge cut

The cut requiring that the muons in the final Z-sample be oppositely charged rejects three events which would otherwise pass all Z-cuts.

These events were studied in detail. In one of these events, the TOWE bank is missing. The TOWE bank contains the calorimeter energy deposition values which are used in this analysis. The CDF event display for this event (see figure 7.6) shows a large number of tracks pointed towards the bottom right of the detector, and also a number of hits over a wide angle in both the CMU and the CMP detectors. This wide angle of hits does not exhibit the characteristics of a muon. It is assumed that if the TOWE bank were present for this event, then the calorimeter energy deposition values would be sufficient to

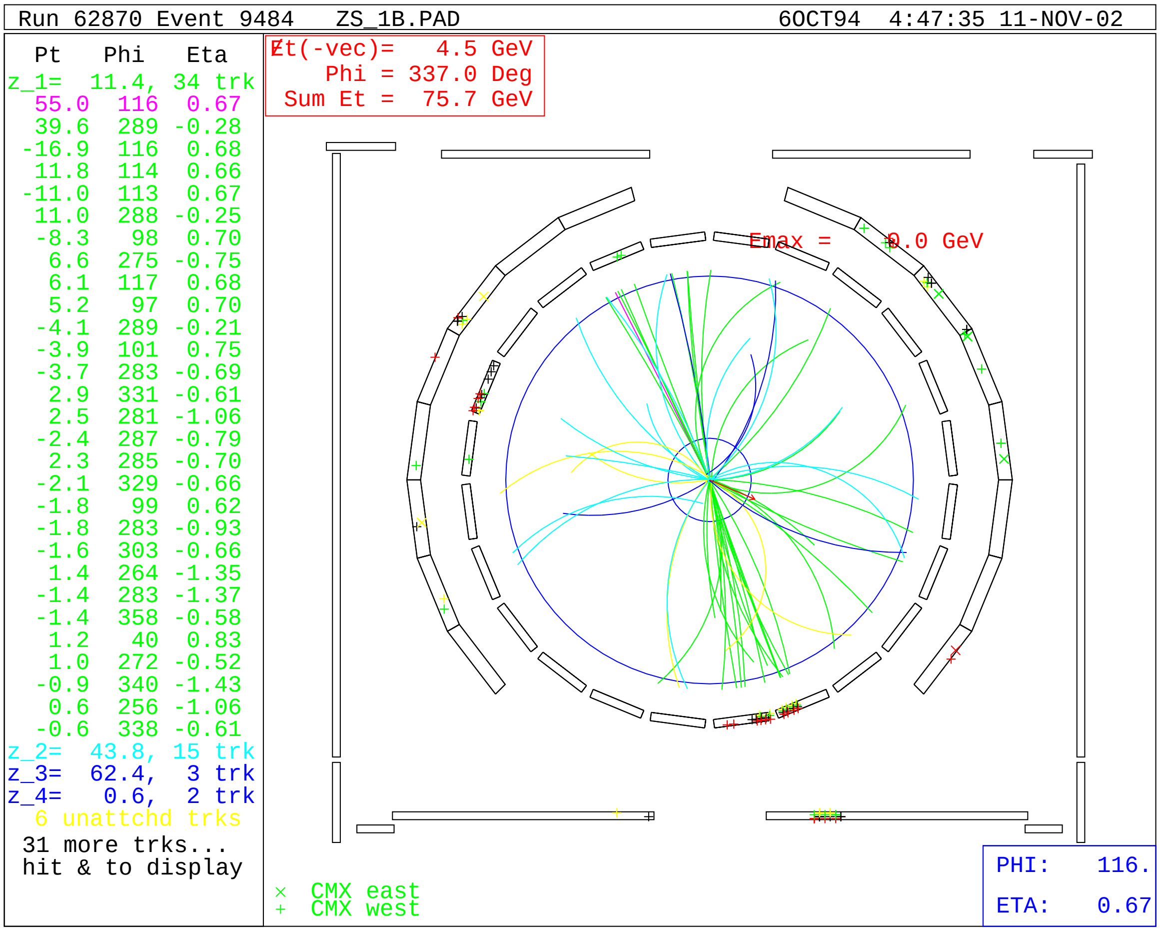

```
Run 62870 Event 9484    ZS_1B.PAD                    6OCT94   4:47:35 11-NOV-02

  Pt    Phi   Eta
z_1=  11.4, 34 trk
  55.0  116  0.67
  39.6  289 -0.28
 -16.9  116  0.68
  11.8  114  0.66
 -11.0  113  0.67
  11.0  288 -0.25
  -8.3   98  0.70
   6.6  275 -0.75
   6.1  117  0.68
   5.2   97  0.70
  -4.1  289 -0.21
  -3.9  101  0.75
  -3.7  283 -0.69
   2.9  331 -0.61
   2.5  281 -1.06
  -2.4  287 -0.79
   2.3  285 -0.70
  -2.1  329 -0.66
  -1.8   99  0.62
  -1.8  283 -0.93
  -1.6  303 -0.66
   1.4  264 -1.35
  -1.4  283 -1.37
  -1.4  358 -0.58
   1.2   40  0.83
   1.0  272 -0.52
  -0.9  340 -1.43
   0.6  256 -1.06
  -0.6  338 -0.61
z_2=  43.8, 15 trk
z_3=  62.4,  3 trk
z_4=   0.6,  2 trk
  6 unattchd trks
 31 more trks...
 hit & to display
```

Figure 7.6: Like-sign "Z event" with no TOWE bank

cause this event to be rejected in the final Z-selection. There are no events in the final Z sample which have a missing TOWE bank, and so the effect of this anomalous event is ignored.

In the first of the other two more interesting events (see figure 7.7) the questionable "muon" is pointed towards the lower left corner of the detector, just under a jet which actually deposits a lot of energy in the calorimeter. The "muon" is a CMIO, and doesn't actually strike any of the muon chambers. It seems quite likely that the "muon" has been misidentified, and is in fact a jet. The beam-constrained Z Pt for this event is 49 GeV.

In the second event (see figure 7.8) both muons are pointed at the CMX chambers.

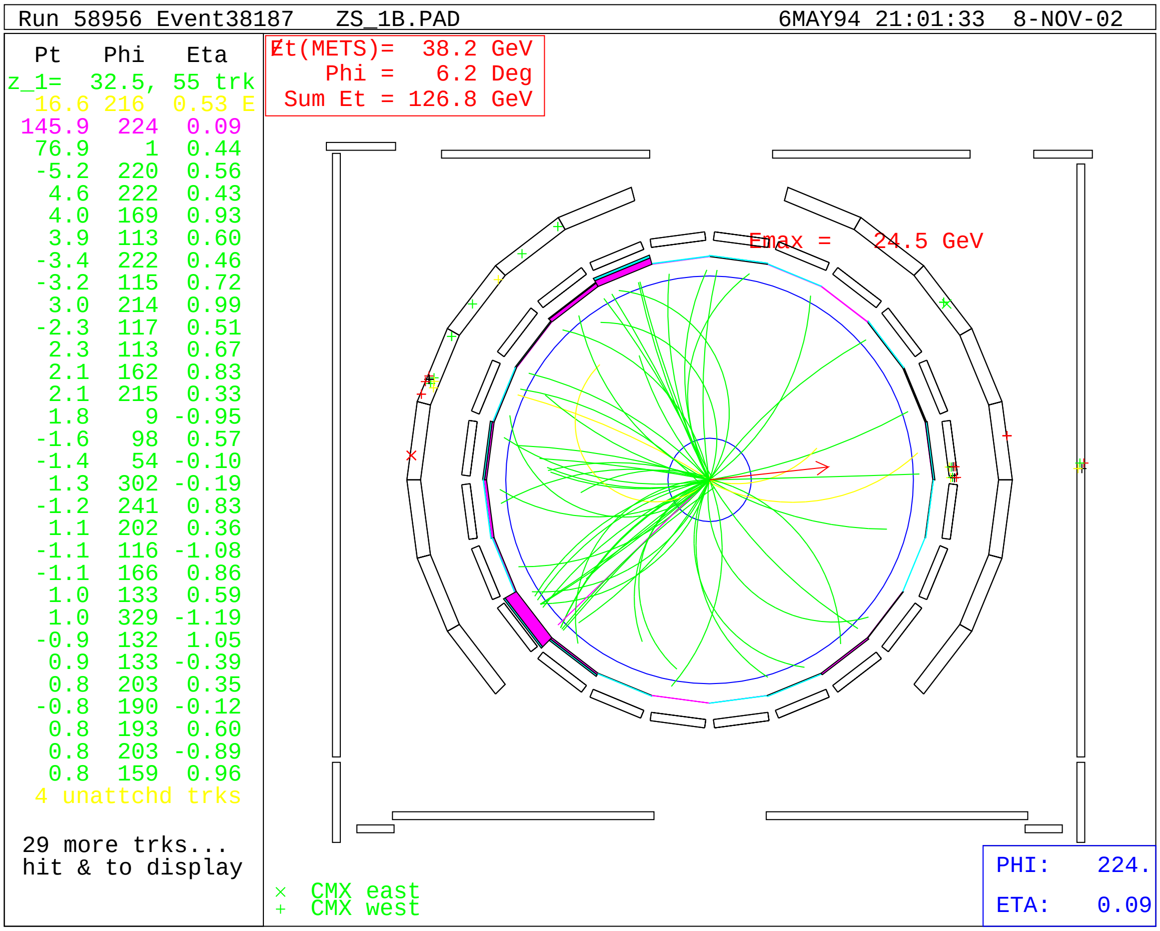

```
Run 58956 Event38187    ZS_1B.PAD                           6MAY94 21:01:33   8-NOV-02

  Pt    Phi    Eta
z_1=  32.5, 55 trk
  16.6 216   0.53 E
 145.9  224   0.09
  76.9    1   0.44
  -5.2  220   0.56
   4.6  222   0.43
   4.0  169   0.93
   3.9  113   0.60
  -3.4  222   0.46
  -3.2  115   0.72
   3.0  214   0.99
  -2.3  117   0.51
   2.3  113   0.67
   2.1  162   0.83
   2.1  215   0.33
   1.8    9  -0.95
  -1.6   98   0.57
  -1.4   54  -0.10
   1.3  302  -0.19
  -1.2  241   0.83
   1.1  202   0.36
  -1.1  116  -1.08
  -1.1  166   0.86
   1.0  133   0.59
   1.0  329  -1.19
  -0.9  132   1.05
   0.9  133  -0.39
   0.8  203   0.35
  -0.8  190  -0.12
   0.8  193   0.60
   0.8  203  -0.89
   0.8  159   0.96
  4 unattchd trks

 29 more trks...
 hit & to display

E̸t(METS)=   38.2 GeV
     Phi =    6.2 Deg
  Sum Et = 126.8 GeV

Emax =    24.5 GeV

×  CMX east
+  CMX west

PHI:    224.
ETA:    0.09
```

Figure 7.7: “Punch-through” same-sign event number one

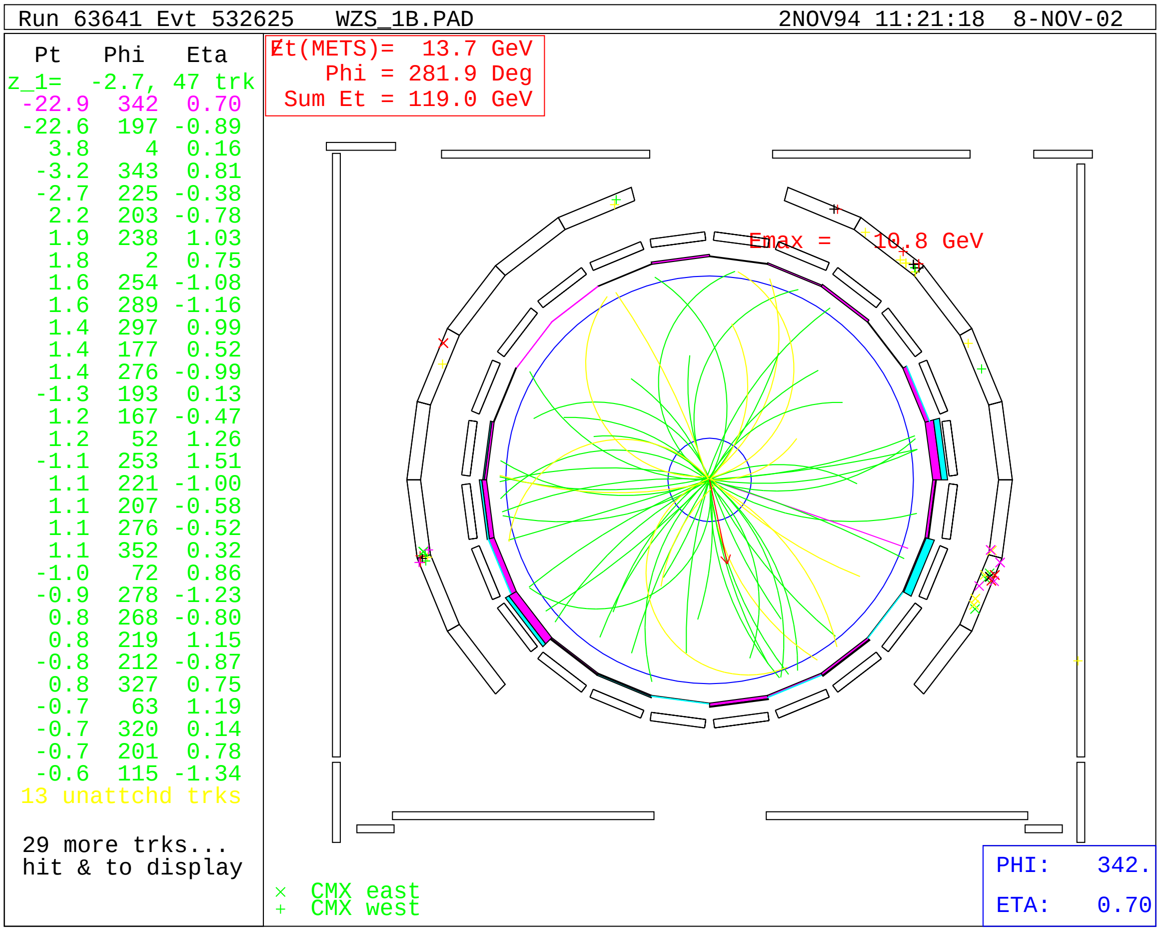

```
  Pt    Phi    Eta
z_1=  -2.7, 47 trk
 -22.9  342  0.70
 -22.6  197 -0.89
   3.8    4  0.16
  -3.2  343  0.81
  -2.7  225 -0.38
   2.2  203 -0.78
   1.9  238  1.03
   1.8    2  0.75
   1.6  254 -1.08
   1.6  289 -1.16
   1.4  297  0.99
   1.4  177  0.52
   1.4  276 -0.99
  -1.3  193  0.13
   1.2  167 -0.47
   1.2   52  1.26
  -1.1  253  1.51
   1.1  221 -1.00
   1.1  207 -0.58
   1.1  276 -0.52
   1.1  352  0.32
  -1.0   72  0.86
  -0.9  278 -1.23
   0.8  268 -0.80
   0.8  219  1.15
  -0.8  212 -0.87
   0.8  327  0.75
  -0.7   63  1.19
  -0.7  320  0.14
  -0.7  201  0.78
  -0.6  115 -1.34
 13 unattchd trks

 29 more trks...
 hit & to display
```

Figure 7.8: “Punch-through” same-sign event number two

Opposite Charge Cut Efficiency	Number of Background Events in Final Sample
$100.00^{+0.00}_{-0.07}\%$	$4.1^{+2.9}_{-2.9}$

Table 7.16: final set of efficiencies for the opposite-sign charge cut

The event has a Z mass of 61 GeV, which is not typical of a Z event. There are also a number of CMX chamber hits for the "muon" pointed at the lower right corner of the detector, which are somewhat suspicious. This event is consequently a good candidate for rejection as not a Z event. The beam-constrained Z Pt for this event is 15 GeV.

As further confirmation that the same-sign events are not Z events, figure 7.9 shows the invariant mass of all same-sign "dimuon" events which have a track that fails one of the calorimeter energy deposition cuts. As expected, there are quite a few more events (twenty-seven versus two) because punch-through events tend to be associated with larger calorimeter energy depositions.

It is possible to estimate the number of punch-through events in the final Z sample by looking at the relative frequency of opposite-sign versus same-sign events which have a track that fails both of the calorimeter energy deposition cuts. Figure 7.10 shows that there are 43 events in the opposite-sign category, and 21 events in the same-sign category. As can be seen (and as has been shown already in section 7.7.1, neither plot indicates the presence of Z events. There are approximately twice as many opposite-sign events as same-sign events, and hence there are expected to be twice as many punch-through events in the final Z sample as there are in the same-sign "dimuon" sample.

Consequently, since there are two legitimate same-sign "punch-through" events, it can therefore be estimated that there are roughly four "punch-through" events in the final Z sample. This is summarized in table 7.16. Although the Z Pt values for these events can be quite high, the fact that there are so few events of this type to begin with makes it possible to ignore their effect on the overall analysis.

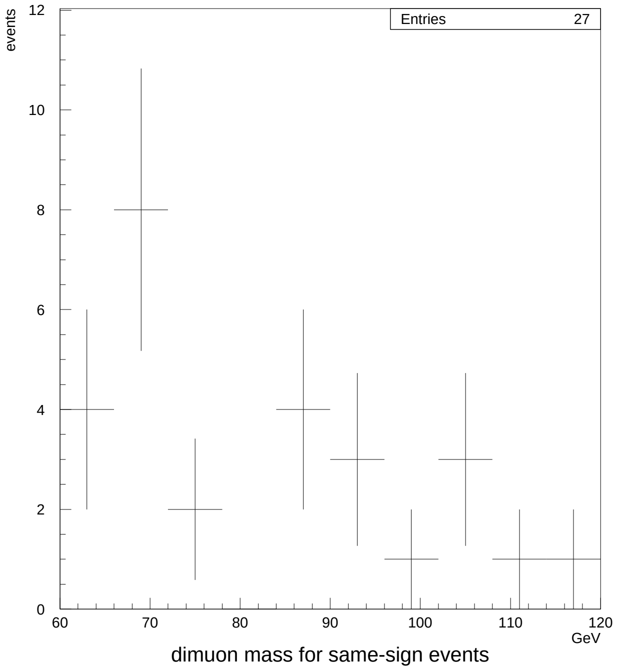

Figure 7.9: same-sign events which fail the calorimeter cuts

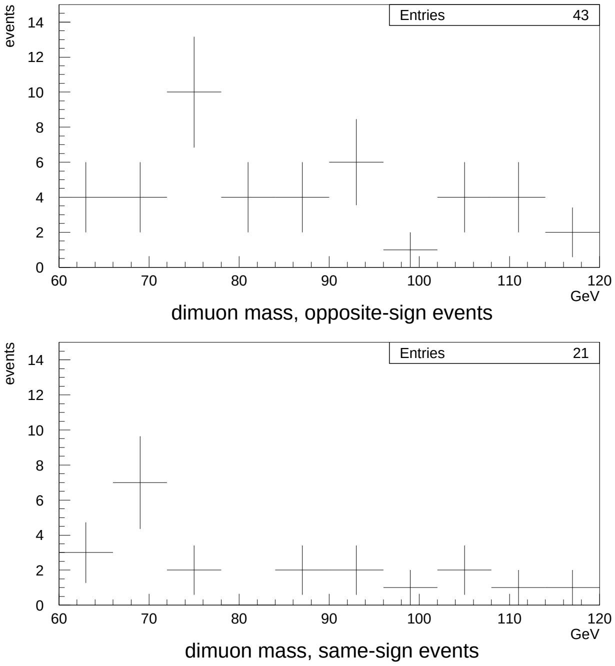

Figure 7.10: opposite-sign versus same-sign events which fail both calorimeter cuts

7.7.3 Efficiency of the cosmic ray filter

In the previous chapter the appropriate time difference cuts which select or reject a sample of predominantly cosmic rays were determined. Also determined were the single track hadron TDC timing cuts which should be used when the hadron TDC information is available for only one of the two tracks. As part of the selection a minimum non-beam-constrained angular separation of 160 degrees was used, which was believed to be approximately fully efficient for cosmic rays (see figure 6.6).

The maximum vertex separation cut and the hadron TDC timing cuts are taken to be uncoupled in this part of the analysis. This is due to the fact that the hadron TDC timing cuts are very efficient at removing cosmic rays. If the maximum vertex separation cut is applied after the hadron TDC timing cuts have already been applied, then the resulting event rejection does not appear to include any cosmic ray events. Additionally, there do not appear to be any Z events which fail both the hadron TDC timing cuts and also the maximum vertex separation cuts.

The hadron TDC cuts remove 54 events. These cuts are applied in four stages, depending on wether or not the hadron TDC information is available for both tracks, for only one track, for neither track, or if there is a third track in the event which indicates that one of the primary tracks is actually a cosmic ray. Figure 6.1 is a useful chart to accompany the description below.

1. If the hadron TDC timing information is available for both muon legs, then the event is rejected if the hadron TDC timing information for the lower hemisphere track is between 15 ns and 31 ns greater than that for the upper hemisphere track, and if the tracks have a three-dimensional non-beam-constrained angular separation greater than 160 degrees. This cut rejects 45 events and allows 2,688 events to pass.

2. If the hadron TDC timing information is available for only one of the two muon tracks and if the three-dimensional non-beam-constrained angular separation of the tracks is greater than 160 degrees, then the following rejection algorithm is applied. The

event is rejected if the hadron TDC value is available for only the upper ("incoming") hemisphere track and if the value is less than -10 ns. Alternately, the event is rejected if the hadron TDC timing information is available for only the lower ("outgoing") hemisphere track and if the value is either less than -5 ns or greater than 15 ns. These cuts reject 8 events and allow 479 events to pass.

3. When the hadron TDC timing information is unavailable for both muons then no cuts are applied. There are 9 events in this category.

4. All additional tracks with a 3-dimensional angular separation greater than 160 degrees from either of the tracks that form the Z are studied. If the hadron TDC information is available for the additional track as well for the Z track to which it is correlated, the time difference is examined. If it is between 15 ns and 31 ns, and if the hadron TDC timing is directionally consistent with the track being a cosmic ray, then that event is determined to be a "physics-plus-cosmic" event, and the event is rejected. This cut rejects one event.

Hadron TDC timing information is not required for an event to trigger and be written to tape. Hence, such information can be considered to be unbiased with respect to the trigger. Of the 3,176 events in the final Z sample. 2,688 events have hadron TDC timing information for both muons, 479 events have hadron TDC timing information available for only one of the two muons, and 9 events do not have hadron TDC timing information available for either muon.

Figure 7.11 shows the eta distribution for triggered muons which do not have hadron TDC timing information associated with them. The overall efficiency of the hadron TDC detector for such muons is $98.35^{+0.21}_{-0.23}$. Figure 7.12 shows the same eta distribution, but for non-triggered muons. The overall efficiency of the hadron TDC detector for such muons is $83.18^{+0.73}_{-0.78}$. As can be seen, there are no high eta muons ($\eta > 1.3$) which have hadron TDC timing information available, since these high eta muons travel outside of the hadron TDC scintillators. However, even if a maximum eta of 1.0 is imposed, the hadron TDC

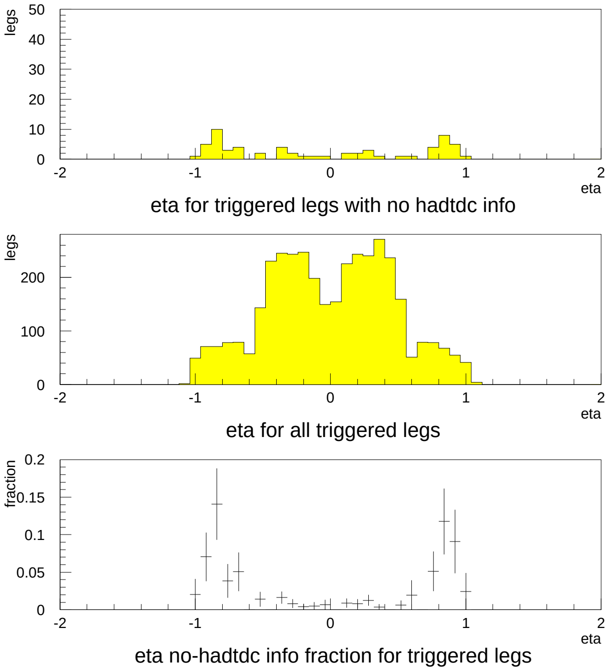

Figure 7.11: no hadron TDC timing info eta fraction for triggered muons

detector efficiency only increases marginally, to $85.81^{+0.84}_{-0.87}$. The reason why the hadron TDC detector has a lower efficiency for non-triggered muons versus the triggered muons is that a non-triggered muon is usually pointed at holes in the muon coverage, and these holes are correlated to holes in the hadron TDC coverage, hence the lower efficiency.

Figure 7.13 shows the cosmic ray fraction versus eta, for events which contain hadron TDC timing information for both legs. As can be seen, the cosmic ray fraction drops to zero well before eta reaches a magnitude of one, and also well inside the full eta distribution for the entire set of triggered Z legs. This isn't surprising because cosmic rays are expected to be moving in a downwards direction, as opposed to a sideways direction. Therefore, the fact that hadron TDC timing information is unavailable for high eta muons ($\eta > 1.3$) has little affect on cosmic ray removal (which depends on the hadron TDC timing information being present), because such muons are less likely to be cosmic rays.

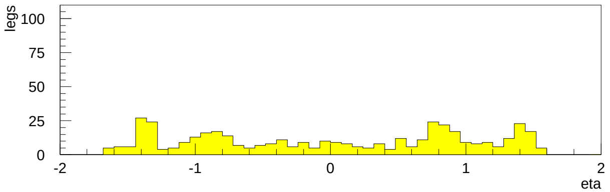

eta for non-triggered legs with no hadtdc info

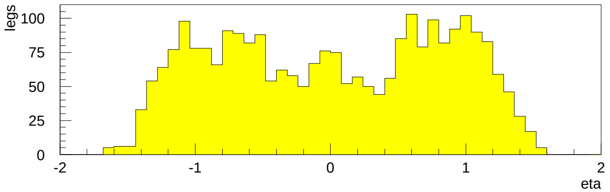

eta for all non-triggered legs

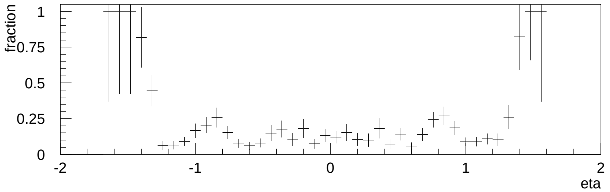

eta no-hadtdc info fraction for non-triggered legs

Figure 7.12: no hadron TDC timing info eta fraction for triggered muons

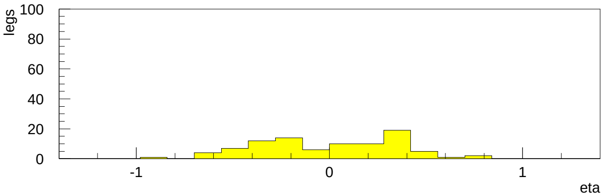

eta for legs which fail cosmic filter

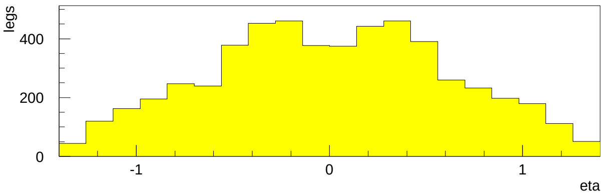

eta for Z legs with hadtdc info

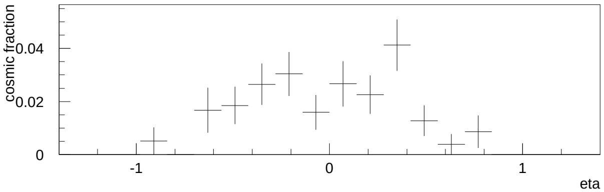

cosmic ray fraction versus eta

Figure 7.13: cosmic ray fraction versus eta

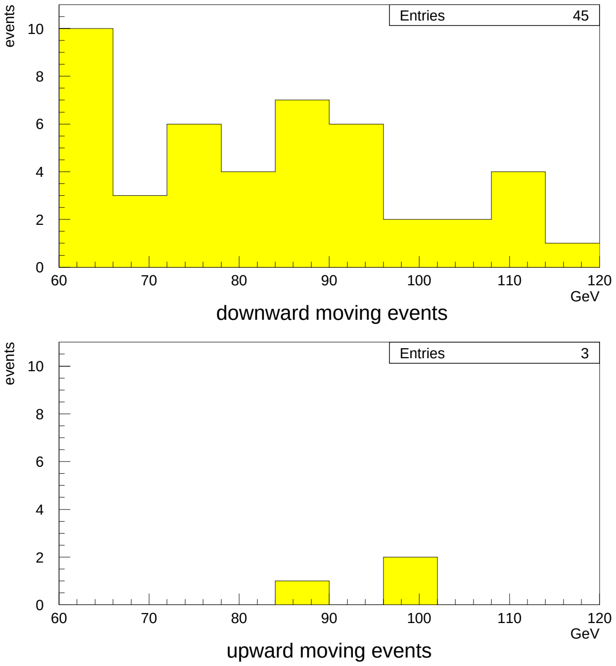

downward moving events

upward moving events

Figure 7.14: dimuon mass for downward and upward-moving events

7.7.3.1 First stage - the hadron TDC timing information is available for both muons

Figure 7.14 shows the dimuon mass for events consistent with being a “downward-moving” cosmic ray which is rejected by the cosmic ray filter, in comparison to their “upward-moving” counterparts. There are three Z events in the “upward-moving” plot. The expectation is that there will be an equivalent number of Z events in the downward-moving plot. In the “downward-moving” plot, there indeed appears to be a small signal at the Z-mass peak amongst what appears to be mostly background events.

As a further check figure 7.15 shows the number of 10 GeV jets seen in the two groups of events. Roughly one-third of Z events are expected to have one or more 10 GeV jets, and none of the cosmic events are expected to have a 10 GeV jet associated with them. For the “upward-moving” events, which are believed to be mostly Z events, one of the three events does indeed have a 10 GeV jet. For the “downward-moving” events, which

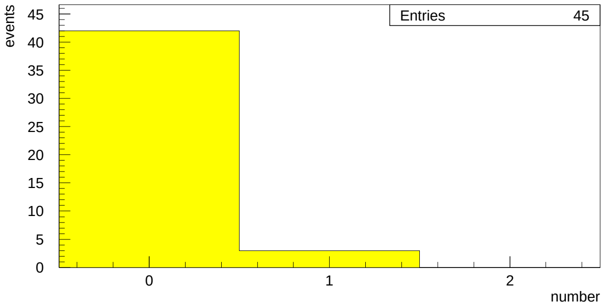

10 GeV jets for downward moving events

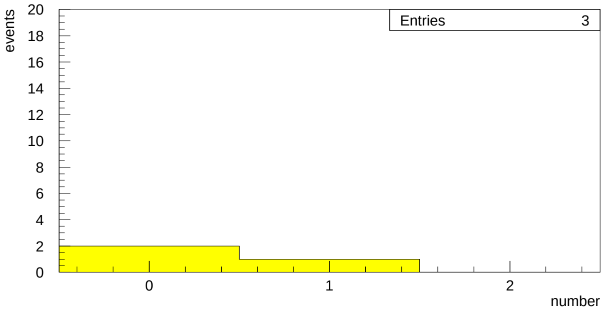

10 GeV jets for upward-moving events

Figure 7.15: 10 GeV jets for downward and upward-moving events

are believed to be mostly cosmic events with a small number ($3.0^{+1.7}_{-1.7}$) of Z events, only three out of 45 events contain a 10 GeV jet, implying that the total number of Z events in the "downward-moving" sample is $9.0^{+5.2}_{-5.2}$. If an average of the two estimates is taken, the number of predicted Z events rejected by the cosmic ray filter is $6.0^{+5.4}_{-5.4}$ (13% of the events identified as cosmic rays in the stage 1 cosmic ray filter are in fact Z events), which indicates that the number of cosmic ray events successfully rejected by stage 1 of the cosmic ray filter is $39.0^{+5.4}_{-5.4}$. Since 2,688 of 2,694 Z events pass stage 1 of the cosmic ray filter, the overall Z selection stage 1 cosmic ray filter efficiency is $99.78^{+0.10}_{-0.15}$.

In figure 7.25 there is no indication of the presence of cosmic rays in a sample of events which pass the cosmic ray filter but fail the maximum vertex separation cut (it is known that many cosmics fail the maximum vertex separation cut but they appear to have already been successfully rejected by the hadron TDC cuts in the cosmic ray filter). In fact, if an attempt is made to determine the number of cosmic rays in the graph for figure 7.25, the value is $-2^{+3.8}_{-3.8}$, consistent with zero. However, the statistics in figure 7.25 are very low. Stating that there are zero cosmics in a sample of 25 events is one thing. Extrapolating “zero in 25 events” to “zero in 3,176 events” (the full set of Z events) is not warranted. A great deal of effort was made in the previous chapter to make the selection of cosmic rays when the hadron TDC timing information was present for both legs fully efficient. The hadron TDC cuts (when the timing information is present for both muons) reject a total of 46 events (45 events in the first stage, and one event in the fourth stage, which will be described in detail below). Therefore, roughly 40 out of 46 of the events identified by the stage 1 and stage 4 cosmic ray filters are believed to be cosmics, the balance being Z events.

A simple trick is used to determine how many events fail to be rejected by the stage 1 and stage 4 cosmic ray filters. Figure 6.4 is used. This graph shows that there is a large tail for the hadron TDC time difference value - while cosmic ray events are believed to have a hadron TDC time difference between 15ns and 31ns, and Z events are expected to have a hadron TDC time difference less than this, the hadron TDC timing uncertainty can cause events to mix from one group to another, and this is the main reason for the occasional misidentification of cosmic ray events. Figure 7.16 shows the hadron TDC time difference for the identified sample of cosmic ray events (events which fail stage 1 of the cosmic ray filter) and the corresponding hadron TDC time difference for the passing Z events. Note that there are believed to be approximately 6 events within the graph for the cosmic ray events which are believed to actually be Z events. Therfore, the cosmic ray graph is distorted due to contamination by Z events. The Z event hadron TDC time difference graph indicates a way to subtract the effect of the Z event contamination within the cosmic ray sample. Taking the distortion by Z events into account, the cosmic ray event graph indicates that a cosmic ray has a hadron TDC time difference of approximately 21ns. Therefore, if the incoming cosmic ray track has a hadron TDC time which is mismeasured (late) by not less than 6 ns then the event will be identified as a Z, since the resulting hadron TDC time difference would then be less than 15 ns. Alternately, if the outgoing cosmic ray track has a hadron TDC time which is mismeasured (late) by not less than 10 ns then the event will also be identified as a Z, since in this case the hadron TDC time difference would be greater than 31 ns. The number of Z events in the tail of figure 6.4 can be used to determine the likelihood that a cosmic ray event will be misidentified as a Z event. 14.5% of the Z events have a hadron TDC time difference greater than 6 ns, and 6.3% of the Z events have a hadron TDC time difference greater than 10 ns. Weighting these fractions appropriately, this implies that approximately 10.4% of the time a cosmic ray will have a hadron TDC time difference sufficiently mismeasured that the event will not be identified as a cosmic ray by stage 1 of the cosmic ray filter, since the hadron TDC time difference for the tracks will not be within the allowed cosmic ray window. When a cosmic ray event is misidentified as a Z event due to hadron TDC timing mismeasurements, it is expected that approximately two-thirds of the time the hadron TDC time difference will be less than 15 ns (the start of the timing window for cosmic rays) and approximately one-third of the time the hadron TDC time difference will be greater than 31 ns (the end of the timing window for cosmic rays). There are a total of 8 events in the final Z sample with a hadron TDC time difference greater than 31 ns, and the dimuon mass plot of these events indicates the likely presence of one cosmic ray event (see figure 7.17). The likely cosmic ray event has a beam-constrained dimuon mass of 64 GeV, zero 10 GeV jets, and a track angular separation of over 170 degrees. From this it can be inferred that the total contamination of cosmic ray events in the final Z sample (for cosmic rays which fail to be rejected by stage one of the cosmic ray filter because they have tracks with mismeasured hadron TDC times) is approximately three events.

The hadron TDC timing mismeasurements are sufficient enough to cast an element of doubt on any event's classification as a Z event (for 6 events the hadron TDC timing mismeasurements, coupled with the angular track separations and apparent directionality of the muon tracks, are believed to cause Z events to be mistakenly classified as cosmic rays). If the timing mismeasurements in the Z events occur at the same rate in cosmic ray events, then it is belived that approximately 10.4% of the cosmic ray events will be reclassified as

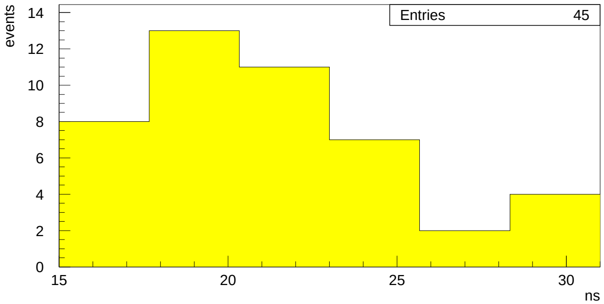

hadtdc timing difference for cosmic ray events

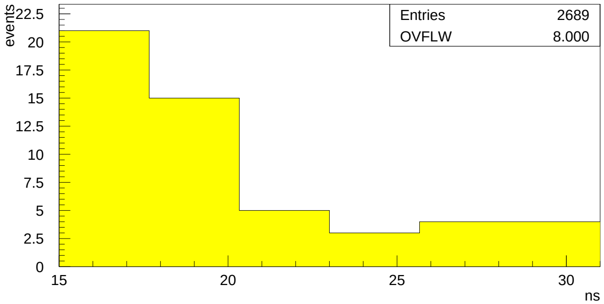

hadtdc timing difference for Z events

Figure 7.16: hadron TDC time difference for both cosmic rays and Z events

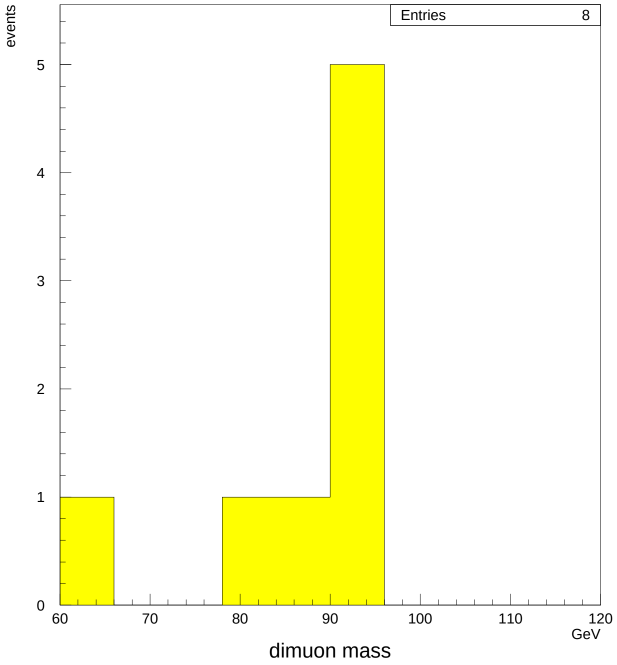

Figure 7.17: dimuon mass for events with a very large hadron TDC timing difference

Z events. Therefore, it is possible to estimate the number of cosmic ray events which fail to be rejected by the stage 1 cosmic ray filter, due to hadron TDC timing mismeasurements. This contamination in the final Z sample is approximately $5.34^{+2.31}_{-2.31}$ events. This figure is consistent with the number of cosmic ray events (three events) which are estimated to exist in the final Z sample after studying figure 7.17.

7.7.3.2 Second stage - the hadron TDC timing information is available for only one muon

The stage 1 cosmic ray filter is extremely efficient at rejecting cosmic rays. In stage 1 and stage 4 the distribution prior to cosmic ray removal is believed to be 2,694 Z events and 40 cosmic ray events. In stage 2, there are 487 events prior to cosmic ray removal. If the event numbers are scaled appropriately, the number of predicted cosmic ray events in this group of events amounts to $7.1^{+1.0}_{-1.0}$.

The stage 2 cosmic ray filter is not as efficient at rejecting cosmic ray events, because the hadron TDC information is only available for one of the legs. The events used in the stage 1 analysis are used to determine the relevant efficiencies for the stage 2 filter.

The stage 2 filter works differently depending on whether or not the hadron TDC timing information is present for an upper hemisphere or a lower hemisphere track.

If the track with hadron TDC timing information available is an upper hemisphere track (and if the opposing track has a non-beam-constrained angular separation greater than 160 degrees), then the event is rejected if the hadron TDC time is less than -10 ns. Figure 6.8 shows that this cut would reject forty out of forty-eight events classed as probable cosmic rays, and hence the efficiency of this cut is $83^{+6}_{-7}\%$. This part of the stage 2 cosmic ray filter rejects a total of 4 events.

If the track with hadron TDC timing information available is a lower hemisphere track (and if the opposing track has a non-beam-constrained angular separation greater than 160 degrees), then the event is rejected if the hadron TDC time is either less than -5 ns or greater than 15 ns. Figure 6.9 shows that this cut would reject twenty-five out of forty-eight events classed as probable cosmic rays, and hence the efficiency of this cut is $52^{+8}_{-8}\%$. This part of the stage 2 cosmic ray filter rejects a total of 4 events.

If the above cosmic ray filter efficiencies are applied to the expected number of cosmics (7 events), and assuming that there are equal numbers of "upper-hemisphere" and "lower-hemisphere" stage 2 events, then the stage 2 cosmic ray filter will reject 2.9 out of 3.5 upper-hemisphere cosmic ray events, and 1.8 out of 3.5 lower-hemisphere cosmic ray events, for a total of 4.7 out of 7.1 cosmic ray events.

Figure 7.18 shows the dimuon mass distribution for the eight events which are rejected by the stage 2 cosmic ray filter. None of the events has a 10 GeV jet associated with them. There is no reason to dispute the notion that the expected number of cosmic ray events in this sample is 4.7, and consequently the expected number of Z events in this sample is 3.4. Consequently, the overall Z selection efficiency of the stage 2 cosmic ray filter is $99.4^{+0.3}_{-0.6}\%$. Furthermore, if 4.7 out of 7.1 cosmic ray events are believed to be rejected by the cosmic ray filter, and taking into account that 13% of events identified as cosmic rays in the stage 1 cosmic ray filter are in fact Z events, then the expected contamination in the final set of Z events due to the stage 2 cosmic ray filter is 2.9 cosmic rays.

7.7.3.3 Third stage - the hadron TDC timing information is not available for either muon

There are only 9 events which have no hadron TDC timing information available for either muon. If a simple scaling is applied as before, the estimate is that there will be a total of $0.13^{+0.02}_{-0.02}$ cosmic ray events in this sample. No cuts are applied to events in this group. The Z selection efficiency of the cosmic ray filter for these events is 100%.

7.7.3.4 Fourth stage - other tracks in the event

In this stage of the cosmic ray filter, all tracks in all events are scanned when either of the potential Z legs has hadron TDC timing information available. If an additional opposing track is found which has an appropriate angular separation and which also has hadron TDC timing information consistent with the pair actually being a cosmic ray, then

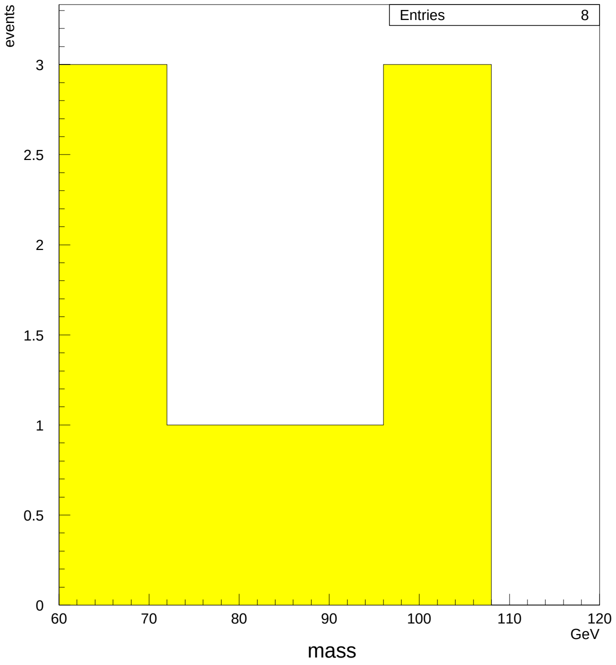

Figure 7.18: dimuon mass for identified stage 2 cosmic ray events

the event is classed as a "physics-plus-cosmic" event, and the event is rejected. One event fails this cut.

Figure 7.19 is a CDF event display of the misidentified Z event which is most likely to be a W-event plus a simultaneous cosmic ray event. The cosmic ray angles in from the top-right towards the left, and the W-muon is directed downward. The W-muon leg and the leg exiting the detector to the left form a dimuon mass of 88 GeV with a large dimuon Pt of 145 GeV (this would cause it to be ranked as the 6th largest Z Pt except for the fact that this event is rejected by the cosmic ray filter). The proposed incoming cosmic ray muon (from the top-right) has a hadron TDC timing value of -7 ns. The outgoing cosmic ray muon has a hadron TDC timing of 11 ns. The overall time difference is 18 ns, which makes the track pair almost certain to be a cosmic ray.

It is reasonable to assume that the efficiency of the stage 4 cosmic ray filter is 100%, since the rejected event is not believed to be a Z event. An estimate of the number of events which fail to be rejected by this cut is presented below.

In the 3,176 identified Z events, there are 6,352 muon legs. 5,556 of these muons have a low enough eta where they could conceivably contain a cosmic ray, and they also have hadron TDC timing information. Therefore, as a rough estimate, $87.5^{+0.4}_{-0.5}\%$ of potential cosmic ray tracks have hadron TDC timing information available. The stage 4 cosmic ray filter only rejects cosmic rays when the hadron TDC timing information is available for both tracks, and therefore, if the above percentage is squared, it will only apply for approximately $76.6^{+0.5}_{-0.6}\%$ of cosmic rays. This means that the expected number of cosmic rays which the stage 4 cosmic ray filter fails to reject is $0.31^{+0.1}_{-0.1}$ events.

7.7.3.5 Cosmic Ray Filter Summary - determining the number of cosmic rays in the final Z sample

Figure 7.20 shows the distribution of the dimuon Pt for rejected cosmic rays (with error bars), compared to the dimuon Pt for Z events (scaled to the number of rejected cosmic ray events). As can be seen, the two plots are similar. Consequently, there is no reason to

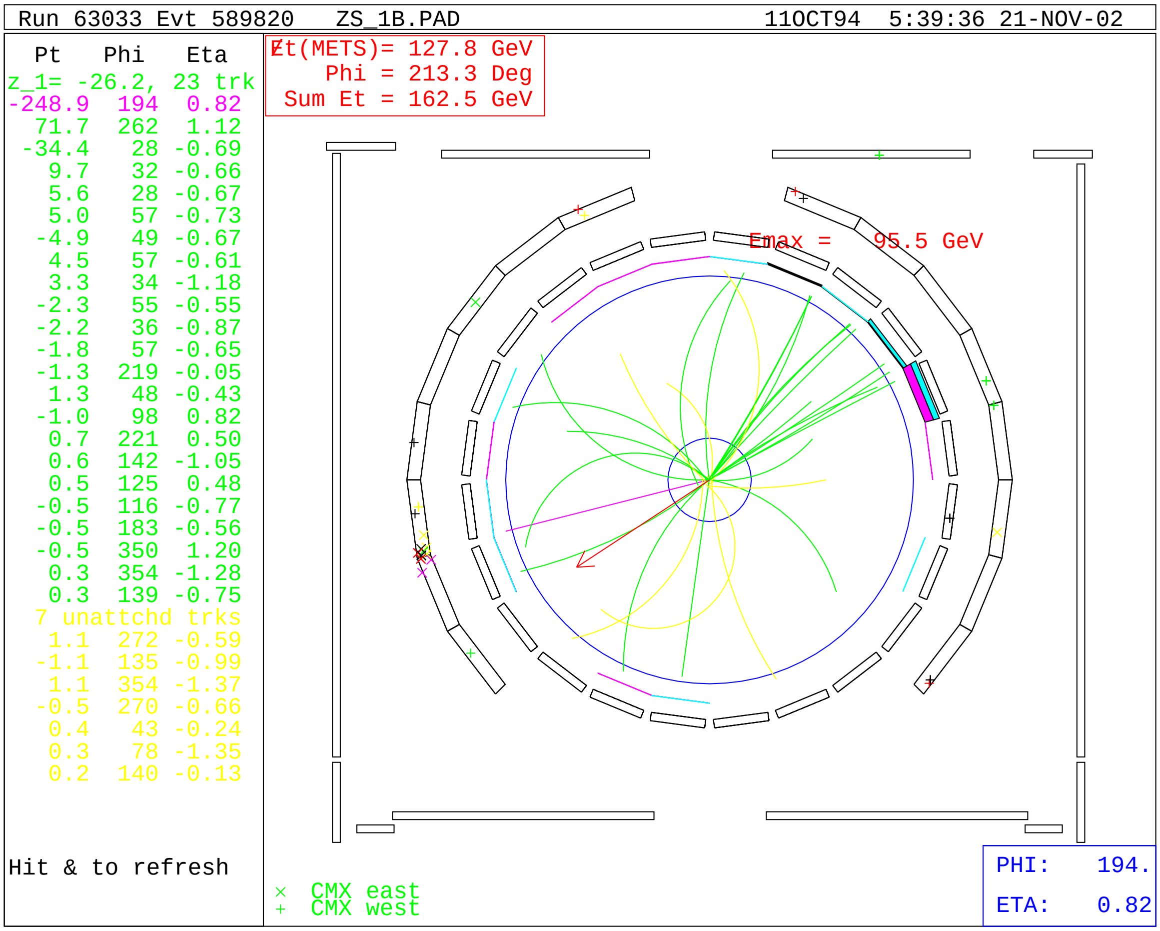

```
Run 63033 Evt 589820    ZS_1B.PAD                     11OCT94   5:39:36 21-NOV-02
```

```
  Pt    Phi   Eta
z_1= -26.2, 23 trk
-248.9  194  0.82
  71.7  262  1.12
 -34.4   28 -0.69
   9.7   32 -0.66
   5.6   28 -0.67
   5.0   57 -0.73
  -4.9   49 -0.67
   4.5   57 -0.61
   3.3   34 -1.18
  -2.3   55 -0.55
  -2.2   36 -0.87
  -1.8   57 -0.65
  -1.3  219 -0.05
   1.3   48 -0.43
  -1.0   98  0.82
   0.7  221  0.50
   0.6  142 -1.05
   0.5  125  0.48
  -0.5  116 -0.77
  -0.5  183 -0.56
  -0.5  350  1.20
   0.3  354 -1.28
   0.3  139 -0.75
  7 unattchd trks
   1.1  272 -0.59
  -1.1  135 -0.99
   1.1  354 -1.37
  -0.5  270 -0.66
   0.4   43 -0.24
   0.3   78 -1.35
   0.2  140 -0.13

Hit & to refresh
```

```
Ɇt(METS)= 127.8 GeV
     Phi = 213.3 Deg
  Sum Et = 162.5 GeV
```

Figure 7.19: The possible W-plus-cosmic event which was misidentified as a Z event

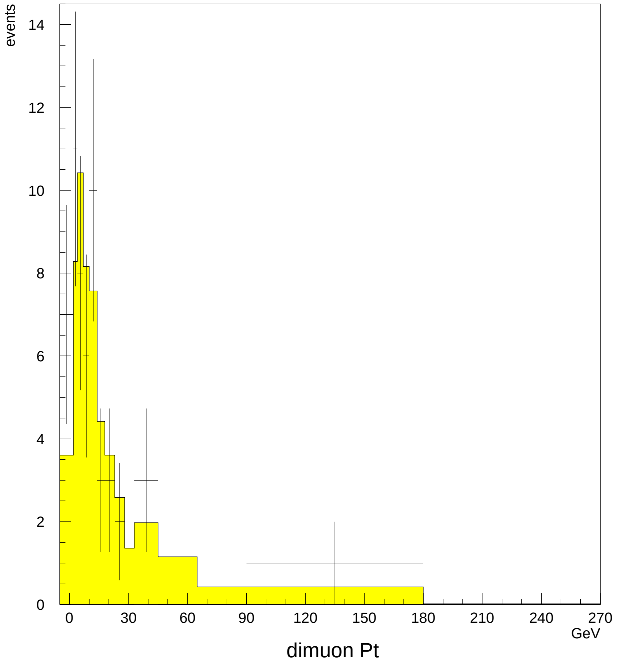

Figure 7.20: dimuon Z Pt for rejected cosmic ray events, compared to the final Z distribution

think that the handful of cosmic ray events which pass the cosmic ray filter and make their way into the final Z sample change the shape of the Z Pt spectrum in any significant way.

The results of the analyses of each of the stages of the cosmic ray filter shown in table 7.17. 3,176 events out of 3,185.4 Z events are accepted by the cosmic ray filter, representing an overall efficiency of $99.7^{+0.1}_{-0.1}\%$.

The final cosmic ray filter efficiency and Z event contamination values are summarized in table 7.18.

7.7.4 Efficiency of the beam-constrained vertex separation cut

This is a global cut since this cut directly affects the entire event (most cuts are single-track cuts and affect only the track in question). The purpose of this cut is to reject

Cosmic Ray Filter Stage	Passing Events	Predicted Cosmic Contamination	Rejected Z events	Rejected Cosmic Rays
1: both tracks have hadtdc info	2,688	5.34	6.0	39.0
2: one track has hadtdc info	479	2.90	3.4	4.7
3: neither track has hadtdc info	9	0.13	0.0	0.0
4: search for coupled cosmics	2,779	0.31	0.0	1.0
Summary	3,176	$8.6^{+2.9}_{-2.9}$	9.4	44.7

Table 7.17: results from cosmic ray filter

Cosmic Ray Filter Efficiency	Number of Cosmic Ray Events in Final Sample
$99.7^{+0.1}_{-0.1}\%$	$8.6^{+2.9}_{-2.9}$

Table 7.18: final set of efficiencies for the cosmic ray filter

the last of the three main sources of background, multiple vertex events. Figure 6.1 is a useful chart to accompany the description below.

The vertex separation cut will cause the rejection of events whose Z-candidate tracks originate at different vertices which are more than 5 cm apart. This can occur if there are multiple vertices within the event (for example, two muon W-decays), or if one of the tracks in the event was highly mismeasured and the tracking code misidentified the track's originating vertex (resulting in the rejection of a Z-event).

This cut will additionally reject cosmic rays. However, the cosmic ray filter is very efficient (see above) and it is not necessary to consider the effect of the overlapping cuts (since there are not believed to be any Z events which fail both the cosmic ray filter and also the vertex separation cut).

Figure 7.21 shows the distance between the beam-constrained vertices. Not shown are the 3,116 events for which the distance is zero. The cut is placed at 5 cm and a total of 25 events fail this cut.

Figure 7.22 shows the invariant mass distribution of the events which fail the vertex

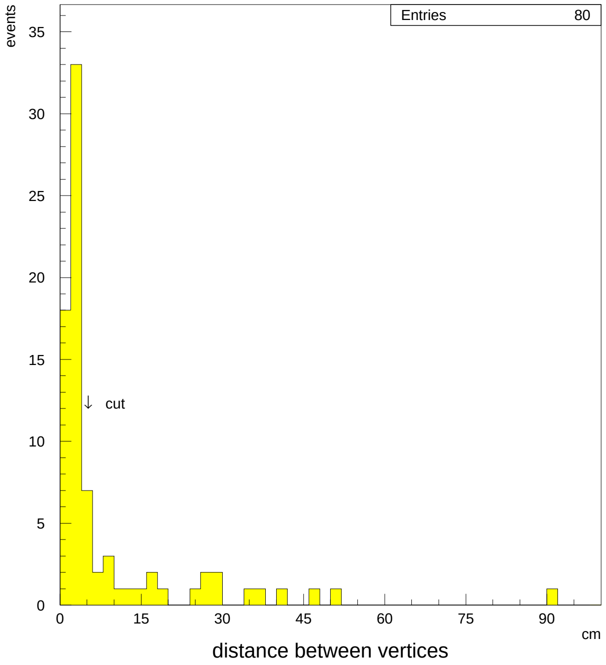

Figure 7.21: distance between beam-constrained vertices

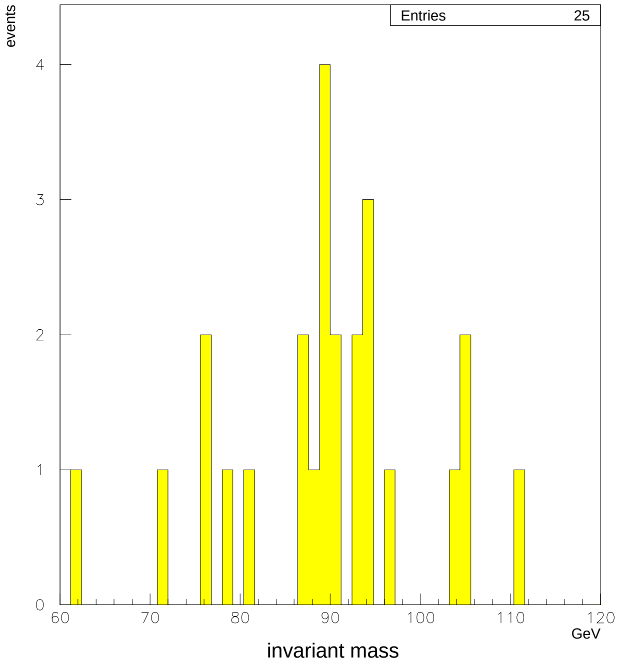

Figure 7.22: invariant mass for events which fail the vertex separation cut

distance cut. This plot appears to show that the events which fail the cut are made up of legitimate Z events and also non-Z events, since the invariant mass distribution has a characteristic Z-mass peak, but also a well-populated tail. However, the fact that so many of the bins have zero events in them can be deceiving. To do a direct comparison it is necessary to replot both this invariant mass distribution as well as the Z-event invariant mass distribution, using comparable large binning. This is shown in figure 7.23. The shaded area represents a normalized plot of the Z-candidate mass distribution, and the crosses represent the events which failed the vertex separation cut. The chi-squared value obtained by comparing these two plots is 13, and there are only 6 degrees of freedom. This confirms the earlier hypothesis that there appears to be some fraction of non-Z events in the sample of events which fails the vertex separation cuts.

Figure 7.24 shows the distribution of jets for the same group of events. This dis-

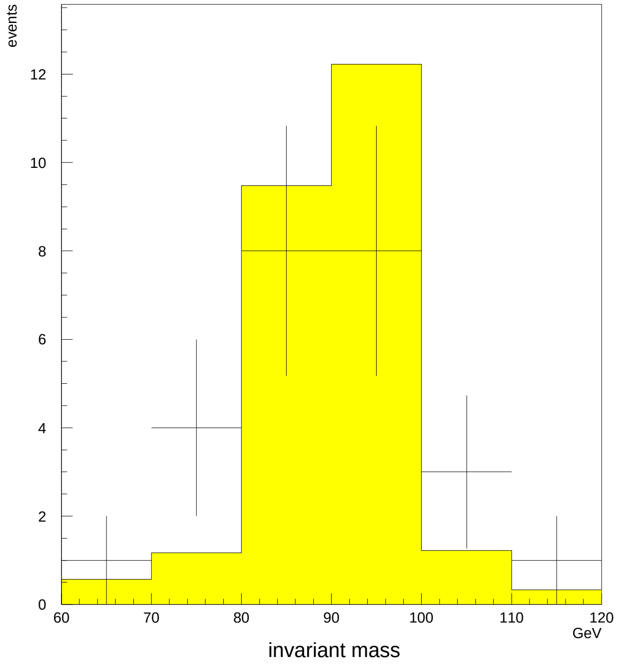

Figure 7.23: invariant mass for events which fail the vertex separation cut compared to the Z-candidate invariant mass plot

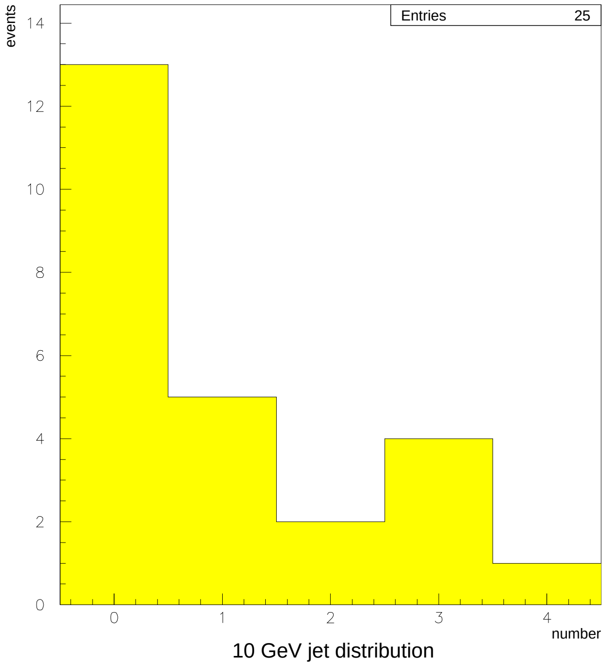

Figure 7.24: 10 GeV jet distribution for events which fail the vertex separation cut

tribution does not exhibit the characteristic traits of a random sample of Z-events. Here, there are too many events with a large number of jets.

Figure 7.25 shows a direct comparison between the normalized Z-candidate events (shaded region) and the events which fail the vertex separation cut (crosses). The differences within the plot imply that there are approximately 4 background events (most of the events with large numbers of jets in them) within the group of events which fail the vertex separation cut. Hence, the 5 cm vertex separation cut appears to remove twenty-two Z-candidate events and four background events. Since 3,176 out of 3,198 events pass the cut, the efficiency of this cut is $99.31^{+0.12}_{-0.16}\%$ efficient.

It is also possible to estimate the number of multiple-vertex background events which this cut fails to reject (when the vertex separation is less than 5 cm), since the number of background events with a vertex separation greater than 5 cm is now known. To accomplish

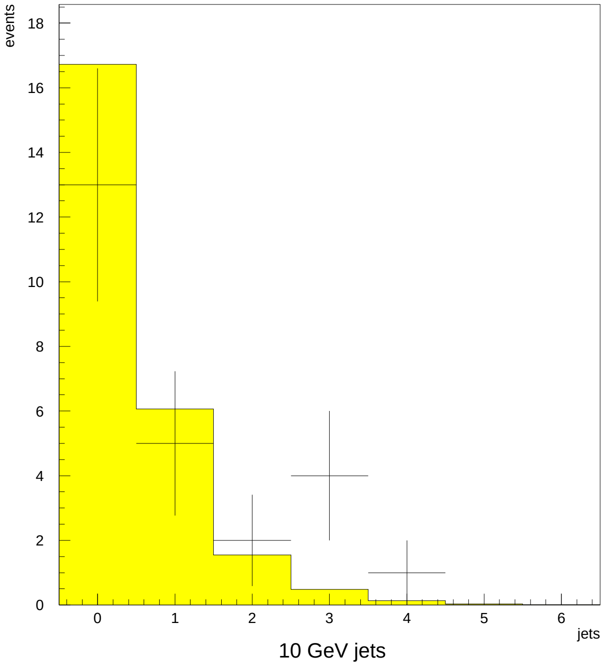

Figure 7.25: 10 GeV jet distribution for events which fail the vertex separation cut compared to the Z-candidate event distribution

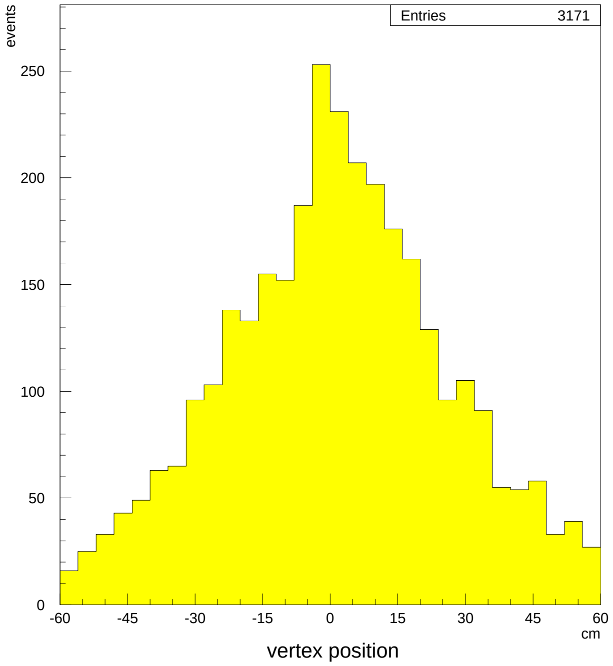

Figure 7.26: distribution of the vertex position

Vertex Separation Cut Efficiency	Number of Background Events in Final Sample
$99.31^{+0.12}_{-0.16}\%$	$0.44^{+0.22}_{-0.22}$

Table 7.19: final set of efficiencies for the global vertex separation cut

this, the Z-vertex plot of figure 7.26 is used. Pairs of points are picked at random from this plot, and the fraction of pairs which have a vertex separation less than 5 cm is determined. This fraction was estimated to be approximately 10%. This means that for every multiple vertex event with a vertex separation less than 5 cm, there are nine multiple vertex events with a vertex separation greater than 5 cm. This implies that the number of background events which make it into the final sample of Z-candidate events because they have a small vertex separation is approximately $0.44^{+0.22}_{-0.22}$. Table 7.19 shows the final set of efficiencies for this cut.

7.7.5 Efficiency of the impact parameter cut

It was determined that the impact parameter sum was not an appropriate variable to cut on (this is a standard cut in CDF analyses). This was because of the fact that the beam was not aligned perfectly with, nor was it completely parallel to, the beamline center at x=y=0. The slight slope of the beam meant that the impact parameter was correlated to the phi-angle of the track (see figure 7.27). When the tracks of a Z-candidate are back-to-back this correlation cancels out in the impact parameter sum. However, high Pt Z-candidates tend to have angular phi differences much less than 180 degrees (see figure 7.28). When the impact parameters of two non back-to-back tracks are added together, the effect of the beam's slope does not cancel out in the sum. The sum of the impact parameters is consequently larger for high Pt Z-candidate events than for low Pt Z-candidate events (see figure 7.29). Therefore, the impact parameter sum is not an appropriate variable to cut on, since cutting on this parameter would ultimately bias the Z Pt distribution in favor of low Pt Z events.

7.7.6 Summary of the Silver Selection Efficiency Studies

Table 7.20 summarizes the background estimates and the silver muon selection efficiencies. Note that the track-finding efficiency is not included in the overall calculation. For "5th" axial tracks (tracks which pass through the entire Central Tracking Chamber, including all five axial superlayers) the track-finding efficiency is believed to be $99.7^{+0.1}_{-0.1}\%$, and for tracks which fail to pass completely through the Central Tracking Chamber the track-finding efficiency can be much lower. This will be explained in detail in a later chapter.

7.8 Calculation of "Gold" Selection Efficiencies

Events where both muons are pointed at the same detector system have already been taken into account by double counting secondary legs which are "gold".

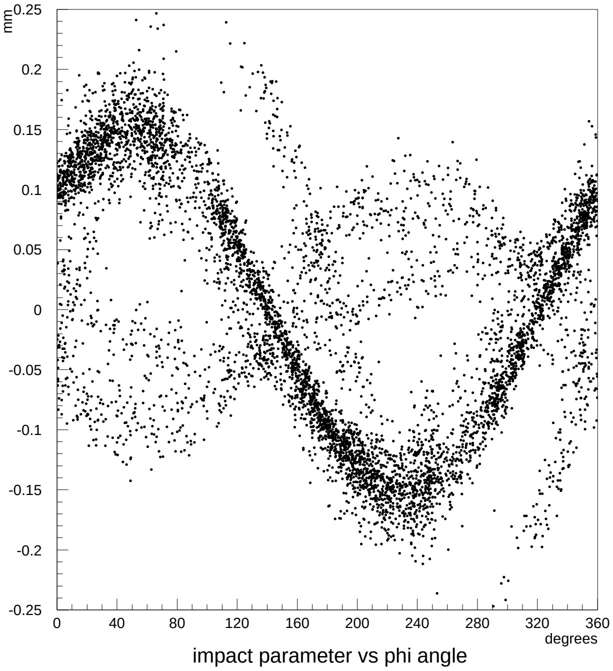

Figure 7.27: effect of the beam's slope on the impact parameter

Background Type	Number of Background Events in Final Sample
punch-through events	$4.1^{+2.9}_{-2.9}$
cosmic ray events	$8.6^{+2.9}_{-2.9}$
multiple vertex events	$0.4^{+0.2}_{-0.2}$
TOTAL BACKGROUND	$13.1^{+3.6}_{-3.6}$

Silver cut type	Overall Efficiency
combined calorimeter cuts	$95.3^{+0.3}_{-0.4}\%$
cosmic ray filter	$99.7^{+0.1}_{-0.1}\%$
multiple vertex cut	$99.31^{+0.12}_{-0.16}\%$
SILVER MUON SELECTION EFFICIENCY	$94.4^{+1.2}_{-1.5}\%$

Table 7.20: Summary of the background and silver muon selection efficiencies

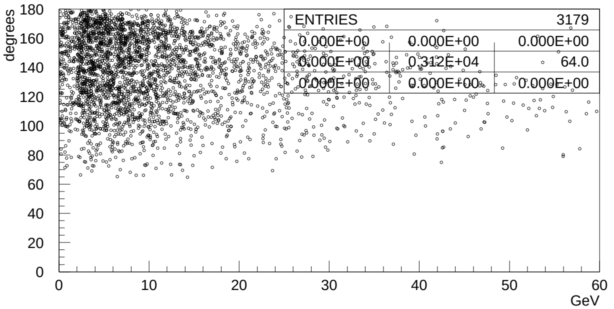

track 3D angle vs Z Pt

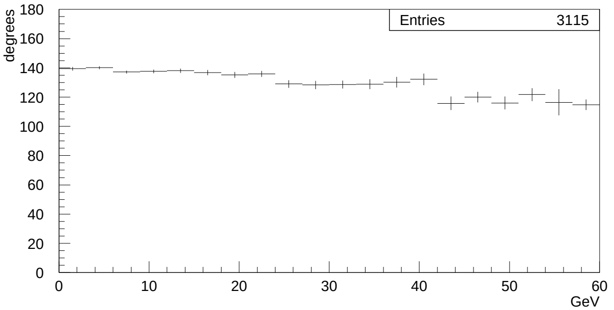

average track 3D angle vs Z Pt

Figure 7.28: Z Pt as a function of the 3-dimensional angle between the muon tracks

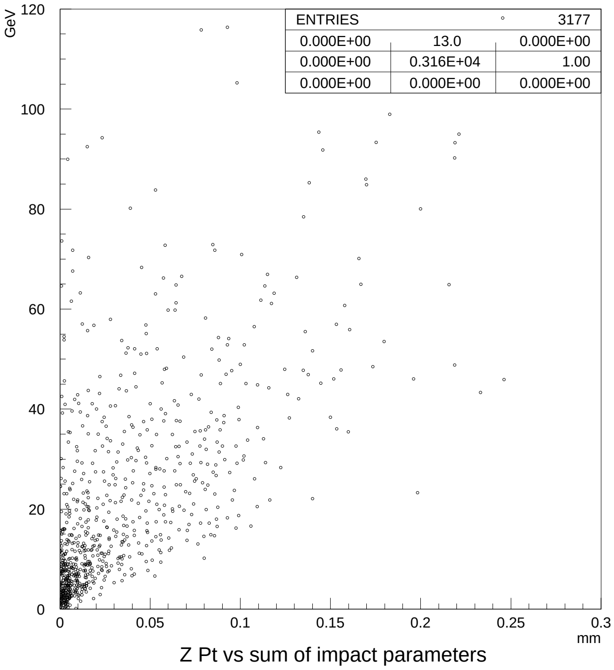

Figure 7.29: Z Pt as a function of the sum of the impact parameters

7.8.1 Uncorrected Gold Selection Efficiencies

First an initial efficiency calculation is made according to trigger region. No attempt is made yet to correct completely for the small inherent trigger problems which existed throughout the data runs. Efficiencies are calculated relative to the previous column, as the cuts become more and more stringent from left to right. See table 7.21. The “L2 trig” efficiencies are calculated using the Z data set. As expected, the errors in this particular column for the “U” and “X” trigger regions are much larger than the other columns because a large fraction of the otherwise useful data set cannot be used, because of the prescale. For example, in the case of the CMU the quoted efficiency values are good to a couple of percent of the quoted value except for the “L2 trig” column. For this column the quoted efficiency value is only accurate to approximately 10% of its stated value.

Next, table 7.21 is remade as table 7.22. The only difference is that the less accurate “L2 trig” efficiencies which were extracted from the Z data set have been replaced with the much more accurate “L2 trig” efficiencies which were derived using the live vs. working integrated luminosity measurements from table 5.1. It should be noted that these values which are thought to be much more accurate are in agreement with the previous values. However, the previous “L2 trig” efficiencies had the TRL-L2PROC handshaking problem automatically built into them, and the new values do not take this failure into account. Hence, when this correction is made, the new “L2 trig” values will decrease slightly (see table 7.23).

7.8.2 Corrected Gold Selection Efficiencies

Next, we make the necessary corrections to the final efficiency calculations. The effect of the level 1 and level 2 problems are inserted into the “L1 dat” and “L2 trig” columns. Note that the level 1 correction only needs to be made for the fraction of events where both muons are pointed towards the CMU. It is only in this class of events where “over” muons can exist and it can therefore be impossible to know which (if any) leg was affected by a trigger problem. Hence the correction is small. See table 7.23. For

trigger region	stub and dx	L1 sim	L1 dat	L1 trig	L2 sim	L2 trig	L3 trig
U	87.62		88.41	100.00	90.57	49.60	99.35
+	1.91		1.95	0.00	1.88	4.87	0.52
-	2.15		2.25	0.76	2.27	4.85	1.48
P	97.47	89.95	99.88	100.00	90.37	99.73	97.33
+	0.50	1.00	0.10	0.00	1.01	0.19	0.60
-	0.62	1.10	0.29	0.22	1.14	0.34	0.72
X	98.63	78.77	100.00	100.00	90.63	45.32	98.21
+	0.46	1.63	0.00	0.00	1.29	2.89	0.78
-	0.61	1.74	0.37	0.37	1.49	2.86	1.17

+	one sigma upper limit
-	one sigma lower limit
stub and dx	effect of requiring the stub and dx cut
L1 sim	effect of requiring the level 1 trigger simulation including gated muon chambers
L1 dat	effect of requiring that the corresponding muon trigger tower fires
L1 trig	effect of requiring that FRED outputs trigger level 1
L2 sim	effect of requiring that the track fires the level 2 simulation
L2 trig	effect of requiring that the track fires level 2 trigger
L3	effect of requiring that the muon trigger level 3

Table 7.21: Uncorrected overall muon selection efficiency, by trigger region

trigger region	stub and dx	L1 sim	L1 dat	L1 trig	L2 sim	L2 trig	L3 trig
U	87.62		88.41	100.00	90.57	48.76	99.35
+	1.91		1.95	0.00	1.88	1.61	0.52
-	2.15		2.25	0.76	2.27	1.61	1.48
P	97.47	89.95	99.88	100.00	90.37	100.0	97.33
+	0.50	1.00	0.10	0.00	1.01	0.00	0.60
-	0.62	1.10	0.29	0.22	1.14	0.00	0.72
X	98.34	78.77	100.00	100.00	90.63	42.63	98.21
+	0.52	1.63	0.00	0.00	1.29	1.41	0.78
-	0.66	1.74	0.37	0.37	1.49	1.41	1.17

Table 7.22: Uncorrected selection efficiencies, by trigger region, using integrated luminosity measurements to calculate “L2 trig”

trigger region	stub and dx	L1 sim	L1 dat	L1 trig	L2 sim	L2 trig	L3 trig
U	87.62		88.10	100.00	90.57	48.28	99.35
+	1.91		1.95	0.00	1.88	1.61	0.52
-	2.15		2.25	0.76	2.27	1.61	1.48
P	97.47	89.95	99.88	100.00	90.37	99.00	97.33
+	0.50	1.00	0.10	0.00	1.01	0.00	0.60
-	0.62	1.10	0.29	0.22	1.14	0.00	0.72
X	98.34	78.77	100.00	100.00	90.63	42.21	98.21
+	0.52	1.63	0.00	0.00	1.29	1.41	0.78
-	0.66	1.74	0.37	0.37	1.49	1.41	1.17

Table 7.23: Corrected selection efficiencies, by trigger region, using integrated luminosity measurements to calculate “L2 trig”

the level 2 TRL-L2PROC problem an overall reduction in the stated efficiencies is made corresponding to how serious the problem was believed to have been. Since the effects are small no modification of the error estimate has been made.

It is now possible to determine the final selection efficiencies. This is shown in table 7.24. The first column is the overall efficiency including the effect of the prescale. The second column shows the overall efficiency of the trigger without the effect of the prescale, a number which is often of interest to analyses within the CDF collaboration.

7.9 The CMU-CMX Live Integrated Luminosity Overlap

In addition to calculating the overall selection efficiencies for each trigger region it is necessary to calculate the prescale correlation factors, and then to calculate the “live integrated luminosity overlap” between each pair of trigger regions.

7.9.1 Prescale Correlation Factors

This can be determined by first calculating prescale correlation factors, using the Z-muon data set. This “live integrated luminosity overlap” must be included in the final

trigger region	overall efficiency	overall efficiency without prescaling
U	33.53	68.78
+	3.76	+ 2.61
-	3.75	- 2.84
P	76.25	76.25
+	1.64	+ 1.64
-	1.74	- 1.74
X	29.10	68.27
+	2.18	+ 2.07
-	2.11	- 2.10

+	one sigma upper limit
-	one sigma lower limit

Table 7.24: High Pt muon selection efficiencies

Monte Carlo if the event selection is to be correctly simulated. There is only one prescale correlation factor we need to worry about, because only two of the trigger regions were ever prescaled. It is thus necessary to calculate the relative prescale correlation factor for the CMU and CMX trigger regions only. This is done, once again, with the help of the Z-muon data set.

The prescale correlation factor can be computed in two different ways. The techniques are mirror images of one another. First, the full set of CMU-CMX Z-events is extracted. One leg must be gold and the other leg must pass all silver muon cuts and must also pass the trigger cuts at least as far as the level 2 simulation. This allows the second leg to be studied in an unbiased way. If it fails level 2 it can be assumed that it failed because of the prescale, in which case one prescale was on while the other was off and the prescales were anti-correlated for this event. Otherwise, if the second leg passed the level 2 trigger, then the prescales were both off in which case they were correlated. (Note that the level 2 handshaking problem would automatically manifest itself into any correlation result we obtained here, which is needed at this point).

For the case of gold “X” events, 24 of 27 secondary “U” legs passed the “U” level 2

trigger region	live int lum pb^{-1}	uncorrected live int lum overlap pb^{-1}	prescale correlation factor	live int lum overlap pb^{-1}
U	53.12	38.41	0.89	34.18
+	1.75	1.27	0.06	2.56
-	1.75	1.27	0.10	4.00
X	40.50	39.16	0.89	34.85
+	1.34	1.29	0.06	2.61
-	1.34	1.29	0.10	4.08
average				34.51
+				1.83
-				2.86

Table 7.25: Live integrated luminosity overlap for prescaled trigger regions

trigger and 3 events did not (they were prescaled). For the case of gold "U" events, coincidentally, 24 of 27 secondary "X" legs passed the level 2 "X" trigger, and 3 events did not (again, they were prescaled). Both techniques resulted in a prescale correlation factor of $0.89^{+0.06}_{-0.10}$. This suggests that roughly 89% of the time when one of these triggers was not prescaled the other prescale was also off. About 11% of the time when one prescale was off, the other prescale was on.

The prescale correlation factor allows us to determine the "live integrated luminosity overlap". Table 7.25 shows the result. The "live integrated luminosity" and the "uncorrected live integrated luminosity" values are taken from table 5.2 in the previous chapter. In one case the "U" region is used to determine the "X" region integrated luminosity overlap, and in the other case the "X" region is used to determine the "U" region integrated luminosity overlap. The two values are in agreement. The average of the two results is taken as the final answer.

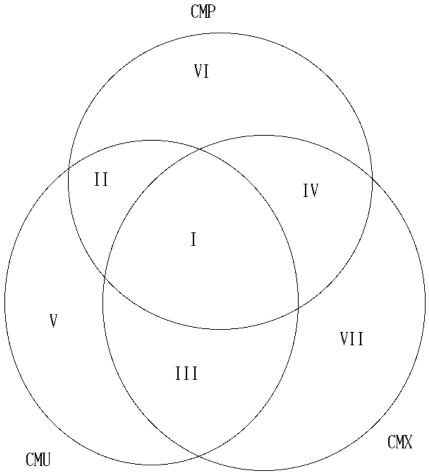

Figure 7.30: Venn diagram depicting the live luminosity intersections

intersection by number	intersection by region	integrated luminosity pb^{-1}
I + II + III + V	U	53.12
I + II + IV + VI	P	107.27
I + III + IV + VII	X	40.50
I + II	$U \cap P$	52.01
I + III	$U \cap X$	34.51
I + IV	$P \cap X$	40.25

Table 7.26: Integrated luminosity equations

7.9.2 Venn Diagram of the Integrated Luminosity Intersections by Trigger Region

As illustrated in figure 7.30, there are three trigger regions (U, P and X) and consequently there are seven distinct live integrated luminosity intersections of interest, labeled I thru VII on the figure.

So far, six measurements can be derived from previous results. They are shown in table 7.26.

intersection by number	intersection by region	integrated luminosity pb^{-1}
I	$U \cap P \cap X$	34.27
II	$U \cap P \cap \overline{X}$	17.74
III	$U \cap \overline{P} \cap X$	0.24
IV	$\overline{U} \cap P \cap X$	5.97
V	$U \cap \overline{P} \cap \overline{X}$	0.87
VI	$\overline{U} \cap P \cap \overline{X}$	49.29
VII	$\overline{U} \cap \overline{P} \cap X$	0.02
total		108.40

Table 7.27: Integrated luminosity summary

Since there are a total of seven unknowns (I through VII) and there are only six equations above, then all that is needed is one additional measurement to be taken and all seven intersections can be evaluated.

The easiest calculation is that for region VII. From figure 7.30 it can be seen that region VII corresponds to the period of time when "X" was live and neither "U" nor "P" was live. This can be written as:

$\mathrm{VII} = \overline{U} \cap \overline{P} \cap X$

When "P" was not live it was also not prescaled and therefore it was not working. There is a total of $0.63\mathrm{pb}^{-1}$ of data for when "X" was working and "P" was not working (note that "U" was working during this time). The prescale factor means that "X" would have been live for approximately $0.22\mathrm{pb}^{-1}$ of this data. The prescale correlation factor between "U" and "X" was 0.89, and therefore region VII (when the "U" was not live) amounts to $0.02\mathrm{pb}^{-1}$ (11% of the above). The integrated luminosity values for all seven regions can now be evaluated via simple algebra. They are summarized in table 7.27.

Background Type	Number of Background Events in Final Sample
punch-through events	$4.1^{+2.9}_{-2.9}$
cosmic ray events	$8.6^{+2.9}_{-2.9}$
multiple vertex events	$0.44^{+0.22}_{-0.22}$
TOTAL BACKGROUND	$13.1^{+3.6}_{-3.6}$

Table 7.28: Summary of background analysis

7.10 Z Selection Efficiency Summary

Armed with the overall selection efficiency values for each trigger region, the "live integrated luminosity" values for each trigger region, and the corresponding "live integrated luminosity overlap" for each of our overlap regions we are ready to proceed to the next step, namely to make the first physics plots of interest. The important information is summarized in tables 7.27, 7.28 and 7.29.

fiducial region	overall efficiency	overall efficiency without prescaling
U	33.53	68.78
+	3.76	2.61
-	3.75	2.84
P	76.25	76.25
+	1.64	1.64
-	1.74	1.74
X	29.10	68.27
+	2.18	2.07
-	2.11	2.10
Silver Cuts	94.4	not applicable
+	1.2	
-	1.5	

trigger region	live int lum pb^{-1}
U	53.12
+	1.75
-	1.75
P	107.27
+	3.54
-	3.54
X	40.50
+	1.34
-	1.34

Table 7.29: Summary of selection efficiency measurements. Note that the track-finding efficiency is not included.

Chapter 8

Monte Carlo Tuning

8.1 Raw Data Sample

Having identified the 3,176 Z candidate events which will be used in this analysis, it is time to present the uncorrected physics plots of interest. There are many corrections which need to be made in order to get the final differential cross-section, the Z Pt spectrum. For now the detector readout information is used to calculate the raw Z invariant mass and Pt spectra. As has been shown already, the background contamination in this sample of Z events is very small.

It is well-known from introductory physics that momentum and energy are conserved quantities. There is no exception here. The Z candidates are usually slow-moving (meaning their momentum is small) but they are also quite massive (a large mass implies a large energy). The muons into which the Zs decay are light and share the large energies of the Z boson. Each muon's 4-vector is known (the 4-vector is a particle's momentum 3-vector combined with its total energy). Using the measured 4-vectors of the two outgoing muons and the conservation laws it is possible to determine the original 4-vector of the hypothesized Z. It is then an easy task to calculate quantities such as the invariant mass or the transverse momentum.

The dimuon invariant mass is given by:

$$Invariant\ Mass = \sqrt{2 \times (E_1 E_2 - P_{x_1} P_{x_2} - P_{y_1} P_{y_2} - P_{z_1} P_{z_2})}$$

where $(P_{x_1}, P_{y_1}, P_{z_1}, E_1)$ and $(P_{x_2}, P_{y_2}, P_{z_2}, E_2)$ are the muon 4-vectors.

The dimuon transverse momentum is given by:

$Transverse\ Momentum = \sqrt{(P_{x_1} + P_{x_2})^2 + (P_{y_1} + P_{y_2})^2}$

There are three types of plots exhibited at this stage of the analysis. Online plots use the level 3 trigger track parameters or 4-vectors. Offline plots use the full offline reconstructed track parameters, which are more precise. Offline beam-constrained plots are yet more precise because they are derived from a constrained fit of each muon track (through the known beam-collision point). Note that not all of the dimuon candidate events are used in these plots - for now only the 2,458 events which had both muon tracks pointed at all of the CTC superlayers are studied. A muon which passes through all of the layers of the CTC will have the most precise tracking information associated with it.

Figures 8.1 to 8.3 show the Z mass plot at each level of precision. Note that approximately one third of the dimuon events could not be reconstructed properly with the level 3 trigger information and hence the online plots contain information for only 1,538 Z events (instead of 3,176 events seen in the more inclusive offline analysis). The measured width of the invariant mass narrows as the errors associated with measuring the muon track parameters decrease, as would be expected. Figures 8.4 to 8.6 show the dimuon Pt plot, again at each level of precision. As would be expected, as the level of precision increases (and the errors associated with individual measurements consequently decrease) then the distributions tend to sharpen, because the degree to which the distributions are being smeared by the measurement errors decreases.

8.2 Iterations of the Monte Carlo Packages

This analysis endured several Monte Carlo package iterations before the final Monte Carlo was settled on. Initially a standard Monte Carlo called Pythia version 5.6 [30] and a set of structure functions called CTEQ 3L [44] were used in conjunction with the full CDF detector simulation. This version of Pythia was several years old, and upon generating Z mass spectra it was found that there was a noticeable difference between the shape of

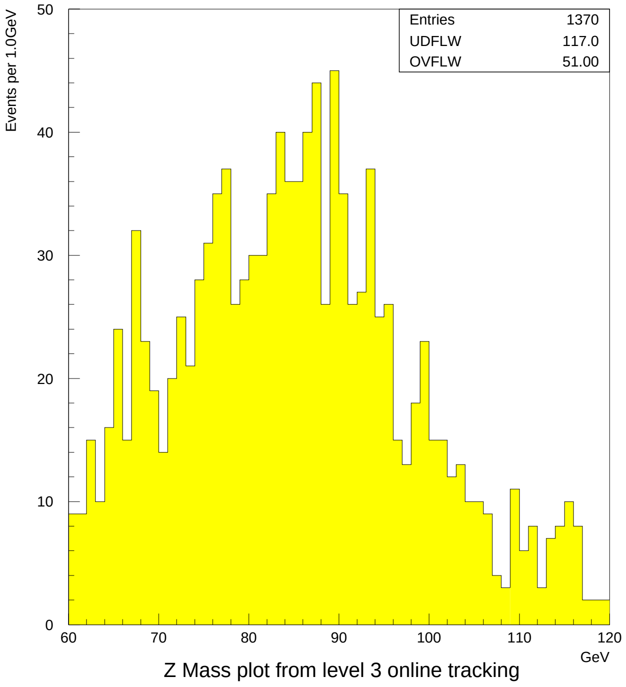

Figure 8.1: Z mass plot, online tracking

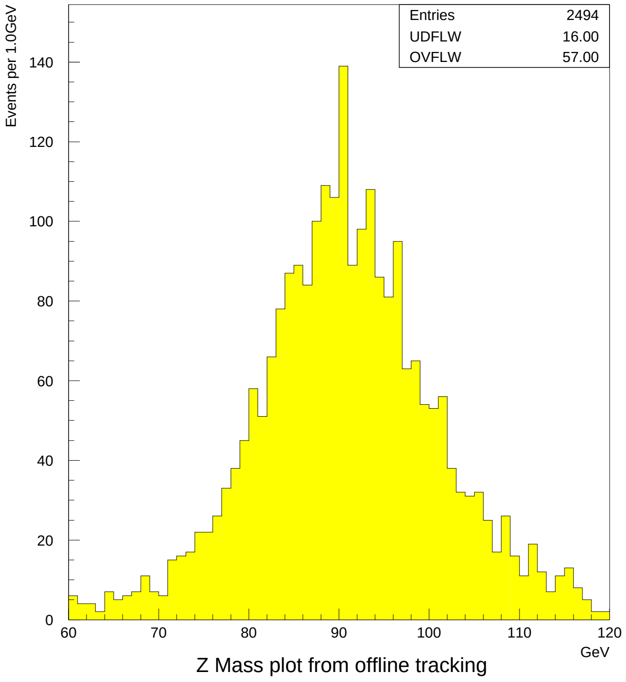

Figure 8.2: Z mass plot, offline tracking

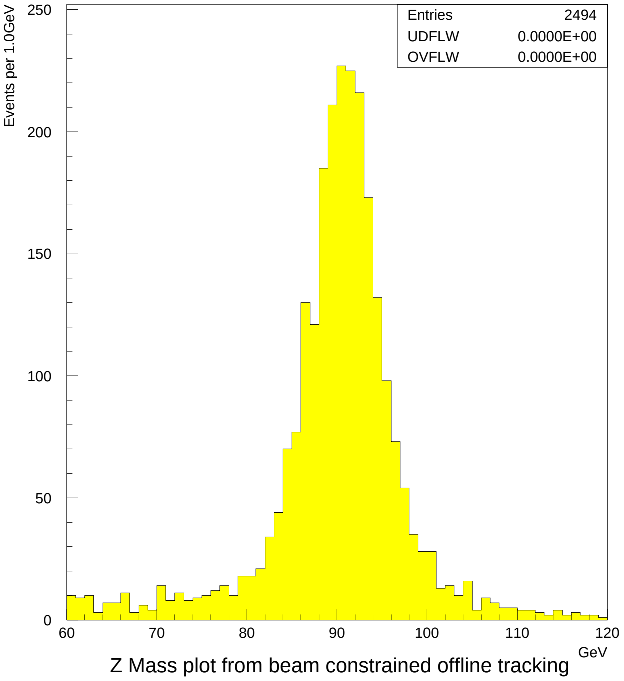

Figure 8.3: Z mass plot, beam constrained

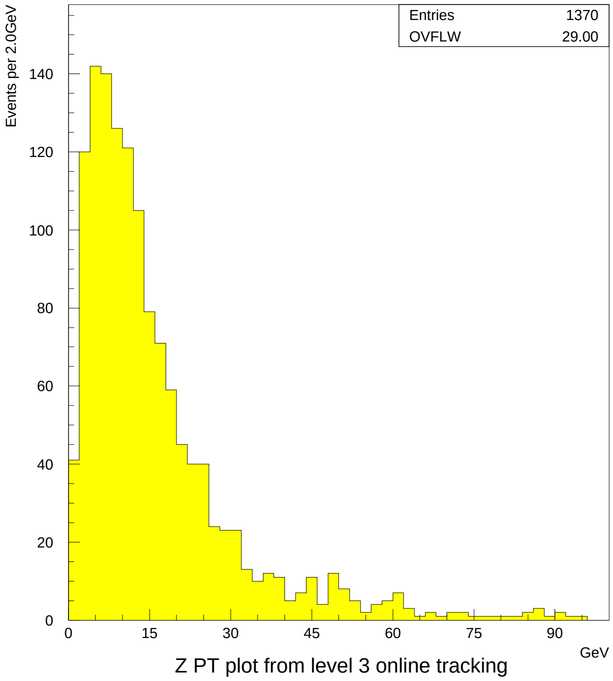

Figure 8.4: Z Pt plot, online tracking

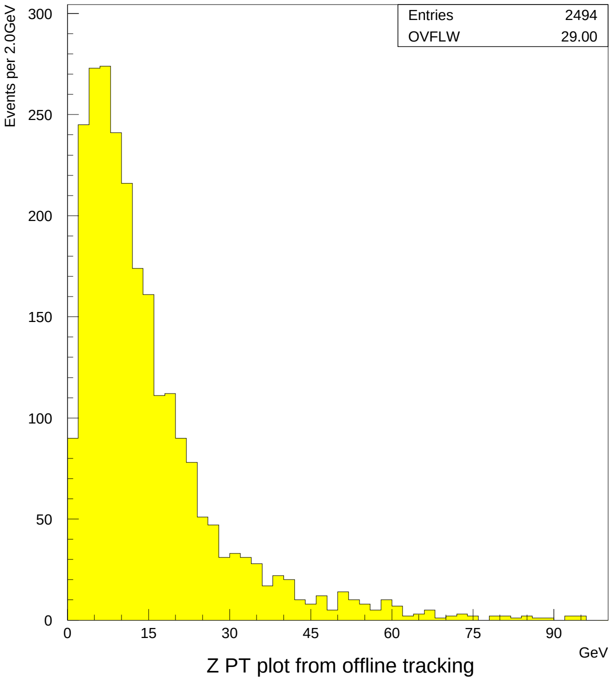

Figure 8.5: Z Pt plot, offline tracking

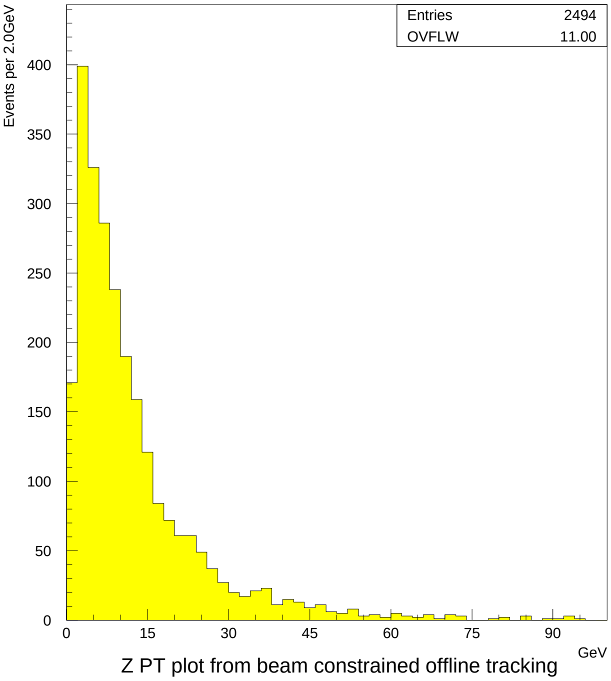

Figure 8.6: Z Pt plot, beam constrained

the Z mass from the data and the shape of the Z mass from the Monte Carlo, even after taking measurement errors into account. The Monte Carlo was generating comparably too few events at high mass and too many events at low mass. While the agreement was quite close, a preponderance of data events in the high mass tail would no doubt have led to speculation of possible new physics, and hence an attempt had to be made to pin down these potentially awkward or wondrous discrepancies.

Other CDF analyses used a package called PHOTOS version 2.0 (in conjunction with Pythia v5.6). The purpose of Photos v2.0 is to correctly simulate the 2nd order internal QED radiative corrections since it was known that Pythia v5.6 did not do this properly and this correction affects roughly ten percent of the total Z cross-section. What is done is to turn off this part of the simulation in Pythia and have Photos do it instead. Upon integrating the Photos Monte Carlo package [28] the noticed discrepancies between the data and the Monte Carlo were significantly reduced. However, they had not disappeared.

The penultimate Monte Carlo package iteration involved updating the version of Pythia from version 5.6 to version 6.157, which was released in February, 2001. This version of the Pythia Monte Carlo was used in conjunction with the latest set of structure functions (called CTEQ 5L [44]) and it was found to generate a Z-mass spectra which (after running the generated events through the full CDF detector simulation) matched the data almost perfectly. Furthermore, when Photos was integrated into the updated code no significant improvement was found. Photos was left in place more as a testament to the work involved in integrating it into the final simulation package than a belief that it actually improved the Monte Carlo simulation. Each successive Monte Carlo coding improvement required the generation of millions of simulated Monte Carlo events before a definitive conclusion on whether or not it was satisfactorily emulating the measured data.

Finally, an unfortunate bug was reported with Pythia v6.157. This bug affected the cross-section of Z production and therefore affected the analysis. It became necessary to upgrade Pythia to v6.203 which was released in November, 2001. While the overall shape

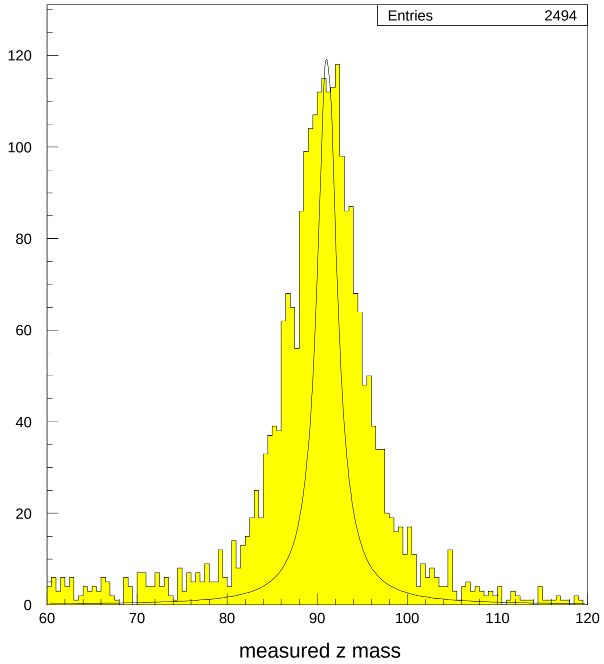

Figure 8.7: Measured dimuon mass with natural Z lineshape superimposed

of the Z mass did not change, the production rates did indeed change slightly. In the end the match between the Monte Carlo and the data was excellent, as later plots will show.

8.3 Monte Carlo Representaion of the Error Scale Factor

It is clear that the dimuon mass distribution which is obtained experimentally is much broader than the well-known Z mass lineshape because it has been smeared by measurement errors. Figure 8.7 shows the measured dimuon mass histogram for run 1b with the radiation corrected Z mass lineshape superimposed (henceforth the term "radiation corrected" will be dropped). The natural Z lineshape has a sigma of about 2.5 GeV, while the measured dimuon mass has a sigma of about 5 GeV.

For each candidate muon the collection of digitations from the track detectors are fit to a five parameter curve. The measured parameters from the fit have estimated errors associated with them. The parameters are the curvature, the phi angle, d0 ("d-zero", the distance from the beamline to the extrapolated point of closest approach of the track), the cotangent (which gives the eta direction) and z0 ("z-zero", the distance along the beamline to the point of closest approach). The five element by five element covariant error matrix provided by the fit gives not only the errors for each individual track parameter, but also the correlation of the errors between the different track parameters themselves. When two such candidate muons are combined, standard error propagation [9] is used to determine experimentally the errors in the derived quantities. In this case, the derived quantities are the dimuon mass and the dimuon Pt values.

8.3.0.1 The Standard Way to Fix the Errors

It is well-known that the standard CDF tracking errors are underestimated. The resulting measured Z mass plot is, as a result, broader than the event errors indicate it should be. Figure 8.8 shows how the natural Z lineshape gets smeared as the event error increases. Before any corrections are applied, the average dimuon mass error for run 1b data is estimated to be 1.3GeV. The measured dimuon spectrum, shown as the last of the plots in figure 8.8, clearly indicates that the tracking errors are indeed underestimated.

The standard way to deal with this problem at CDF is to scale the errors by an appropriate factor (note that boosting the measured errors by an arbitrary scale factor involves scaling the covariant error matrix by the square of this scale factor, if the final errors are to be measured appropriately). The accepted error scale factor at CDF is 2.0, which would put the average run 1b dimuon mass error at 2.6GeV.

Figure 8.9 shows the measured run 1b dimuon mass plot with a 2.6GeV smeared natural Z lineshape plot superimposed. Figure 8.10 shows the same measured run 1b dimuon mass plot with a 3.1GeV smeared natural Z lineshape plot superimposed. The greater degree of similarity between the latter plots is an indication that a scale factor of 2.0 may not be appropriate for this analysis. It is possible to use the dimuon mass spectrum to accurately

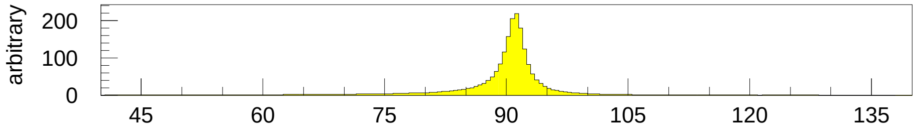

natural Z lineshape, no smearing

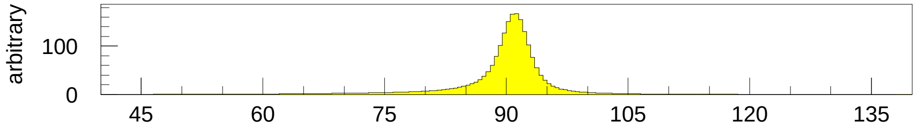

natural Z lineshape, 1 GeV smearing

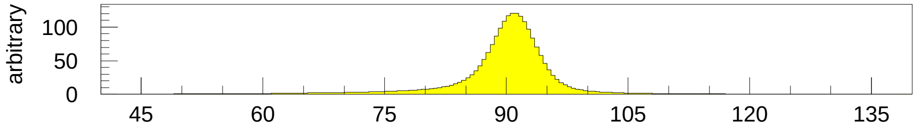

natural Z lineshape, 2 GeV smearing

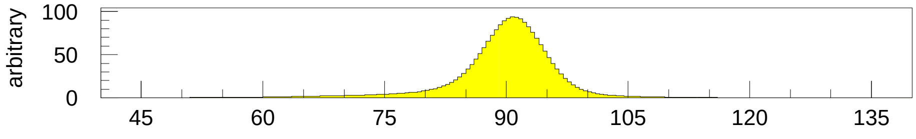

natural Z lineshape, 3 GeV smearing

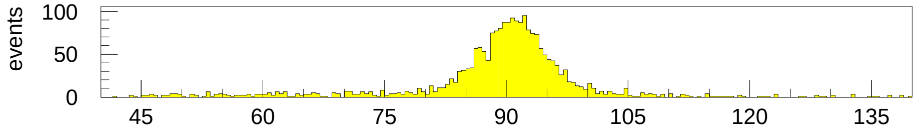

measured dimuon mass, run 1b

Figure 8.8: smearing of the natural Z lineshape

determine the error scale factor specific to our data set, a sample of high Pt dimuons. The determined error scale factor applicable to this sample does indeed differ from the CDF-accepted value of 2.0.

8.3.1 Using the Z Mass to Determine the Error Scale Factor

Determining an overall scale factor which will be used to increase the track errors to their correct level is a non-trivial process. This is because the dimuon mass error is different for each event, and it tends to increase as the dimuon mass increases. Figure 8.11 shows the measured error in the dimuon mass versus the measured dimuon mass itself for both run 1a and run 1b data. Both graphs in this figure assume a CDF-accepted error scale factor value of 2.0.

As has been stated, standard error propagation is used to determine experimentally the errors in derived quantities [9] such as the dimuon mass. Hence, the final error in the measured Z mass comes explicitly from the measured errors in the two sets of individual track parameters. The dominant source of error which contributes to the final error in the Z mass is the measurement of the curvature for each track. The transverse momentum of a track is actually a simple scaling of the measured curvature value. The estimated error depends heavily on how many of the CTC superlayers register a hit for the track. More specifically, the estimated error depends on how many and which of the axial superlayers register hits, since it is the axial superlayers which are the superlayers which are used to determine the curvature of a track.

The CTC is roughly a three meter long cylinder with a radius of about 1.3 meters (see figure 2.4). It has 5 axial superlayers (numbered 0,2,4,6 and 8) and 4 stereo superlayers (numbered 1,3,5 and 7). An axial superlayer lies on each side of a stereo superlayer. Superlayer zero is closest to the beam-pipe. and superlayer eight is furthest away. Tracks which pass typical high Pt muon selection cuts and which are pointed at any of the central muon detectors (CMU, CMP, CMX) will pass through all nine of the superlayers (tracks are required to have a beamline z-offset of less than 60 centimeters which means they will

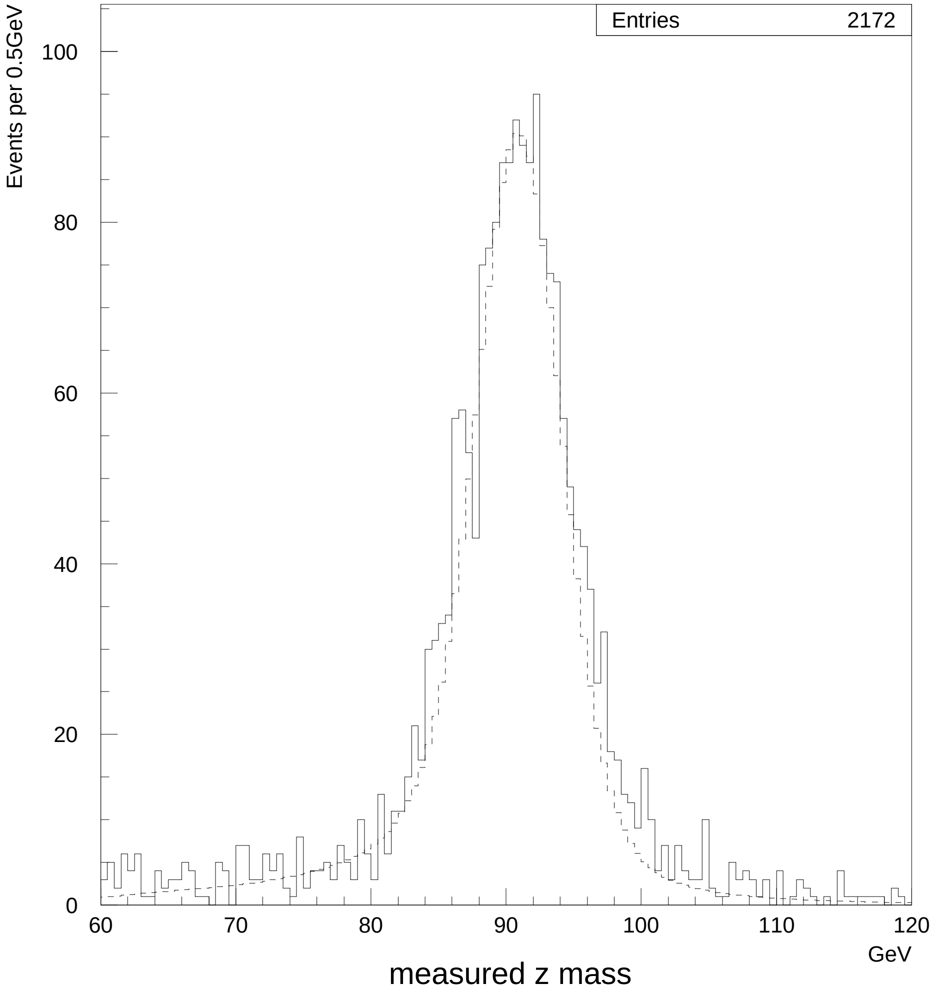

Figure 8.9: measured mass with 2.6GeV smeared Z lineshape superimposed

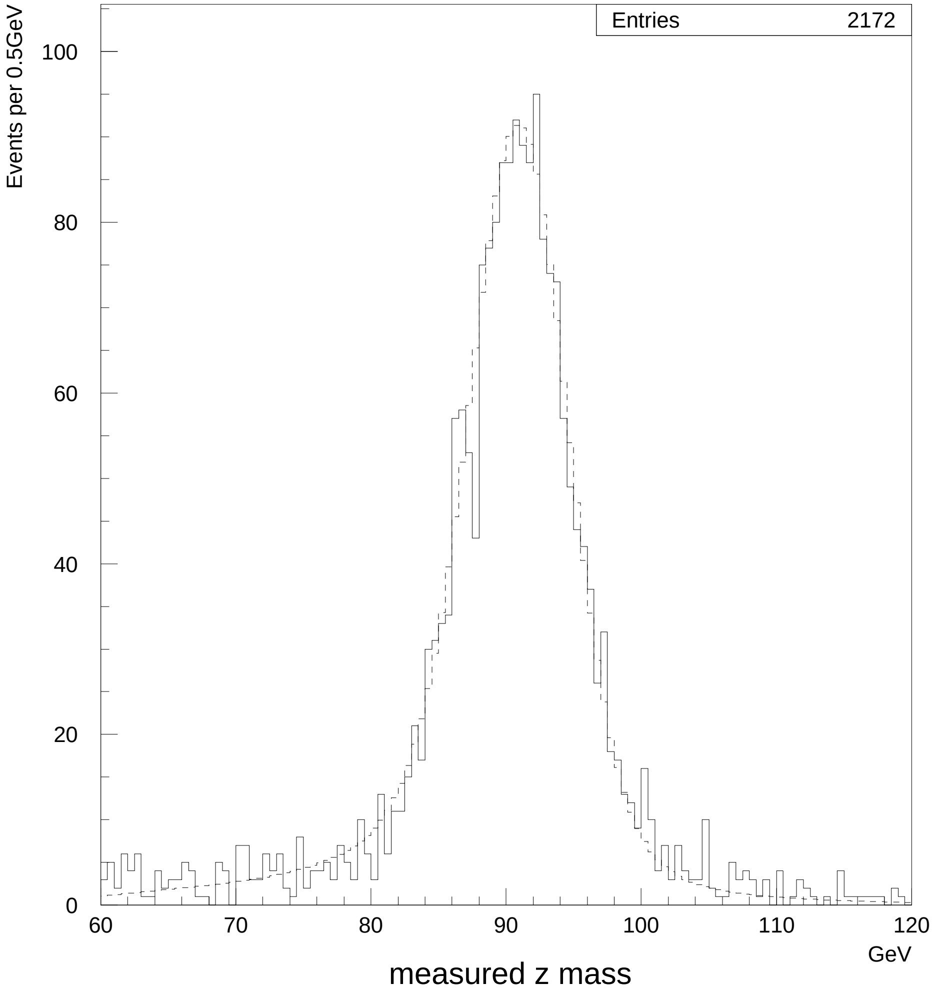

Figure 8.10: measured mass with 3.1GeV smeared Z lineshape superimposed

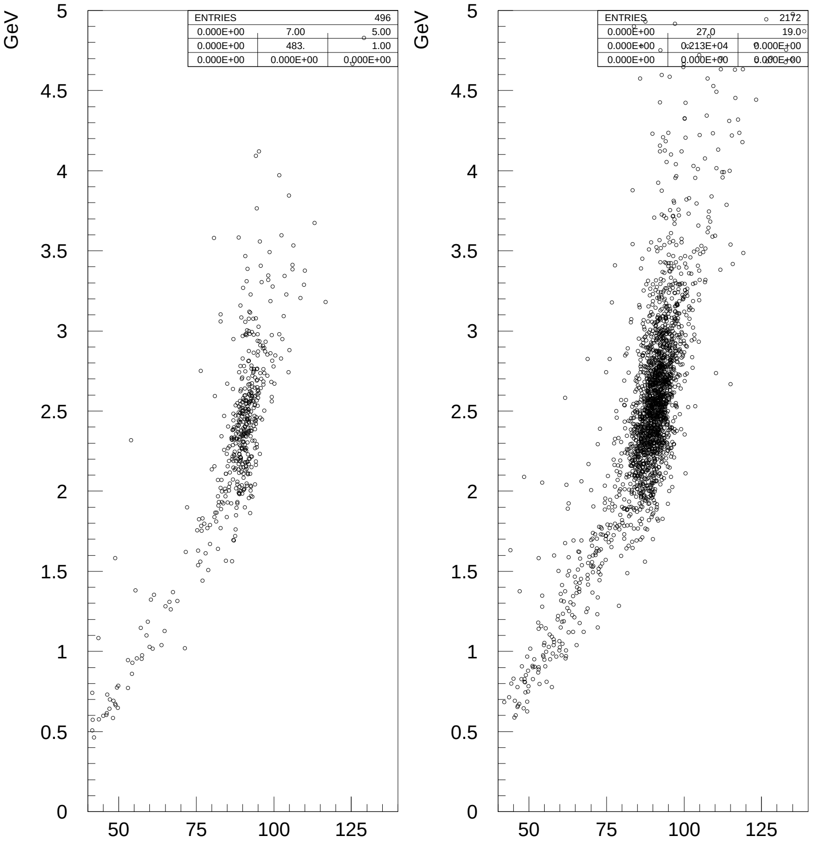

run 1a

run 1b

Figure 8.11: dimuon mass error vs the measured dimuon mass

always start off within the confines of the CTC since the CTC extends out to a maximum z-value of about 150 centimeters in either direction). Tracking errors associated with measured parameters such as the curvature will be smaller when more information about the track is known, and the most information the CTC can generate about a track occurs when the track in question registers hits in all of the CTC superlayers. If all five of the axial superlayers have been hit then the best and most accurate track fit (a 5-point fit) is performed to determine the curvature. Not all tracks will register hits in each superlayer, however, and if this happens then the track fit which is performed will have larger errors because not as many points will be used in the fit process. Not only can a track's eta be large enough that it exits the CTC before it reaches one or more of the axial superlayers furthest from the interaction point, but tracks can fail to register hits in one or more of the CTC axial superlayers because individual superlayers are not fully efficient. The CTC efficiency actually improves with increasing superlayer number, the assumed explanation being that as the distance from the interaction point increases the density of charged particles decreases in the CTC and hence there are less likely to be CTC wire hits other than those of the track being fit. As we shall see later in this chapter, the CTC superlayer efficiency is almost 100% for superlayer 8 (the outermost superlayer), but only about 85% for superlayer 0 (the innermost superlayer).

In this analysis each track is required to register at least three axial superlayer hits (out of a maximum of five possible). Since higher eta tracks can fail to pass through all five of the axial superlayers, requiring any three out of five axial superlayers to be hit effectively becomes a more stringent three out of four or even three out of three for higher eta tracks. This results in lower acceptance efficiencies as the track eta increases. These lower acceptances are further exacerbated by the fact that higher eta tracks will miss the more efficient outer axial superlayers and our selection will be more dependent on the inner less efficient axial superlayers. It is through the understanding of these efficiencies (and the resulting track resolutions) that it became possible to include the higher-eta tracks in this analysis, and hence to wind up with a much larger dimuon Z data set than comparable CDF analyses.

Tracks which do not hit all of the superlayers will have larger estimated errors associated with measured parameters such as the curvature, since the track fit will not be as constrained as it would be if more points were used in the fit. It is hypothesized that the magnitude of the measured errors depends most on the hits used in the fit at the track's extremities. In this analysis beam-constraining is used as part of the track fit, and hence one track extremity position (the interaction point) is known. This means that the axial CTC superlayer which is the final one to register hits for the track is the one which will have the greatest impact on the track fit resolution. Since this analysis requires at least three-out-of-five axial superlayers to be hit, then there are three types of tracks to consider. These are "5th-axial" (if the last axial superlayer to be hit is the 5th axial superlayer), "4th-axial" (if the last axial superlayer to be hit is the 4th axial superlayer), and "3rd-axial" (if the last axial superlayer to be hit is the 3rd axial superlayer).

Figure 8.12 shows the muon Pt fractional errors for the three different types of track legs which are used in this analysis. A scale factor of 2.0 is assumed for each plot. The graph for all tracks is plotted first, and then underneath are the plots for each track classification. The first of the three plots is for "5th-axial" tracks. The vast majority of tracks fall into this "5th-axial" category. "5th-axial" tracks have a maximum eta up to about 1.0, and the 5th axial superlayer is almost 100% efficient. The second plot is for "4th axial" tracks. Most of these were high eta tracks which exited the CTC after hitting the 4th axial superlayer, but some were tracks which passed through but failed to register a hit in the last superlayer (only about 20 of the 382 tracks fell into the latter category). The third plot is for "3rd-axial" tracks. From a comparison of the three plots in can be surmised that the final axial superlayer which has registered a hit is an excellent variable for classifying the different tracking resolutions, since there are clear demarcations between the three plots. The final axial superlayer which has registered a hit does indeed determine the track's overall resolution. If the fifth and final axial superlayer registers hits (a "5th-axial"

Dimuon Classification	Events (Track Resolution)
5-5	2430
5-4	381
5-3	364
4-4	0
4-3	1
3-3	0

Table 8.1: Dimuon events according to track resolution classification

track), then the tracking errors will fall into the smallest range of values. If the fifth axial superlayer is missed but the 4th axial superlayer registers hits (a "4th-axial" track) then the tracking errors will be larger and fall into a mid-range of measured errors, and if both the fifth and fourth axial superlayers are missed but the third axial superlayer is hit (a "3rd-axial" track) then the tracking errors will fall into the largest range of values which are found in this analysis.

The objective is to determine an overall scale factor which will be used to adjust the tracking errors to their correct level. Three types of individual track resolution classifications have been identified and defined (5th-axial, 4th-axial and 3rd-axial). Z events are comprised of two tracks, and the errors of the two tracks are combined together via standard error propagation to determine the error in the Z mass. Hence, there are a total of six possible track resolution classification combinations. They are "5-5", "5-4", "5-3", "4-4", "4-3", and "3-3" ("5-4" would stand for a "5th-axial, 4th-axial dimuon event"). Table 8.1 shows the breakdown of the different types of Z events according to each leg's tracking resolution classification. Table 8.1 indicates that all but one of the events has at least one "5th-axial" track.

A small number of events are not used in the determination of the error scale factor, one of them being the solitary "4-3" event. It is important to understand why. The axial superlayers are all very efficient. For example, when a track is pointed at the outermost superlayer (superlayer 8), as will be shown later in this chapter (see table 8.5), there is

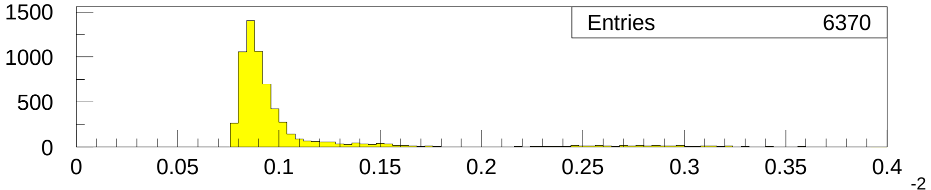

track Pt fractional error, all tracks

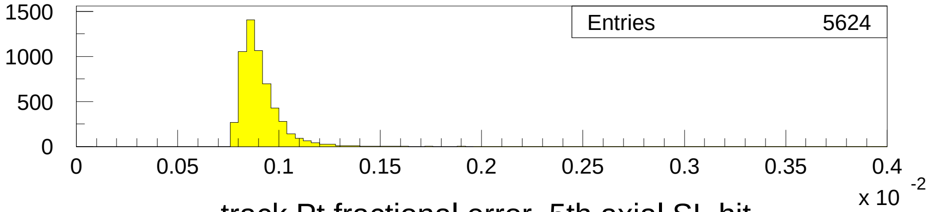

track Pt fractional error, 5th axial SL hit

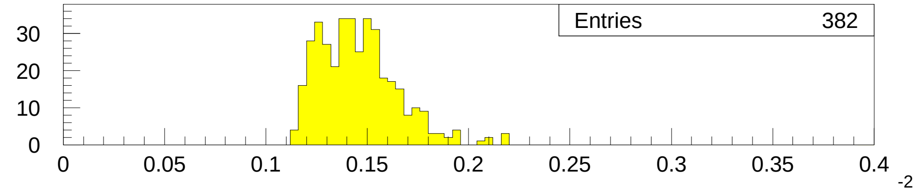

track Pt fractional error, 4th axial SL hit

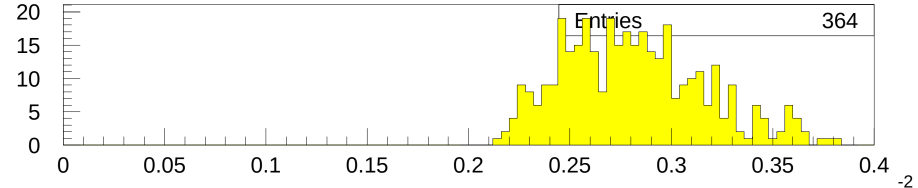

track Pt fractional error, 3rd axial SL hit

Figure 8.12: track Pt fractional errors according to track resolution classification

a 99.8% probability that the track will register a hit in it. However, approximately one in five hundred (0.2%) of these tracks will not register a hit in this superlayer due to its slight inefficiency. There are close to 2,500 "5-5" events, which means a handful of the "5-4" events would have been classified as "5-5" except that one of the tracks failed to register a hit in the outermost superlayer. The solitary "4-3" event is a similar type of event to this example. The primary leg would have been "5th-axial" but it failed to register a hit in the outermost superlayer, and the event was ultimately classified as a "4-3" event. Therefore, in a small number of events, the outermost superlayer which a track is pointed at does not match the outermost superlayer which actually registers a hit. The CDF Monte Carlo simulation does not suffer from this "problem". All detectors are 100% efficient in the Monte Carlo simulation. Consequently, there is never a difference between the Monte Carlo predicted track classification and the Monte Carlo measured track classification. The error scale factor is ultimately determined via a comparison between the Data and the CDF Monte Carlo. Hence, the small number of data events (the solitary "4-3" event for example), where the predicted track classification does not match the measured track classification, are not used in the determination of the error scale factor, because the topology of these events is known to be different from the Monte Carlo events. This is accomplished via the use of a routine called CMUOTR [29].

The routine CMUOTR took a track's initial position and momentum 4-vector and predicted where the track exited the CTC. A simple look-up table then determined which was the last axial superlayer that the track would have passed through before it exited the CTC. The routine CMUOTR used the physical positions of the CTC superlayers in this look-up. However, the superlayers were very inefficient at the boundaries and the CMUOTR routine was "tuned" with the high Pt muon data set to ensure that the prediction matched the data as closely as possible. This involved modifying individual axial superlayer boundary positions by one or two centimeters. The inner boundary for superlayer 6 was physically located at an exit radius of 101.1cm, but the "tuned" value was determined to be 103.0cm. The inner boundary for superlayer 8 was physically located at an exit radius of 124.3cm, but the "tuned" value was determined to be 125.8cm. The intent of the tuning was to determine the CTC boundary position where the number of tracks predicted to miss a certain CTC superlayer and which registered hits in that superlayer equaled the number of tracks which were predicted to hit the axial superlayer but failed to register a hit in that superlayer (the overall CTC inefficiency must first have been excluded - only tracks near the superlayer boundaries are of interest). Whether or not the CTC registered a track hit was fairly unpredictable if the track exited the CTC within about one centimeter of the "tuned" boundary value.

The slight differences in the data between the predicted "tuned" CMUOTR dimuon classification and the actual track resolution classification can be seen in table 8.2. For example, 2,445 of the dimuon events, according to the routine CMUOTR, were classified as "5-5" events. However, in twenty-four of these events one leg failed to register a hit in either the last axial superlayer (22 events) or else it failed to register a hit in the last two axial superlayers (2 events). Upon careful examination, eighteen of these twenty-four events had a track which failed to register a hit in the last axial superlayer, despite the fact that the track parameters predicted that these tracks would pass completely through the last axial superlayer. These events are considered to be examples of the overall inefficiency of the CTC. The other six events failed to register a hit in the final axial superlayer, and the track parameters predicted that these tracks would exit the CTC just after they had entered the final axial superlayer - they would only pass through a small portion of the axial superlayer. These events are most likely to be examples of CTC inefficiency at the superlayer boundary. The correlative example of the efficiency problem at the superlayer boundary can be seen further down the table. 372 events were predicted to be "5-4" events, as classified by the routine CMUOTR, but seven of them were classified in the data as "5-5" events. In this group of seven events both tracks caused the CTC to register hits in the final superlayer, but the routine CMUOTR predicted that one of the tracks would exit the CTC just before the final superlayer was reached. Therefore, at the CMUOTR boundary between the 5th and 4th axial superlayers, roughly equal numbers of events either caused a superlayer to fire when it was predicted to miss, or else resulted in a superlayer miss when the prediction was for a hit. A similar statement can be made for the other CMUOTR boundary of importance, the boundary between the 4th and 3rd axial superlayers. This was confirmation that the CMUOTR "tuning" had been successful.

In the determination of the error scale factor, the small number of events where the CMUOTR classification prediction did not match the actual track resolution classification were not used because they had a slightly different topology from the Monte Carlo simulation events, which assumed a perfectly efficient CTC. Once the error scale factor has been determined, these "ignored" events could then be used in the rest of this analysis without any problem (for reasons which should become clear later, the solitary "4-3" event always remained a problem, and post error-scale-factor-determination it was reclassified as a "5-3" event for the purposes of scaling the errors associated with this event, which ultimately meant that the tracking errors for one event were very slightly underestimated, hardly anything to worry about).

Ideally, each individual track resolution classification would have the same error scale factor. However, it became apparent that this was not the case. One overall error scale factor value is not sufficient to correct the tracking error values to their correct level. A Monte Carlo containing a full CDF detector simulation and previously determined selection and trigger efficiency estimates (see earlier chapters) was used to generate dimuon Z events. The Monte Carlo had as one of its inputs an error scale factor parameter. This error scale factor was applied to the tracking error matrix within the simulated event in order to generate Monte Carlo "measured" tracking values via Gaussian smearing. Hence, the Monte Carlo was used to generate "measured" Z mass spectra for many different error scale factors. Tens of millions of Monte Carlo Z events were generated after the Monte Carlo had been carefully tuned to match the data. When the error scale factor was small (and hence the tracking errors were small) then the Monte Carlo "measured" Z mass spectra was narrow, and when the error scale factor was large (and hence the tracking errors were large) then the Monte Carlo "measured" Z mass spectra was wide. The resulting Monte

CMUOTR Classification	Events	Track Resolution Classification	Events
5-5	2445	5-5	2424
		5-4	20
		5-3	1
		4-4	0
		4-3	0
		3-3	0
5-4	372	5-5	6
		5-4	356
		5-3	10
		4-4	0
		4-3	0
		3-3	0
5-3	359	5-5	0
		5-4	5
		5-3	353
		4-4	0
		4-3	1
		3-3	0

Table 8.2: Comparison between CMUOTR classification and actual track resolution classification

Carlo “measured” Z mass plots were compared with the experimentally measured Z mass plot. A minimum chi-squared analysis was performed in order to determine the value of the error scale factor for which the Monte Carlo measured Z mass spectrum most closely matched the experimentally measured Z mass spectrum.

This analysis was performed for all 3,176 candidate Z events, and an overall error scale factor value was obtained. The same analysis was then performed as a check that the error scale factor did not depend on the track resolution classification (for example, instead of allowing all of the original candidate Z events, only events with one type of track resolution classification, such as “5-5” events, were allowed in both the experimental and the Monte Carlo event selection). It was discovered that the different track resolution classifications had different error scale factors associated with them. There is a small problem which should be pointed out here. The Monte Carlo applied the same error scale factor to each track within an event. There was no easy way to modify this on a per track basis in order, for example, to allow “5th-axial” tracks to be treated differently from “4th-axial” or “3rd-axial” tracks within the same event. What this analysis basically did was treat the three dimuon track classifications separately and determine an average error scale factor for the events within each classification. For the “5-5” events this method presents no problems because the two muon tracks are both “5th-axial” tracks, and if only “5-5” events are used to determine the error scale factor then the determined value is also the appropriate value for each track. But for the “5-4” and the “5-3” events the two muon tracks within each event have one “5th-axial” track and one non-“5th-axial” track. The average error scale factor which is determined for these two groups of tracks (with different track resolution classifications) is actually a weighted average of the error scale factor for the “5th-axial” tracks combined with the error scale factor for the non-“fifth-axial” tracks. The initial incorrect assumption that the error scale factor is the same for all tracks (5th-axial, 4th-axial and 3rd-axial) has been replaced by an incorrect assumption that there is one error scale factor value for the “5-5” events, a different value for the “5-4” events and a third value for the “5-3” events. However, although this latter assumption is also incorrect, it represents an improvement. First, most of the Z candidate events are “5-5” events, and by excluding events with non-“5th-axial” tracks the resulting error scale factor determination is believed to be very accurate (the determined value successfully represents the error scale factor for all of the “5th-axial” tracks). For the “5-4” and “5-3” events, the determined error scale factor values turn out to be smaller than the “5-5” error scale factor value. These smaller values represent weighted averages of the “5th-axial” tracking errors and the non-“5th-axial” tracking errors, and since the non-“5th-axial” tracking errors are typically two or three times larger than the errors for the “5th-axial” tracks (see figure 8.12), it is the non-“5th-axial” tracking errors which are presumed to be the dominant errors in these events. This method thus comes very close to determining the error scale factor for the “4th-axial” and the “3rd-axial” tracks, since it is the non-“5th-axial” tracking errors which are the dominant ones during error propagation. However, the values which are actually determined are weighted averages of the two tracks. Since the determined “5-4” and “5-3” error scale factors are smaller than the “5-5” error scale factor, and the numbers are weighted averages, then since the “5-5” error scale factor is larger than the “5-4” and “5-3” values then the actual “4th-axial” and “3rd-axial” error scale factors are believed to be slightly smaller than the “5-4” and “5-3” weighted values which this analysis determines. Ultimately, the actual “4th-axial” and “3rd-axial” error scale factor values are of no concern, because this analysis uses the weighted average error scale factor values for each of the combined “5-4” and the “5-3” classifications, and it is believed that this is a reasonable way to proceed with this analysis. For one thing, it is significantly better than the usual method of applying a universal error scale factor correction to all of the events, for all types of tracks, regardless of which axial superlayers were missed by a given track.

8.3.2 Final Determination of the Error Scale Factors According to their Track Classifications

Monte Carlo events are generated using a range of trial error scale factors (from 1.60 to 3.00 in increments of 0.05, for a total of 29 trial error scale factors). Approximately one million Monte Carlo events are generated for each trial error scale factor. Both the data and the Monte Carlo events are separated into three groups according to each event's track classification ("5-5", "5-4" and "5-3"). Z mass histograms are created for the data and also for each Monte Carlo trial error scale factor, according to the three different track classifications for an event. The bin width used in each histogram is 0.5 GeV.

A chi-squared fit value is then determined [10] by analyzing a histogram of the measured dimuon mass values coupled to a histogram corresponding to a Monte Carlo prediction. The total number of events in the Monte Carlo histogram is matched to the total number of data events. An individual chi-squared value can be determined for each bin. The chi-squared for a bin is defined as:

$$\chi^2 = \frac{(data\ events - predicted\ events)^2}{predicted\ events}$$

[46]

The individual bin chi-squareds are added together to give a total chi-squared value for the entire fit. Chi-squared values are determined over varying fit ranges (mainly to verify that the results do not depend on the relatively unpopulated Z mass tails). Five fit ranges are used. The "TINY" fit range spans 80 to 100 GeV. The "NARROW" fit range spans 70 to 110 GeV. The "MEDIUM" fit range spans 60 to 120 GeV. The "WIDE" fit range spans 50 to 130 GeV. And the "MAX" fit range spans 40 to 140 GeV.

For a given track classification a chi-squared value between the data and the Monte Carlo is thus determined not only for each of the twenty-nine trial error scale factors but also for each of the five fit ranges. Curves are then generated for the different chi-squareds as a function of the trial error scale factors (an example is shown in figure 8.13, which is the "5-5" track resolution chi-squared vs trial error scale factor plot for the "MEDIUM" fit range), and a parabolic fit of degree five is performed using a minimization routine called MINUIT [12] to determine the most likely trial error scale factor. The fit also returns the "error" in the determined error scale factor, but this "error" is only valid if the errors in the chi-squared values are themselves valid.

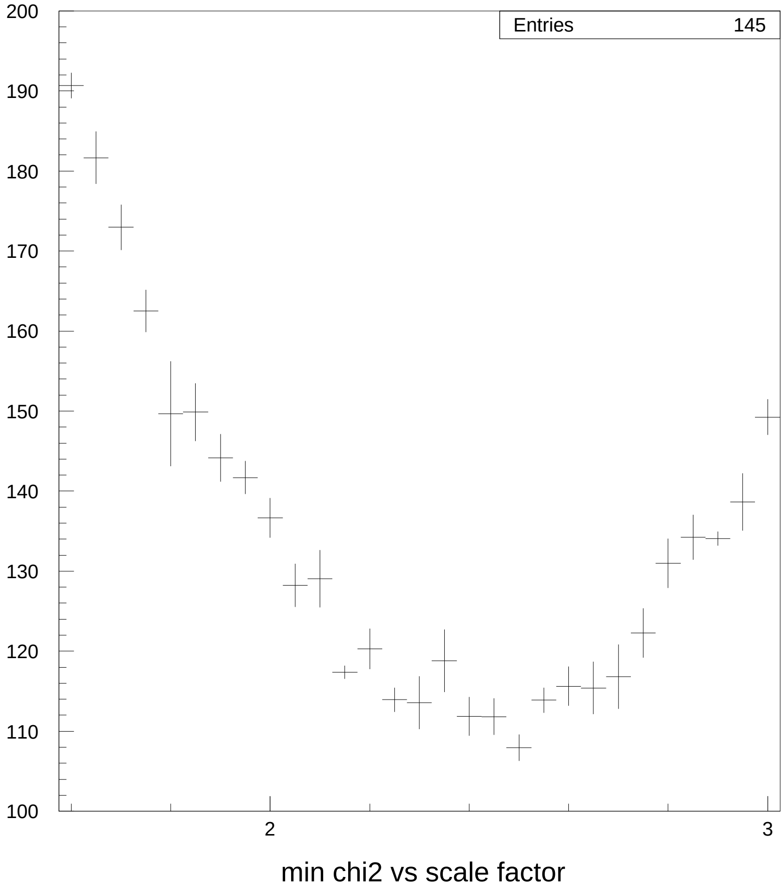

Figure 8.13: Chi-squared value versus trial error scale factor, “5-5” MED fit

As more and more Monte Carlo events are generated, the error in the final chi-squared values decrease. However, the user resources were not unlimited, and one million Monte Carlo events per trial error scale factor meant that the final chi-squareds did not lie on a smooth curve (as is readily apparent in figure 8.13). This jitter stems from the statistics in the Monte Carlo histograms, and it must be understood if the error in the minimum is to be determined correctly. To understand the jitter each set of individual trial error scale factor Monte Carlo events is divided into five equal-sized groups. A chi-squared value is determined for each of these five sub-groups of Monte Carlo events, and the average chi-squared is determined as well as the RMS in the chi-squared. The RMS values are the errors in each average value of chi-squared. If you look at figure 8.13 you will see that the total number of entries is 145 (which is five times twenty-nine, twenty-nine being the total number of trial error scale factors) and the error bars are of varying heights, indicating the random uncertainty involved in repeating each measurement five times. The MINUIT curve fit takes the error bars for each of the 29 data points into account when it determines the best fit curve, which presents one final problem here. The chi-squared RMS values are themselves inaccurate since only five data points are used per trial error scale factor, meaning that a MINUIT best fit curve will be biased to pass closely to points which have lower chi-squared RMS values (and hence smaller error bars). This in turn would cause an incorrect fit to be determined, since the relative error bar heights are fairly random in nature (since so few data points were used). For example, in figure 8.13 the error bars (and hence the chi-squared RMS values) for a scale factor of 2.90 are noticeably smaller than their neighbors, and a MINUIT best fit curve would therefore be biased to pass too closely to this point (a point where the RMS values had fluctuated low). This potential problem is solved by first determining the average RMS value for all of the trial error scale factors, and graphs like figure 8.13 are replotted using this average chi-squared error for all of the data points (each error bar is therefore the same height, and a MINUIT determined best fit curve will then not be biased to pass closer to some points over others). The best fit curve estimate performed by MINUIT will then return not only the correct minimum, but also a dependable error estimate in the returned minimum. The curve which is fitted is a polynomial of degree five, and an example (the replot of figure 8.13) can be seen in figure 8.14. Note that the error bars are now all the same height.

The determined best fit curve is then used to determine the error in the error scale factor. The one-sigma confidence region for the error scale factor occurs when the value of chi-squared has increased by 1 unit above its minimum value [11]. This is determined via a short computer program which uses the polynomial of degree 5 fitted values as its input, and it returns the plus and minus one-sigma values for the error scale factor. An analysis of the best fit curve in figure 8.14 finds a minimum chi-squared of 111.904 which occurs at an error scale factor of $2.4391^{+0.0934}_{-0.0934}$. In the end, the size of the error bars in figure 8.14 did not affect the uncertainty in the determined error scale factor, since the steepness of the minimum chi-squared was what was used to determine that value. However, MINUIT did return the errors in the polynomial fitted values, and a rough check was performed which verified that the uncertainty in the MINUIT-fitted polynomial values did indeed result in the same uncertainty in the determined error scale factor that the steepness of the chi-squared curve generated.

Figure 8.15 shows the determined error scale factors in graphical form as a function of fit range type (TINY, NARROW, MEDIUM, WIDE or MAX). Table 8.3 shows a complete compilation of the all the relevant information found at the best fit curve's minima. As can be seen, the determined error scale factors are consistent across all possible fit ranges, but differ amongst the three dimuon track classifications. The average error scale factor as well as the average error are the definitive values which will be used in the rest of the analysis. Table 8.4 shows the final determined values of interest. Figure 8.16 is an updated version of figure 8.12, where the errors are believed to have been scaled correctly.

8.4 Monte Carlo Representation of the Axial Superlayers

After the error scale factors had been determined the next task was to create a Monte Carlo data set which contained simulated data which had the correct fraction of "5-5", "5-4"

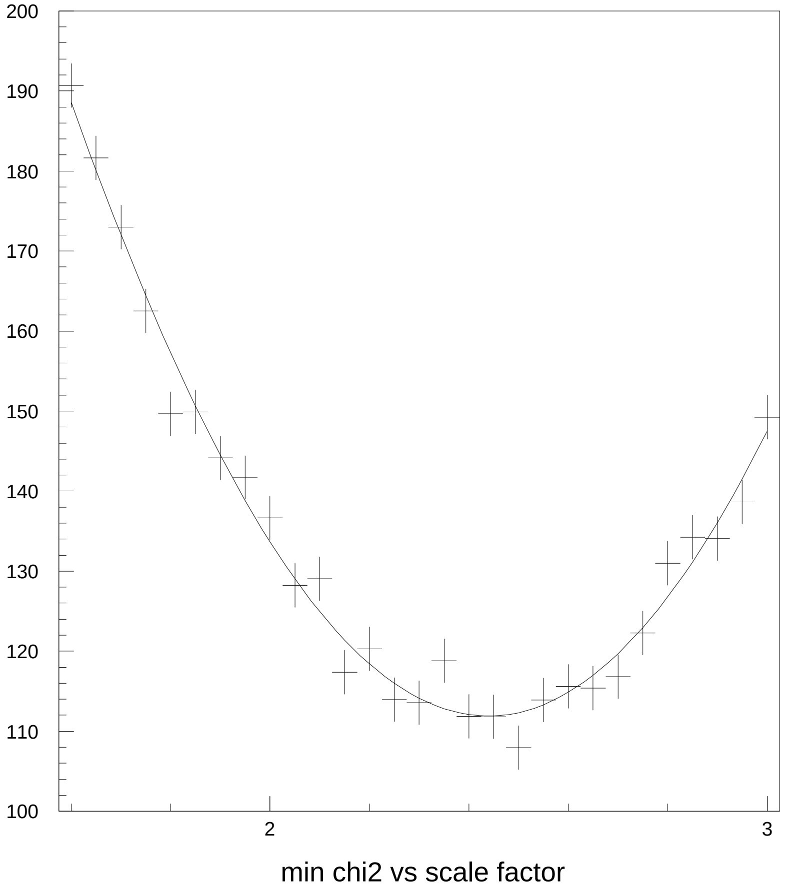

Figure 8.14: MINUIT best fit curve, “5-5” MED fit with correct error bars

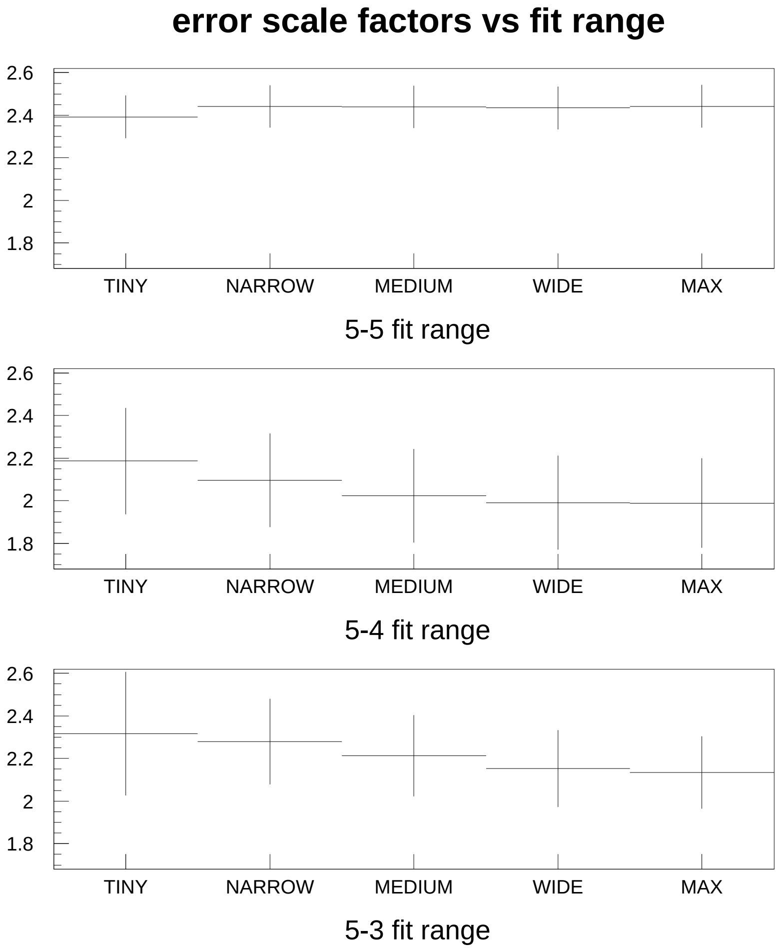

Figure 8.15: error scale factors as a function of the fit range, for the three track classifications

fit range	mass range (GeV)	total bins	dimuon classification	minimum chi-squared	determined error scale factor
TINY	80-100	40	5-5	30.07	$2.393^{+0.104}_{-0.104}$
TINY	80-100	40	5-4	25.65	$2.186^{+0.256}_{-0.217}$
TINY	80-100	40	5-3	33.36	$2.316^{+0.304}_{-0.264}$
NARROW	70-110	80	5-5	68.72	$2.442^{+0.098}_{-0.098}$
NARROW	70-110	80	5-4	59.14	$2.096^{+0.226}_{-0.220}$
NARROW	70-110	80	5-3	83.10	$2.279^{+0.210}_{-0.202}$
MEDIUM	60-120	120	5-5	111.90	$2.439^{+0.093}_{-0.093}$
MEDIUM	60-120	120	5-4	82.57	$2.023^{+0.226}_{-0.222}$
MEDIUM	60-120	120	5-3	111.10	$2.213^{+0.196}_{-0.191}$
WIDE	50-130	160	5-5	236.52	$2.435^{+0.095}_{-0.096}$
WIDE	50-130	160	5-4	97.89	$1.991^{+0.224}_{-0.215}$
WIDE	50-130	160	5-3	124.17	$2.152^{+0.184}_{-0.179}$
MAX	40-140	200	5-5	331.93	$2.442^{+0.102}_{-0.101}$
MAX	40-140	200	5-4	105.49	$1.989^{+0.219}_{-0.208}$
MAX	40-140	200	5-3	129.65	$2.135^{+0.179}_{-0.174}$

+	one sigma upper limit
-	one sigma lower limit

Table 8.3: Determined error scale factors according to dimuon classification and fit range

track classification	error scale factor
5-5	$2.4300^{+0.099}_{-0.098}$
5-4	$2.0571^{+0.230}_{-0.216}$
5-3	$2.2190^{+0.215}_{-0.202}$

+	one sigma upper limit
-	one sigma lower limit

Table 8.4: Final error scale factors according to track classification

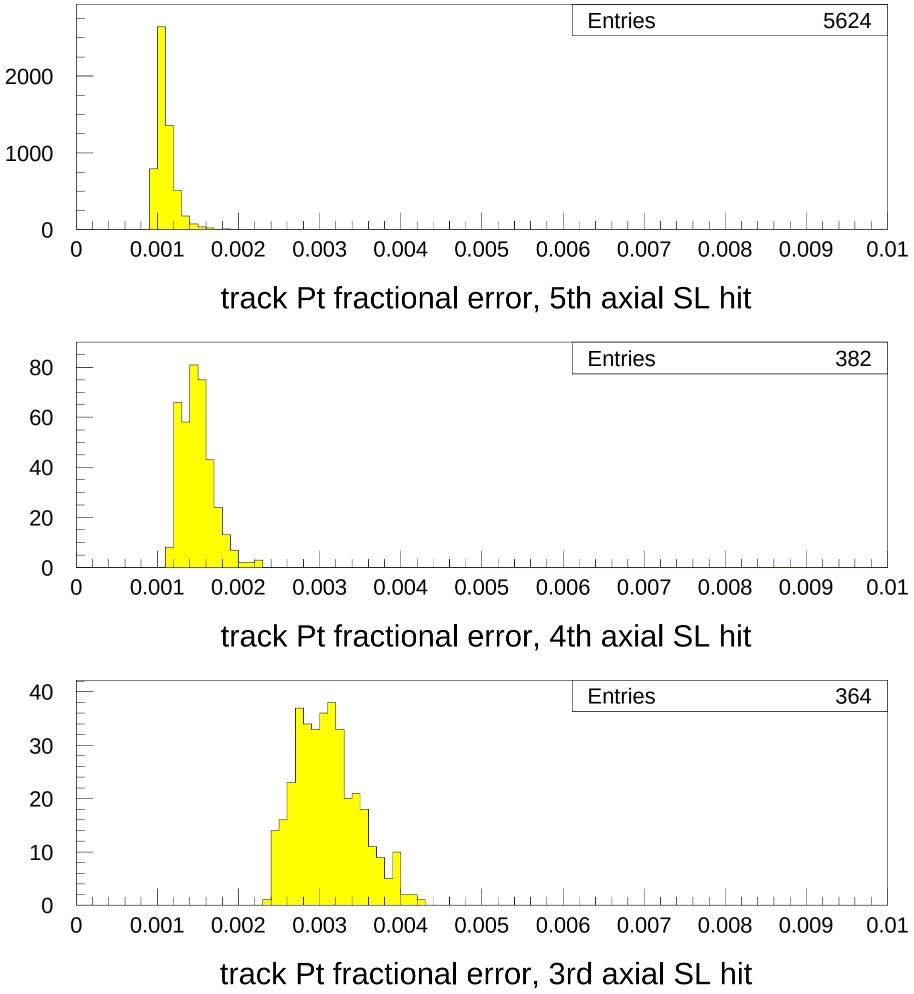

Figure 8.16: track Pt fractional errors according to track resolution classification, after errors have been scaled

and "5-3" events. The routine CMUOTR [29] was used to predict which superlayers a track would pass through, and since it had already been tuned so that the simulation matched the data as closely as possible, this routine was integrated into the CDF Monte Carlo in order to accomplish this.

The basic remaining difference between the CDF Monte Carlo simulation and the data is that the CDF Monte Carlo simulation does not take chamber inefficiency into account. In the CDF Monte Carlo simulation all detectors are 100% efficient. This is of course not the case. It is a relatively simple task to make efficiency cuts after the fact (via a simple random number generator) in order to determine whether or not a given simulated Monte Carlo event would have been reconstructed and detected properly in real life (on the average), and this is what is done. For example, the efficiency for each trigger region was determined previously and, for each simulated muon, a random number is used to determine if the simulated muon would have passed the trigger. Additional random numbers are generated to take into account the level 2 prescaling and the associated prescaling correlations, which effectively turned different trigger regions on and off for different periods of time during data taking. It is also necessary to take into account run 1a and run 1b effects on the Monte Carlo data set. There were some known dead CMU and CMX chambers which are included in the simulation, and dead chambers differed between runs 1a and 1b. Through a thorough understanding of the detector the final Monte Carlo simulation should accept events in the same way the detector did in real life. It is hoped that similar distributions of muon tracks will be obtained from the simulation that appear in the data, whether the muons be "gold" or "silver", whether they be at low or at high eta, and whether the corresponding trigger region be U, P, X or I.

However, the CTC poses added complexities. First, the CTC chamber inefficiency results in a worsening of the resolution of some tracks in the data. For example, if a generated track is pointed towards the last axial superlayer (a low-eta central track) then 100% of the time the CDF Monte Carlo simulation will cause that track to register hits in all of the CTC superlayers, and the track resolution in the CDF Monte Carlo simulation will be excellent. However, from studying the data it is known that sometimes one or more of the superlayers which a given track passes through will not register a hit. Consequently, a track's measured resolution can be worse than what the corresponding CDF Monte Carlo simulation track resolution would be for a track traveling along an identical trajectory. Therefore, the simplistic addition of a random number generator to the Monte Carlo to determine whether or not a track registered hits in a given axial superlayer is insufficient for this analysis, because the CDF Monte Carlo will have already used the zero-missed-superlayers hit information to determine the track's resolution, and if the random number generator predicts that the track would have failed to register a hit in an important superlayer, then the CDF Monte Carlo's track resolution will be erroneously more precise than it should otherwise be.

Second, the higher eta tracks which do not pass through all layers of the CTC are problematic because events with high-eta tracks essentially piggyback their way into the final data set due to the presence of a low-eta (eta less than 1.0) triggering central muon. The low eta ("5th axial") offline track reconstruction efficiency at CDF is well-known to be $99.7^{+0.1}_{-0.1}\%$ [33] and was verified using high Pt electrons and the CDF calorimeter. However, at higher eta the track reconstruction efficiency drops off sharply. This rapid efficiency reduction is mostly due to the fact that tracks at higher eta miss the outer more efficient axial superlayers and consequently the probability that such a track is reconstructed is reduced, because of a greater reliance on the less efficient inner axial superlayers. The Z muon data set was used to determine the efficiency of each axial superlayer, and the individual axial superlayer efficiencies are shown in table 8.5. It should be noted that these figures do not include the track reconstruction inefficiency, since only events where both tracks have already been successfully reconstructed can be used. These figures were then used, via some simple mathematical combinatory, to determine the efficiency of the 3-of-5 axial superlayers hit requirement which is imposed in this analysis after the offline track reconstruction has been performed. Hit inefficiency correlations between the superlayers was determined to be unimportant. For example, it seemed quite plausible that if no hit

axial superlayer	efficiency (%)
0	$84.8^{+0.6}_{-0.7}$
2	$95.0^{+0.4}_{-0.4}$
4	$99.3^{+0.2}_{-0.2}$
6	$99.8^{+0.2}_{-0.1}$
8	$99.8^{+0.2}_{-0.1}$

Table 8.5: Individual axial superlayer hit efficiency

was registered in superlayer 0 then there was a greater likelihood that no hit would be registered in superlayer 2 (for example, if there was a lot of debris hitting the wires in superlayer 0, the same debris might be hitting the wires in superlayer 2 as well, and hence it seemed plausible that tracks which failed to register a hit in superlayer 0 would be more likely to fail to register a hit in superlayer 2). A correlation was indeed found. However, the correlation was very small and its effect was consequently quite minor and did not need to be taken into account. Table 8.6 shows the overall efficiency of the 3-of-5 axial superlayers hit requirement for the three different CMUOTR predicted track classifications. As can be seen, requiring three axial superlayer hits is almost 100% efficient for tracks predicted to pass through all five axial superlayers, approximately 99% efficient for tracks predicted to miss the outermost axial superlayer, and only about 80% efficient for tracks predicted to miss the last two axial superlayers (meaning that the three axial superlayers the track did pass through would all have to register hits for the track to pass the cut).

Note that the values in these tables do not include any additional inefficiency inherent in the offline track reconstruction itself. As has been stated the offline track reconstruction efficiency is well known for the low-eta tracks. However, many events reach the final data set because of a high-eta muon track which has a different topology from the low-eta tracks which were able to be carefully studied in previous chapters. The number of events which make it into the final data set which contain a high-eta muon (the CMUOTR predicted “5-4” and “5-3” events) depend partly on the track reconstruction efficiency for

CMUOTR predicted track classification	efficiency (%)
5th axial	$99.99^{+0.0}_{-0.1}$
4th axial	$99.1^{+0.2}_{-0.2}$
3rd axial	$80.6^{+0.6}_{-0.7}$

Table 8.6: Overall CTC 3-of-5 axial superlayers hit efficiency

the high eta tracks, and a study to determine this would be ideal. This is the crux of the problem. The higher-eta track reconstruction inefficiency is not well-known, especially with regards to the track classification definitions which are used in this analysis. Any misunderstood inefficiency in the lower statistic high-eta track reconstruction efficiency would affect the final Monte Carlo data set in an unpredictable way. The high Pt muon data set, on its own, is insufficient to conduct such a study. It is assumed that a study with electrons could be performed to determine the relevant track reconstruction efficiency values. However, there is a reasonable alternative which this analysis utilizes. It was decided to tune the Monte Carlo simulation in such a way that the fraction of events which contained a high-eta muon relative to the events which contained two low-eta central muons matched the corresponding ratio found in the data. This had to be done twice, once for the "5-4" events relative to the "5-5" events, and once for the "5-3" events relative to the "5-5" events.

This coincidentally solved several nagging problems simultaneously. For example, the superlayer boundary positions in the CDF Monte Carlo simulation did not match the data perfectly. Although it was possible to tune the routine CMUOTR, and then be able to accurately predict which axial superlayers a given track would register hits in (the individual axial superlayer efficiencies notwithstanding), a modification in the CMUOTR prediction had no effect on the corresponding CDF Monte Carlo track resolutions, and consequently the CDF Monte Carlo track resolutions were usually incorrect near the superlayer boundaries. By simply tuning the final Monte Carlo low-eta and high-eta event fractions to be the same as the data, it was possible to remove groups of events which obviously did not match the data and replace them (when necessary) with events which did match the data. For example, events from regions of phase space where the CDF Monte Carlo simulation returned a too-precise track resolution (which was typical at the CTC superlayer boundaries) were removed and replaced with events from nearby regions of phase space which had already been removed through the normal Monte Carlo event selection process. Whenever something like this was done, replaced events were always chosen from nearby in phase space, to ensure that the event topology was not being altered in some systematic way. A more standard Monte Carlo acceptance method would have been to accept tracks (and ultimately an entire event) at rates which corresponded to the overall efficiencies for that track's phase space (taking into account the trigger and the track reconstruction efficiencies, for starters). However, with the method which was employed, some known deficiencies in the CDF Monte Carlo simulation could actually be overcome.

8.5 Monte Carlo Representation of the Integrated Luminosity

Each detector region was either live, prescaled (meaning that the trigger was not live for that event), or not working. There were three trigger regions ("U", "P" and "X"). A gold muon was classed as either "Ug", "Pg" or "Xg". Each Z event had either one or two gold muons. A silver muon was classed as either "Us", "Ps", "Xs", "I5", "I4" or "I3" (the "I" classifications correspond either to tracks which were pointed at holes in the muon coverage, or else to tracks which were pointed at a muon detector region which was deemed not to be working for the run in question). Each Z event had either zero or one silver muon. This resulted in a total of 27 different possible configurations of a dimuon trigger. The different sets of known dead chambers in runs 1a and 1b increased this total by a factor of 2.

Of the 27 possible trigger configurations within each run, many simply never happened. For example, the "P" trigger was never prescaled (reducing the total combinatorics

run	integrated luminosity pb^{-1}	configuration classification	U status	P status	X status
1a	5.22	1	live	live	live
1a	13.36	2	live	live	broken
1a	0.77	3	live	broken	prescaled
1b	29.05	1	live	live	live
1b	4.38	4	live	live	prescaled
1b	0.24	5	live	broken	live
1b	5.97	6	prescaled	live	live
1b	0.10	3	live	broken	prescaled
1b	49.26	7	prescaled	live	prescaled
1b	0.03	8	prescaled	live	broken
1b	0.02	9	prescaled	broken	live
All	**108.40**				

Table 8.7: Integrated luminosities for each trigger configuration

from 27 to 18). Additionally, at least one of the triggers had to be working. Also, a necessary precondition for the "P" trigger to be working was that the "U" trigger was not broken. Three predominant trigger configurations were identified for run 1a, and a total of nine trigger configurations were identified for run 1b. Table 8.7 summarizes the integrated luminosities for each possible trigger configuration. This table is an expanded version of table 7.27.

8.6 Monte Carlo Representation of the Single Muon High Pt Selection Efficiencies

The relevant live, broken, and prescaled integrated luminosities were then coded into the Monte Carlo simulation. The Monte Carlo was set up in such a way that the single muon high Pt selection efficiencies could be varied, as desired.

Millions of events were generated using Pythia and then simulated using this modified Monte Carlo. If the simulation was accurate then the events which passed the simulation should have very similar characteristics to the 3,176 dimuon event data set.

Of the events which passed the simulation, the Monte Carlo assigned the primary track one of three possible classifications, triggered "U", triggered "P", or triggered "X". The secondary track was assigned one of eleven possible classifications, triggered and non-triggered "U" (5th axial), triggered and non-triggered "P" (5th axial), triggered and non-triggered "X" (5th axial) and also 4th axial "X" and 3rd axial "X", 5th axial "I", 4th axial "I" and finally 3rd axial "I". Since there were so few 4th and 3rd axial "X" tracks, it was decided to reclassify them as 4th and 3rd axial "I" tracks. The combinatorics (taking into account duplicate definitions) resulted in a total of twenty-four different ways to classify a dimuon event.

First, the effect of setting all of the high Pt muon trigger selection efficiencies to 100% was studied. Table 8.8 shows the number of events in each of the 24 dimuon classifications for 62,653 Z events which passed this configuration of the Monte Carlo simulation. Some explanation of table 8.8 is warranted. The first row of table 8.8 is "U U", and almost all of these events (1,148 out of 1,168) were "double gold" events. The reason a small number of these events are not "double golds" is that the selection cuts require that the measured track parameters be highly correlated to the measured chamber hits. Consequently, since the simulation reproduces the tracking measurement errors, then it is to be expected that not all of the simulated tracks will result in simulated triggers. From the numbers in the table, the Monte Carlo selection efficiency in the "U" region is $99.14^{+0.20}_{-0.24}\%$, in the "P" region it is $99.90^{+0.03}_{-0.03}\%$, and in the "X" region it is $99.34^{+0.15}_{-0.19}\%$. These efficiency values by chance are all close to the 5th axial track-finding efficiency of 99.7%, which is the selection efficiency that is impossible to determine using only muon data. This similarity makes it possible to ignore the effect of the track-finding efficiency (for 5th axial tracks). The second row of table 8.8 is "P U", and approximately half of these events are not "double gold" events. This is to be expected since approximately half of the time the "U" trigger was prescaled (the "P" trigger was never prescaled).

primary region	secondary region	total "5-5" events	total double golds	5th G-S	4th G-S	3rd G-S
U	U	1,168	1,148	20		
P	U	3,437	1,638	1,799		
X	U	679	561	118		
U	P	1,639	1,638	1		
P	P	6,923	6,909	14		
X	P	3,798	3,795	3		
U	X	665	561	104		
P	X	8,788	3,795	4,993		
X	X	1,304	1,287	17		
U	I	4,847	0	4,847	1,120	1,282
P	I	15,592	0	15,592	4,942	5,711
X	I	4,060	0	4,060	1,287	1,405
ALL	**ALL**	**46,906**			**7,349**	**8,398**

Table 8.8: Monte Carlo Z events classed by secondary leg for a 100% efficient muon trigger

Next, the previous data-determined high Pt single muon selection efficiencies (see table 7.29) are incorporated into the Monte Carlo simulation. These values were $68.78^{+2.61}_{-2.84}\%$ for the "U" trigger region, $76.25^{+1.64}_{-1.74}\%$ for the "P" trigger region, $68.27^{+2.07}_{-2.10}\%$ for the "X" trigger region, and $94.4^{+1.2}_{-1.5}\%$ for the "silver" selection cuts (these data-determined selection efficiencies are only applicable for 5th axial tracks). Table 8.9 shows the resulting event distribution classifications, using the same initial group of 62,653 Z events from table 8.8. When the actual data-determined high Pt single muon selection efficiencies are used within the Monte Carlo 47,577.2 events pass (this figure represents approximately three-quarters of the events which pass when the muon chambers are set to 100% efficiency in the Monte Carlo).

The simulated event totals are then normalized to the data according to the secondary track's CMUOTR predicted axial classification. The 3,176 Z events contained 2,445 "5-5" events, 372 "5-4" events, and 359 "5-3" events (see table 8.2). The results are shown in table 8.10.

A comparison of the dimuon classification populations between the Monte Carlo

primary region	secondary region	total "5-5" events	total double golds	5th G-S	4th G-S	3rd G-S
U	U	1,021.48	543.08	478.40		
P	U	2,522.05	859.04	1,663.01		
X	U	452.34	263.42	188.92		
U	P	1,112.28	859.04	253.24		
P	P	6,389.24	4,016.94	2,372.30		
X	P	2,558.32	1,975.52	582.80		
U	X	446.52	263.42	183.10		
P	X	6,436.23	1,975.52	4,460.71		
X	X	1,137.15	599.84	537.31		
U	I	3,147.08	0	3,147.08	770.34	881.76
P	I	11,223.12	0	11,223.12	3,768.27	4,354.64
X	I	2,616.54	0	2,616.54	878.63	959.19
ALL	**ALL**	**35,964.37**			**5,417.24**	**6,195.59**

Table 8.9: Monte Carlo Z events classed by secondary leg for the previosuly DATA-determined U, P and X muon trigger efficiencies

primary region	secondary region	total "5-5" events	total double golds	5th G-S	4th G-S	3rd G-S
U	U	69.44	36.92	32.52		
P	U	171.46	58.40	113.06		
X	U	30.75	17.91	12.84		
U	P	75.62	58.40	17.22		
P	P	434.37	273.09	161.28		
X	P	173.92	134.30	39.62		
U	X	30.36	17.91	12.45		
P	X	437.56	134.30	303.26		
X	X	77.31	40.78	36.53		
U	I	213.95	0	213.95	52.90	51.09
P	I	762.99	0	762.99	258.77	252.33
X	I	177.88	0	177.88	60.34	55.58
ALL	**ALL**	**2,445**			**372**	**359**

Table 8.10: Normalized Monte Carlo Z events classed by secondary leg for the previosuly DATA-determined U, P and X muon trigger efficiencies

and the Data is then made to verify that the Monte Carlo is generating the appropriate fractions. Figure 8.17 shows each of the normalized twenty-four Monte Carlo event classification populations (logarithmic histogram), along with the number found in the Z data set (crosses). The first bin is titled "UgUg", which represents events which have primary tracks with a gold muon in the "U" trigger region and secondary tracks with a gold muon also in the "U" trigger region. The second bin "UgUs" represents events with similar primary tracks, but the secondary track in this case consists of muons located in the "U" trigger region which pass the silver cuts but not the gold cuts. The final bin "XgI3" represents events which have primary tracks with a gold muon in the "X" trigger region, and secondary tracks not located in any working trigger region (hence the "I" for CMI) (in this case they are "3rd axial" tracks). The agreement between the Monte Carlo and the data appears to be excellent.

A test of how well the Monte Carlo and the data agree involves determining an overall value of chi-squared. The chi-squared value for an individual bin is defined as:

$$\chi^2 = \frac{(data\ events - predicted\ events)^2}{predicted\ events}$$

The individual chi-squareds are added together to determine an overall chi-squared value for the entire fit. In this case the overall chi-squared value is 47.6. This is a little large, since the expected overall chi-squared value is 21 (24 bins minus the three normalization constraints). A large part of the discrepancy originates with the "UgI5" bin, where the number of data events is less than the number of Monte Carlo events by approximately 3.5 sigma (representing a contribution to the overall chi-squared of approximately 12).

This brings up an interesting observation. Bins containing events such as "UgI5" have only one triggering muon. Events which can have at most one triggering muon were not used during the determination of the different muon trigger efficiencies, because such a sample of events does not lend itself to unbiased trigger efficiency studies. The best way to determine the muon trigger efficiencies would be to use as many events as possible. With the implementation of the Monte Carlo, it becomes possible to use all of the events to determine

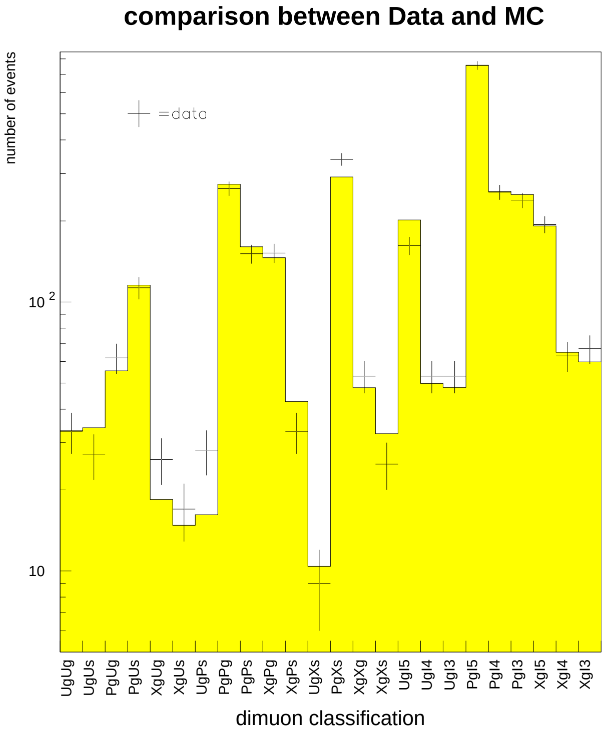

Figure 8.17: Muon classification population differences between the Monte Carlo and the Data for Data-measured selection efficiencies

primary region	secondary region	total "5-5" events	total double golds	5th G-S	4th G-S	3rd G-S
U	U	67.32	33.24	34.08		
P	U	170.86	55.50	115.36		
X	U	33.23	18.44	14.79		
U	P	71.70	55.50	16.20		
P	P	434.11	273.96	160.15		
X	P	188.57	145.95	42.62		
U	X	30.36	18.44	10.40		
P	X	437.56	145.95	291.19		
X	X	77.31	48.00	32.41		
U	I	213.95	0	201.69	49.81	48.55
P	I	762.99	0	759.27	257.22	253.08
X	I	177.88	0	191.75	64.97	60.38
ALL	**ALL**	**2,445**			**372**	**359**

Table 8.11: Normalized Monte Carlo Z events classed by secondary leg for the Monte Carlo determined U, P and X muon trigger efficiencies

the muon trigger efficiencies. This is done by performing a minimum chi-squared fit. All of the muon selection efficiencies are varied and many Monte Carlo histograms of the dimuon classifications are obtained. The chi-squared value between the dimuon classifications in the data histogram and each of the Monte Carlo histograms is determined. The most likely values for the efficiencies correspond to when the value of chi-squared is a minimum.

Table 8.11 shows the dimuon classification populations after the minimum chi-squared fit is performed (and after the three axial normalizations have been made).

Figure 8.18 shows each of the normalized twenty-four Monte Carlo event classification populations (logarithmic histogram), along with the number found in the Z data set (crosses). The agreement (using the Monte Carlo minimum chi-squared fit method to determine the selection efficiencies) is better than if the selection efficiencies are data-determined (see figure 8.17). Whereas the overall chi-squared value was 47.6 using the data-determined selection efficiencies, it is reduced to 37.4 if the selection efficiencies are determined using the Monte Carlo.

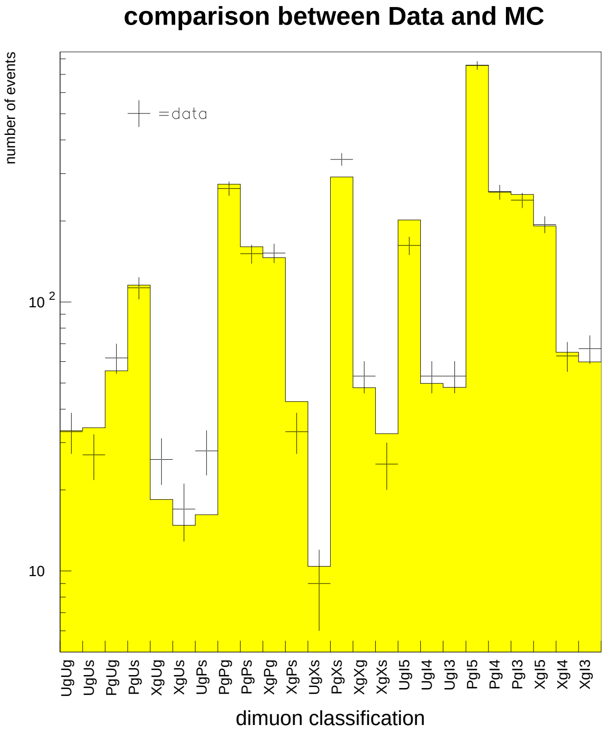

Figure 8.18: Muon classification population differences between the Monte Carlo and the Data for Monte Carlo-measured selection efficiencies

fiducial region	data-measured selection efficiency	Monte Carlo measured selection efficiency
U	68.78	65.9
+	2.61	2.9
-	2.84	2.8
P	76.25	76.7
+	1.64	1.2
-	1.74	1.4
X	68.27	75.2
+	2.07	2.6
-	2.10	2.6
Silver Cuts	94.4	92.3
+	1.2	4.4
-	1.5	4.2

Table 8.12: Summary of selection efficiency measurements.

Table 8.12 shows the updated Monte Carlo determined selection efficiencies, compared to the previously determined data-measured selection efficiencies. The errors in the Monte Carlo determined selection efficiencies are found by varying each selection efficiency until the overall chi-squared value increases by one unit of chi-squared. The biggest change is the CMX selection efficiency, which has increased by about two sigma over the previous data-determined value. All other selection efficiencies and their errors are approximately the same as before.

Figure 8.19 shows, for each of the twenty-four dimuon classifications, the sigma difference between the predicted number of Monte Carlo events and the number of events found in the data. The overall agreement is very good. There are three bins with close to 3-sigma effects. There are too many “UgPs” events (28 detected versus 16.2 predicted), too many “PgXs” events (339 detected versus 292.0 predicted), and too few “UgI5” events (162 detected versus 204.9 predicted). While the agreement between the Monte Carlo and the data is much better than it was ever thought could be achieved, these nagging small differences have no definitive explanation. It is believed that better results might be obtained if the integrated luminosity values (which are fixed) were varied in much the same

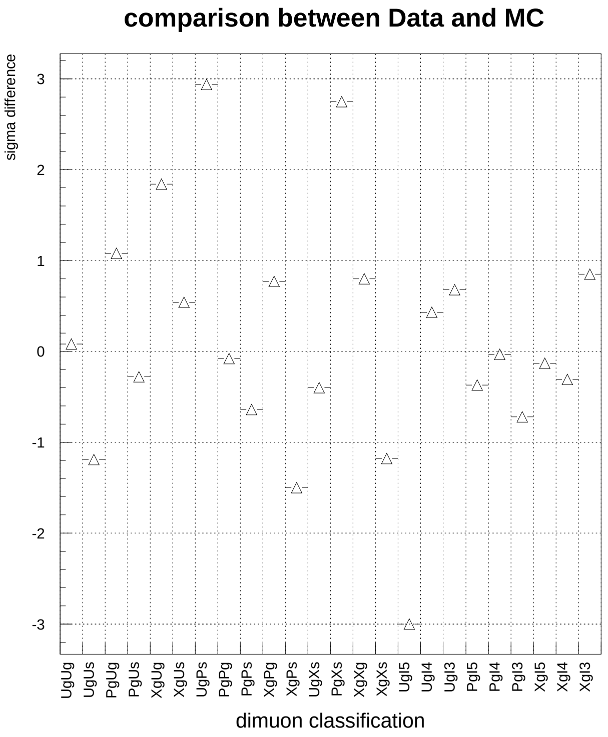

Figure 8.19: Sigma difference between the final Monte Carlo and the Data, according to dimuon classification

way that the selection efficiencies were varied. However, because of the interdependencies of the integrated luminosities, and because of the fact that the agreement between the Monte Carlo and the data is considered to be excellent, no attempt was made to investigate these insignificant discrepancies further.

8.7 Monte Carlo Representation of the Z Mass

All previously determined values are integrated into the final version of the Monte Carlo. These include the selection efficiencies for each muon system, the error scale factors for the different ways to classify a Z event, each muon detector's live, prescaled and broken time fractions (these are cross-referenced with the live, prescaled and broken time fractions for each of the other muon detectors), and the "tuned" boundary positions of the CTC axial superlayers. Additional modifications not previously mentioned include the addition of some code to simulate the fact that a couple of CMU and CMX wedges were not working (different wedges had problems depending on whether the run was 1a or 1b). Every effort is made to get the correct acceptance for events of type “5-5” in the simulation. For example, the track reconstruction efficiency for this class of events is integrated into the Monte Carlo simulation. The “5-4” and “5-3” events are a different matter. As has been explained above, certain regions of phase space are not allowed in the simulation because the CTC detector simulation represents the transitions at axial superlayer boundaries as a sharp step from precisely measured tracks inside the boundary to poorly measured tracks just outside. Also, the track reconstruction efficiency for the higher eta “4th” and “3rd” axial tracks is unknown, as has been explained previously, making it impossible to set up an accurate simulation. For these classes of events the number of events in the simulation is scaled to match the number of events in the data. As a consequence, it is not necessary to integrate into the simulation the correct values for the track reconstruction efficiency. However, based on the reduction in phase space due to the non-allowed CTC phase space regions, coupled with the required normalization factor relative to the normalization required to scale the “5-5” events correctly, the track reconstruction efficiency for 4th and 3rd axial tracks is estimated to be 85-90% (compare this figure to 99.7% for “5th” axial tracks). This figure is not used in this analysis, but is included here simply for completeness.

Millions of events were generated using Pythia and then simulated using this modified Monte Carlo. If the simulation was accurate then the events which passed the simulation should have had very similar characteristics to the 3,176 dimuon event data set.

Figure 8.20 shows the difference between the Monte Carlo and the data for the different track resolution classifications. The Monte Carlo has been normalized to the data (there were 2,430 5-5 events, 381 5-4 events and 365 5-3 events, as defined by which axial superlayers registered hits within the CTC). As can be seen, the agreement between the monte carlo and the data is excellent for all track resolution classifications. A slight overall mass shift is observed for the 5-4 events. While not important for the Z Pt analysis, it is nevertheless an interesting observation.

Figure 8.21 shows the overall difference between the Monte Carlo and the data when all of the track resolutions are combined together. Here, the data events are subtracted from the Monte Carlo events, to make it easier to understand how the two curves differ. The total chi-squared value obtained after comparing the two histograms ia approximately one per degree of freedom. Hence, the agreement between the data and the Monte Carlo is regarded as excellent.

8.8 Monte Carlo Representation of the Z Pt

The Z Mass spectrum is very well-known, and if the different detector efficiencies, luminosities, and tracking resolutions could be determined accurately, then a Monte Carlo would be expected to reproduce good agreement with the observed Z mass spectrum. In the previous section a Monte Carlo which incorporated a full detector simulation was able to precisely duplicate the observed Z mass spectrum. However, the Z Pt spectrum is not all that well-known, and hence it will not be surprising if there are noticeable discrepancies for the Z Pt spectrum between the Monte Carlo and the Data.

8.8.1 Discrepancies Between the Monte Carlo Z Pt and the Data Z Pt

Figure 8.6 shows the measured Z Pt distribution. There are a very large number of events at low Z Pt, and a small number of events at higher Z Pt values. In order to make the histograms easier to study, irregular sized binning is used. Instead of using an x-axis with bin widths corresponding to equal GeV energy ranges, the Pt histogram is replotted with bins which span different GeV ranges. The bin widths are chosen to be small at small Z Pt values, and large at large Z Pt values. With the new x-axis bin widths, it is possible to get a better understanding of the behavior of the spectrum of events as a function of Pt

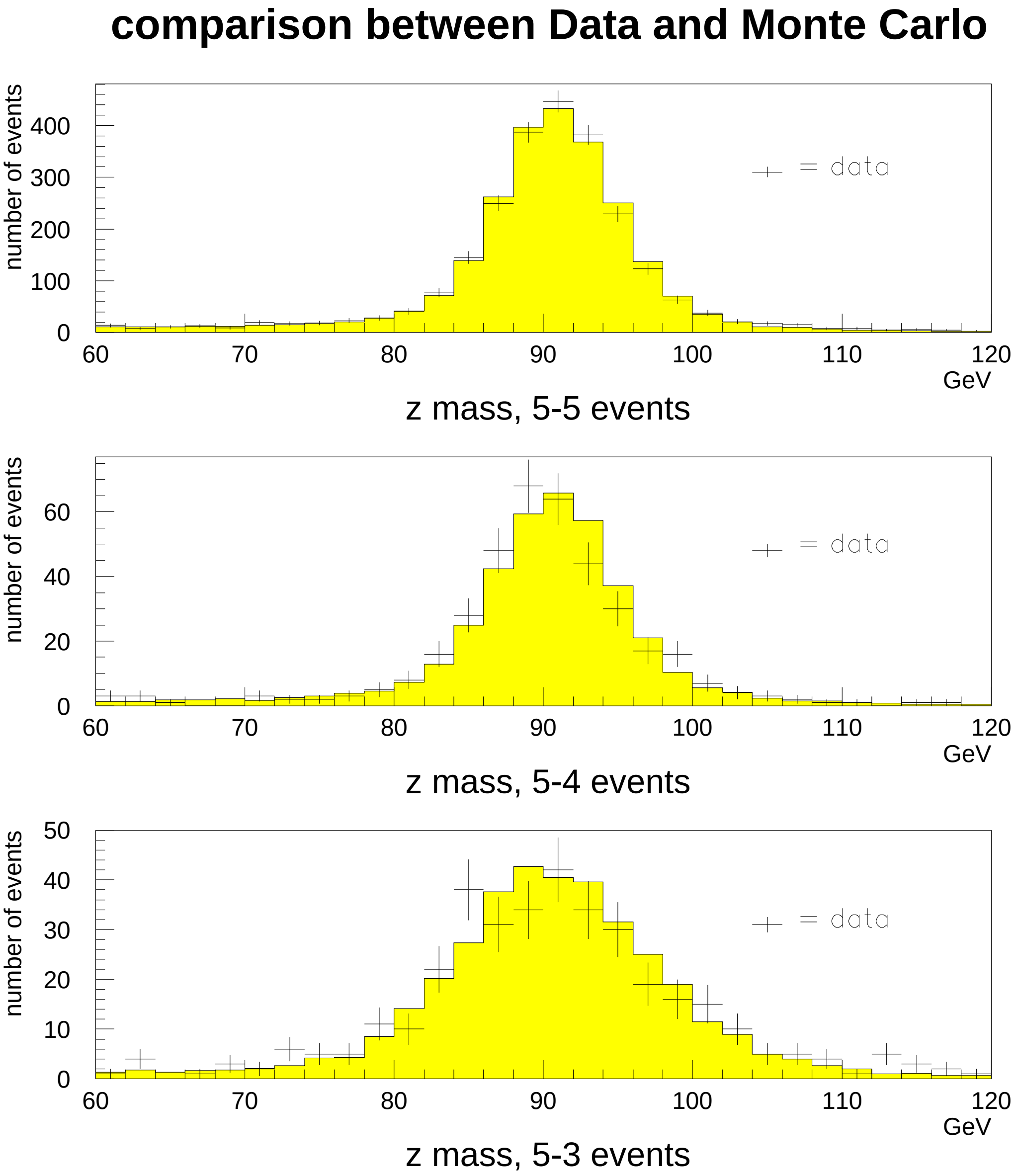

Figure 8.20: Difference between data and MC for 5-5, 5-4 and 5-3 events

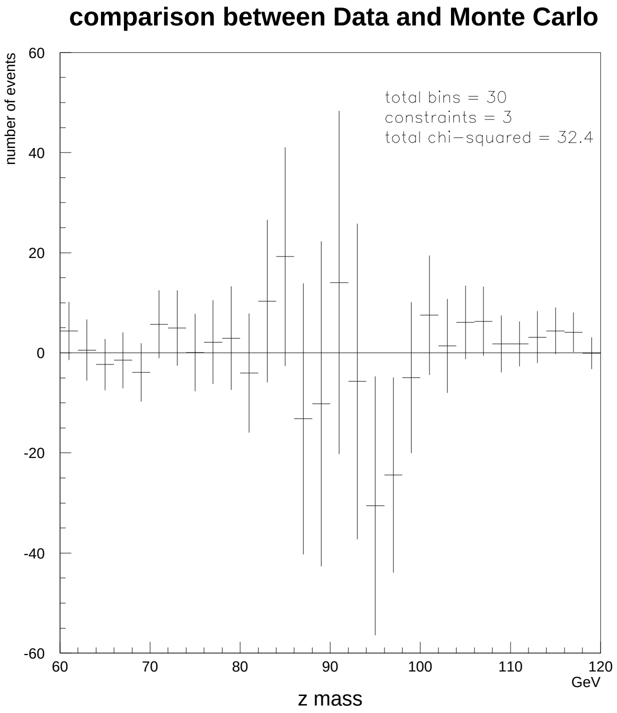

Figure 8.21: Overall difference between data and MC: data events minus Monte Carlo events

simply by looking at the plot because the vertical axis does not need to be as compressed as with constant bin widths.

Table 8.13 defines the bins which are used. (These irregular bins are the same bins that were used in the CDF Z Pt differential cross-section in the electron channel paper [42], except that the last, largest bin in this data set was not defined in the previous data set because the maximum Z Pt value in the previous data set was not as large as the maximum Z Pt value found in this analysis). Figure 8.22 shows a histogram of the Z Pt for all 3,176 events in the final data set. The top plot shows the first 30 bins with a linear y-axis, and the bottom plot shows a logarithmic plot of the entire spectrum. The graphs have irregular shapes mainly because the x-axis has irregularly sized bins.

Pt Bin	Delta-Pt (GeV/c)	Events Observed
1	0.0 - 0.5	18
2	0.5 - 1.0	36
3	1.0 - 1.5	73
4	1.5 - 2.0	85
5	2.0 - 2.5	106
6	2.5 - 3.0	109
7	3.0 - 3.5	130
8	3.5 - 4.0	142
9	4.0 - 4.5	113
10	4.5 - 5.0	108
11	5.0 - 5.5	92
12	5.5 - 6.0	99
13	6.0 - 6.5	90

continued on next page

Pt Bin	Delta-Pt (GeV/c)	Events Observed
14	6.5 - 7.0	111
15	7.0 - 7.5	94
16	7.5 - 8.0	84
17	8.0 - 8.5	73
18	8.5 - 9.0	81
19	9.0 - 9.5	78
20	9.5 - 10.0	70
21	10.0 - 10.5	76
22	10.5 - 11.0	58
23	11.0 - 11.5	64
24	11.5 - 12.0	51
25	12.0 - 13.0	96
26	13.0 - 14.0	100
27	14.0 - 15.0	69
28	15.0 - 16.0	80
29	16.0 - 17.0	64
30	17.0 - 18.0	47
31	18.0 - 19.0	52
32	19.0 - 20.0	43
33	20.0 - 22.0	83
34	22.0 - 24.0	73
35	24.0 - 26.0	62
36	26.0 - 28.0	51
37	28.0 - 30.0	36
38	30.0 - 34.0	55

continued on next page

Pt Bin	Delta-Pt (GeV/c)	Events Observed
39	34.0 - 38.0	50
40	38.0 - 42.0	33
41	42.0 - 46.0	26
42	46.0 - 50.0	18
43	50.0 - 60.0	33
44	60.0 - 70.0	22
45	70.0 - 80.0	9
46	80.0 - 90.0	7
47	90.0 - 100.0	9
48	100.0 - 125.0	5
49	125.0 - 150.0	7
50	150.0 - 200.0	4
51	200.0 - 300.0	1

Table 8.13: Z Pt binning

Figure 8.23 shows the Monte Carlo predicted number of events in each bin overlaid with the number of events found in the Data (these graphs use irregular bins defined in [41]) for each of the different track resolutions. As can be seen, there is excellent apparent agreement for each of the track resolutions. However, differences are noticeable if the data event totals are subtracted from the Monte Carlo prediction totals. Figure 8.24 shows the differences for each of the track resolutions, and figure 8.25 shows the combined plot (all events, where the bins are defined in [41]). There are slightly too few data events at low Z Pt (below around 7 GeV), slightly too many data events in the 7-20 GeV range, and above around 20 GeV the number of data events in each bin roughly matches the number of events predicted by the Monte Carlo (although the number of data events continues to remain on the high side).

8.8.2 Tuning Pythia

The observed discrepancies between the Data and the Monte Carlo imply that this version of the Monte Carlo is unsatisfactory for predicting accurately the Z Pt distribution.

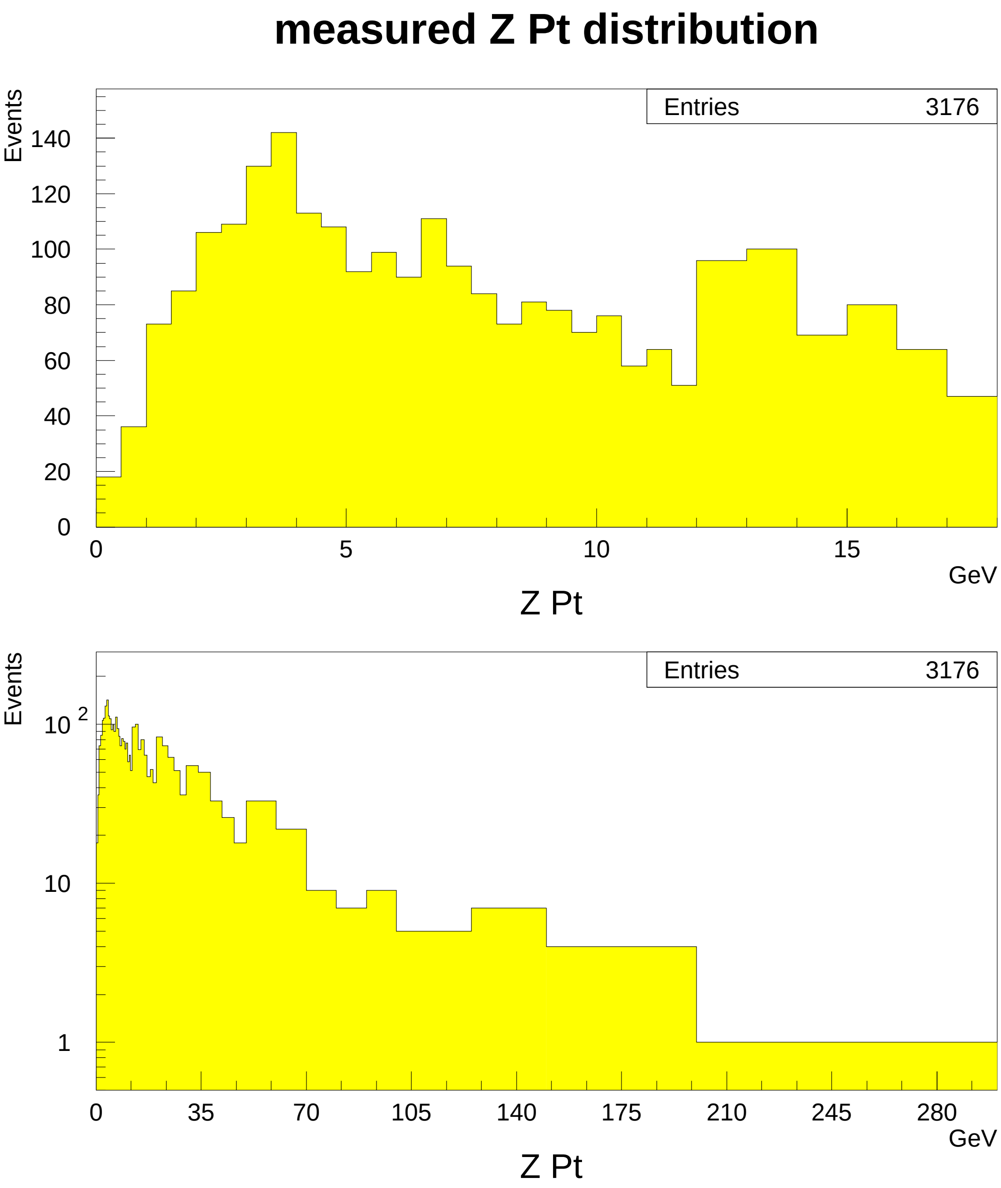

Figure 8.22: Z Pt distribution using irregular binning

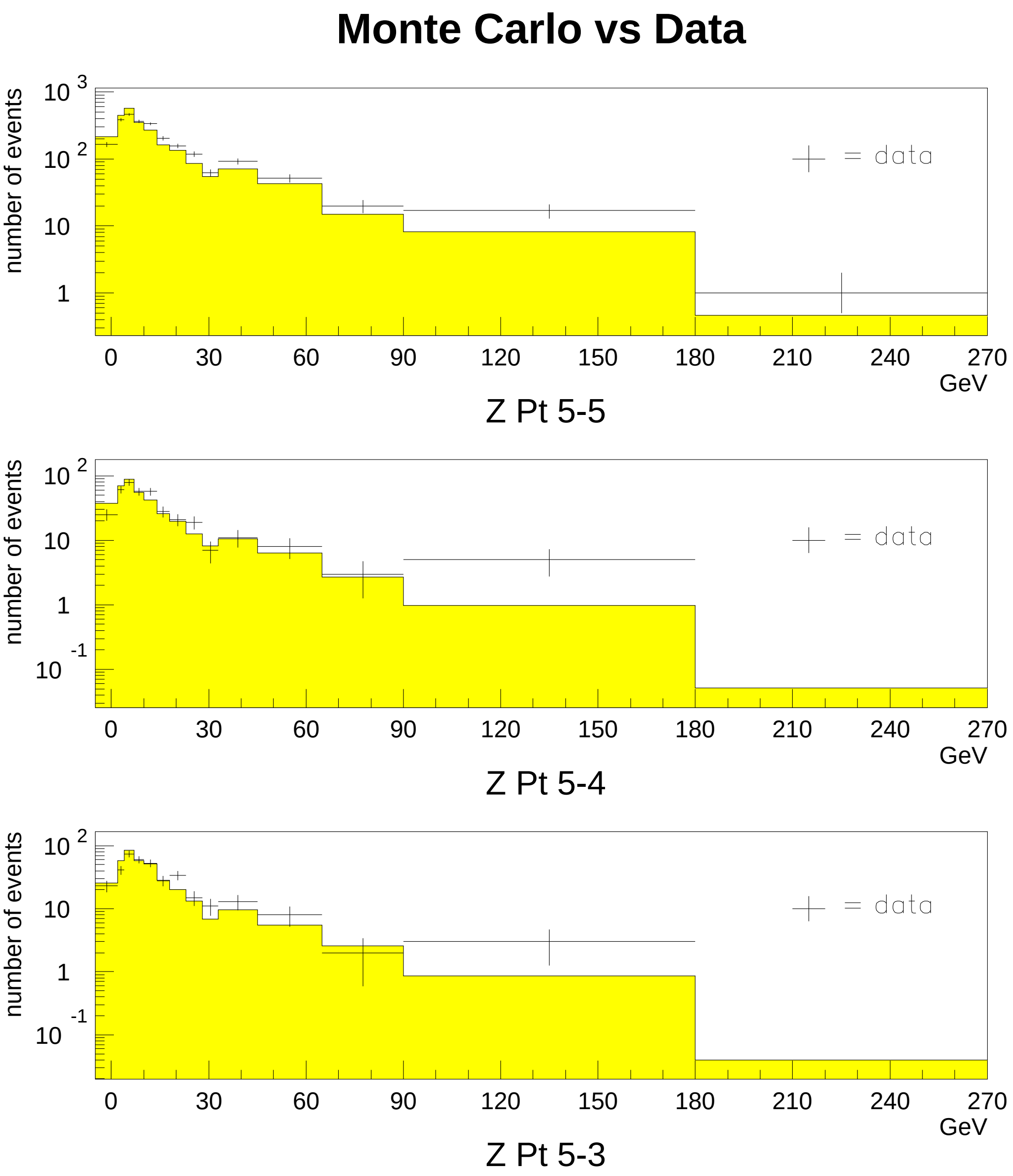

Figure 8.23: Difference between data and MC for 5-5, 5-4 and 5-3 events

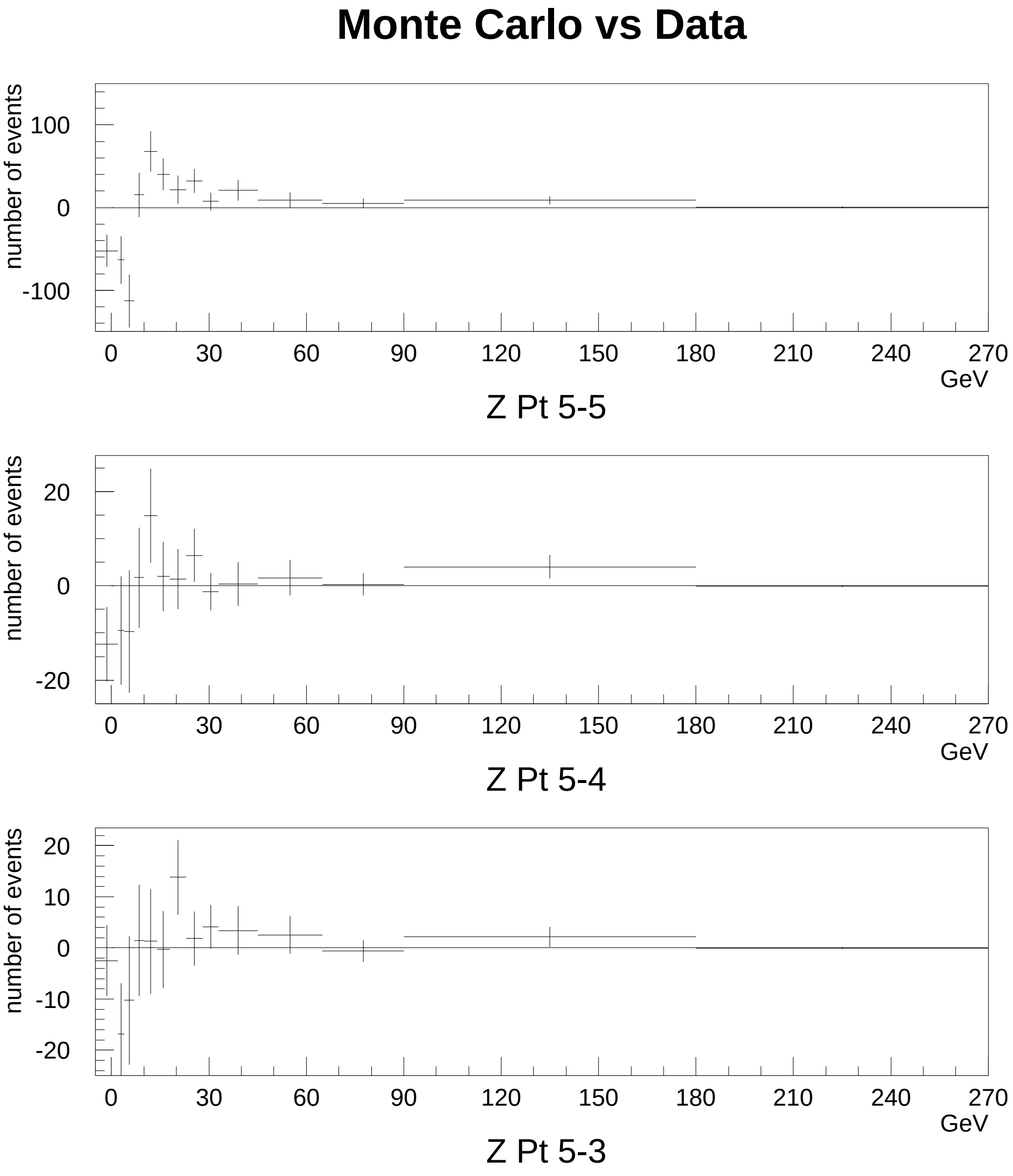

Figure 8.24: Overall difference between data and MC; data events minus Monte Carlo events

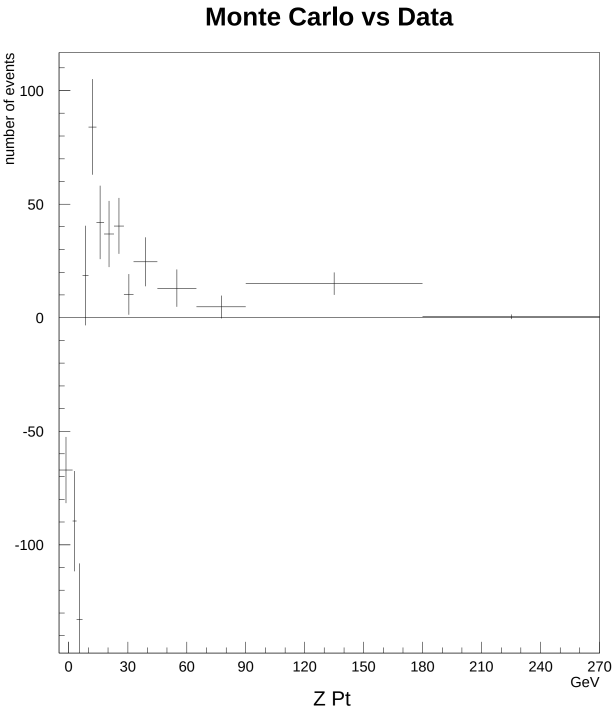

Figure 8.25: Overall difference between data and MC; data events minus Monte Carlo events

Since the Monte Carlo is believed to correctly simulate the detector response, it is believed that the discrepancies must originate at the event generation level.

The Pythia manual states the following. *"The initial-state algorithm in Pythia is not quite as sophisticated as the final-state one. This is partly because initial-state radiation is less well understood theoretically, partly because the programming task is more complicated and ambiguous."* Pythia is a versatile event generator. It is possible to change the shape of the generated Z Pt distribution by adjusting any of several tuning parameters. When the parameters are tuned correctly then the higher order calculations which Pythia does not attempt to perform have been approximated.

There are four Pythia parameters which are tuned in this analysis in order to approximate the Z Pt distribution which, after going through the detector response simulation, results in a smeared and accepted Monte Carlo Z Pt distribution which matches the data-measured distribution.

They are called PARP62, PARP64, PARP91 and PARP93. They affect the Z Pt shape, but have no noticeable affect on the Z mass shape.

PARP64 affects the squared transverse momentum evolution scale in parton-shower development for use as a scale in alpha-s and parton distributions, for jets which recoil against the Z boson. This parameter was tuned to a value of 0.20. This parameter primarily affected the relative height of the peak of the Z Pt distribution. The higher the peak, the more the peak moved to lower values of Z Pt.

PARP62 is an effective cut-off of the transverse momentum evolution scale, below which parton showers are not evolved. This parameter was tuned to a value of 3.25. This parameter primarily affected a region below and on the right side of the Z Pt peak. The value as tuned slightly broadened the distrbution both below and on the right side of the Z Pt peak by removing events from higher up the Z Pt curve (while still to the right of the Z Pt peak).

PARP91 affects the width of a Gaussian primordial transverse momentum evolution scale inside the colliding hadrons. The partons are given a transverse momentum kt smearing of $(exp(-kt^2/parp(91)^2))kt*d(kt)$. This produces additional smearing of the boson Pt at low Pt. The parameter was tuned to a value of 3.75. This parameter primarily affected the location of the Z Pt peak.

PARP93 is an upper cut-off for the primodial transverse momentum evolution smearing mentioned above. The parameter was tuned to a value of 3.0. This parameter primarily affected the width of the Z Pt peak.

8.8.3 Comparison of the Final Monte Carlo to the Data

Figure 8.26 shows the comparison between the normalized Monte Carlo and the Data, for each of the CMUOTR predicted track resolution classifications. There are 2,445 "5-5" events, 372 "5-4" events, and 359 "5-3" events. On the left of the figure the first 30 bins are shown (the y-axis is linear), and on the right of the figure all the bins are shown (the y-axis is logarithmic). The overall chi-squared for the "5-5" comparison is excellent - there are 51 bins and the total chi-squared is 55. The "5-4" and "5-3" plots have much lower statistics, but they also have reasonable values for chi-squared (83 and 40, respectively).

The fact that the Z Pt spectrum is a rapidly rising and then falling curve makes it preferable to plot the average event Z Pt value as the bin center (rather than each bin's midpoint Z Pt value). Additionally, the fact that the bin sizes are irregular makes it hard for the human eye to compare successive bins meaningfully. This problem is solved by plotting the number of events per GeV, instead of the raw number of events.

Table 8.14 shows the approximate bin centers, as well as the number of observed "5-5" Data events and predicted "5-5" Monte Carlo events (after Pythia tuning) within each bin (here, the Monte Carlo events have been normalized to the Data events). Only the "5-5" event populations are given because the "5-4" and "5-3" events are not included in the final cross-section calculations (since their populations are being scaled relative to the number of events in the "5-5" population). Figure 8.27 shows the corresponding linear graph from 0 to 20 GeV on the left, and a logarithmic graph for the entire spectrum on the right.

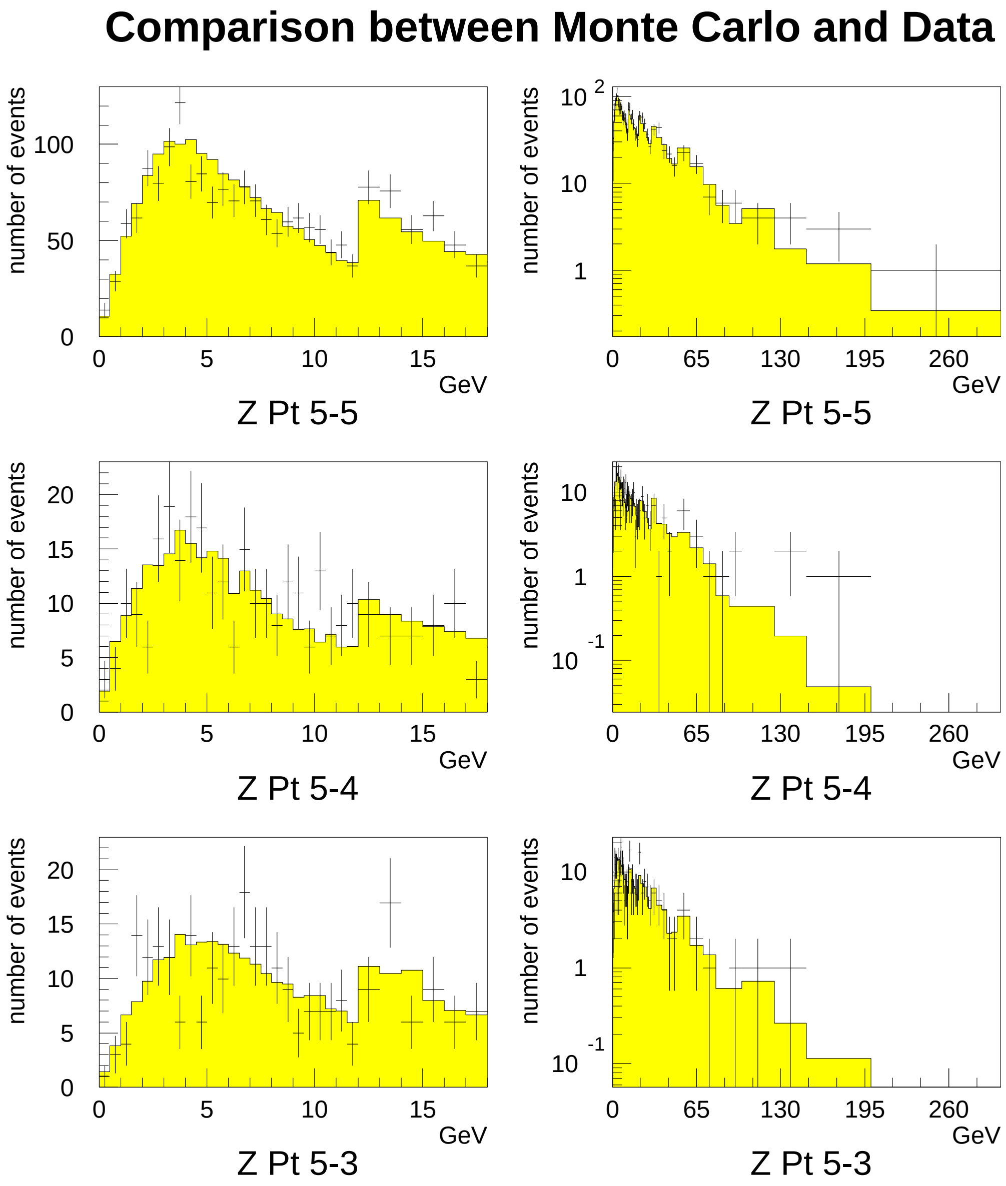

Figure 8.26: Graphs showing the difference between data and MC for each track resolution classification

Pt Bin	Delta-Pt (GeV/c)	Bin Center (Gev/c)	Events Observed	Events observed per GeV	Monte Carlo events per GeV
1	0.0 - 0.5	0.34	14	28	21
2	0.5 - 1.0	0.78	29	58	65
3	1.0 - 1.5	1.27	59	118	105
4	1.5 - 2.0	1.76	62	124	138
5	2.0 - 2.5	2.26	88	176	168
6	2.5 - 3.0	2.75	80	160	190
7	3.0 - 3.5	3.25	99	198	203
8	3.5 - 4.0	3.75	122	244	200
9	4.0 - 4.5	4.25	81	162	205
10	4.5 - 5.0	4.74	85	170	191
11	5.0 - 5.5	5.25	70	140	184
12	5.5 - 6.0	5.74	77	154	169
13	6.0 - 6.5	6.25	71	142	163
14	6.5 - 7.0	6.75	78	156	156
15	7.0 - 7.5	7.24	71	142	145
16	7.5 - 8.0	7.75	61	122	133
17	8.0 - 8.5	8.25	54	108	129
18	8.5 - 9.0	8.74	60	120	115
19	9.0 - 9.5	9.25	62	124	112
20	9.5 - 10.0	9.75	57	114	101
21	10.0 - 10.5	10.25	56	112	95
22	10.5 - 11.0	10.75	44	88	88

continued on next page

Pt Bin	Delta-Pt (GeV/c)	Bin Center (Gev/c)	Events Observed	Events observed per GeV	Monte Carlo events per GeV
23	11.0 - 11.5	11.24	48	96	79
24	11.5 - 12.0	11.74	37	74	77
25	12.0 - 13.0	12.49	78	78	71
26	13.0 - 14.0	13.48	76	76	62
27	14.0 - 15.0	14.50	56	56	55
28	15.0 - 16.0	15.49	63	63	50
29	16.0 - 17.0	16.48	48	48	44
30	17.0 - 18.0	17.49	37	37	43
31	18.0 - 19.0	18.51	39	39	37
32	19.0 - 20.0	19.49	32	32	35
33	20.0 - 22.0	20.98	61	30.5	29.8
34	22.0 - 24.0	22.96	58	29.0	24.3
35	24.0 - 26.0	24.98	49	24.5	19.8
36	26.0 - 28.0	26.96	37	18.5	16.8
37	28.0 - 30.0	28.98	27	13.5	14.5
38	30.0 - 34.0	31.89	42	10.5	11.4
39	34.0 - 38.0	35.96	44	11.0	8.4
40	38.0 - 42.0	39.88	24	6.0	7.0
41	42.0 - 46.0	43.86	22	5.5	4.9
42	46.0 - 50.0	47.95	16	4.0	4.2
43	50.0 - 60.0	54.60	23	2.3	2.6
44	60.0 - 70.0	64.50	17	1.7	1.6
45	70.0 - 80.0	74.61	7	0.7	1.0
46	80.0 - 90.0	84.82	6	0.6	0.6
47	90.0 - 100.0	94.29	6	0.6	0.3

continued on next page

Pt Bin	Delta-Pt (GeV/c)	Bin Center (Gev/c)	Events Observed	Events observed per GeV	Monte Carlo events per GeV
48	100.0 - 125.0	110.12	4	0.16	0.20
49	125.0 - 150.0	138.12	4	0.16	0.07
50	150.0 - 200.0	173.06	3	0.060	0.024
51	200.0 - 300.0	225.91	1	0.010	0.003

Table 8.14: Z Pt binning, bin centers, and number of events observed

8.9 Monte Carlo Tuning Summary

A Monte Carlo that simulated all relevant aspects of the detector was implemented. Of special importance in this analysis was the need to correctly simulate the different tracking resolutions, the different overlapping integrated luminosities for each of the detector regions, as well as the different muon selection efficiencies. In fact, it became possible to use Monte Carlo to independently measure the muon selection efficiencies which had been painstakingly determined in an earlier chapter.

The final Monte Carlo Z mass plots were found to be in excellent agreement with the data. After additional "tuning" at the event generator level, the Monte Carlo Z Pt plots were also found to be in excellent agreement with the data. The lack of any sizeable discrepancy indicates that the detector is fully understood for the purposes of this analysis, and also that there does not appear to be any detectable, previously unknown, physics process present that could affect the final results. This in turn indicates that the Monte Carlo is suitable in the study of the Z Pt spectrum, including the Z Pt differential cross-section spectrum.

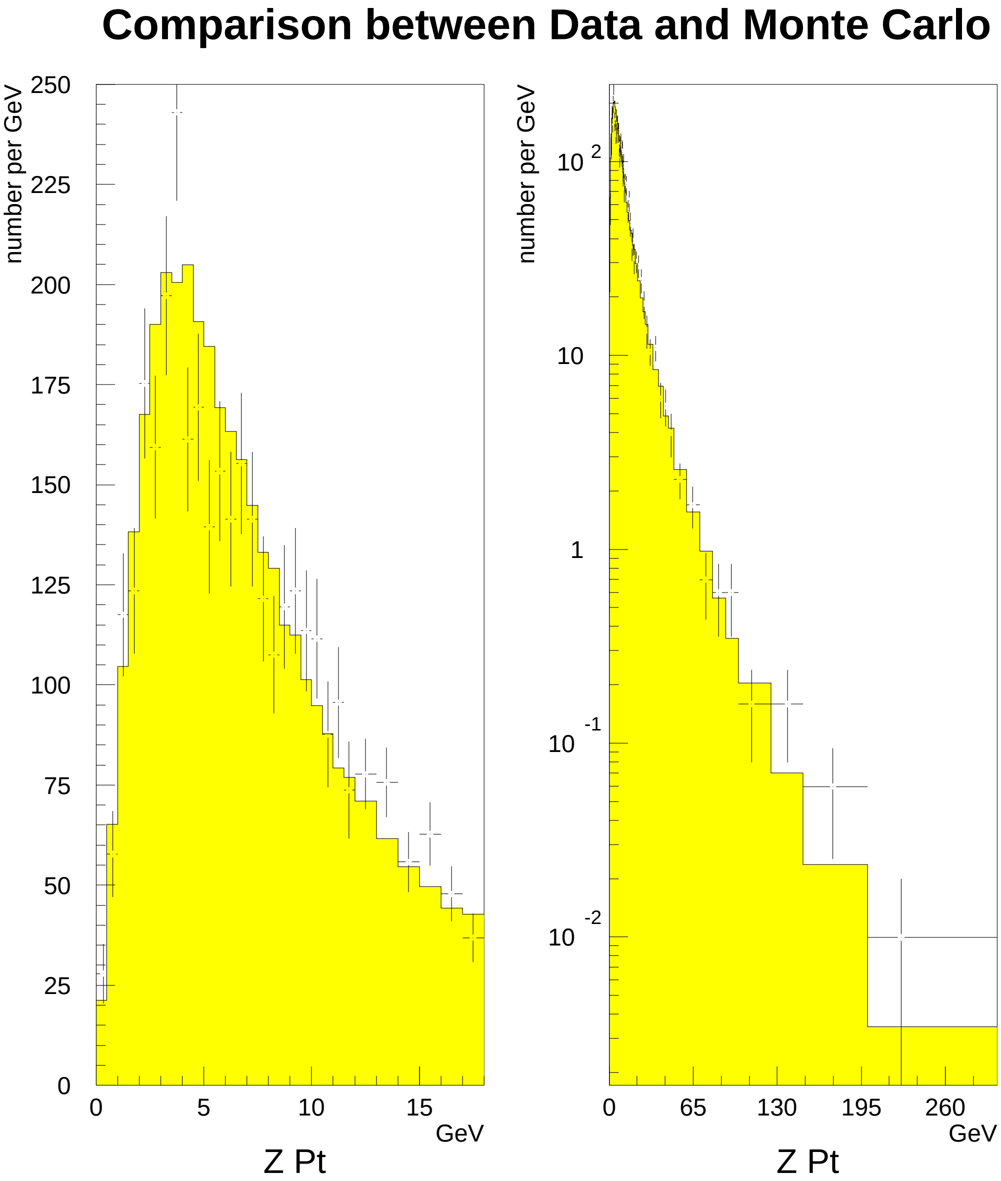

Figure 8.27: Linear graph showing the difference between data and MC

Chapter 9

The Cross-Section Measurements

9.1 The Overall Z Production cross-section in the muon channel

The measured Z production cross-section in the muon channel is given by:

$$\sigma_{Z\longrightarrow\mu^+\mu^-} = \frac{(N_{observed}-N_{background})\times F_Z}{A_Z\times\int\mathcal{L}}, \quad [45]$$

where $N_{observed}$ is the number of observed events, $N_{background}$ is the number of background events, F_Z is a correction factor to account for the fact that a small fraction of the observed events are not Z but Drell-Yan, A_Z is the overall acceptance (this figure includes the selection efficiency) and $\int\mathcal{L}$ is the integrated luminosity.

The "5-5" events are being used in the cross-section measurement. There are 2,445 events in the final "5-5" sample, and there are a total of 25 Z events which fail global event cuts not simulated in the Monte Carlo (the vertex difference cut and the cosmic ray filter). Therefore, $N_{observed} = 2,470$ events (see section 8.3.1).

There are measured to be $13.1^{+}_{-}3.6$ background events in the full 3,176 event dimuon data set (see section 7.7.6). Therefore, normalizing to the "5-5" event total: $N_{background} = 10.1^{+}_{-}2.8$ events

The dimuon mass interval of this measurement is $60 < M_{\mu\mu} < 120$GeV. The factor F_Z is given by

$$F_Z = \frac{\int_{0\ GeV}^{\infty}(Z\ only\ cross\ section)}{\int_{60\ GeV}^{120\ GeV}(Z\ plus\ DrellYan\ cross\ section)} = 1.005 \pm 0.002 \quad [42]$$

The acceptance A_Z (this factor includes the selection efficiency) is determined from the fraction of "5-5" events which pass the final Monte Carlo. In a sample of 674,906 Monte Carlo events, 63,754 pass the Monte Carlo detector simulation, resulting in an overall acceptance fraction of 0.0945 ± 0.0003. The systematic uncertainty in the acceptance is determined by varying the four selection efficiencies ("U", "P", "X", and "I"). When they are simultaneously increased by one sigma (determined in chapter 8), 64,599 of these events pass the Monte Carlo detector simulation, resulting in an overall increased acceptance fraction of 0.0957 ± 0.0003. This increase in the acceptance fraction corresponds to a 1.3% reduction in the cross-section. Hence, the overall acceptance factor A_Z is assigned a systematic error of 1.3% (the statistics error on this value is negligible).

The total integrated luminosity ($\int \mathcal{L}$) used in this analysis (corresponding to when any of the three trigger regions "U", "P" or "X" were live) is 108.4 pb^{-1}. CDF assigns a systematic error on this measurement of 3.9%.

The total $\sigma_{Z \longrightarrow \mu^+\mu^-}$ cross-section is then calculated.

$\sigma_{Z \longrightarrow \mu^+\mu^-} = 241.3 \pm 5.3(stat) \pm 3.4(syst) \pm 10.2(lum)\ pb$

or

$\sigma_{Z \longrightarrow \mu^+\mu^-} = 241.3 \pm 6.3(stat + syst) \pm 10.2(lum)\ pb$

As previously determined, the CDF measurement for the $\sigma_{Z \longrightarrow e^+e^-}$ cross-section is:

$\sigma_{Z \longrightarrow e^+e^-} = 249 \pm 5(stat + syst) \pm 10(lum)\ pb$ [42]

These results differ by 0.96 standard deviations, and therefore they can considered to be in agreement.

9.2 The Raw Z Pt Differential Cross-section

There are two previously stated effects which cause the Z Pt spectrum to change (in shape and amplitude) when the transition is made from the detector-independent spectrum to the detector-measured spectrum.

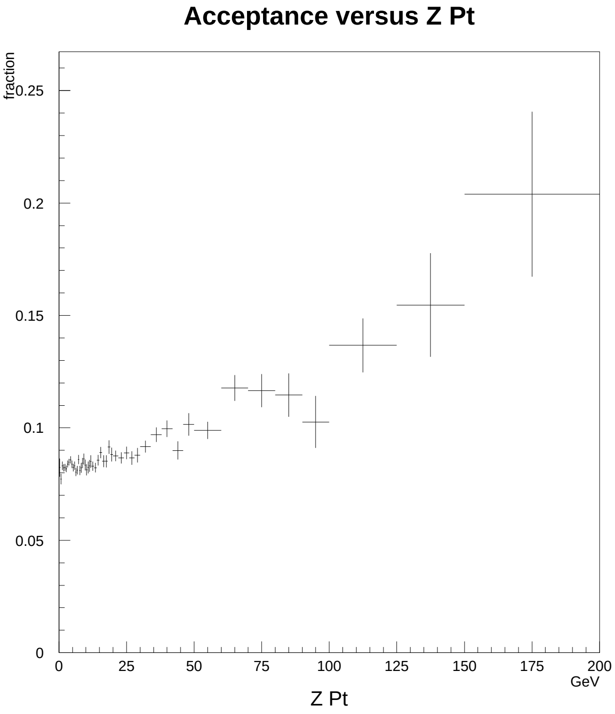

Figure 9.1: Z Pt acceptance

The detector has a varying efficiency at detecting Z events with different Z Pt values. The detector has a larger acceptance for Z events with larger Z Pt values. Hence, in the raw Z Pt histogram there are preferentially more events at larger Z Pt values, because the detector is better at detecting such events. Figure 9.1 shows the Monte Carlo determined acceptance (the selection efficiencies are included in the acceptance) as a function of the Z Pt.

Figure 9.2 illustrates the effect of the acceptance on the shape of the Z Pt spectrum (since the accepted events are normalized to the generated events, the large loss of events is not shown). This plot is made prior to the effect of the tracking measurement errors (only generated Z Pt values are used). The crosses represent the Monte Carlo accepted spectrum.

The tracking measurement errors have very little impact on the total number of accepted events, but they do affect the overall shape of the detector-measured spectrum by

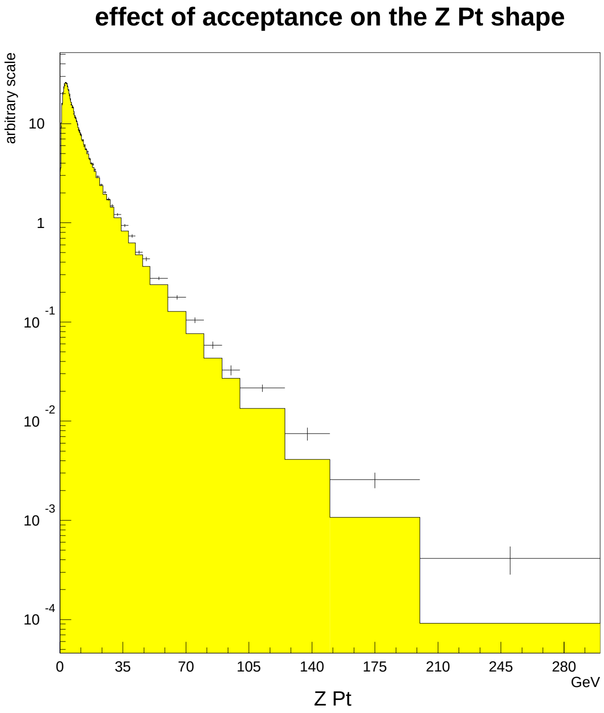

Figure 9.2: effect of the acceptance on the Z Pt shape

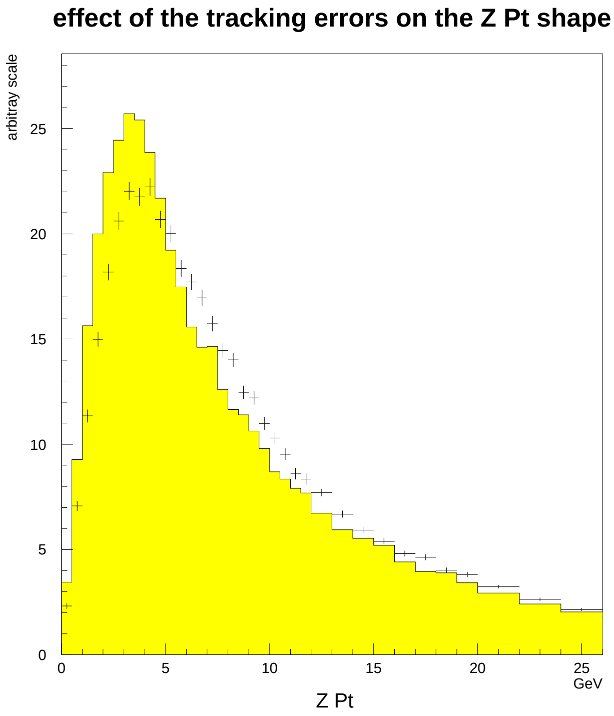

Figure 9.3: effect of the tracking errors on the Z Pt shape

smearing it. The region where the shape changes most noticeably is near the Z Pt peak, as shown in figure 9.3. The histogram is comprised of Monte Carlo generated Z Pt values for events which pass the detector simulation. The crosses are comprised of the Monte Carlo measured Z Pt spectrum.

What is desired is to create a detector-independent plot corresponding to the production of Z events with specific Z Pt values, as opposed to a detector-dependent plot corresponding to the number of Z events which are detected at CDF with measured Z Pt values. As a result of the extensive tuning of both the Pythia generator as well as of the CDF detector simulation, the Pythia generated Z Pt spectrum corresponds to this detector-independent curve. By setting the area under the number-per-GeV curve equal to the overall Z production cross-section, the muon Z Pt differential cross-section plot is produced.

Figure 9.4 shows the detector-independent Z Pt spectrum. On the left is a linear plot showing the well-populated low-Pt region, and on the right is a logarithmic plot. The y-axis units are pb/GeV. Only Monte Carlo statistical errors are shown in this plot.

9.3 The Z Pt Differential Cross-section Errors

It is necessary to determine the systematic errors for the differential cross-section spectrum above. Earlier in this chapter the systematic error for the overall Z production cross-section was determined to be 1.3% for the combined acceptance and selection efficiency measurement and other CDF analyses quote a 3.9% systematic error for the integrated luminosity measurement. The statistical error for the overall Z production cross-section was 2.0%. For the Z Pt differential cross-section, however, the spectrum is dependent on both the measured error scale factor and the tuning of Pythia. As can be seen above in figure 9.3, the shape of the measured Z Pt spectrum depends on the degree to which the tracking errors have been adjusted. This in turn affects the shape of the Pythia-tuned Z Pt spectrum, otherwise the Monte Carlo accepted and smeared spectrum will not match the data-measured spectrum.

To determine the dependency of the Z Pt differential cross-section on the tracking error scale factor, the following is observed. The event differences for various Monte Carlo parameterizations are compared. The smeared Z Pt event totals when the error scale factor is set to its nominal value (2.45) are subtracted from the generated event totals (the error scale factor is zero in this case, since the tracking errors are zero), and figure 9.5 is produced. This graph exhibits a shape which is indicative of how the Z Pt spectrum changes if the error scale factor increases.

The error scale factor for "5-5" events is then increased by one sigma (to 2.55) and the Monte Carlo is rerun. Figure 9.6 shows the original Monte Carlo measured distribution (histogram) overlaid with the modified Monte Carlo measured distribution (crosses). The curves are similar, although there is a noticeable difference in their distributions (which

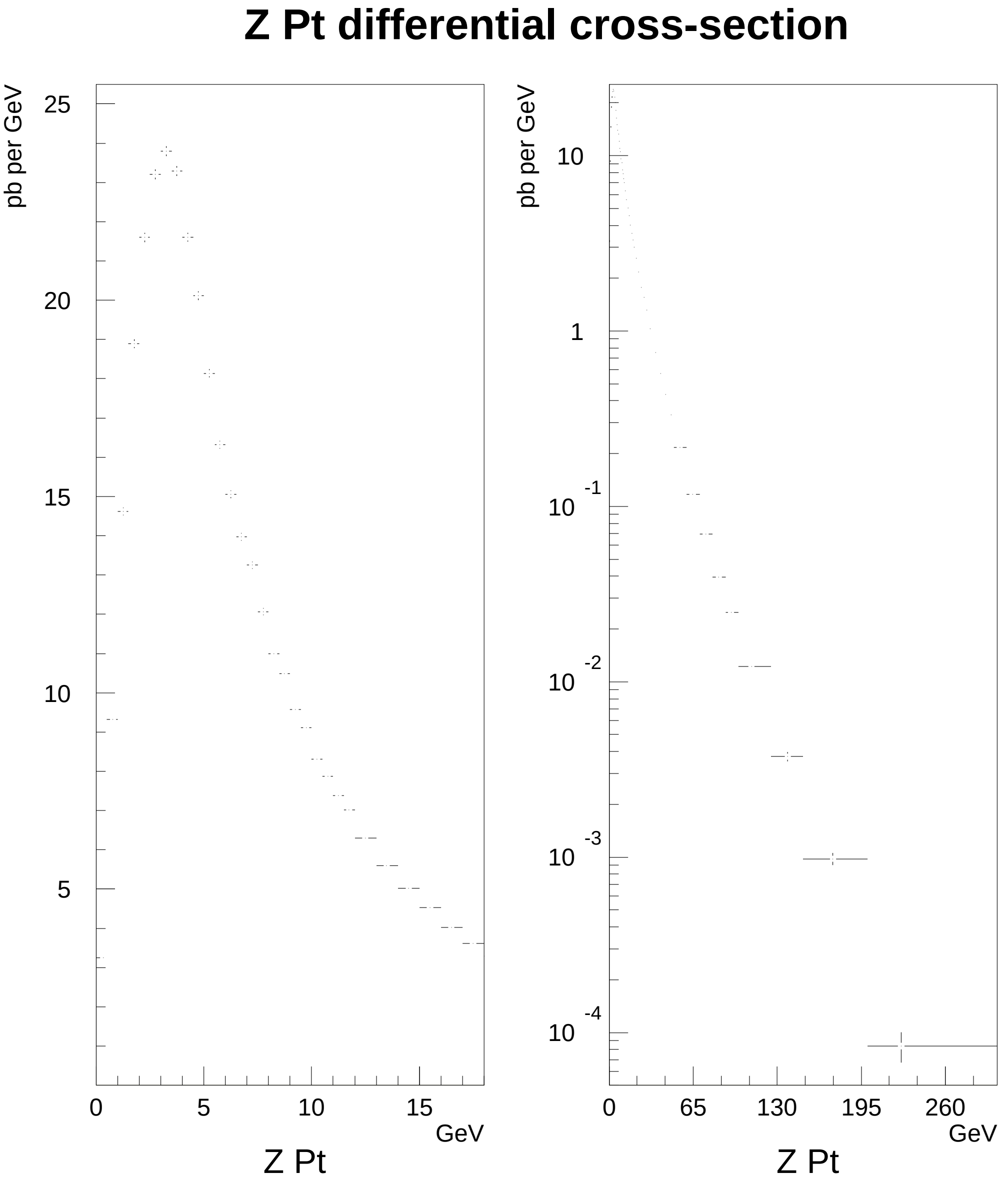

Figure 9.4: The detector-independent Z Pt spectrum

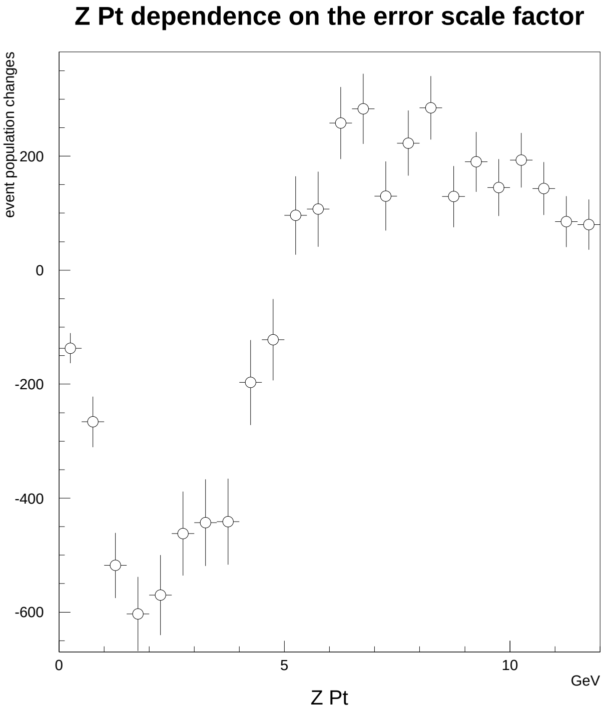

Figure 9.5: Difference between the smeared MC spectrum and the non-smeared MC spectrum

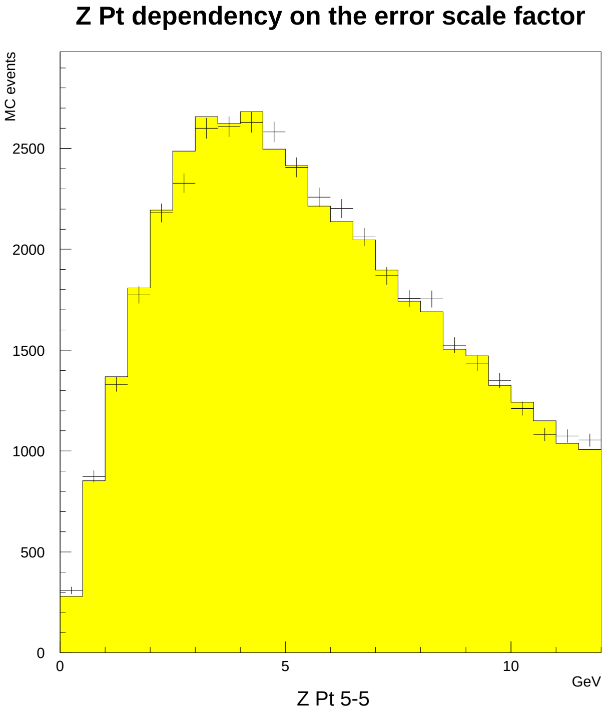

Figure 9.6: Effect on the measured MC spectrum when the error scale factor is increased by one sigma

would result in a different tuned Pythia parameters had the increased error scale factor been used instead).

Figure 9.7 shows the fractional event population changes. Despite the relatively poor statistics, the same characteristic shape change in the Z Pt spectrum as before can be discerned. These fractional population changes give a good estimate for the dependency of the Z Pt spectrum on the error scale factor, and hence for the dependency of the Z Pt spectrum on the Pythia tuning. An 2% systematic error is assigned when the Z Pt is below 5 GeV, and a 1% systematic error is assigned when the Z Pt is above 5 GeV.

It is necessary to take into account one other error before the final Z Pt differential cross-section plot is made. This is the Monte Carlo statistical error. Although a very large

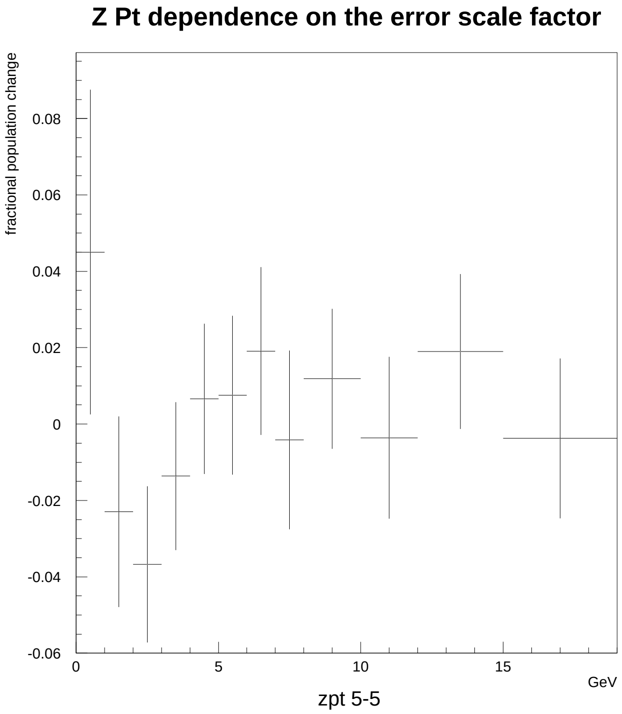

Figure 9.7: Fractional population changes when the error scale factor is increased

number of Monte Carlo events were simulated, the cross-section for the large Z Pt bins is so low that the Monte Carlo statistical error actually dominates in the high Pt region.

9.4 The Z Pt Differential Cross-section Measurement

Table 9.1 shows the differential Z Pt cross sections and their respective errors. Not shown are the overall normalization errors. There is a 2% overall normalization error from the statistics of the event sample and a 3.9% overall systematic normalization error from the measurement of the integrated luminosity. Figure 9.8 is the corresponding plot with all of the statistical and systematic errors included (including both of the normalization errors).

Pt Bin	Delta-Pt (GeV)	Bin Center (Gev)	$d\sigma/dP_T$ (pb/GeV)	syst (no lum) %	stat (MC) %
1	0.0 - 0.5	0.34	3.25	2.4	1.4
2	0.5 - 1.0	0.78	9.32	2.4	0.8
3	1.0 - 1.5	1.27	14.62	2.4	0.7
4	1.5 - 2.0	1.76	18.89	2.4	0.6
5	2.0 - 2.5	2.26	21.60	2.4	0.5
6	2.5 - 3.0	2.75	23.21	2.4	0.5
7	3.0 - 3.5	3.25	23.80	2.4	0.5
8	3.5 - 4.0	3.75	23.29	2.4	0.5
9	4.0 - 4.5	4.25	21.60	2.4	0.5
10	4.5 - 5.0	4.74	20.12	2.4	0.6
11	5.0 - 5.5	5.25	18.14	1.6	0.6

continued on next page

Pt Bin	Delta-Pt (GeV)	Bin Center (Gev)	$d\sigma/dP_T$ (pb/GeV)	syst (no lum) %	stat MC %
12	5.5 - 6.0	5.74	16.32	1.6	0.6
13	6.0 - 6.5	6.25	15.06	1.6	0.7
14	6.5 - 7.0	6.75	13.97	1.6	0.7
15	7.0 - 7.5	7.24	13.25	1.6	0.7
16	7.5 - 8.0	7.75	12.07	1.6	0.7
17	8.0 - 8.5	8.25	10.99	1.6	0.8
18	8.5 - 9.0	8.74	10.49	1.6	0.8
19	9.0 - 9.5	9.25	9.58	1.6	0.8
20	9.5 - 10.0	9.75	9.12	1.6	0.8
21	10.0 - 10.5	10.25	8.31	1.6	0.9
22	10.5 - 11.0	10.75	7.87	1.6	0.9
23	11.0 - 11.5	11.24	7.38	1.6	0.9
24	11.5 - 12.0	11.74	7.02	1.6	1.0
25	12.0 - 13.0	12.49	6.30	1.6	0.7
26	13.0 - 14.0	13.48	5.60	1.6	0.8
27	14.0 - 15.0	14.50	5.01	1.6	0.8
28	15.0 - 16.0	15.49	4.53	1.6	0.8
29	16.0 - 17.0	16.48	4.02	1.6	0.8
30	17.0 - 18.0	17.49	3.61	1.6	0.9
31	18.0 - 19.0	18.51	3.30	1.6	1.0
32	19.0 - 20.0	19.49	3.01	1.6	1.0
33	20.0 - 22.0	20.98	2.60	1.6	0.8
34	22.0 - 24.0	22.96	2.17	1.6	0.9
35	24.0 - 26.0	24.98	1.77	1.6	1.0
36	26.0 - 28.0	26.96	1.55	1.6	1.0

continued on next page

Pt Bin	Delta-Pt (GeV)	Bin Center (Gev)	$d\sigma/dP_T$ (pb/GeV)	syst (no lum) %	stat MC %
37	28.0 - 30.0	28.98	1.31	1.6	1.1
38	30.0 - 34.0	31.89	1.03	1.6	0.9
39	34.0 - 38.0	35.96	0.75	1.6	1.0
40	38.0 - 42.0	39.88	0.57	1.6	1.2
41	42.0 - 46.0	43.86	0.43	1.6	1.4
42	46.0 - 50.0	47.95	0.33	1.6	1.6
43	50.0 - 60.0	54.60	0.22	1.6	1.2
44	60.0 - 70.0	64.50	0.12	1.6	1.7
45	70.0 - 80.0	74.61	0.070	1.6	2.2
46	80.0 - 90.0	84.82	0.040	1.6	2.9
47	90.0 - 100.0	94.29	0.025	1.6	3.6
48	100.0 - 125.0	110.12	0.012	1.6	3.2
49	125.0 - 150.0	138.12	0.0037	1.6	5.9
50	150.0 - 200.0	173.06	0.0010	1.6	8.1
51	200.0 - 300.0	225.91	0.00008	1.6	19.6

Table 9.1: Z Pt differential cross-sections and the different errors

9.5 Comparison with the Electron Channel

The Z Pt differential cross-section has previously been measured in the electron channel [42]. This measurement deconvolutes the measured Z Pt spectrum in order to produce a data-predicted Z Pt differential cross-section spectrum. The muon and electron results are compared.

The measured integrated luminosity error is not included in the comparison, since this error should affect the two event samples the same way. Figure 9.9 shows this comparison. The circles represent the muon Z Pt differential cross-section values, and the squares represent the electron Z Pt differential cross-section values. As can be seen, the curves have the same shape, and almost all of the error bars between the two plots overlap.

The muon plot has a noticeably smaller peak than the electron plot. However, the measured muon Z production cross section, while in agreement with the measured electron Z production cross-section, is 3% smaller than the electron value. As a final check the

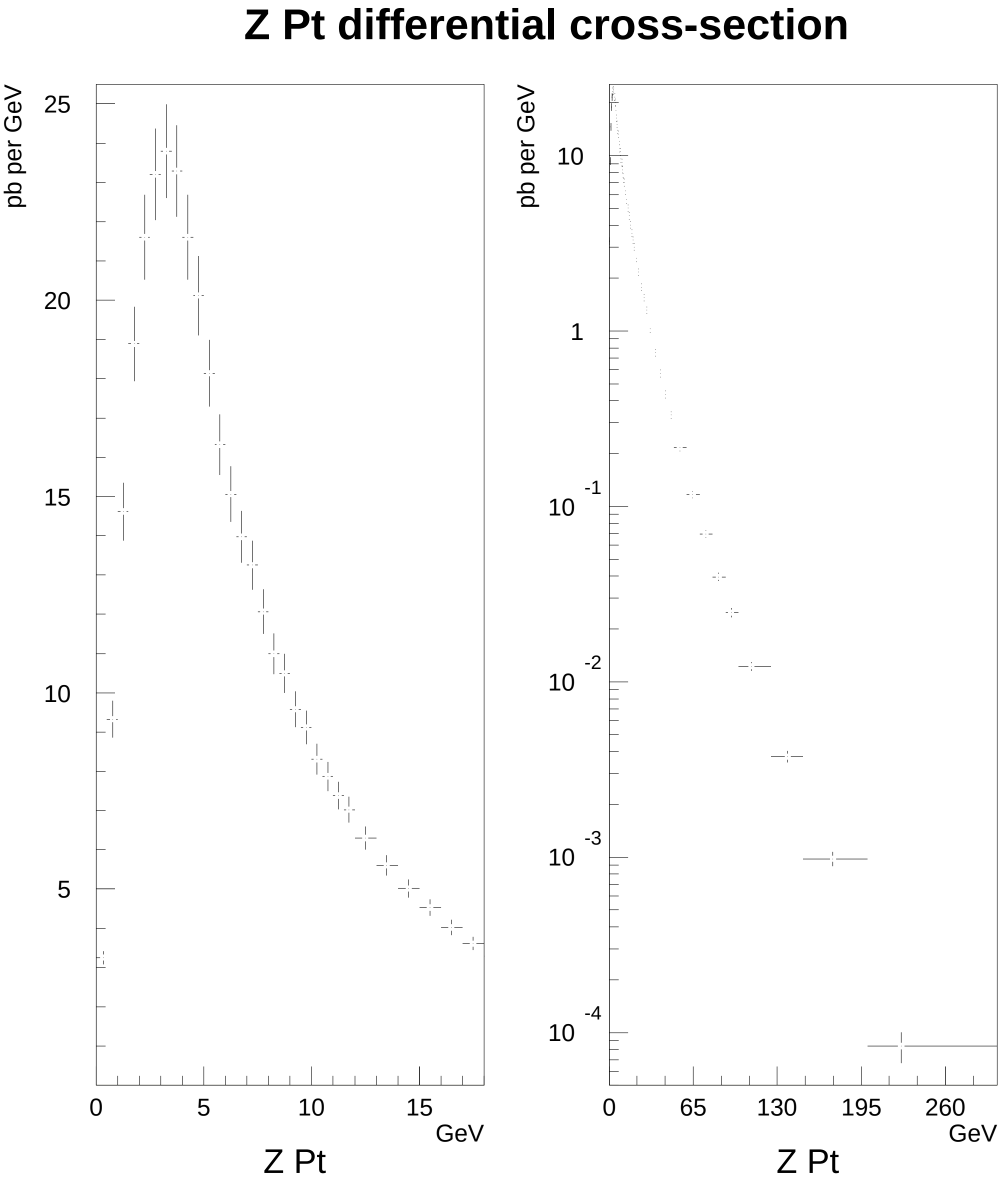

Figure 9.8: The Z Pt differential cross-section measurement

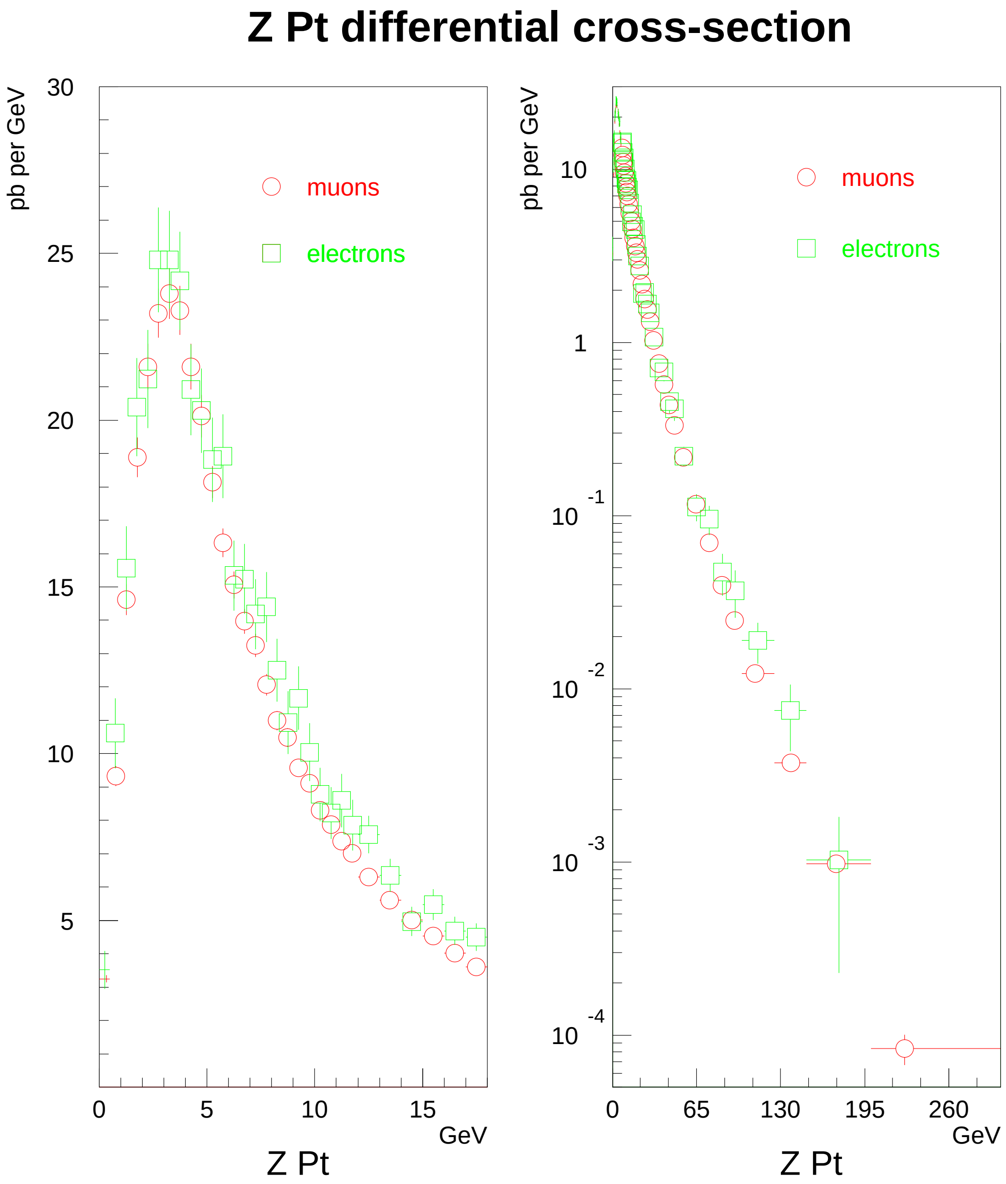

Figure 9.9: The Z Pt differential cross-section measurements in the muon and electron channels

electron Z production cross-section is normalized to the muon Z production cross-section and the curves are compared again. Figure 9.10 shows this comparison. As can be seen, there is no discernible difference in the shape of the two curves.

9.6 Conclusions

The code used to simulate the CDF detector response was extended significantly to represent the trigger selection of events. It was found that the extended Monte Carlo represented the event sample well. In addition, the Monte Carlo was tuned to simulate the tracking errors as well as the trigger and selection efficiencies. The Monte Carlo uses Pythia v6.2 [30] in conjunction with PHOTOS and the CTEQ 5L [44] structure functions. It was determined that the Pythia tuning parameters had to be adjusted in order to represent the low transverse momentum shape of the event sample, and again the modified Monte Carlo was determined to represent the event sample well. The overall Z production cross-section in the muon channel was then measured to be:

$\sigma_{Z \longrightarrow \mu^+\mu^-} = 241.3 \pm 6.3(stat + syst) \pm 10.2(lum)\ pb$

This measurement, agrees well with a similar measurement in the electron channel [42].

Finally, the muon Z Pt differential cross-section spectrum was produced (see figure 9.8). This plot was found to be in excellent agreement with the corresponding electron Z Pt differential cross-section spectrum, also shown (figure 9.9. In fact, when the electron spectrum is normalized to the muon spectrum it is hard to discern any difference between the two when they are plotted coincidentally (see figure 9.10).

No evidence for physics beyond the standard model is observed.

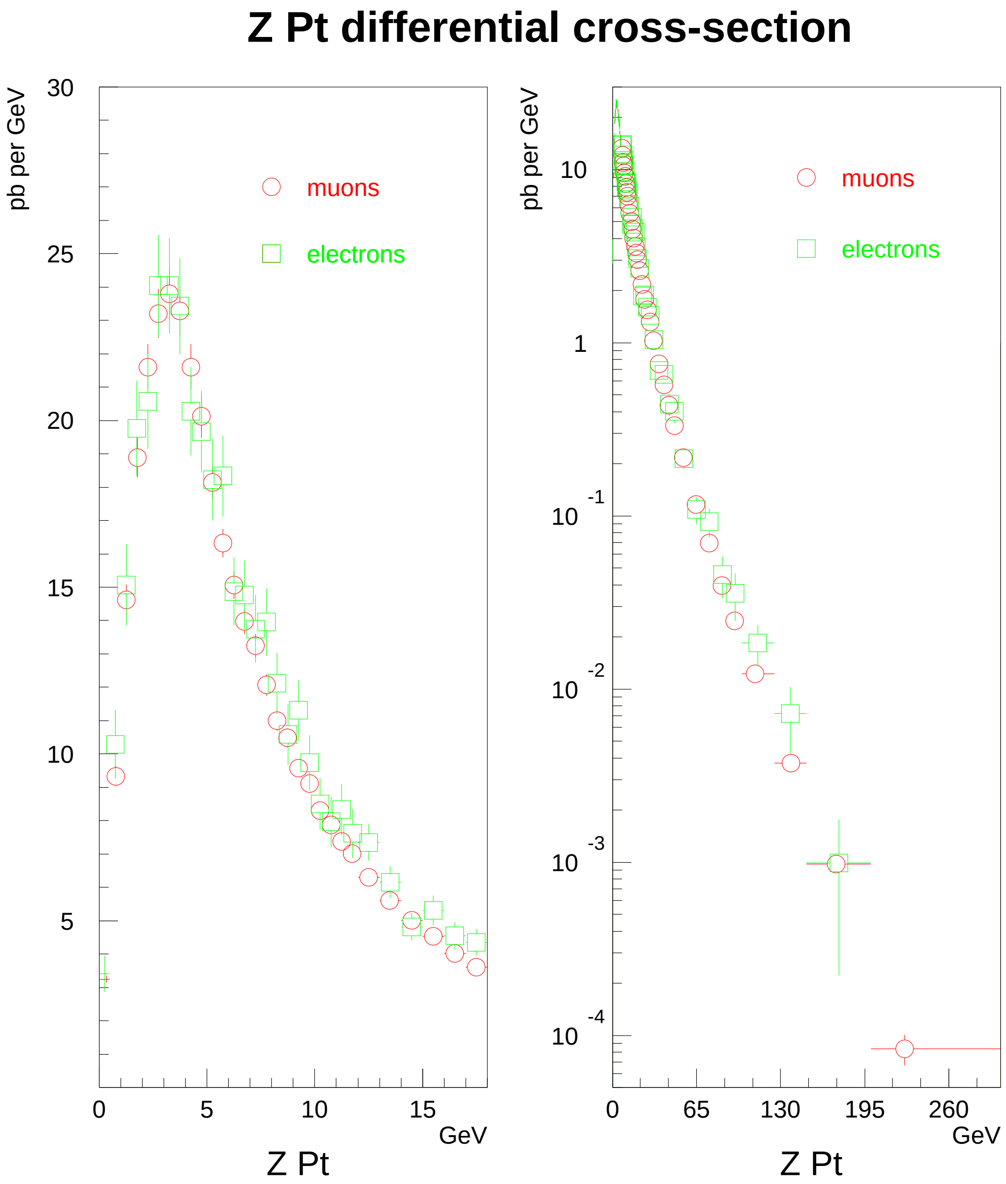

Figure 9.10: The Z Pt differential cross-section measurements in the muon and electron channels, when the electron Z production cross-section is normalized to the muon Z production cross-section

Appendices

Appendix A

The CDF Collaboration, run 1a

F. Abe,[13] M. G. Albrow,[7] D. Amidei,[16] J. Antos,[28] C. Anway-Wiese,[4] G. Apollinari,[26] H. Areti,[7] P. Auchincloss,[25] F. Azfar,[21] P. Azzi,[20] N. Bacchetta,[18] W. Badgett,[16] M. W. Bailey,[24] J. Bao,[34] P. de Barbaro,[25] A. Barbaro-Galtieri,[14] V. E. Barnes,[24] B. A. Barnett,[12] P. Bartalini,[23] G. Bauer,[15] T. Baumann,[9] F. Bedeschi,[23] S. Behrends,[2] S. Belforte,[23] G. Bellettini,[23] J. Bellinger,[33] D. Benjamin,[32] J. Benlloch,[15] D. Benton,[21] A. Beretvas,[7] J. P. Berge,[7] S. Bertolucci,[8] A. Bhatti,[26] K. Biery,[11] M. Binkley,[7] F. Bird,[29] D. Bisello,[20] R. E. Blair,[1] C. Blocker,[29] A. Bodek,[25] V. Bolognesi,[23] D. Bortoletto,[24] C. Boswell,[12] T. Boulos,[14] G. Brandenburg,[9] E. Buckley-Geer,[7] H. S. Budd,[25] K. Burkett,[16] G. Busetto,[20] A. Byon-Wagner,[7] K. L. Byrum,[1] C. Campagnari,[7] M. Campbell,[16] A. Caner,[7] W. Carithers,[14] D. Carlsmith,[33] A. Castro,[20] Y. Cen,[21] F. Cervelli,[23] J. Chapman,[16] M.-T. Cheng,[28] G. Chiarelli,[8] T. Chikamatsu,[31] S. Cihangir,[7] A. G. Clark,[23] M. Cobal,[23] M. Contreras,[5] J. Conway,[27] J. Cooper,[7] M. Cordelli,[8] D. P. Coupal,[29] D. Crane,[7] J. D. Cunningham,[2] T. Daniels,[15] F. DeJongh,[7] S. Delchamps,[7] S. Dell'Agnello,[23] M. Dell'Orso,[23] L. Demortier,[26] B. Denby,[23] M. Deninno,[3] P. F. Derwent,[16] T. Devlin,[27] M. Dickson,[25] S. Donati,[23] R. B. Drucker,[14] A. Dunn,[16] K. Einsweiler,[14] J. E. Elias,[7] R. Ely,[14] E. Engels, Jr.,[22] S. Eno,[5] D. Errede,[10] S. Errede,[10] Q. Fan,[25] B. Farhat,[15] I. Fiori,[3] B. Flaugher,[7] G. W. Foster,[7] M. Franklin,[9] M. Frautschi,[18] J. Freeman,[7] J. Friedman,[15] H. Frisch,[5] A. Fry,[29] T. A. Fuess,[1] Y. Fukui,[13] S. Funaki,[31] G. Gagliardi,[23] S. Galeotti,[23] M. Gallinaro,[20] A. F. Garfinkel,[24] S. Geer,[7] D. W. Gerdes,[16] P. Giannetti,[23] N. Giokaris,[26] P. Giromini,[8] L. Gladney,[21] D. Glenzinski,[12] M. Gold,[18] J. Gonzalez,[21] A. Gordon,[9] A. T. Goshaw,[6]

K. Goulianos,[26] H. Grassmann,[6] A. Grewal,[21] G. Grieco,[23] L. Groer,[27] C. Grosso-Pilcher,[5] C. Haber,[14] S. R. Hahn,[7] R. Hamilton,[9] R. Handler,[33] R. M. Hans,[34] K. Hara,[31] B. Harral,[21] R. M. Harris,[7] S. A. Hauger,[6] J. Hauser,[4] C. Hawk,[27] J. Heinrich,[21] D. Cronin-Hennessy,[6] R. Hollebeek,[21] L. Holloway,[10] A. Hölscher,[11] S. Hong,[16] G. Houk,[21] P. Hu,[22] B. T. Huffman,[22] R. Hughes,[25] P. Hurst,[9] J. Huston,[17] J. Huth,[9] J. Hylen,[7] M. Incagli,[23] J. Incandela,[7] H. Iso,[31] H. Jensen,[7] C. P. Jessop,[9] U. Joshi,[7] R. W. Kadel,[14] E. Kajfasz,[7a] T. Kamon,[30] T. Kaneko,[31] D. A. Kardelis,[10] H. Kasha,[34] Y. Kato,[19] L. Keeble,[30] R. D. Kennedy,[27] R. Kephart,[7] P. Kesten,[14] D. Kestenbaum,[9] R. M. Keup,[10] H. Keutelian,[7] F. Keyvan,[4] D. H. Kim,[7] H. S. Kim,[11] S. B. Kim,[16] S. H. Kim,[31] Y. K. Kim,[14] L. Kirsch,[2] P. Koehn,[25] K. Kondo,[31] J. Konigsberg,[9] S. Kopp,[5] K. Kordas,[11] W. Koska,[7] E. Kovacs,[7a] W Kowald,[6] M. Krasberg,[16] J. Kroll,[7] M. Kruse,[24] S. E. Kuhlmann,[1] E. Kuns,[27] A. T. Laasanen,[24] S. Lammel,[4] J. I. Lamoureux,[33] T. LeCompte,[10] S. Leone,[23] J. D. Lewis,[7] P. Limon,[7] M. Lindgren,[4] T. M. Liss,[10] N. Lockyer,[21] O. Long,[21] M. Loreti,[20] E. H. Low,[21] J. Lu,[30] D. Lucchesi,[23] C. B. Luchini,[10] P. Lukens,[7] P. Maas,[33] K. Maeshima,[7] A. Maghakian,[26] P. Maksimovic,[15] M. Mangano,[23] J. Mansour,[17] M. Mariotti,[23] J. P. Marriner,[7] A. Martin,[10] J. A. J. Matthews,[18] R. Mattingly,[2] P. McIntyre,[30] P. Melese,[26] A. Menzione,[23] E. Meschi,[23] G. Michail,[9] S. Mikamo,[13] M. Miller,[5] R. Miller,[17] T. Mimashi,[31] S. Miscetti,[8] M. Mishina,[13] H. Mitsushio,[31] S. Miyashita,[31] Y. Morita,[13] S. Moulding,[26] J. Mueller,[27] A. Mukherjee,[7] T. Muller,[4] P. Musgrave,[11] L. F. Nakae,[29] I. Nakano,[31] C. Nelson,[7] D. Neuberger,[4] C. Newman-Holmes,[7] L. Nodulman,[1] S. Ogawa,[31] S. H. Oh,[6] K. E. Ohl,[34] R. Oishi,[31] T. Okusawa,[19] C. Pagliarone,[23] R. Paoletti,[23] V. Papadimitriou,[7] S. Park,[7] J. Patrick,[7] G. Pauletta,[23] M. Paulini,[14] L. Pescara,[20] M. D. Peters,[14] T. J. Phillips,[6] G. Piacentino,[3] M. Pillai,[25] R. Plunkett,[7] L. Pondrom,[33] N. Produit,[14] J. Proudfoot,[1] F. Ptohos,[9] G. Punzi,[23] K. Ragan,[11] F. Rimondi,[3] L. Ristori,[23] M. Roach-Bellino,[32] W. J. Robertson,[6] T. Rodrigo,[7] J. Romano,[5] L. Rosenson,[15] W. K. Sakumoto,[25] D. Saltzberg,[5] A. Sansoni,[8] V. Scarpine,[30] A. Schindler,[14] P. Schlabach,[9] E. E. Schmidt,[7] M. P. Schmidt,[34] O. Schneider,[14] G. F. Sciacca,[23] A. Scribano,[23] S. Segler,[7] S. Seidel,[18] Y. Seiya,[31] G. Sganos,[11] A. Sgolacchia,[3] M. Shapiro,[14] N. M. Shaw,[24] Q. Shen,[24] P. F. Shepard,[22] M. Shimojima,[31] M. Shochet,[5] J. Siegrist,[29] A. Sill,[7a] P. Sinervo,[11]

P. Singh,[22] J. Skarha,[12] K. Sliwa,[32] D. A. Smith,[23] F. D. Snider,[12] L. Song,[7] T. Song,[16]
J. Spalding,[7] L. Spiegel,[7] P. Sphicas,[15] A. Spies,[12] L. Stanco,[20] J. Steele,[33] A. Stefanini,[23]
K. Strahl,[11] J. Strait,[7] D. Stuart,[7] G. Sullivan,[5] K. Sumorok,[15] R. L. Swartz, Jr.,[10] T. Takahashi,[19]
K. Takikawa,[31] F. Tartarelli,[23] W. Taylor,[11] Y. Teramoto,[19] S. Tether,[15] D. Theriot,[7]
J. Thomas,[29] T. L. Thomas,[18] R. Thun,[16] M. Timko,[32] P. Tipton,[25] A. Titov,[26] S. Tkaczyk,[7]
K. Tollefson,[25] A. Tollestrup,[7] J. Tonnison,[24] J. F. de Troconiz,[9] J. Tseng,[12] M. Turcotte,[29]
N. Turini,[3] N. Uemura,[31] F. Ukegawa,[21] G. Unal,[21] S. van den Brink,[22] S. Vejcik, III,[16]
R. Vidal,[7] M. Vondracek,[10] R. G. Wagner,[1] R. L. Wagner,[7] N. Wainer,[7] R. C. Walker,[25]
G. Wang,[23] J. Wang,[5] M. J. Wang,[28] Q. F. Wang,[26] A. Warburton,[11] G. Watts,[25] T. Watts,[27]
R. Webb,[30] C. Wendt,[33] H. Wenzel,[14] W. C. Wester, III,[14] T. Westhusing,[10] A. B. Wicklund,[1]
E. Wicklund,[7] R. Wilkinson,[21] H. H. Williams,[21] P. Wilson,[5] B. L. Winer,[25] J. Wolinski,[30]
D. Y. Wu,[16] X. Wu,[23] J. Wyss,[20] A. Yagil,[7] W. Yao,[14] K. Yasuoka,[31] Y. Ye,[11] G. P. Yeh,[7]
P. Yeh,[28] M. Yin,[6] J. Yoh,[7] T. Yoshida,[19] D. Yovanovitch,[7] I. Yu,[34] J. C. Yun,[7] A. Zanetti,[23]
F. Zetti,[23] L. Zhang,[33] S. Zhang,[15] W. Zhang,[21] and S. Zucchelli[3]

(CDF Collaboration)

[1] *Argonne National Laboratory, Argonne, Illinois 60439*

[2] *Brandeis University, Waltham, Massachusetts 02254*

[3] *Istituto Nazionale di Fisica Nucleare, University of Bologna, I-40126 Bologna, Italy*

[4] *University of California at Los Angeles, Los Angeles, California 90024*

[5] *University of Chicago, Chicago, Illinois 60637*

[6] *Duke University, Durham, North Carolina 27708*

[7] *Fermi National Accelerator Laboratory, Batavia, Illinois 60510*

[8] *Laboratori Nazionali di Frascati, Istituto Nazionale di Fisica Nucleare, I-00044 Frascati, Italy*

[9] *Harvard University, Cambridge, Massachusetts 02138*

[10] *University of Illinois, Urbana, Illinois 61801*

[11] *Institute of Particle Physics, McGill University, Montreal H3A 2T8, and University of Toronto,*

Toronto M5S 1A7, Canada

[12] *The Johns Hopkins University, Baltimore, Maryland 21218*

[13] *National Laboratory for High Energy Physics (KEK), Tsukuba, Ibaraki 305, Japan*

[14] *Lawrence Berkeley Laboratory, Berkeley, California 94720*

[15] *Massachusetts Institute of Technology, Cambridge, Massachusetts 02139*

[16] *University of Michigan, Ann Arbor, Michigan 48109*

[17] *Michigan State University, East Lansing, Michigan 48824*

[18] *University of New Mexico, Albuquerque, New Mexico 87131*

[19] *Osaka City University, Osaka 588, Japan*

[20] *Universita di Padova, Instituto Nazionale di Fisica Nucleare, Sezione di Padova, I-35131 Padova, Italy*

[21] *University of Pennsylvania, Philadelphia, Pennsylvania 19104*

[22] *University of Pittsburgh, Pittsburgh, Pennsylvania 15260*

[23] *Istituto Nazionale di Fisica Nucleare, University and Scuola Normale Superiore of Pisa, I-56100 Pisa, Italy*

[24] *Purdue University, West Lafayette, Indiana 47907*

[25] *University of Rochester, Rochester, New York 14627*

[26] *Rockefeller University, New York, New York 10021*

[27] *Rutgers University, Piscataway, New Jersey 08854*

[28] *Academia Sinica, Taiwan 11529, Republic of China*

[29] *Superconducting Super Collider Laboratory, Dallas, Texas 75237*

[30] *Texas A&M University, College Station, Texas 77843*

[31] *University of Tsukuba, Tsukuba, Ibaraki 305, Japan*

[32] *Tufts University, Medford, Massachusetts 02155*

[33] *University of Wisconsin, Madison, Wisconsin 53706*

[34] *Yale University, New Haven, Connecticut 06511*

Appendix B

The CDF Collaboration, run 1b

T. Affolder,[21] H. Akimoto,[42] A. Akopian,[35] M. G. Albrow,[10] P. Amaral,[7] S. R. Amendolia,[31] D. Amidei,[24] J. Antos,[1] G. Apollinari,[35] T. Arisawa,[42] T. Asakawa,[40] W. Ashmanskas,[7] M. Atac,[10] P. Azzi-Bacchetta,[29] N. Bacchetta,[29] M. W. Bailey,[26] S. Bailey,[14] P. de Barbaro,[34] A. Barbaro-Galtieri,[21] V. E. Barnes,[33] B. A. Barnett,[17] M. Barone,[12] G. Bauer,[22] F. Bedeschi,[31] S. Belforte,[39] G. Bellettini,[31] J. Bellinger,[43] D. Benjamin,[9] J. Bensinger,[4] A. Beretvas,[10] J. P. Berge,[10] J. Berryhill,[7] S. Bertolucci,[12] B. Bevensee,[30] A. Bhatti,[35] C. Bigongiari,[31] M. Binkley,[10] D. Bisello,[29] R. E. Blair,[2] C. Blocker,[4] K. Bloom,[24] B. Blumenfeld,[17] B. S. Blusk,[34] A. Bocci,[31] A. Bodek,[34] W. Bokhari,[30] G. Bolla,[33] Y. Bonushkin,[5] D. Bortoletto,[33] J. Boudreau,[32] A. Brandl,[26] S. van den Brink,[17] C. Bromberg,[25] N. Bruner,[26] E. Buckley-Geer,[10] J. Budagov,[8] H. S. Budd,[34] K. Burkett,[14] G. Busetto,[29] A. Byon-Wagner,[10] K. L. Byrum,[2] M. Campbell,[24] A. Caner,[31] W. Carithers,[21] J. Carlson,[24] D. Carlsmith,[43] J. Cassada,[34] A. Castro,[29] D. Cauz,[39] A. Cerri,[31] P. S. Chang,[1] P. T. Chang,[1] J. Chapman,[24] C. Chen,[30] Y. C. Chen,[1] M. -T. Cheng,[1] M. Chertok,[37] G. Chiarelli,[31] I. Chirikov-Zorin,[8] G. Chlachidze,[8] F. Chlebana,[10] L. Christofek,[16] M. L. Chu,[1] S. Cihangir,[10] C. I. Ciobanu,[27] A. G. Clark,[13] M. Cobal,[31] E. Cocca,[31] A. Connolly,[21] J. Conway,[36] J. Cooper,[10] M. Cordelli,[12] J. Guimaraes da Costa,[24] D. Costanzo,[31] J. Cranshaw,[38] D. Cronin-Hennessy,[9] R. Cropp,[23] R. Culbertson,[7] D. Dagenhart,[41] F. DeJongh,[10] S. Dell'Agnello,[12] M. Dell'Orso,[31]

R. Demina,[10] L. Demortier,[35] M. Deninno,[3] P. F. Derwent,[10] T. Devlin,[36] J. R. Dittmann,[10] S. Donati,[31] J. Done,[37] T. Dorigo,[14] N. Eddy,[16] K. Einsweiler,[21] J. E. Elias,[10] E. Engels, Jr.,[32] W. Erdmann,[10] D. Errede,[16] S. Errede,[16] Q. Fan,[34] R. G. Feild,[44] C. Ferretti,[31] I. Fiori,[3] B. Flaugher,[10] G. W. Foster,[10] M. Franklin,[14] J. Freeman,[10] J. Friedman,[22] Y. Fukui,[20] S. Gadomski,[23] S. Galeotti,[31] M. Gallinaro,[35] T. Gao,[30] M. Garcia-Sciveres,[21] A. F. Garfinkel,[33] P. Gatti,[29] C. Gay,[44] S. Geer,[10] D. W. Gerdes,[24] P. Giannetti,[31] P. Giromini,[12] V. Glagolev,[8] M. Gold,[26] J. Goldstein,[10] A. Gordon,[14] A. T. Goshaw,[9] Y. Gotra,[32] K. Goulianos,[35] H. Grassmann,[39] C. Green,[33] L. Groer,[36] C. Grosso-Pilcher,[7] M. Guenther,[33] G. Guillian,[24] R. S. Guo,[1] C. Haber,[21] E. Hafen,[22] S. R. Hahn,[10] C. Hall,[14] T. Handa,[15] R. Handler,[43] W. Hao,[38] F. Happacher,[12] K. Hara,[40] A. D. Hardman,[33] R. M. Harris,[10] F. Hartmann,[18] K. Hatakeyama,[35] J. Hauser,[5] J. Heinrich,[30] A. Heiss,[18] B. Hinrichsen,[23] K. D. Hoffman,[33] C. Holck,[30] R. Hollebeek,[30] L. Holloway,[16] R. Hughes,[27] J. Huston,[25] J. Huth,[14] H. Ikeda,[40] M. Incagli,[31] J. Incandela,[10] G. Introzzi,[31] J. Iwai,[42] Y. Iwata,[15] E. James,[24] H. Jensen,[10] M. Jones,[30] U. Joshi,[10] H. Kambara,[13] T. Kamon,[37] T. Kaneko,[40] K. Karr,[41] H. Kasha,[44] Y. Kato,[28] T. A. Keaffaber,[33] K. Kelley,[22] M. Kelly,[24] R. D. Kennedy,[10] R. Kephart,[10] D. Khazins,[9] T. Kikuchi,[40] M. Kirk,[4] B. J. Kim,[19] H. S. Kim,[23] S. H. Kim,[40] Y. K. Kim,[21] L. Kirsch,[4] S. Klimenko,[11] D. Knoblauch,[18] P. Koehn,[27] A. Köngeter,[18] K. Kondo,[42] J. Konigsberg,[11] K. Kordas,[23] A. Korytov,[11] E. Kovacs,[2] J. Kroll,[30] M. Kruse,[34] S. E. Kuhlmann,[2] K. Kurino,[15] T. Kuwabara,[40] A. T. Laasanen,[33] N. Lai,[7] S. Lami,[35] S. Lammel,[10] J. I. Lamoureux,[4] M. Lancaster,[21] G. Latino,[31] T. LeCompte,[2] A. M. Lee IV,[9] S. Leone,[31] J. D. Lewis,[10] M. Lindgren,[5] T. M. Liss,[16] J. B. Liu,[34] Y. C. Liu,[1] N. Lockyer,[30] M. Loreti,[29] D. Lucchesi,[29] P. Lukens,[10] S. Lusin,[43] J. Lys,[21] R. Madrak,[14] K. Maeshima,[10] P. Maksimovic,[14] L. Malferrari,[3] M. Mangano,[31] M. Mariotti,[29] G. Martignon,[29] A. Martin,[44] J. A. J. Matthews,[26] P. Mazzanti,[3] K. S. McFarland,[34] P. McIntyre,[37] E. McKigney,[30] M. Menguzzato,[29] A. Menzione,[31] E. Meschi,[31] C. Mesropian,[35] C. Miao,[24] T. Miao,[10] R. Miller,[25] J. S. Miller,[24] H. Minato,[40] S. Miscetti,[12] M. Mishina,[20] N. Moggi,[31] E. Moore,[26] R. Moore,[24] Y. Morita,[20] A. Mukherjee,[10] T. Muller,[18]

A. Munar,[31] P. Murat,[31] S. Murgia,[25] M. Musy,[39] J. Nachtman,[5] S. Nahn,[44] H. Nakada,[40] T. Nakaya,[7] I. Nakano,[15] C. Nelson,[10] D. Neuberger,[18] C. Newman-Holmes,[10] C.-Y. P. Ngan,[22] P. Nicolaidi,[39] H. Niu,[4] L. Nodulman,[2] A. Nomerotski,[11] S. H. Oh,[9] T. Ohmoto,[15] T. Ohsugi,[15] R. Oishi,[40] T. Okusawa,[28] J. Olsen,[43] C. Pagliarone,[31] F. Palmonari,[31] R. Paoletti,[31] V. Papadimitriou,[38] S. P. Pappas,[44] A. Parri,[12] D. Partos,[4] J. Patrick,[10] G. Pauletta,[39] M. Paulini,[21] A. Perazzo,[31] L. Pescara,[29] T. J. Phillips,[9] G. Piacentino,[31] K. T. Pitts,[10] R. Plunkett,[10] A. Pompos,[33] L. Pondrom,[43] G. Pope,[32] F. Prokoshin,[8] J. Proudfoot,[2] F. Ptohos,[12] G. Punzi,[31] K. Ragan,[23] D. Reher,[21] A. Ribon,[29] F. Rimondi,[3] L. Ristori,[31] W. J. Robertson,[9] A. Robinson,[23] T. Rodrigo,[6] S. Rolli,[41] L. Rosenson,[22] R. Roser,[10] R. Rossin,[29] W. K. Sakumoto,[34] D. Saltzberg,[5] A. Sansoni,[12] L. Santi,[39] H. Sato,[40] P. Savard,[23] P. Schlabach,[10] E. E. Schmidt,[10] M. P. Schmidt,[44] M. Schmitt,[14] L. Scodellaro,[29] A. Scott,[5] A. Scribano,[31] S. Segler,[10] S. Seidel,[26] Y. Seiya,[40] A. Semenov,[8] F. Semeria,[3] T. Shah,[22] M. D. Shapiro,[21] P. F. Shepard,[32] T. Shibayama,[40] M. Shimojima,[40] M. Shochet,[7] J. Siegrist,[21] G. Signorelli,[31] A. Sill,[38] P. Sinervo,[23] P. Singh,[16] A. J. Slaughter,[44] K. Sliwa,[41] C. Smith,[17] F. D. Snider,[10] A. Solodsky,[35] J. Spalding,[10] T. Speer,[13] P. Sphicas,[22] F. Spinella,[31] M. Spiropulu,[14] L. Spiegel,[10] L. Stanco,[29] J. Steele,[43] A. Stefanini,[31] J. Strologas,[16] F. Strumia, [13] D. Stuart,[10] K. Sumorok,[22] T. Suzuki,[40] R. Takashima,[15] K. Takikawa,[40] M. Tanaka,[40] T. Takano,[28] B. Tannenbaum,[5] W. Taylor,[23] M. Tecchio,[24] P. K. Teng,[1] K. Terashi,[40] S. Tether,[22] D. Theriot,[10] R. Thurman-Keup,[2] P. Tipton,[34] S. Tkaczyk,[10] K. Tollefson,[34] A. Tollestrup,[10] H. Toyoda,[28] W. Trischuk,[23] J. F. de Troconiz,[14] S. Truitt,[24] J. Tseng,[22] N. Turini,[31] F. Ukegawa,[40] J. Valls,[36] S. Vejcik III,[10] G. Velev,[31] R. Vidal,[10] R. Vilar,[6] I. Vologouev,[21] D. Vucinic,[22] R. G. Wagner,[2] R. L. Wagner,[10] J. Wahl,[7] N. B. Wallace,[36] A. M. Walsh,[36] C. Wang,[9] C. H. Wang,[1] M. J. Wang,[1] T. Watanabe,[40] T. Watts,[36] R. Webb,[37] H. Wenzel,[18] W. C. Wester III,[10] A. B. Wicklund,[2] E. Wicklund,[10] H. H. Williams,[30] P. Wilson,[10] B. L. Winer,[27] D. Winn,[24] S. Wolbers,[10] D. Wolinski,[24] J. Wolinski,[25] S. Worm,[26] X. Wu,[13] J. Wyss,[31] A. Yagil,[10] W. Yao,[21] G. P. Yeh,[10] P. Yeh,[1] J. Yoh,[10] C. Yosef,[25] T. Yoshida,[28] I. Yu,[19] S. Yu,[30] A. Zanetti,[39] F. Zetti,[21] and S. Zucchelli[3]

(CDF Collaboration)

[1] *Institute of Physics, Academia Sinica, Taipei, Taiwan 11529, Republic of China*

[2] *Argonne National Laboratory, Argonne, Illinois 60439*

[3] *Istituto Nazionale di Fisica Nucleare, University of Bologna, I-40127 Bologna, Italy*

[4] *Brandeis University, Waltham, Massachusetts 02254*

[5] *University of California at Los Angeles, Los Angeles, California 90024*

[6] *Instituto de Fisica de Cantabria, University of Cantabria, 39005 Santander, Spain*

[7] *Enrico Fermi Institute, University of Chicago, Chicago, Illinois 60637*

[8] *Joint Institute for Nuclear Research, RU-141980 Dubna, Russia*

[9] *Duke University, Durham, North Carolina 27708*

[10] *Fermi National Accelerator Laboratory, Batavia, Illinois 60510*

[11] *University of Florida, Gainesville, Florida 32611*

[12] *Laboratori Nazionali di Frascati, Istituto Nazionale di Fisica Nucleare, I-00044 Frascati, Italy*

[13] *University of Geneva, CH-1211 Geneva 4, Switzerland*

[14] *Harvard University, Cambridge, Massachusetts 02138*

[15] *Hiroshima University, Higashi-Hiroshima 724, Japan*

[16] *University of Illinois, Urbana, Illinois 61801*

[17] *The Johns Hopkins University, Baltimore, Maryland 21218*

[18] *Institut für Experimentelle Kernphysik, Universität Karlsruhe, 76128 Karlsruhe, Germany*

[19] *Korean Hadron Collider Laboratory: Kyungpook National University, Taegu 702-701; Seoul National University, Seoul 151-742; and SungKyunKwan University, Suwon 440-746; Korea*

[20] *High Energy Accelerator Research Organization (KEK), Tsukuba, Ibaraki 305, Japan*

[21] *Ernest Orlando Lawrence Berkeley National Laboratory, Berkeley, California 94720*

[22] *Massachusetts Institute of Technology, Cambridge, Massachusetts 02139*

[23] *Institute of Particle Physics: McGill University, Montreal H3A 2T8; and University of Toronto, Toronto M5S 1A7; Canada*

[24] *University of Michigan, Ann Arbor, Michigan 48109*

[25] *Michigan State University, East Lansing, Michigan 48824*

[26] *University of New Mexico, Albuquerque, New Mexico 87131*

[27] *The Ohio State University, Columbus, Ohio 43210*

[28] *Osaka City University, Osaka 588, Japan*

[29] *Universita di Padova, Istituto Nazionale di Fisica Nucleare, Sezione di Padova, I-35131 Padova, Italy*

[30] *University of Pennsylvania, Philadelphia, Pennsylvania 19104*

[31] *Istituto Nazionale di Fisica Nucleare, University and Scuola Normale Superiore of Pisa, I-56100 Pisa, Italy*

[32] *University of Pittsburgh, Pittsburgh, Pennsylvania 15260*

[33] *Purdue University, West Lafayette, Indiana 47907*

[34] *University of Rochester, Rochester, New York 14627*

[35] *Rockefeller University, New York, New York 10021*

[36] *Rutgers University, Piscataway, New Jersey 08855*

[37] *Texas A&M University, College Station, Texas 77843*

[38] *Texas Tech University, Lubbock, Texas 79409*

[39] *Istituto Nazionale di Fisica Nucleare, University of Trieste/ Udine, Italy*

[40] *University of Tsukuba, Tsukuba, Ibaraki 305, Japan*

[41] *Tufts University, Medford, Massachusetts 02155*

[42] *Waseda University, Tokyo 169, Japan*

[43] *University of Wisconsin, Madison, Wisconsin 53706*

[44] *Yale University, New Haven, Connecticut 06520*

Bibliography

[1] A. Pickering, *Constructing Quarks*, for an excellent history on the development of elementary particle physics

[2] P. Huang and C. Quigg, *Intermediate Bosons: Weak Interaction Couriers*, Science, Vol 210, p1205, 1980

[3] C. Quigg, *Elementary Particles and Forces*, Scientific American, 1980

[4] F. Abe, et al (The CDF Collaboration), *The CDF Detector: An Overview*, Nucl. Instr. and Meth. **A271**, 387-403 (1988).

[5] D. Amidei, et al, *The Silicon Vertex Detector of the Collider Detector at Fermilab*, Nucl. Instr. and Meth. **A350**, 73-130

[6] Lee Holloway, Pisa, June 15, 1989

[7] F. James and M. Roos, Nucl. Phys. B172, 475 (1980)

[8] C.J. Clopper and E.S. Pearson, Biometrika 26, 404 (1934)

[9] B. Roe, *Probability and Statistics in Experimental Physics*

[10] Flannery, Teukolsky, Vettering, *Numerical Recipes*

[11] Flannery, Teukolsky, Vettering, *Numerical Recipes, p532ff, Use of Constant Chi-Squared Boundaries as Confidence Limits*

[12] MINUIT, Application Software Group, Computing and Networks Division, CERN, Geneva, Switzerland

[13] F. Abe, et al, (The CDF Collaboration) *Observation of Top Quark Production in $\bar{p}p$ Collisions with the CDF Detector at Fermilab*, Phys. Rev. Lett. **74**, 2626 (1995).

[14] E. Laenen, et al, *Phys Lett.* **B321**, 254, (1994).

[15] F. Abe, et al, (The CDF Collaboration), *Measurement of the $p\bar{p}$ Total Cross Section at $\sqrt{s} = 546$ GeV and 1.8 TeV*, Fermilab Preprint FERMILAB-PUB-93-234-E (Nov 1993); Submitted to Phys. Rev. D.

[16] F. Abe, et al, (The CDF Collaboration), *The Charge Asymmetry in W Boson Decays Produced in $\bar{p}p$ Collisions at $\sqrt{s} = 1.8TeV$*, to be published in Phys. Rev. Lett..

[17] R. R. Wilson, *The Tevatron*, Phys. Today **10**, 23-30 (1977).

[18] F. Abe, et al (The CDF Collaboration), *The CDF Detector: An Overview, Nucl. Instr. and Meth.* **A271**, 387-403 (1988).

[19] F. Bedeschi, et al, *Design and Construction of the CDF Central Tracking Chamber*, Nucl. Instr. and Meth. **A268**, 50-74 (1988).

[20] L. Balka, et al, *The CDF Central Electromagnetic Calorimeter*, Nucl. Instr. and Meth. **A267** 272-279 (1988).

[21] *The CDF Beam-Beam Counters*, Nucl. Instr. and Meth

[22] *Deeply Inelastic Large Impact Collisions*

[23] Pseudorapidity, η, is defined as

$$\eta = -\ln\left(\tan\left(\frac{\theta}{2}\right)\right)$$

with θ measured assuming a z-vertex position of zero unless otherwise noted.

[24] *The CDF Vertex Detector*, Nucl. Instr. and Meth. (1994).

[25] S. Bertolucci, et al, *The CDF Central and Endwall Hadron Calorimeter*, Nucl. Instr. and Meth. **A267** 301-314 (1988).

[26] G. Ascoli, et al, *CDF Central Muon Detector*, Nucl. Instr. and Meth. **A268** 33-40 (1988).

[27] G. Kane, *Modern Elementaty Particle Physics*, p10

[28] thanks to Willis Sakumoto for helping me to integrate this package into the standard CDF code environment, and also for his advice on anything related to the CTC and also to QED radiative effects on the Z mass.

[29] thanks to Phil Schlabach for all of his help, especially for his routine called CMUOTR which was invaluable for figuring out the boudaries of the different CTC superlayers.

[30] T. Sjostrand, Computer Physics Commun. 82 (1994) 74.

[31] A. Gauthier, et al, *Design and Performance of Drift Chambers for the Central Muon Upgrade of the CDF Detector*, Nucl. Instr. and Meth.

[32] F. Abe, et al, (The CDF Collaboration), *Evidence for Top Quark Production in* $p\bar{p}$ *Collisions at* $\sqrt{s} = 1.8$ *TeV*, Fermilab Preprint FERMILAB-PUB-94-097-E (April 1994). Submitted to Phys. Rev. D.

[33] F. Abe, et al, (The CDF Collaboration), Phys. Rev. D52, 4784 (1995).

[34] G. Drake, et al, *CDF Front End Electronics: The RABBIT System*, Nucl. Instr. and Meth. **A269**, 68-81 (1988).

[35] D. Amidei, et al, *A Two Level Fastbus Based Trigger System for CDF*, Nucl. Instr. and Meth. **A269**, 51-62 (1988).

[36] G. Ascoli, et al, *CDF Central Muon Level 1 Trigger Electronics*, Nucl. Instr. and Meth. **A269**, 63-67 (1988).

[37] O. Rind, *A Study of Isolated Photons in Hadronic Decays of the Z at LEP using the L3 Detector*

[38] W. Badgett, *Measurement of* $\sigma \cdot B(W \to \mu\nu)$, $\sigma \cdot B(Z^0 \to \mu^+\mu^-)$ *and* $R_\mu = \sigma \cdot B(W \to \mu\nu)/\sigma \cdot B(Z^0 \to \mu^+\mu^-)$ *and Extraction of* $BR(W \to \mu\nu)$ *and* $\Gamma(W)$ *in* $p\bar{p}$ *Collisions at* $\sqrt{s} = 1.8$ *TeV*, Ph.D. thesis, University of Michigan (1994).

[39] G. W. Foster, et al, *A Fast Hardware Track Finder for the CDF Central Tracking Chambers*, Nucl. Instr. and Meth. **A269**, 93-100 (1988).

[40] J.T. Carrol, et al, *The CDF Level 3 Trigger*, Nucl. Instr. and Meth. **A300**, 552-567 (1991).

[41] The CDF Collaboration *Measurement of the Z Pt Distribution in* $\bar{p}p$ *Collisions at* $\sqrt{s} = 1.8$ *TeV*, Submitted to Phys. Rev. Lett. July 1991.

[42] The CDF Collaboration *Measurement of the Z Pt Distribution in* $\bar{p}p$ *Collisions at* $\sqrt{s} = 1.8$ *TeV in the electron channel*, T. Affolder, et al, Physical Review Letters Vol 85, Number 5, January 2000.

[43] this value is based on next to leading order theoretical calculations and was supplied by W. Sakumoto the day before I had to turn my thesis in to my committee

[44] *GLOBAL QCD ANALYSIS OF PARTON STRUCTURE OF THE NUCLEON: CTEQ5 PPARTON DISTRIBUTIONS*, hep-ph/9903282; to be published in Eur. Phys. J. C 1999.

[45] Measurement of Z^0 and Drell-Yan prduction cross sections using dimuons in $\bar{p}p$ Collisions at $\sqrt{s} = 1.8$ TeV, F. Abe et al, Physical Review Letters Vol 59, 1999.

[46] Numerical Recipes, Press, Flannery, Teukolsky and Vettering, p470ff.